FACULTY
OF MATHEMATICS
AND PHYSICS
Charles University

DOCTORAL THESIS

Marta García Rivas

Interaction between solar convection and magnetic fields

Astronomical Institute of Charles University

Supervisor of the doctoral thesis:	Jan Jurčák PhD.
Study programme:	Theoretical Physics, Astronomy and Astrophysics (P4F1)

Prague 2024

I declare that I carried out this doctoral thesis on my own, and only with the cited sources, literature and other professional sources. I understand that my work relates to the rights and obligations under the Act No. 121/2000 Sb., the Copyright Act, as amended, in particular the fact that the Charles University has the right to conclude a license agreement on the use of this work as a school work pursuant to Section 60 subsection 1 of the Copyright Act.

In .... date ....

Author's signature

Acknowledgements

First of all, I would like to thank my supervisor, Jan Jurčák for his immense support. Not only did he share his great knowledge with me and guide me through the scientific part of the PhD, but he was always ready to help, support and be available for me. I would like to thank Jan for his immense patience and for always providing the clarity to see the forest through the trees. His calm, simple and efficient way of dealing with any situation is admirable and I have tried to learn as much as possible from him. Of course, this work would not have been possible without him.

Secondly, I would like to thank Nazaret Bello González. It is thanks to her that I decided to follow solar pores. Her motivation, determination and happiness are something I admire a lot. The way she talks about science is very inspiring. This PhD would not have started without her. Every visit to KIS, with her and KIS colleagues, is a delight.

I would like to thank my colleagues at the Astronomical Institute of the CAS who, in one way or another, have contributed scientifically and personally to this thesis. The May 2022 observing campaign was a great success thanks to the expertise of Michal Sobotka, and the work routine we have been immersed in since then has been very interesting. I would like to thank the flare team for allowing me to learn a lot from them. A special thanks goes to Jana Kašparová, who is always available, helpful and ready to join other projects, like outreach activities. I also don't want to forget about Galina Motorina who, although she is no longer working with us, has been a good friend and colleague. She included me in her flare project, which has opened many interesting doors for which I will always be grateful. But life is not all about work, and I am very thankful for being surrounded by creative, funny and, overall, nice people who make everyday an enjoyable experience.

This work has been supported by (1) project 204119 from the Grant Agency of Charles University, (2) the Czech Science Foundation grant project 18-06319S, (3) the Czech-German common grant, funded by the Czech Science Foundation under the project 23-07633K and by the Deutsche Forschungsgemeinschaft under the project BE 5771/3-1 (eBer-23-13412), (4) the institutional support ASU:67985815 from the Czech Academy of Sciences, and (5) the Czech Science Foundation grant project 22-07155S.

On a more personal note, I would like to thank my friends, the new and old. My Czech life started with a warm welcome from Martina, Kuba, and Sajri with whom we have shared great adventures, moments and tons of beer. I could not have had a better welcoming and introduction to the Czech life. Looking forward to the next bonfire! To Víctor and Esther, my Spanish anchors in Czechia, thank you for all the good moments. We have come a long way since we first met at the Czech course! Even though a great distance separates us, my Spanish friends have always been there. Christmas is the time of reunions but WhatsApp audios in the form of podcasts and never-ending calls in the forest have been something that has kept us together. Special mention to los Voldemores: Lucía, Carlos and Doran, and to Espe, Pipe and Mayra. I am also looking forward to meeting the new member of the group, Carmen. Those who know me well know that I tend to finish everything at the last minute, so if I have forgotten to mention anyone, sorry, I was in a hurry!

A mi familia, a mis padres y a mis hermanos Ana y Javichi, por estar siempre, siempre, siempre ahí, apoyándome en lo que haga falta. Yo digo rana y ellos saltan, cada uno a su modo. Muchas gracias por todo. Y por supuesto, gracias a los nuevos miembros, Marta y Alba, quienes llenan nuestros días (y nuestro teléfono) de fotos y vídeos y de alegría. También quiero recordar a Abuelita quien, aunque llegó a ver el inicio de esta aventura, no llegó a verla acabada. A ella, como a mis padres, les quiero agradecer tantas semillas que sembraron cuando yo era niña y que han ido floreciendo

con los años. La tira del cómic de Tintín es en honor a ella, en recuerdo de tantas horas que pasamos en su casa viendo y leyendo Las Aventuras de Tintín.

Last but not least, I must thank my 24/7 furry partner, Calima. Her active spirit and her willingness to do anything regardless of the time of day or weather, is something to be admired! She has walked side by side with me through this PhD, so I think it is only fair that she gets a title as well. Woof, woof, Dogtor Calima!

Title: Interaction between solar convection and magnetic fields

Author: Marta García Rivas

Institute: Astronomical Institute of Charles University

Supervisor: Jan Jurčák PhD., Astronomical Institute of the Czech Academy of Sciences

Abstract: Jurčák et al. (2018) demonstrated the existence of a constant vertical magnetic field at the umbra-penumbra boundary of stable sunspots. Due to the similar magnetoconvective modes observed in umbrae and pores, we aim to investigate the similarities between umbrae and pores in terms of their magnetic properties. In addition, we intend to monitor the magnetic properties during the transition between different magnetoconvective modes. We find that the magnetic properties at the boundary of a pore behave similarly to sunspots umbral boundaries during the formation, stability and decay. Although a pore also has a critical vertical field, it is weaker than in sunspots. The formation of penumbral filaments around a protospot does not seem to be related to the pre-existing type of magnetoconvection. In all observed cases, the penumbral filaments form at the umbral boundary and extend radially outwards, while the Evershed flow is observed from the beginning.

Keywords: Sunspots, solar pores, photosphere, spectropolarimetry, magnetoconvection

Název práce: Interakce konvekce a magnetických polí na Slunci

Autor: Marta García Rivas

Ústav: Astronomický ústav UK

Vedoucí doktorské práce: Jan Jurčák PhD., Astronomický ústav AV ČR, v. v. i.

Abstrakt: Jurčák et al. (2018) prokázali existenci konstantního vertikálního magnetického pole na hranici umbra-penumbra stabilních slunečních skvrn. Vzhledem k podobným magnetokonvekčním režimům pozorovaným v umbrách a slunečních pórech je naším cílem prozkoumat podobnosti mezi umbrami a póry z hlediska jejich magnetických vlastností. Kromě toho máme v úmyslu sledovat magnetické vlastnosti během přechodu mezi různými magnetokonvekčními režimy. Zjistili jsme, že magnetické vlastnosti na hranici pórů se chovají podobně jako v případě umbrální hranice slunečních skvrn během jejich vzniku, stability a zániku. Ačkoli póry mají také kritické vertikální pole, je slabší než u slunečních skvrn. Vznik penumbrálních filamentů kolem formující se skvrny zřejmě nesouvisí s typem magnetokonvekce, kterou pozorujeme předtím. Ve všech pozorovaných případech se penumbrální filamenty tvoří na hranici umbry a rozšiřují se radiálně směrem ven, přičemž Evershedův tok v nich pozorujeme od začátku.

Klíčová slova: Sluneční skvrny, sluneční póry, fotosféra, spektropolarimetrie, magnetokonvekce

Contents

Acronym index

AIA	Atmospheric Imaging Assembly
AR	active region
BFI	Broadband Filter Imager
CME	coronal mass ejection
EIS	EUV Imaging Spectrometer
EUV	extreme-ultraviolet
EVE	EUV Variability Experiment
FWHM	full width at half maximum
FOV	field of view
FUV	far UV
GFPI	“Göttingen” Fabry-Pérot Interferometer
G-T	Gough and Tayler
HMI	Helioseismic and Magnetic Imager
HMI$_{\mathrm{dcon}}$	HMI data corrected for scattered light
IFU	integral field unit
IRIS	Interface Region Imaging Spectrograph
LOS	line-of-sight
LTE	local thermodynamic equilibrium
M-E	Milne-Eddington
MERLIN	Milne-Eddington gRid Linear Inversion Network
MHD	magnetohydrodynamic
MMF	magnetic moving feature
NIR	near-infrared
NFI	Narrowband Filter Imager
NUV	near UV
PIL	polarity inversion line
RF	response function
RTE	radiative transfer equation
SDO	Solar Dynamics Observatory
SIR	Stokes Inversion based on Response functions
SO	Solar Orbiter
SOT	Solar Optical Telescope
SP/Hinode	Spectropolarimeter on board of Hinode
UP	umbra-penumbra
UV	ultraviolet
VFISV	Very Fast Inversion of the Stokes Vector
VTT	Vacuum Tower Telescope
XRT	X-Ray Telescope

List of Figures

Preface

The Sun, the brightest astronomical object observed from the Earth, has piqued the interest of humans since the beginning of time. Numerous astronomical observatories are found all over the globe dating back hundreds, even thousands, of years. Understanding solar behaviour (solstices, equinoxes) has always been fundamental in order to adapt human lives and survival activities accordingly. The prediction of uncommon phenomena, such as eclipses, proved their models right or terrified the masses (recurring topic in popular culture, such as in Fig. 1).

The mystical role played by the Sun in societies has evolved side by side with our understanding of it. From a God (Inti, Ra, Helios, Tonatiuh, Surya, Kinich Ahau...) to a standard G-type main sequence star, our Sun has been devalued in exchange for a richer and more complex perception of our Universe. We have learned that there is no magic. There might be unknown forces influencing our lives and surroundings, but it is a matter of study and technology to get to discover them.

Figure 1 Popular representation of the confrontation between the old conception of Sun-as-a-God and the modern understanding of solar events. Extract from *The Adventures of Tintin: Prisoners of the Sun*. © Hergé/Tintinimaginatio 2024.

To understand the relationship between the Sun and the periodical seasons, the solar disc has been thoroughly observed throughout history. Sometimes some dark spots could be observed on the solar surface with the naked eye, what we now know as sunspots. There are records of sunspot observations from China dating back to more than a thousand years. Yet, the power of the naked eye is small and only big sunspots could be detected. It was only with the invention of the telescope in the XVII century that the surface of the Sun could be zoomed in and more information from those mysterious dark spots could be retrieved. First, it had to be verified that those spots were really on the solar surface and not something floating between the telescope and the Sun. Galileo Galilei proved not only that the sunspots belong in the solar surface, but also that the Sun rotates around itself. Scientists started to keep records of the sunspots and found an 11-year cycle of solar activity during which the Sun gradually shifts from a spotless surface to a smudged surface covered in numerous, irregular sunspots located closer and closer to the solar equator. In contrast, long periods where sunspots were not visible and the Earth's climate experienced drastic changes, like the Maunder minimum, intrigued scientists and are still under study.

Telescopes revealed that sunspots consist of two distinct components: a darker, roundish core called the umbra, surrounded by a less dark, radial structure known as the penumbra. Yet, the nature of sunspots remained a mystery until the development of spectrometers and the discovery of the magnetic effects on the light (Zeeman effect).

This breakthrough allowed G. Hale to determine that these dark structures on the solar surface are caused by strong magnetic fields. While sunspots are the most prominent dark features on the solar surface, they are not unique. Smaller but still significant dark structures, named pores, look like sunspot umbrae but lack penumbrae around them.

It is evident how significantly each technological advancement impacts astronomy in general and solar physics in particular. The development of better telescopes that capture more photons, and enhance spatial resolution, allowing us to resolve areas as small as tens of kilometers on the Sun, has led to major leaps in our understanding of our star. Moreover, the development of new instruments that enable observations of the solar atmosphere at different layers enriches our comprehension of the solar components and their coupling. The immense amount of energy produced in the solar core is initially transported by radiation and then by convection in the outermost layer of the solar interior. Figure 2 summarizes the atmosphere of the Sun. The solar surface or photosphere, is the first visible atmospheric layer. It is covered by granulation patterns that are the tops of convective cells and, occasionally, by sunspots or pores. Counterintuitively, the temperature gradually rises along the following layer, the chromosphere, and then abruptly reaches 10^6 K in the corona. Throughout the atmosphere, the effects of magnetic fields are visible in the form of sunspots, prominences (filaments outside the disc), or coronal holes (open magnetic field lines that reach the interplanetary medium). The upper layers of the atmosphere are where highly energetic, magnetic-induced events that can affect Earth are ejected, named solar flares. Advancements in solar physics are essential; although the Sun's mystical role in societies has evolved, its importance in our lives is immutable.

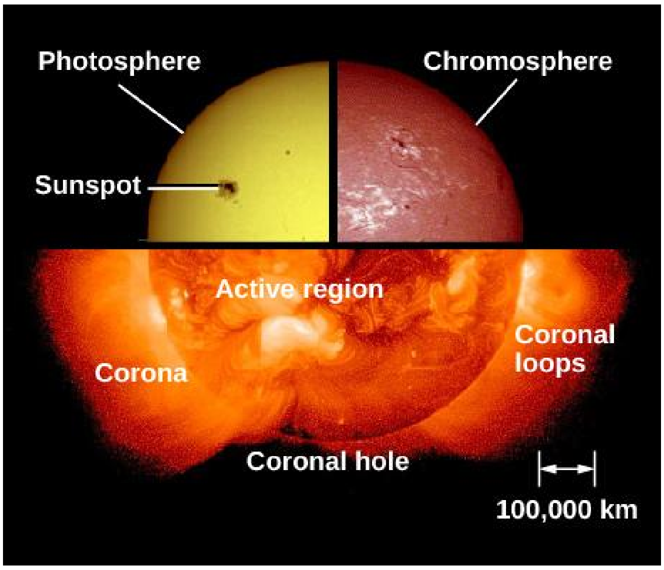

Figure 2 Illustration of the solar atmospheric layers with some magnetic-induced features at different heights.

This work builds on the advances in the understanding of sunspots and pores that new instruments have brought to the scientific community. Using spectropolarimetric observations, we aim to add a little more to the overall picture of the similarities and differences between sunspots and pores and the role that the magnetic fields play in their evolution. The better we understand their processes, the better we can prepare for potential hazards to Earth. We look forward to the European Solar Telescope and the developments it will bring to our understanding of our star.

1 Solar spots: background

Solar magnetic fields are known to be produced in the solar interior by a dynamo mechanism (see e.g., Charbonneau, 2005). This dynamo effect results from the complex interactions between convective moving plasma and differential rotation influenced by the stresses produced in the tachocline. These interactions not only generate magnetic fields but also produce large-scale flows, like the meridional circulation, and induce a periodic change from a stronger toroidal field during the Solar cycle maximum to poloidal fields during the Solar minimum. The toroidal flux ropes may rise due to buoyancy from the deep convective region to the solar atmosphere.

Tubes of strong magnetic fields, in their loop configuration from the solar interior to the atmosphere and back, can have visible imprints on the photosphere. They are seen as dark structures of variable size: from smaller dark spots (pores) to bigger, complex structures composed of a dark umbra surrounded by a less dark penumbra. In this Chapter we describe the general properties of sunspots and pores, the physical differences between umbrae and penumbrae and the characterisation of UP boundaries. Moreover, we will discuss their formation and decaying processes. We briefly address the effects of complex sunspots and active regions (ARs) in the upper atmosphere, where magnetic reconnection can occur and produce flares.

1.1 General properties

Sunspots are the biggest magnetic structures seen on the solar surface. They are generally formed by a dark umbra surrounded by a filamentary penumbra. However, intricate active regions produce complex sunspots where umbrae may share penumbral filaments, umbrae may be divided by one or more light bridges, or there may be orphan penumbrae. Figure 1.1 depicts NOAA 13664, a complex AR that produced numerous sunspots and pores and was responsible for the largest geomagnetic storm of Solar Cycle 25. Sunspot size is very variable as well: from large sunspots of up to $\sim 60\,000$ km to small sunspots of ~ 3500 km (e.g., Bray et al., 1964; Cho et al., 2015). Very large sunspots are, nonetheless, an exception. Sunspot lifetimes are in the order of days to weeks, where long-lived sunspots may survive more than one passage across the solar disc.

Sunspots are usually embedded in bipolar regions due to the loop configuration of the magnetic tube. In its return to the solar interior, the magnetic tube is typically divided into smaller tubes that form smaller dark structures. As a consequence, leading sunspots are typically larger and have longer lifetimes than following sunspots. An intricated magnetic configuration in ARs that are formed by mixed polarities may lead to magnetic reconnection in the upper part of the loops that are at corona heights.

Sunspots are surrounded by horizontal plasma flows that move radially outwards in the already nearly non-magnetised quiet Sun. This circulation creates an annular cell surrounding the sunspot, which has been called moat (e.g., Sheeley, 1972). The moat moves at a faster pace in closer proximity to the sunspot boundary and decelerates radially with increasing distance from the sunspot (Löhner-Böttcher et al., 2013). Moat flows only appear around sunspots, and it has been demonstrated that they are inherently linked to penumbral flows (Strecker et al., 2022).

Pores are visually simple structures on the photosphere: They are composed of a dark core, as a sunspot umbra, but without a penumbra around them. Yet, a more comprehensive definition that considers the history of the dark core should be used. The term pore can be subclassified as:

- **Protospots**: Dark structures that eventually develop penumbrae and turn into sunspots.
- **(Regular) pores**: Dark structures that do not exhibit penumbrae at any stage of their lifetime.
- **Naked spots**: Umbrae that lost their surrounding penumbrae.

Pores show a variety of sizes, ranging from areas similar to those of granules (smaller than 1 Mm^2) to larger than 40 Mm^2, with an average size of $\sim 5\mathrm{Mm}^2$ (see e.g., Verma et al., 2014; Cho et al., 2015). Although pores are typically smaller than sunspots, some sunspots are smaller than pores. Large pores are prone to align in chains or ring-like structures, while small pores tend to be more circular and have a smoother boundary, according to a statistical study done by Verma et al. (2014). Pores from their large statistical sample tended to form in ARs accompanied by sunspots, while only $\sim 10\%$ were isolated pores. It should be noted that pore studies usually do not distinguish between pore subtypes, and statistical analyses may be biased.

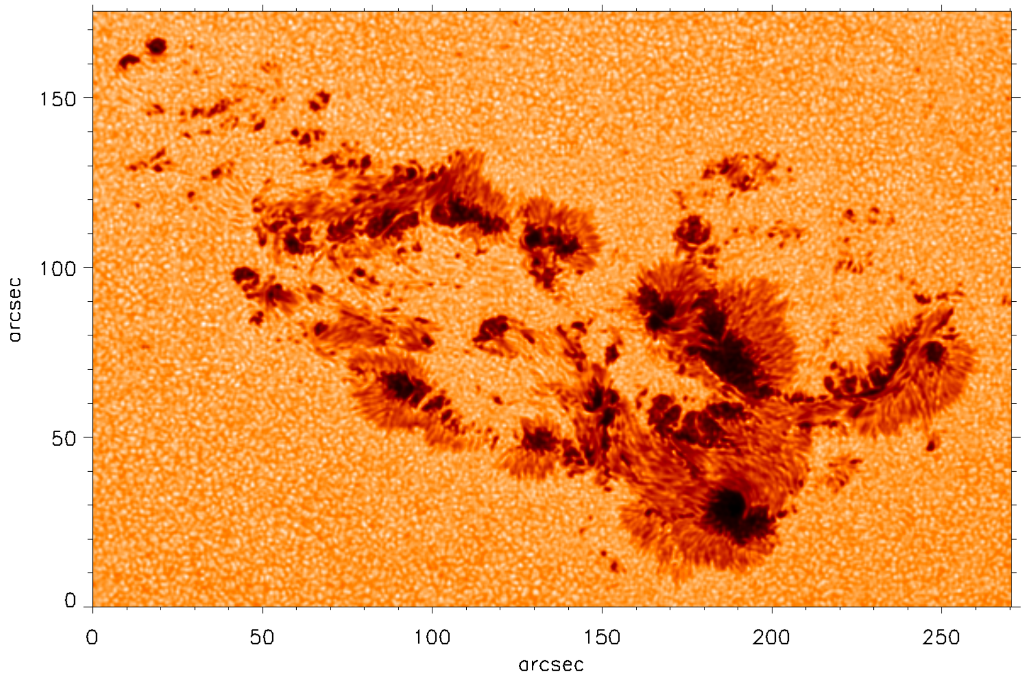

Figure 1.1 Continuum intensity image of sunspots and pores in the AR NOAA 13664 observed on the 8 May 2024 at 00:52 UT. This AR produced the strong May 2024 geomagnetic storms that led to auroras displayed at Earth latitudes lower than 40°. Data from HMI/SDO.

In general, pores are brighter than sunspot umbrae. This is intrinsically related to the strength of the magnetic field: darker cores are produced by stronger magnetic fields (e.g., Kopp et al., 1992). Moreover, pores are on average less stable than sunspots, and their lifetime is only a few hours to a few days (Suetterlin, 1998).

Opposite to sunspots, pores do not exhibit a moat flow around them due to the lack of penumbra. However, granular flows towards pores are observed around them (Wang et al., 1992; Roudier et al., 2002; Vargas Domínguez et al., 2010). Occasionally, small granules penetrate into the pore and move towards the centre similar to umbral dots (e.g., Sobotka et al., 1999b).

1.2 Magnetic field configuration

The magnetic field that generates sunspots and pores is shaped as a magnetic tube that emerges from the deepest convective layers due to buoyancy through the solar surface altering the quiet Sun convective flows. Since Hale (1908) it has been known that sunspots anchor magnetic fields with a strength over 3000 G. Pores, on the other hand, have a smaller magnetic field strength of $\sim$ 2000 G. The mean magnetic properties are correlated to factors such as the area, temperature and darkness. Bigger sunspots are darker and cooler because they are formed by a stronger $\boldsymbol{B}$ that inhibits the convection more effectively. Furthermore, sunspots magnetic field strength (B) is correlated to the solar cycle due to the emergence of stronger fields close to the solar maximum, as stipulated by Valio et al. (2020), who detected a larger amount of bigger, darker and cooler sunspots on the solar disc at the solar maximum.

Full-Stokes spectropolarimetric observations of photospheric lines allow us to retrieve the stratification of the magnetic configuration at different photospheric optical depths, as explained in Chapter 2. Optical depths are not to be confused with atmospheric heights. The solar surface is highly corrugated, meaning that the same optical depth (τ) is located at different geometrical heights depending on the physical parameters in the region of interest. As an example, $\tau = 1$ in sunspots is located at lower heights than the surrounding granulation and this cavity is called Wilson depression (see Fig. 1.2). This is a consequence of the global radial pressure balance that sunspots keep with their surrounding. In the presence of strong magnetic pressure, the gas pressure and temperature within the sunspot decrease, evacuating the flux tubes. A decrease in pressure (p), temperature (T) and density (ρ) leads to lower opacities (especially of the H^- bound-free opacity that dominates the photosphere) and lowers the height from where radiation is emitted. The height-induced variations of pressure and magnetic field strength also produce adjustments in the magnetic structure to keep this balance. As a consequence, the magnetic configuration must also be described in terms of τ.

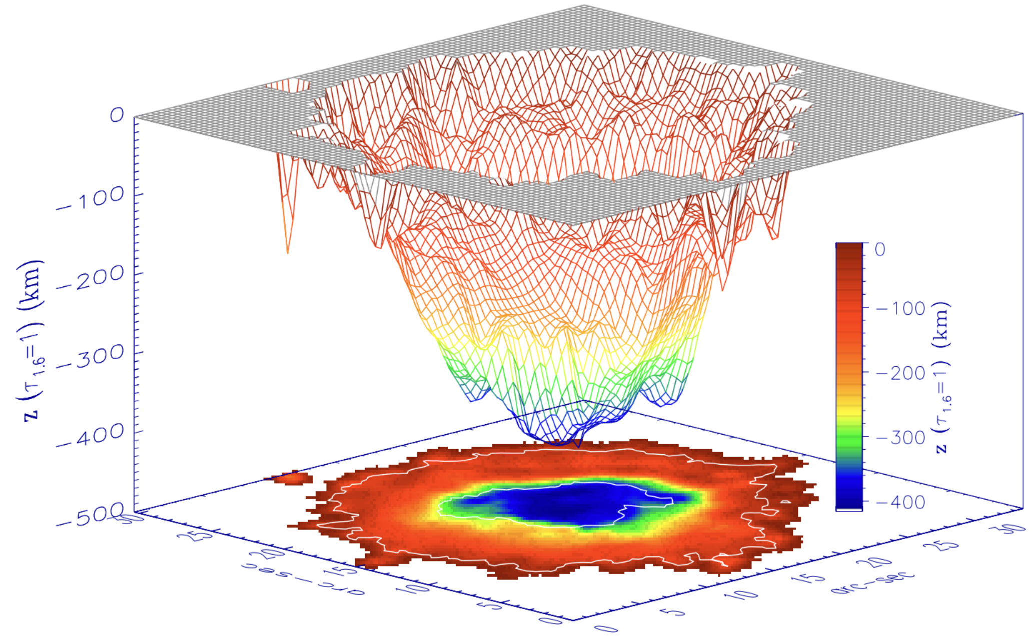

Figure 1.2 Illustration of the geometrical height variation of the Wilson depression at constant optical depth. Figure retrieved from Mathew et al. (2004) with permission © ESO.

Radial variations of the magnetic properties across sunspots, from the centre of the umbra to the outer penumbra used to be investigated by fitting concentric ellipses (or other curves) from the external penumbral boundary to the centre of the spot. The magnetic properties were azimuthally averaged along each curve. As seen in Fig. 1.3 for a constant τ[1], B diminishes and the magnetic field inclination (γ) increases with increasing radial distance, turning $\boldsymbol{B}$ more horizontal. Umbral regions and pores are dominated by the vertical component of the vector magnetic field (B_{ver}), and it gets more inclined towards the boundaries. The bigger the spots are, the more inclined $\boldsymbol{B}$ is at the (UP or pore) boundary. While pores, due to their smaller size, keep a mostly vertical structure, sunspots' B_{ver} weakens gradually until penumbral filaments are formed. The progressive strengthening of horizontal component of the vector magnetic field (B_{hor}) along umbrae results in the dominance of B_{hor} in penumbral regions.

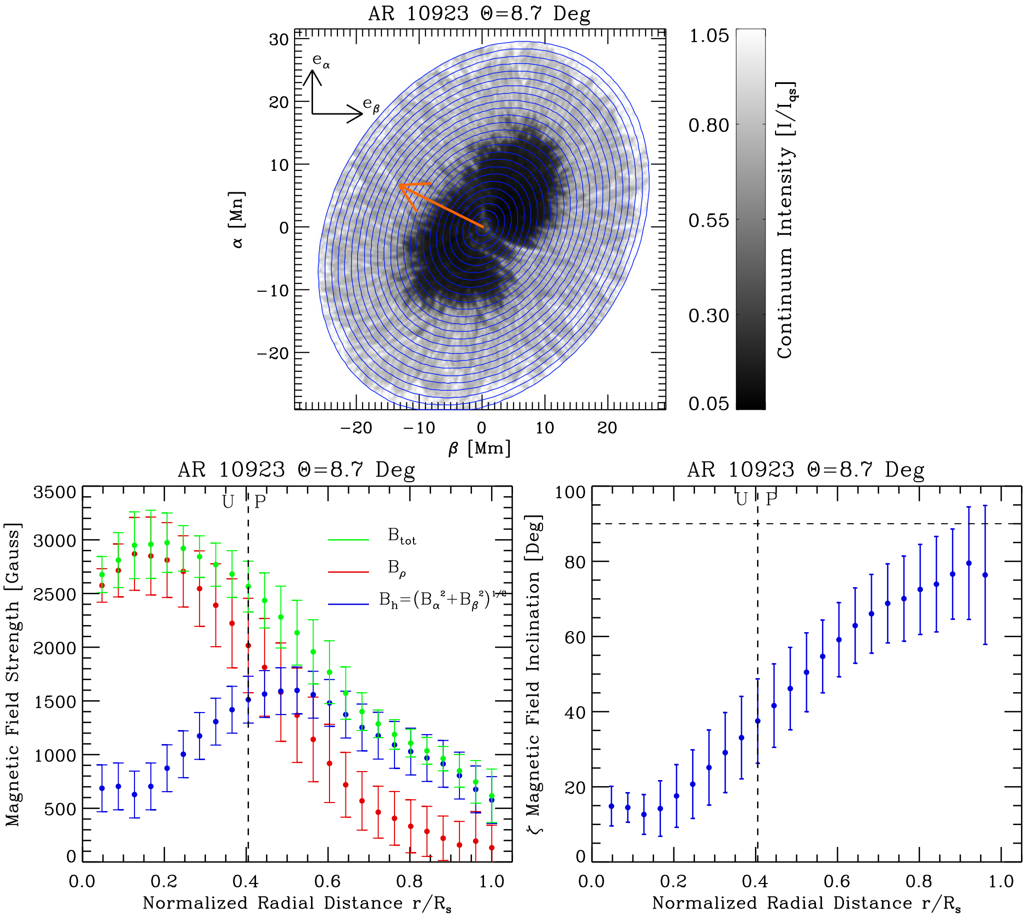

Figure 1.3 Radial variations of the total, vertical and horizontal magnetic field (bottom left) and inclination (bottom right) averaged along concentric ellipses fitted to the boundary of the sunspot (top). The red arrow points to the disc centre. Figure retrieved from Borrero et al. (2011a) with permission.

The ideal symmetric vertical magnetic configuration is not real for most of the sunspots. Umbrae may be divided into several umbral cores separated by light bridges. Also, penumbrae show a very intricated structure due to the overlay of more horizontal, weaker fields called spines, embedded in more vertical background fields that are the extension of the umbral vertical field within the penumbra, defined as inter-spines (Lites et al., 1993).

In sunspots, the magnetic structure ends more or less abruptly with the penumbra. However, the distance between photometric and magnetic pores boundaries is larger

---

[1] The use of a Milne-Eddington (M-E) code retrieves a height-averaged $\boldsymbol{B}$. Further details in Chapter 2.

and spans a few arc seconds (Keppens et al., 1996). Nonetheless, magnetic fields around sunspots and pores affect the surrounding granulation properties (e.g., W. Schmidt et al., 1988).

As illustrated in Fig. 1.4, at higher levels of the atmosphere (i.e., smaller values of τ) the magnetic tube expands horizontally and it forms a magnetic canopy at the external side of the penumbra. The magnetic boundary is therefore gradually shifted further from the photometric boundary. Only the most vertical magnetic fields reach higher heights while the horizontal fields remain at the lowest photospheric level. The (simpler) umbral magnetic field weakens vertically with height with a gradient of - (1–4) $\mathrm{G\,km^{-1}}$ (see references in Balthasar, 2018). On the other hand, the complex penumbral structure shows a variety of vertical gradients. Positive vertical gradient patches have been observed in the inner and middle penumbra at the edges of penumbral filaments at deep photospheric layers (J. Joshi et al., 2017), which are produced by horizontal, weaker fields remaining at deeper layers and stronger, vertical heights reaching higher vertical heights. For the same reason, positive vertical gradients are also found at the edges and outside sunspot boundaries, where the weak, granular magnetic fields are taken over by the stronger magnetic canopy. Pores exhibit a steepest vertical gradient with values spanning from -4 $\mathrm{G\,km^{-1}}$ to even -8.2 $\mathrm{G\,km^{-1}}$ (Balthasar, 2018).

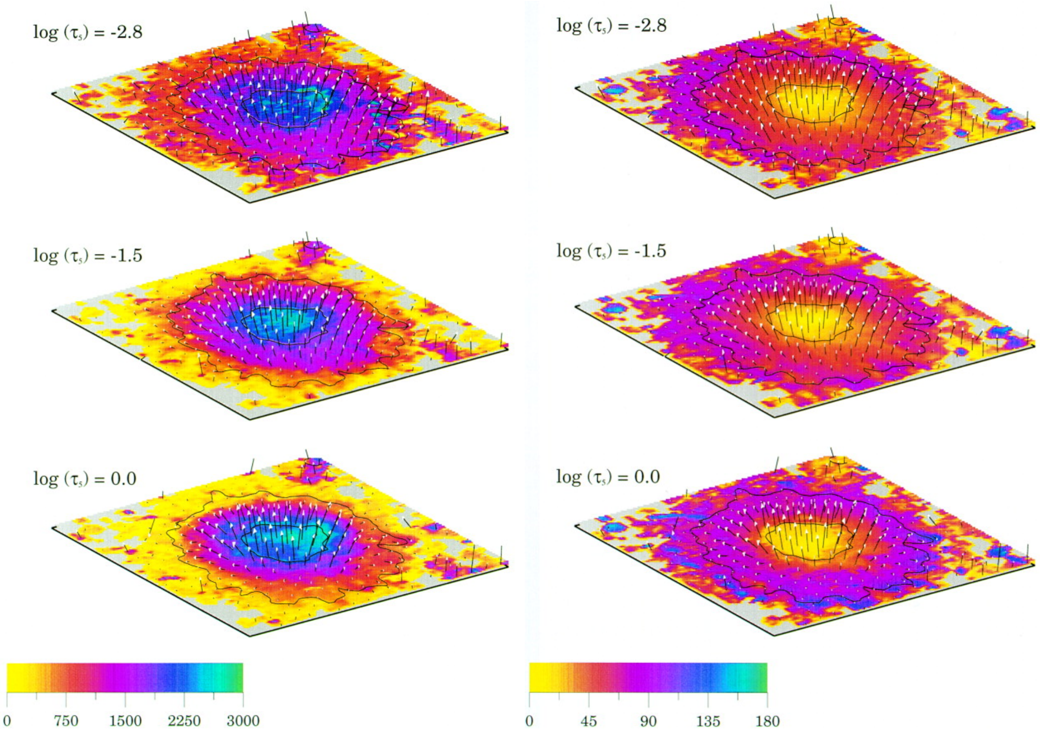

Figure 1.4 Stratified photospheric magnetic field strength (left) and inclination (right) of a sunspot located close to the disc centre. The arrow's length is proportional to B and the direction portrays γ. Figure retrieved from Westendorp Plaza et al. (2001) with permission.

We have discussed the general case where sunspots are formed by only one polarity. However, there are sunspot configurations with mixed polarity, such as δ-spots. In general terms, the more complex the magnetic configuration of a sunspot group is, the higher the probability that magnetic reconnection takes place in the corona, producing flares or coronal mass ejections (CMEs).

1.2.1 Magnetic reconnection

Magnetic reconnection[2] is the reconfiguration of magnetic field lines that results in the rapid release of stored magnetic energy. The intricated magnetic configuration within sunspots and ARs favour these reconnections at different scales. On a small scale, penumbral microjets are small brightenings detected above penumbrae at chromospheric heights (Katsukawa et al., 2007). They are fast events (~ 1 min) produced by the reconnection between weak (more horizontal) and strong (more vertical) fields compactly embedded in penumbrae, as supported by simulations (Magara, 2010).

On a large scale, solar flares are eruptions of electromagnetic radiation produced during magnetic reconnection at coronal heights (see Fig. 1.5). They last from minutes to hours and they are mostly produced close to the polarity inversion line (PIL) of an AR. The amount of expelled energy is so large that flares are the most energetic process within the Solar System (Fletcher et al., 2011). The released magnetic energy is rapidly converted to other forms of energy that yield several physical processes, such as bulk plasma heating, plasma motions (e.g. CMEs) or the acceleration of charged particles. While the magnetic reconnection occurs at the magnetically dominated (low-β[3]) corona, the lower atmosphere is the dominant source of radiative energy, from both non-thermal and thermal particles (e.g., Chupp et al., 1973). A significant portion of the released magnetic energy is deposited into the chromosphere by beams of accelerated particles from where it is dissipated in the form of flows and radiation in many spectral ranges. The rapidly heated chromospheric plasma evaporates (expands; e.g., Young et al., 2013; Graham et al., 2015; Polito et al., 2016b) as it forms hot flare loops ($\sim 10^6$ K) that reach the corona. The chromospheric footpoints of the loops are seen as bright flare ribbons.

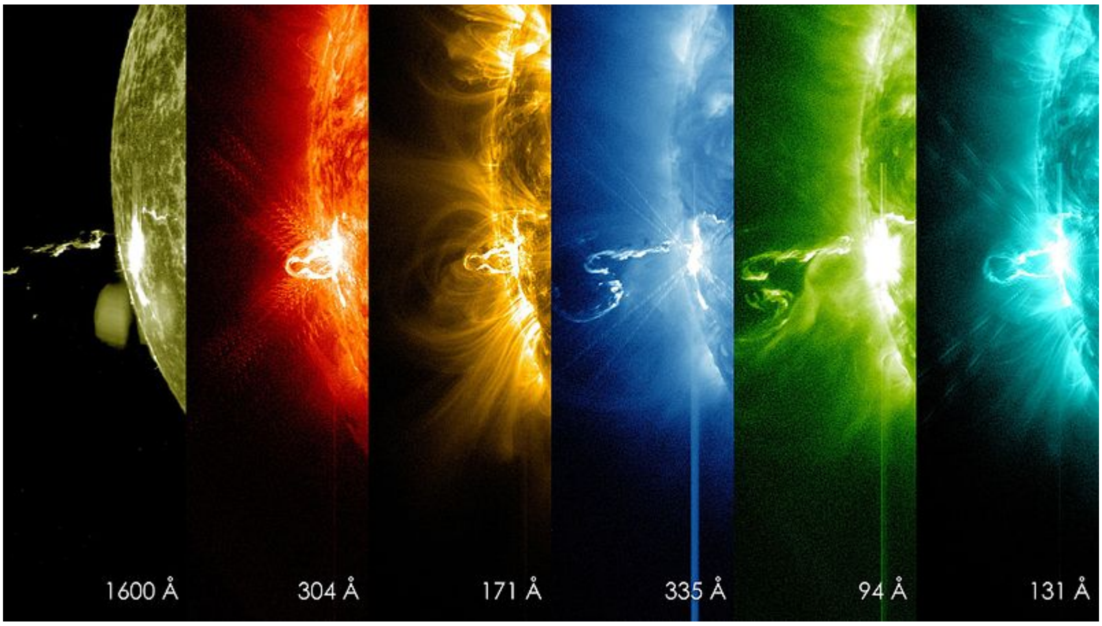

Figure 1.5 Solar flare observed on the limb by AIA/SDO. The multi-waveband observations show the extent and temperature variations of the flare. Credit: NASA/SDO.

---

[2] Even if it is off-topic, we want to briefly introduce the physics behind the paper reproduced in Appendix A and connect it to the topic of this PhD thesis. Sunspots, pores and flares are only different aspects of solar magnetic fields.

[3] plasma-β ($\beta = P_{\mathrm{g}}/P_{\mathrm{m}}$, where P_{g} is the gas pressure and P_{m} is the magnetic pressure) determines whether the dynamics of a system are dominated by the gas and the magnetic field follows the plasma motions ($\beta >> 1$), or whether it is the magnetic field who determines the plasma motions ($\beta << 1$)

The heated structures are seen bright due to numerous excited spectral lines and often to a smaller contribution of enhanced continuum. Continuum emission is apparent in white-light flares, where the visible continuum is enhanced. The generating mechanisms are still poorly understood since flare-induced photospheric emission places strong demands on beam excitation models, and continuum enhancements due to hydrogen recombination have not been unambiguously located at photospheric or chromospheric heights (e.g., Jurčák et al., 2018a). Moreover, flare continuum enhancements were expected to occur only in very energetic flares, but even small flares can produce continuum enhancements. Therefore, the full extent of the precursors and consequences of magnetic reconnection is still under study.

1.3 Magnetoconvection

Magnetoconvection is a type of flow where the thermal convection interacts with an external magnetic field. In regions with strong magnetic fields, the magnetoconvection dramatically affects the natural flows of solar plasma, such as in the case of AR. These fields inhibit the transverse plasma motion, thus reducing the convective heat transport from the solar interior. Chandrasekhar (1961) investigated the effects of inclined magnetic fields on convection and concluded that B_{ver} affects the (magneto-)convective mode, while B_{hor} shapes the convective cells. Hence, the umbral and penumbral magnetic configuration modifies the convection distinctively. Figure 1.6 presents examples of the fine structure of a sunspot, where distinct magnetoconvective structures are visible.

1.3.1 Umbral magnetoconvection

Umbrae emit $\sim 20\%$ of the average photospheric radiation. This corresponds to temperature decreases up to ~ 2000 K with respect to granulation (Thomas et al., 2004), where the photospheric quiet Sun temperature is 5780 K. The temperature drop depends on B, so darker sunspots are colder due to a more efficient hindrance of the convection. However, the convection is not fully hindered in the umbrae and we see more efficient magnetoconvective structures, such as umbral dots or light bridges.

Umbral dots

An umbral dot is a transient small-scale bright feature embedded in umbrae and pores that is interpreted as an obvious sign of magneto-convection. This implies that the convection is not fully hindered within umbrae or pores and that their magnetic structure is similar in terms of magnetoconvection. In the monolithic sunspot model, umbral dots are naturally created as predicted by simulations ran by Schüssler et al. (2006). Since the umbral $\boldsymbol{B}$ is mostly vertical and plasma moves along the magnetic lines ($\beta < 1$), mostly vertical, upward-downward movements are expected. Indeed, high-resolution observations have demonstrated that umbral dots are dominated by central upflows and are surrounded by confined downflows (e.g., Ortiz et al., 2010; Riethmüller et al., 2013). Simulations predicted a central dark lane on them that was first detected with observations from Hinode datasets (e.g., Bharti et al., 2007). However, the dark lane is not always present in high-quality observations (e.g., Riethmüller et al., 2013).

The typical size of umbral dots spans from 240–300 km. While they do not have a typical lifetime, since it ranges from a few minutes to a couple of hours, more than 2/3 of umbral dots have short lifetimes and a mean lifetime of 6–8 min (Sobotka et al., 1997; Riethmüller et al., 2008; Yadav et al., 2018). Umbral dots with longer lifetimes tend to be larger and brighter. Regarding their magnetic properties, the magnetic field weakens and the temperature rises in the deep photosphere compared with the surrounding umbra (Riethmüller et al., 2013).

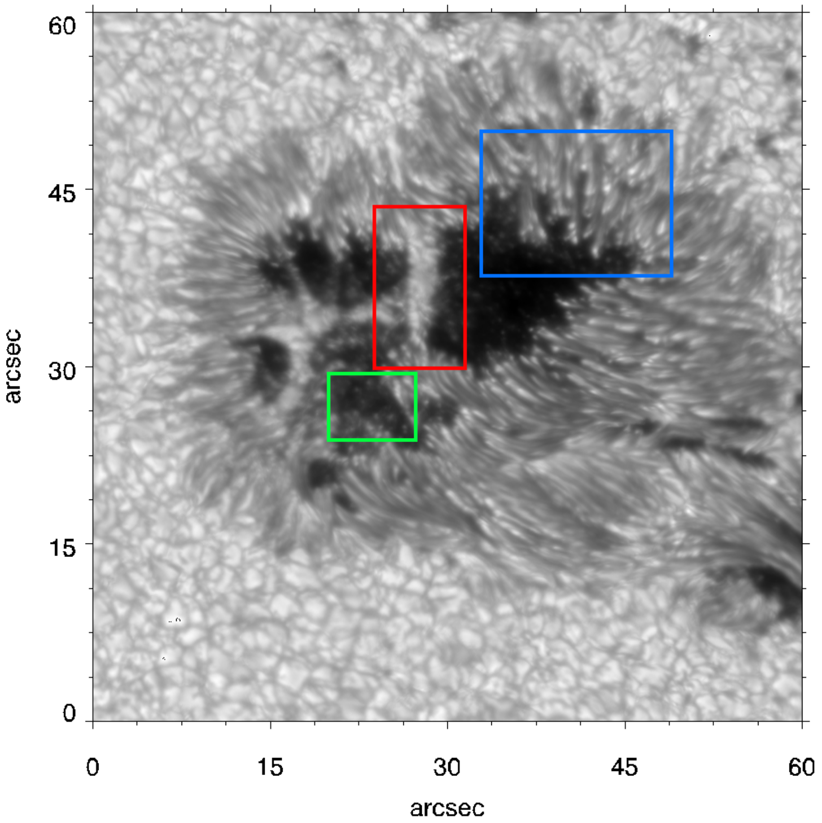

Figure 1.6 Fine structure of a sunspot illustrating different modes of magnetoconvection: A light bridge (red square), umbral dots (green square) and penumbral filaments with their brighter penumbral grains (blue square). G-band snapshot of a sunspot in NOAA 13014 recorded with HiFI+/GREGOR the 18 May 2022 by M. García-Rivas and M. Sobotka.

The distribution of umbral dots in umbrae is not uniform, but they seem to be located at the boundary of cellular shapes, as reported by Watanabe (2014). Also, their results suggested that umbral dots were less dense and more clustered during the later evolutionary stages of the sunspots. Visually, umbral dots can be classified according to their position within the umbra: central umbral dot if it is located inside the umbra or peripheral umbral dot if it is close to the UP boundary (Grossmann-Doerth et al., 1986). It has been observed that peripheral umbral dots migrate towards the centre of the umbra at a velocity correlated to the background γ, while central umbral dots have small irregular motions. Accordingly, peripheral umbral dots show stronger up- and downflows than central umbral dots (Riethmüller et al., 2013).

Light bridges

A light bridge is a bright structure that separates umbral cores in sunspots and pores. Like umbral dots, light bridges are a consequence of convection in the presence of a strong magnetic field.

Light bridges are typically formed by weaker and more horizontal fields than the surrounding umbrae at photospheric levels (e.g., Beckers et al., 1969; Lites et al., 1991; Leka, 1997). The γ decrease and B increase with height above the light bridge points to the existence of a magnetic canopy, as stated by Jurčák et al. (2006). They concluded that light bridges are structures formed in deep layers by field-free or weak-field plasma interfering with a stable umbra. Similar to umbral dots, light bridges present a dark lane along them (Berger et al., 2003).

Convective cells in light bridges can be granular (”photospheric” light bridge), filamentary (”penumbral” light bridge) or a combination of both, depending on the inclination of B. Light bridges are also classified as strong if they completely divide umbral cores or faint if they only penetrate umbrae (Sobotka et al., 1993; Sobotka et al., 1994; Rimmele, 2008). Their sizes differ from widths smaller than $1''$ to several arc seconds and they can be as dark as umbral dots or as bright as photospheric granulation. The observed flows (upflows in bright granules and downflows in dark lanes) are comparable to convective flows present in other structures, such as umbral dots or regular granulation (Lagg et al., 2014).

1.3.2 Penumbral magnetoconvection

Penumbrae emit, on average, $\sim 75\%$ of the energy flux radiated in the quiet Sun due to average field strengths of 1000–2000 G in them. This corresponds to mean temperature decreases of ~ 300 K with respect to quiet Sun values (Solanki, 2003). On a local scale, the penumbral intensity varies due to the complex fine structure produced by the ”uncombed structure” of the magnetic field. On a global scale, penumbrae are brighter than umbrae, hence the convection is more effective in this part of the sunspot.

Penumbral filaments

The radially oriented filamentary structures that form penumbrae are called penumbral filaments. They are co-spatial with the weaker, more horizontal magnetic fields (spines) described in Sect. 1.2.

Penumbral filaments are typically formed by a bright head that points towards the umbra (penumbral grains; Muller, 1973) and a central, dark lane along the fibril seen at $\tau < 1$. The central lane is produced by the encounter and closing of canopy-like magnetic fields (Tiwari et al., 2013; Scharmer et al., 2002). Filaments are brightest at their heads and they gradually dim towards their tail. The brightness variation is a consequence of the filaments’ elongated $\cap$-loop shape, which produces distinctive plasma flows along the fibrils.

The rise of hot sub-photospheric plasma at the heads of the filaments is seen as a brightening at photospheric levels. That is, penumbral grains are characterised by upflows (Ichimoto et al., 2007). The penumbral grains that emerge close to the UP boundary show an apparent inward motion (towards the umbra) while the penumbral grains that arise at the outer penumbra move outwards, away from the penumbra (Sobotka et al., 1999a; Zhang et al., 2013; Sobotka et al., 2024). Peripheral umbral dots and penumbral grains show similar physical characteristics (Sobotka et al., 2009a), which is in line with the observations of penumbral grains migrating towards the umbra and turning into peripheral umbral dots (Sobotka et al., 1995). Rimmele (2008) and Sobotka et al. (2009b) confirmed the existence of bright and dark filamentary tails oriented towards the penumbra attached to peripheral umbral dots, with similar behaviour to the simulations done by Rempel et al. (2009), that surmise that peripheral umbral dots are only the transition between central umbral dots to penumbral grains of penumbral filaments. These analyses, based on observations and simulations, therefore suggest that the umbral and penumbral magnetoconvection modes are dependent on the inclination of the magnetic field.

Evershed (1909) discovered a radial, photospheric flow, now known as the Evershed effect or Evershed flow. He ran systematic observations to discover that it is a horizontal flow (he could not observe it close to the disc centre) that flows outwards from the spot centre (he detected the same blue-/red-shift patterns in the southern and northern hemispheres, and opposite patterns on opposite sides of the central meridian), and it increases outwards. As stated by himself, it was disappointing that his solid hypothesis invalidated the splendid discovery of the Zeeman effect in sunspots, which seemed to demand a vortex. Nowadays it is known that this radial, horizontal motion is the continuation of the hot plasma that rises at the penumbral heads and flows along the extended, almost horizontal, radial penumbral filaments while leaking laterally (producing downflows on the side of filaments Scharmer et al., 2011) and cooling by radiation. The average Evershed flow velocity is 2–4 $\mathrm{km\,s^{-1}}$ and it can reach velocities of up to 10 $\mathrm{km\,s^{-1}}$ (e.g. Shine et al., 1994). Finally, the cooler gas re-enters towards sub-photospheric layers producing observable downflows.

Few works have reported the existence of radial, inward, photospheric flows during the formation of sunspots (Schlichenmaier et al., 2012; Romano et al., 2014) or associated with unusual events (Kleint et al., 2013; Louis et al., 2014). The so-called counter-Evershed flows can also be carried by regular penumbral filaments, surrounded by penumbral filaments carrying normal Evershed flows (Siu-Tapia et al., 2018). These rare events, however, have been proved to be very usual; Castellanos Durán et al. (2021) ran a statistical analysis that showed that $\sim$ 85% of the AR embedded transient counter-Evershed flows with a median lifetime of $\sim$ 10 h.

1.3.3 Umbra-penumbra boundary

The visible dissimilarity between umbrae and penumbrae in continuum intensity (I_c) produced by the characteristic umbral and penumbral (magneto)convective modes suggested that there was a magnetic parameter responsible for the sharp photometric UP boundary. UP boundaries were characterised by an azimuthal average of the magnetic properties along an ellipse located at the radial distance where $I_\mathrm{c} \simeq 0.50 I_\mathrm{QS}$ (e.g. $r/R_\mathrm{s} = 0.4$ in Borrero et al., 2011a). However, this method fails to accurately outline the UP boundary. A different method was employed by Jurčák (2011), who azimuthally averaged the magnetic properties along I_c thresholds that characterised the inner and external boundaries of penumbrae in stable sunspots. While the magnetic properties (B, B_ver, γ) on the external boundaries fluctuated, only B and γ changed significantly along the UP boundary. Contrary, B_ver showed hints of being constant along the UP boundary (see Fig. 1.7). This result led to a statistical Bayesian analysis of 88 scans from the Spectropolarimeter on board of Hinode (SP/Hinode), from which Jurčák et al. (2018b) verified that B_ver is invariant along UP boundaries of stable spots defined at $I_\mathrm{c} = 0.50 I_\mathrm{QS}$ (see Fig. 1.8). The inversions were performed with the Stokes Inversion based on Response functions (SIR) code that kept $\boldsymbol{B}$ constant with τ. The retrieved critical vertical magnetic field ($B_\mathrm{ver}^\mathrm{crit}$) value was in the range of 1849–1885 G with a likelihood of 99%; the most probable value was 1867 G. Moreover, the results suggested that B_ver is independent of the umbral area or the solar cycle stage.

Schmassmann et al. (2018) investigated a long-lived sunspot for 10 days during its first passage across the solar disc. They confirmed the detection of a $B_\mathrm{ver}^\mathrm{crit}$ in the stable sunspot with a value of 1693 G ±15 ($1\sigma_t$-error) from inversions performed with a M-E code. The deviation of the retrieved value with respect to the $B_\mathrm{ver}^\mathrm{crit}$ obtained by Jurčák et al. (2018b) was explained by the different experimental setup and analysis methods between the Helioseismic and Magnetic Imager (HMI) and SP/Hinode, as investigated by Sainz Dalda (2017). On the other hand, Löptien et al. (2020) inverted a stratified $\boldsymbol{B}$ with SIR code and also found a constant B_ver at the UP boundary of

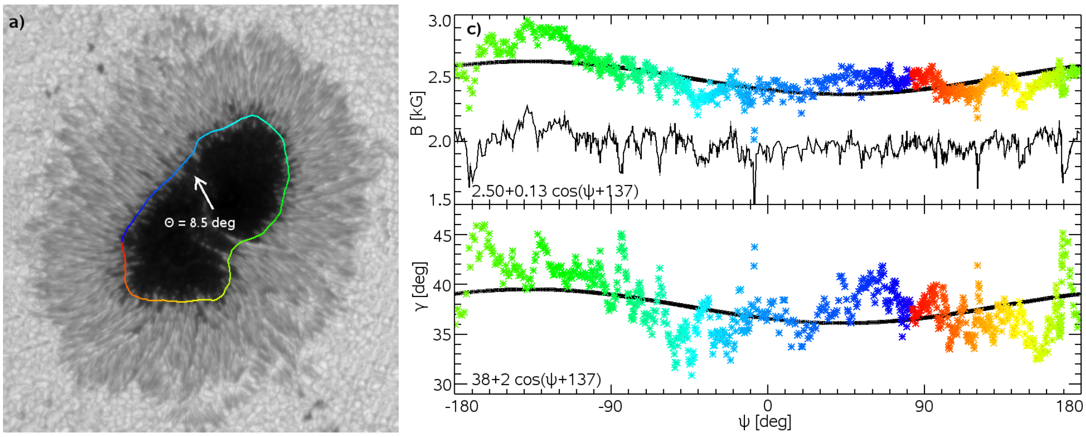

Figure 1.7 Left: I_c map of a sunspot with marked UP boundary. The white arrow indicates the position of the disc centre and the length is proportional to the heliocentric angle. Right: Azimuthal variation of the total field strength (coloured line in the upper plot), the vertical component of the magnetic field (black rugged line in the upper plot) and inclination (coloured line in the bottom plot). Colours indicate the position along the UP boundary in the I_c map. The formula in the upper (bottom) plot is the total magnetic field (inclination) fit that is overplotted in black. Figure adapted from Jurčák (2011) with permission © ESO.

sunspots of different sizes. However, they claim that it is a consequence of using a constant I_c threshold that includes inner, darker penumbral filaments whose weaker B_{ver} counteracts the spines stronger B_{ver} in large sunspots, while brighter penumbral filaments harboured in small sunspots are not outlined by the I_c threshold and only the not so strong umbral B_{ver} is considered. It is important to note that Löptien et al. (2018) investigated sunspots at different evolutionary stages, where most of the small sunspots were unstable (12/18), either forming (5/18) or decaying (7/18).

Why is it important to take into consideration the evolutionary stage? During a sunspot decay, the mean B_{ver} weakens within the umbra and strengthens within the penumbra, suggesting that $\boldsymbol{B}$ gets more vertical in the penumbra due to the disappearance of B_{hor} fields (Watanabe et al., 2014). As proven by Benko et al. (2018) with SP/Hinode scans of a decaying sunspot, the $B_{\text{ver}}^{\text{crit}}$ value found by Jurčák et al. (2018b) in stable sunspots falls well inside the umbra, showing that the B_{ver} is weaker than $B_{\text{ver}}^{\text{crit}}$ at the UP boundary. Complementary, the UP B_{ver} weakens during the first days of decay, strengthens during the final days of the analysis, and always stays weaker than $B_{\text{ver}}^{\text{crit}} = 1867$ G.

Regarding the initial stages of sunspots, Jurčák et al. (2015) captured the formation of a stable UP with the "Göttingen" Fabry-Pérot Interferometer (GFPI) and showed that the unstable UP boundary migrates towards inner umbral regions, occupying regions with sufficiently weak B_{ver} until it stabilises. Hence, the average B_{ver} at the UP boundary strengthens gradually until it reaches a maximum, invariable value. We note that stability does not imply that the UP boundary (B_{ver} value) remains strictly constant but that it oscillates around a fixed position (value). Jurčák et al. (2017a), on the other hand, followed the formation of a penumbra at the boundary of a pore recorded with the SP/Hinode. The pore was formed by fields $B_{\text{ver}} \leq 1400$ G that lead to the total penumbral colonisation of the pore and thus to an orphan penumbra.

The aforementioned investigations hinted at the stabilising role of B_{ver} and lead to an empirical law to be used as a stability criterion of evolving spots: the umbral mode of magnetoconvection prevails in regions with $|B_{\text{ver}}| > B_{\text{ver}}^{\text{crit}}$, while regions with weaker

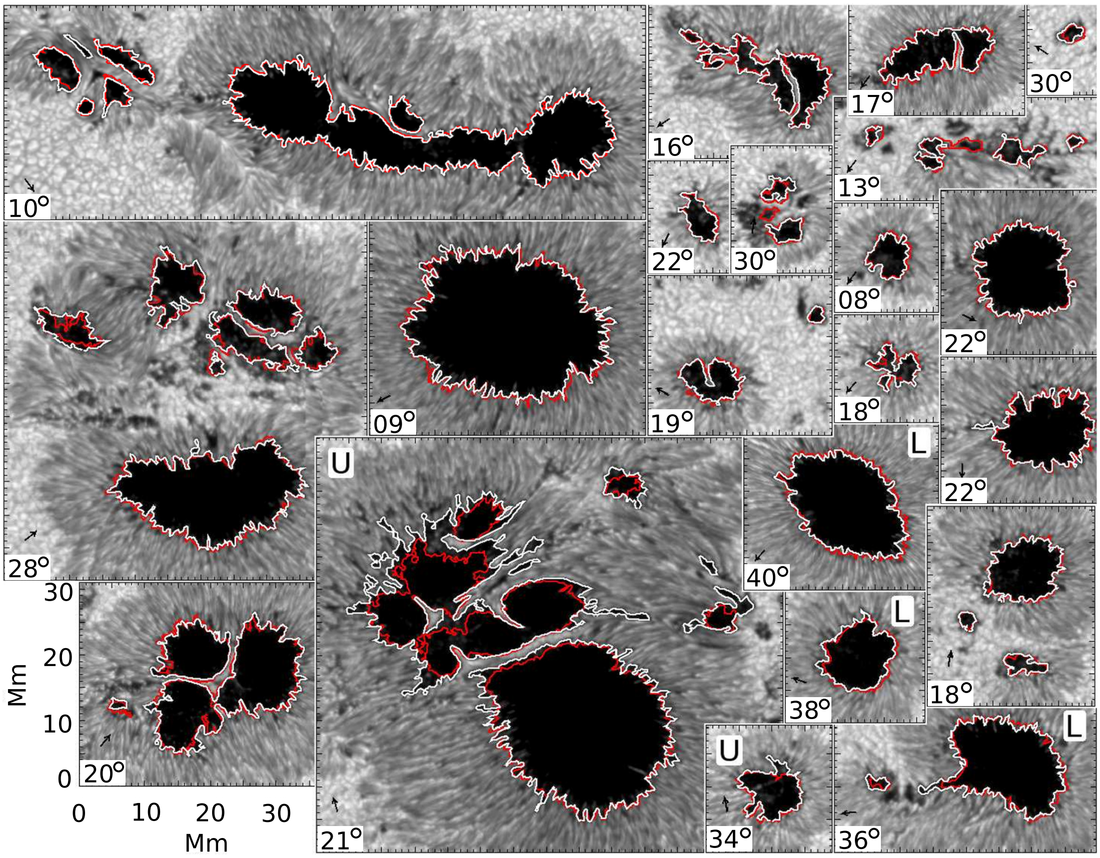

Figure 1.8 Selection of sunspots with UP boundaries defined with an intensity threshold (white; $I_{\rm c} = 0.50 I_{\rm QS}$) and with a critical vertical field threshold (red; $B_{\rm ver}^{\rm crit} = 1867$ G). Contours in sunspots marked with *L* show displacements due to the projection effects. Figure retrieved from Jurčák et al. (2018b) with permission © ESO.

$B_{\rm ver}$ are unstable and prone to vanish against other modes of magnetoconvection, like penumbra, light bridges or even granulation. The empirical law confirms the magnetic nature of the sharp UP boundaries.

1.3.4 Transition between modes of magnetoconvection

The appearance of a pore on the solar surface implies the transformation of regular convective cells into altered granules first, and into a dark structure with umbral mode of magnetoconvection last. This process is originated by flux emergence that results in a small dark structure that grows with time while diminishing its intensity (Loughhead et al., 1961). On the other hand, large pores are formed by coalescence of flux tubes (smaller dark spots) (Zwaan, 1985; Švanda et al., 2021). Many of these large pores will develop a penumbra and are referred to as proto-spots. But, what properties trigger the formation of penumbral filaments in some pores while others remain as simple pores? Based on observations, Zwaan (1987) or Leka et al. (1998) proposed that pores must exceed a threshold magnetic flux (Φ) of (1–1.5)$\times 10^{20}$ MX to have enough magnetic field concentration to form a penumbral structure. On the other hand, Rucklidge et al. (1995) theorised about the existence of a minimum inclination of about 45°, which was confirmed by observations (Jurčák et al., 2014a) and by magnetohydrodynamic (MHD) simulations, where penumbral filaments only developed depending on the forced inclination at the top of the simulation box (Rempel et al., 2009). This implies that, independently of Φ, penumbral filaments only form in the presence of a sufficiently horizontal $\boldsymbol{B}$. The onset of penumbra lasts only a few hours, which is why their observations are very rare.

But, where do penumbral filaments come from? Are they formed by pre-existing flux or are they formed as independent structures from new emerging flux? Two scenarios have been proposed (see Fig. 1.9), each of them in alignment with observations. The first scenario, the ”fallen magnetic flux tubes” model (Wentzel, 1992) or ”falling field lines” scenario, proposes that chromospheric inclined field lines bend down to the photosphere and submerge in the surroundings of the sunspot. Rempel (2011) showed in MHD simulations that the field lines bend because of mass loads originating from pressure-driven upflows. The presence of a chromospheric annular structure around a proto-spot before the photospheric penumbra appears (10 hours according to Shimizu et al., 2012) supports this scenario (also Romano et al., 2014; Murabito et al., 2016). Therefore, penumbral filaments are formed in a top-to-bottom motion from pre-existing umbral flux. In the second scenario, penumbral filaments are formed in a bottom-to-top motion from photospheric emerging flux and they are blocked from further rising by the overlaying magnetic canopy (Leka et al., 1998; Lim et al., 2013; Q. Li et al., 2018). A similar scenario is responsible for the existence of orphan penumbrae (Zuccarello et al., 2014; Kuckein et al., 2012). This scenario is contradicted by observations where penumbral sections are not formed in areas of flux emergence, which are typically the regions of a spot facing spots of opposite polarity within the AR (Schlichenmaier et al., 2010a; Rezaei et al., 2012; Romano et al., 2013; Murabito et al., 2016). Lindner et al. (2023) proposed that horizontal fields form at photospheric layers and are prevented from rising by the chromospheric canopy. However, the ability of the canopy to block the rising photospheric fields is limited when it becomes more vertical. Consequently, the horizontal fields (observed as thin, bright filaments) that are not prevented from rising either dissipate within minutes or rise to higher altitudes, thus failing to form a stable penumbra.

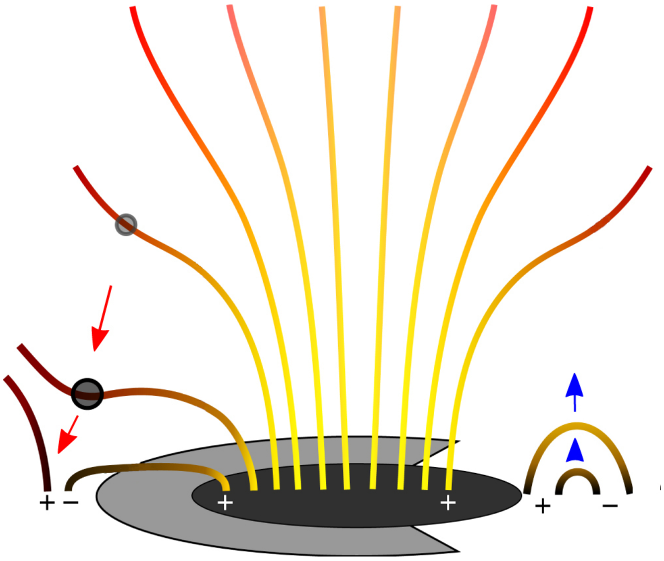

Figure 1.9 Sketch of an umbra (black) with a forming penumbra (grey) by flux emergence (right) and field lines falling due to mass loads (left). Sketch adapted from Bourdin (2017).

The formation of sunspots remains a topic of considerable debate, as does the subsequent decay stage. Firstly, it is not a simple matter to define the onset of the decay process. The decay is a gradual process that takes several days, and sunspots may begin to decay even before they are fully developed (McIntosh, 1981). The appearance of light bridges is a common phenomenon during the decay of sunspots. They are regarded as an indication of the disintegration process (Felipe et al., 2016). Furthermore, the appearance of light bridges may separate umbral cores that initially coalesced during the formation of the sunspot but did not fully merge (Garcia de La Rosa, 1987). This suggests that the presence of a light bridge may indicate the onset of fragmentation.

It has been demonstrated that the disappearance of the photospheric penumbra during the regular, slow decay process is a consequence of the penumbral magnetic fields becoming increasingly vertical (Bellot Rubio et al., 2008; Watanabe, 2014; Verma et al., 2018). However, penumbral sectors can also disappear rapidly, within minutes, in the event of flares caused by magnetic reconnection (Wang et al., 2004; Deng et al., 2005). Moat flows, which are closely associated with penumbrae, cease to exist when penumbrae are no longer present (Strecker et al., 2022).

Sunspot decay has been largely studied in terms of the photometric area due to larger photometric data archives. Linear area decay has been found in many sunspot decay studies (e.g., Hathaway et al., 2008; Martinez Pillet et al., 1993) and it is believed that more than 95% of sunspot area decay linearly (Solanki, 2003). However, some observations support a quadratic decay (Petrovay et al., 1997b; Petrovay et al., 1999; Litvinenko et al., 2015). Decay rates relate to the physical processes that cause the disintegration of the sunspot. In cases where the dissipation takes place over the whole sunspot, like in the turbulent diffusion model proposed by Meyer et al. (1974), the decays are linear. The turbulent erosion model, on the other hand, postulates that the dissipation only occurs at the boundary of the sunspot and, therefore, the decay rate is proportional to the perimeter of the sunspot, hence, quadratic (H. U. Schmidt, 1968; Petrovay et al., 1997a).

How is the magnetic flux expelled from the sunspot? A magnetic moving feature (MMF) is a unipolar or bipolar magnetic structure that is carried away by the moat flow to the network fields (Harvey et al., 1973). MMFs are considered to be the main actor of flux expulsion however, their flux transport is not equivalent to the magnetic flux decay rate of the sunspots (e.g., Harvey et al., 1973; Martínez Pillet, 2002). This might partially be due to the lack of tools to identify the structure of MMFs and the impossibility of differentiating between a sea-serpent structure from bipolar patches. MMFs are consistent with the model of turbulent diffusion.

1.3.5 Gough and Tayler stability criterion

The solar surface is covered by plasma instabilities that are explained as the upper part of convective cells that transport heat from the interior of the sun towards the surface. Schwarzschild proposed a stability criterion against overturning convection for a layered medium with a homogeneous composition in hydrostatic equilibrium in the presence of a gravitational field. This criterion states that convection develops when a perturbation appears in a medium with a temperature gradient steeper than the adiabatic gradient ($\nabla > \nabla_{\mathrm{ad}}$, where $\nabla \equiv \mathrm{d}\ln T/\mathrm{d}\ln p$). In the opposite case, the heat is transported radiatively[4]. Ledoux (1947) included the effect of an inhomogeneous medium (in terms of composition and ionisation) that alters the mean molecular weight with height.

The stability role of the B_{ver} was derived by Gough et al. (1966) who, based on a simple magnetic configuration in a compressible ideally conducting fluid, determined sufficient –but not necessary– conditions for stability against overturning convection, the

---

[4] Schwarzschild (1906) coined the term of radiative equilibrium as the state where, in a strongly radiating and absorbing atmosphere, the radiative heat transfer dominates over heat transfer due to convective mixing. He concluded that the visual solar atmosphere is in radiative equilibrium after comparing theoretical assumptions and the limb darkening observed on the Sun. He did not rule out that adiabatic equilibrium dominated in deeper layers.

Gough and Tayler (G-T) criterion (Eq. 1.1). Opposite to Schwarzschild criterion, which is a necessary and sufficient local criterion, G-T criterion is not local since different layers of the medium are connected by the magnetic field.

Gough et al. (1966) verified their stability criterion against a simple sunspot model constructed by Chitre (1963). The recent studies on the stabilising factor of B_{ver} have brought the G-T criterion back into the spotlight. Mullan et al. (2019) applied G-T criterion to explain the UP boundary in the context of magnetoconvection using empirical sunspot models and the $B_{\text{ver}}^{\text{crit}}$ obtained in the statistical analyses of UP boundaries performed by Jurčák et al. (2018b). They concluded that UP boundaries are formed in the regions where B_{ver} is sufficiently strong to increase the effective ∇_{ad} by more than 100% the non-magnetic value.

Schmassmann et al. (2021) tested the G-T criterion against realistic MHD sunspot simulations (MURaM; Rempel, 2015), see Fig. 1.10. The G-T criterion, according to the notation employed by Schmassmann et al. (2021), is defined as[5]

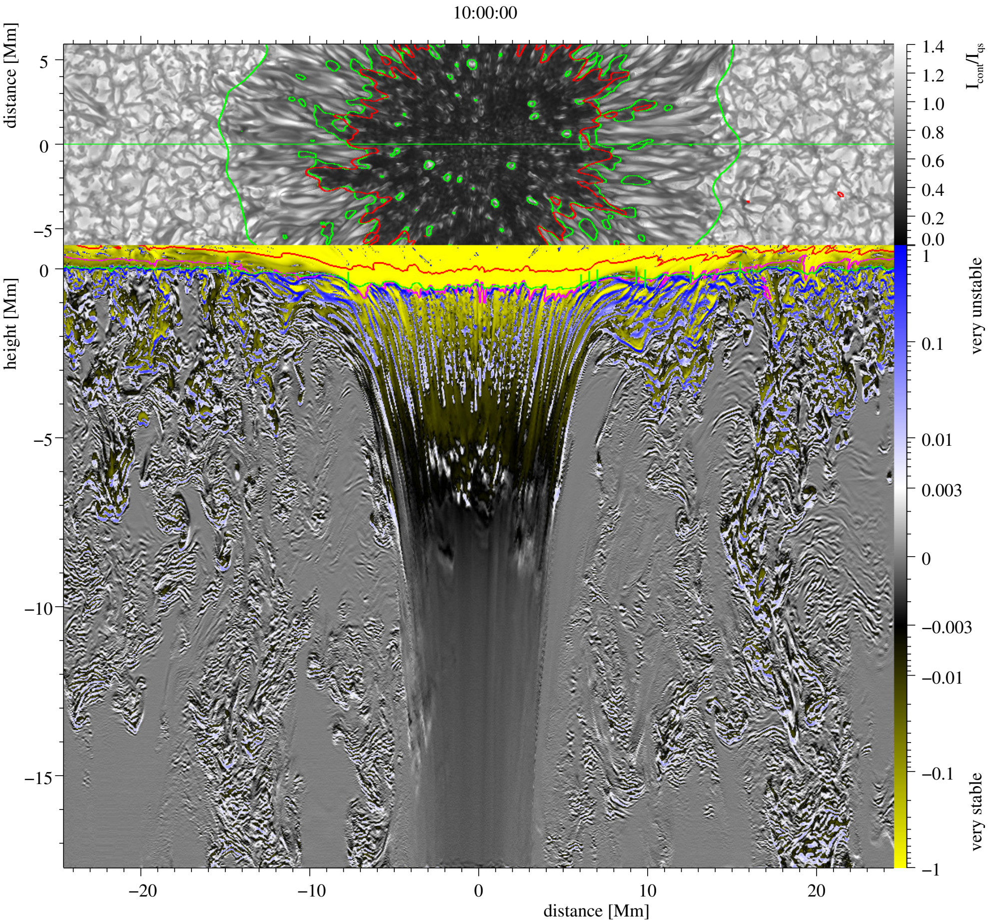

Figure 1.10 Evaluation of the G-T stability criterion on MURaM sunspot simulations. Top: Bolometric intensity where the corrugated green lines outline the penumbra and UP boundaries, the horizontal green line marks the position of the cross-section depicted below, and the red lines indicate the position of $B_{\text{ver}}^{\text{crit}}$=1867 G (Jurčák et al., 2018b). Bottom: Values of the G-T criterion on the cross-section of a sunspot. The vertical green lines mark the penumbra and UP boundaries as encircled above, the horizontal green line marks $\tau = 1$, the magenta line stands for $\beta = 1$, and the red line traces the outer edge of the density ($\rho < 3 \times 10^{-9}$). Figure retrieved from Schmassmann et al. (2021) with permission © ESO.

---

[5] They tested Eq. 1.1 and a form of the same formula that included the variation of Γ_1 with height. Since they found that the new term does not qualitatively affect the results, we omit it in this discussion.

$$\frac{1}{\Gamma_1} - \frac{\mathrm{d_z} \ln \rho}{\mathrm{d_z} \ln p} - \frac{{B_{\mathrm{ver}}}^2}{{B_{\mathrm{ver}}}^2 + 4\pi\,\Gamma_1\,p} < 0, \tag{1.1}$$

where Γ_1 is the first adiabatic exponent $\Gamma_1 = (\partial \ln p / \partial \ln \rho)_{\mathrm{ad}}$.

Figure 1.10 displays the G-T criterion (left-hand side of the equation) as calculated by Schmassmann et al. (2021), where the very stable regions are those with the smallest values (in yellow) and the very unstable are those with the largest values (in blue). While layers above $\tau = 1$ (especially above the umbra) are the most stable, $\tau = 1$ and below are characterised by instabilities triggered by radiative cooling.

They conclude that G-T can be used as a diagnostic tool since it reveals the tripartite nature of sunspot structure, where the sheet that separates umbra and penumbra is called peripatopause, and the magnetopause is the sheet that separates penumbra from the non-magnetic quiet Sun. While the photosphere above $\tau = 1$ is generally stable, the most unstable regions prevail right below $\tau = 1$. The instabilities are produced by radiative cooling at the photosphere, and the depth that they reach depends on the (magneto)convective mode. Three distinctive modes of (magneto)convection are distinguishable. The magnetic trunk is a stable sub-photospheric structure that allows the thin instabilities to sink only to depths of 4 Mm^2. The only type of umbral magnetoconvection observed are umbral dots. Instabilities produced in the penumbra are also thin filaments, but they are more vigorous and reach deeper layers than in the umbral mode. Close to the surface, the instabilities are more horizontal and they become more vertical with depth. The (almost) non-magnetised granulation is the most vigorous and it shows instabilities that can submerge freely to any depth of the box.

Schmassmann et al. (2021) show that the peripatopause and magnetopause are dynamic, permeable boundaries, which is in good agreement with observations. Their work suggests that the $B_{\mathrm{ver}}^{\mathrm{crit}}$ found on photospheric sunspot observations is the surface manifestation of the peripatopause that is produced by different modes of sub-photospheric magnetoconvection.

1.4 Motivation and aims

The main motivation for this PhD research is to study the interaction between solar convection and magnetic fields with a particular focus on the stabilising role of B_{ver}.

Jurčák et al. (2018b) demonstrated the existence of a constant B_{ver} value at UP boundaries of stable sunspots. Due to the similar magnetoconvective modes observed in umbrae and pores, we aim to investigate the similarities between sunspot umbrae and spots without penumbrae (pores, naked spots and proto-spots) in terms of their magnetic properties. In addition, we intend to monitor the magnetic properties during the transition between different magnetoconvective modes.

Investigations concerning the long-term evolution of the magnetic properties of spots are to be conducted using space-based spectropolarimetric observations. The magnetic structure of spots can be investigated in finer detail with data from ground-based telescope, therefore periodic ground-based observing campaigns have been performed. A reproduction of a paper resulting from a very successful but tangential campaign is included in Appendix A.

Given that pores exhibit a magnetic structure similar to that of umbral magnetic fields, we aim to examine the parallels in the evolution of magnetic properties at UP boundaries and the boundaries of pores. Specifically, we aim to investigate the potential existence and value of a $B_{\mathrm{ver}}^{\mathrm{crit}}$ at the boundary of a stable pore, using methodologies previously applied to UP boundaries. These points are addressed in the paper reproduced in Chapter 4 through an analysis of the magnetic properties of a suitable pore, which must meet criteria such as proximity to the disc centre during key evolutionary stages (formation, stability and decay), absence of penumbra development, and sufficient size.

Naked spots, or umbrae that have lost their penumbra, are visually similar to regular pores. We aim to explore whether there are magnetic differences in the decay processes of a sunspot that lead to naked spots compared to those that dissipate shortly after losing their penumbra. This analysis is shown in the paper reproduced in Chapter 5. In addition, we intend to investigate whether spots without penumbrae behave similarly, or whether naked spots retain sunspot characteristics. Since previous analyses related to the stabilising factor of B_{ver} have been performed with data from different instrumentation, leading to different values of $B_{\mathrm{ver}}^{\mathrm{crit}}$, we also aim to quantitatively measure the variations between the $\boldsymbol{B}$ retrieved from the instruments used so far, and to establish their intrinsic dissimilarities.

Proto-spots, or pores in the process of developing a penumbra, are still an enigmatic structure. How do penumbral filaments onset, where is the origin of the onset or how long does it take for the Evershed flow to set in are questions that we aim to answer in the paper reproduced in Chapter 6. In this Chapter, we analyse a proto-spot developing several filamentary segments. By studying the magnetic properties and line-of-sight velocity (v_{LOS}) before, during and after filamentary onset at various locations (limb-side or centre-side) with differing magnetic and flow patterns, we aim to characterise the similarities among varied starting conditions.

2 Diagnostic tools for the vector magnetic field

Spectropolarimetry is a powerful technique that combines the study of spectra and the polarimetric state of light. This technique not only provides a deeper understanding of the emitting object but also allows us to study the vector magnetic fields. Full-Stokes solar spectropolarimetry started to bloom at the end of the 20th century, peaking during the 21st century. This new technique was first introduced in ground-based telescopes, which allowed solar scientists to develop new analysing methods, e.g., inversion codes. The implementation of spectropolarimetry in space-based instruments took a few more years. Figure 2.1 summarises the development of some of the most representative space- and ground-based solar spectropolarimeters.

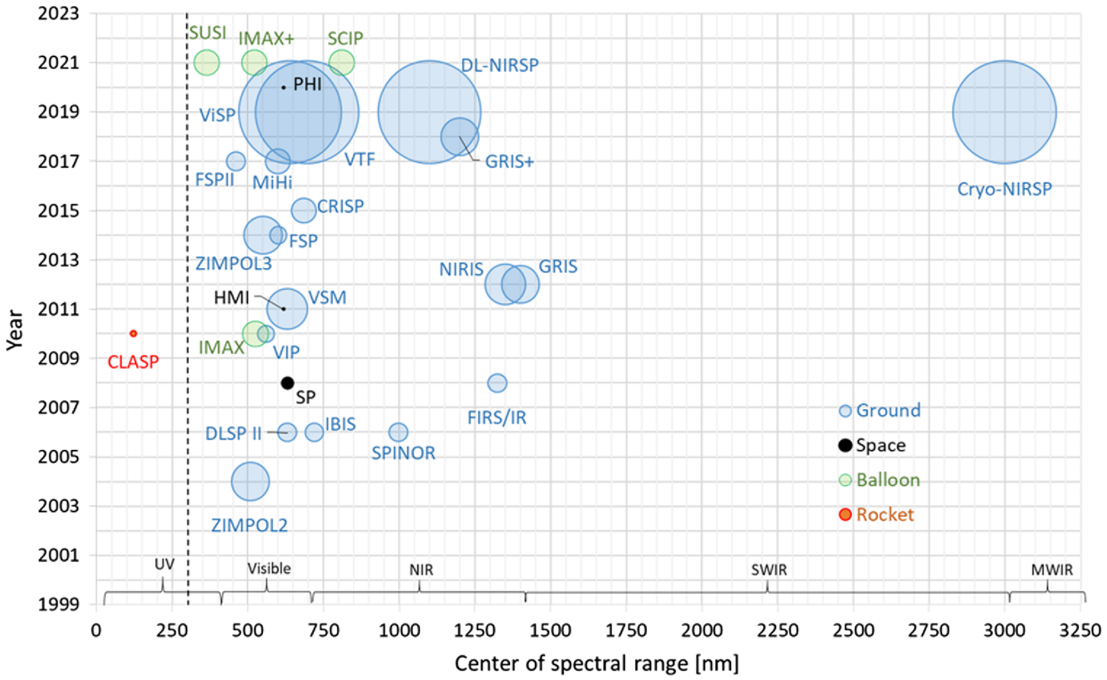

Figure 2.1 Development of some representative solar spectropolarimeters over time. Centre of the spectral range vs. time of introduction of some representative solar optical spectropolarimeters. Circles are proportional to the telescope aperture. Figure retrieved from Iglesias et al. (2019) with permission.

In this chapter, we describe the theoretical foundation required for the development of this thesis. In order to present a coherent formalism, this Chapter is based on the comprehensive works realized by del Toro Iniesta (2007), Stenflo (1994), and Landi Degl'Innocenti et al. (2004).

2.1 Polarization

Polarization is a property of electromagnetic waves in which the vector electric field ($\boldsymbol{E}$) oscillates in a certain direction. In general, light is unpolarized, meaning that $\boldsymbol{E}$ oscillates in random directions. Partially polarized light is a state in which one of the directions is preferred but it is not unique.

An electromagnetic wave travelling in the z direction can be defined in terms of $\boldsymbol{E}$:

$$\begin{aligned} E_{\mathrm{x}} &= A_{\mathrm{x}} e^{i(k\,z - \omega\,t)} \\ E_{\mathrm{y}} &= A_{\mathrm{y}} e^{i(k\,z - \omega\,t + \Delta)}, \end{aligned} \tag{2.1}$$

where E_{x} and E_{y} are the x, y components of the $\boldsymbol{E}$, and they are characterised by their amplitude (A_{x}, A_{y}), their phase shift (Δ), the angular wavenumber (k), the direction of propagation of the wave (z), the angular frequency (ω), and the time (t).

We can differentiate between different types of polarization according to the direction of oscillation, the amplitudes and the phase shift between E_{x} and E_{y}:

- Linear polarization: $\boldsymbol{E}$ is confined to one plane along the direction of propagation. It can be due to the lack of one of the components ($A_{\mathrm{x}} = 0$ or $A_{\mathrm{y}} = 0$) or to a phase $\Delta = 0, \pm\pi$.
- Circular polarization: $\boldsymbol{E}$ is composed by components with equal amplitude ($A_{\mathrm{x}} = A_{\mathrm{y}}$) and a perpendicular phase shift between them ($\Delta = \pm\pi/2$). Consequently, $\boldsymbol{E}$ rotates in a circle around the direction of propagation. Depending on the direction of rotation we see right- or left-hand circularly polarized light.
- Elliptical polarization: It is similar to circular polarization, but in this case, the amplitudes are not equal ($A_{\mathrm{x}} \neq A_{\mathrm{y}}$). Consequently, $\boldsymbol{E}$ rotates describing an ellipse around the direction of propagation, right- or left-handed.

2.1.1 Stokes parameters

The polarization state of the light (total, partial or unpolarized) can be fully described by the Stokes vector,

$$\mathbf{I}(\lambda) = \begin{pmatrix} I(\lambda) \\ Q(\lambda) \\ U(\lambda) \\ V(\lambda) \end{pmatrix}, \tag{2.2}$$

where I stands for the total intensity, Q and U measure the linear polarization, and V measure the circular polarization. All the quantities are wavelength-dependent. Consequently:

- $I = \sqrt{Q^2 + U^2 + V^2}$ in fully polarized light.
- $I > \sqrt{Q^2 + U^2 + V^2}$ in partially polarized light.
- $Q = U = V = 0$ in unpolarized light.

The polarimetric state is in practice measured with differential photometry (see Fig. 2.2), where the Stokes parameters are calculated as temporal averages of the $\boldsymbol{E}$ amplitudes and phase shift:

$$I = \left(\left\langle {A_{\mathrm{x}}}^2 \right\rangle + \left\langle {A_{\mathrm{y}}}^2 \right\rangle\right) \tag{2.3}$$

$$Q = \left(\left\langle {A_{\mathrm{x}}}^2 \right\rangle - \left\langle {A_{\mathrm{y}}}^2 \right\rangle\right) \tag{2.4}$$

$$U = 2\left\langle A_{\mathrm{x}}\, A_{\mathrm{y}} \cos\Delta \right\rangle \tag{2.5}$$

$$V = 2\left\langle A_{\mathrm{x}}\, A_{\mathrm{y}} \sin\Delta \right\rangle. \tag{2.6}$$

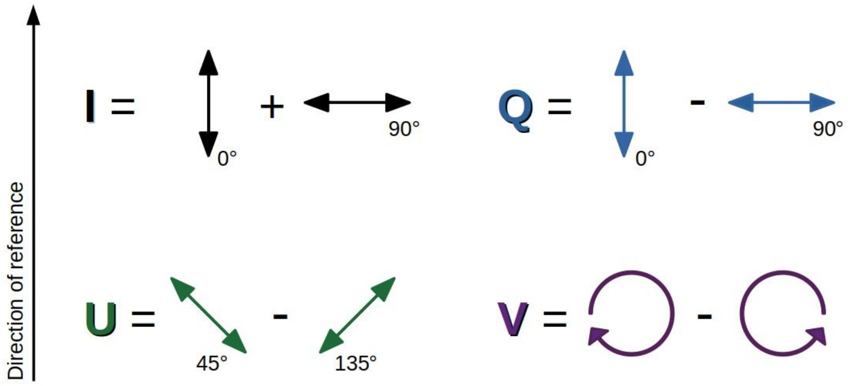

Figure 2.2 Observational definition of Stokes parameters in terms of differential photometry.

In terms of polarization, $Q(\lambda)$ measures the difference between vertical and horizontal linear polarization, $U(\lambda)$ measures the difference between linear polarization at $+45°$ and -45°, and $V(\lambda)$ stands for the difference between left- and right-hand circular polarization. Therefore, spectropolarimeters, by measuring the full Stokes parameters, provide full information on the polarization state of the light emitted by the solar atmosphere. This leads to the question of what physical processes produce spectral line polarization in the solar atmosphere. The most important mechanisms are the scattering processes, the Zeeman, Hanle and Paschen-Back effects. Scattering processes linearly polarize the solar light, and the Hanle effect accounts for the influence of the magnetic field on the scattering polarization. The presence of a magnetic field produces the split of atomic and molecular energy levels, which are explained by the Zeeman and Paschen-Back effects. The Paschen-Back effect is applicable in the presence of ”strong” magnetic fields, where ”strong” refers to a stronger coupling between the spin or the orbital angular momentum and the magnetic field than the coupling between the orbital angular momentum and the spin. On the other hand, the Zeeman effect is valid in the presence of ”weak” magnetic fields where the spin-orbit coupling dominates. Since the spin-orbit coupling increases with the atomic number, ”strong” magnetic fields –and therefore the Paschen-Back effect– only affect light atoms.

Despite the existence of numerous processes that create polarization in the solar atmosphere, each of them prevails in different scenarios. Since the focus of this thesis is on photospheric dark structures produced by strong magnetic fields (”weak” magnetic fields with respect to the spin-orbit coupling), the Zeeman effect prevails in our regions of interest.

2.1.2 Zeeman effect

Pieter Zeeman, while studying the effects of magnetic fields on light sources, discovered a broadening of the sodium D lines when exposed to magnetic fields (Zeeman, 1897b). Hendrik Lorentz explained this phenomenon using his electron theory and predicted that the broadening was actually a splitting of the spectral lines, which was proven with further experiments (Zeeman, 1897a; Zeeman, 1897c). Lorentz’s theory not only accounted for the splitting of spectral lines in the presence of magnetic fields but also predicted their polarization states. This phenomenon, known as the Zeeman effect, earned Zeeman and Lorentz the Nobel Prize in Physics in 1902. The Zeeman effect enabled Hale (Hale, 1908) to demonstrate the magnetic nature of sunspots. Since then, it has become one of the most widely used tools for diagnosing magnetic fields on the solar surface.

Lorentz's classical electron theory was unable to explain all the results produced by the Zeeman effect, making it necessary to adopt a quantum-mechanical approach. The quantum state of an electron within an atom is affected by Coulombic repulsion between electrons (orbit-orbit interaction), spin-spin interactions, and spin-orbit interactions. The Russell-Saunders or L-S coupling method summarizes the total angular momentum of a system of electrons, where the total spin angular momentum, S, accounts for the spin-spin coupling, the total orbital angular momentum, L, accounts for the orbit-orbit coupling and the total angular momentum, J, accounts for the spin-orbit coupling of the system,

$$\mathbf{S} \equiv \sum_{i=1}^{n} \mathbf{s}_i \qquad \mathbf{L} \equiv \sum_{i=1}^{n} \mathbf{l}_i \qquad \mathbf{J} \equiv \mathbf{L} + \mathbf{S}. \tag{2.7}$$

As a result, an atomic state is described by $^{(2S+1)}L_J$ and defined by the atomic numbers l, s, j, and m. The magnetic quantum number m specifies the orientation of the orbital. The Hamiltonian of the state, $\mathbf{H}_0$, incorporates all possible couplings and is characterised by an eigenvalue E_j, which is identical for all the states with the same j, independent of the value of m, where $m = -j, ..., 0, ..., j$. This implies that the quantum state is degenerate and consists of $(2j + 1)$ sublevels,

$$\mathbf{H}_0 \, |l\, s\, j\, m\rangle = E_\mathrm{j} \, |l\, s\, j\, m\rangle. \tag{2.8}$$

In the presence of an external, constant magnetic field, the Hamiltonian must include a new term that accounts for the magnetic effect,

$$\mathbf{H}_\mathrm{B} = \mu \cdot \mathbf{B} + O(\mathrm{B}^2), \tag{2.9}$$

where the magnetic interaction is strongly dependent on the intrinsic magnetic moment of the atom, μ in the presence of not very strong magnetic fields. In the solar atmosphere, the diamagnetic term $O(B^2)$ can be disregarded. The intrinsic magnetic moment is defined as,

$$\mu = \mu_0(\mathbf{J} + \mathbf{S}) \tag{2.10}$$

$$\mu_0 \equiv \frac{e_0\, \hbar}{2\, m\, c} = \frac{h\, \nu_\mathrm{L}}{B}, \tag{2.11}$$

where Bohr's magneton, μ_0, depends on the electrical charge of the electron, e_0, the (reduced) Planck constant, $(\hbar)$ h, the electron mass, m, the speed of light, c, and the Larmor frequency, ν_L.

As a result, the Hamiltonian of the system that includes the new magnetic term shows a shift in the energy that depends on the magnetic quantum number (m) and on the Landé factor (g),

$$(\mathbf{H}_0 + \mathbf{H}_\mathrm{B}) \, |l\, s\, j\, m\rangle = (E_\mathrm{j} + \Delta E) \, |l\, s\, j\, m\rangle \tag{2.12}$$

$$(\mathbf{H}_0 + \mathbf{H}_\mathrm{B}) \, |l\, s\, j\, m\rangle = (E_\mathrm{j} + m\, g\, h\, \nu_\mathrm{L}) \, |l\, s\, j\, m\rangle. \tag{2.13}$$

In cases where the LS coupling prevails, such as in the Zeeman effect, the Landé factor can be expressed by

$$g_\mathrm{LS} = \frac{3}{2} + \frac{s(s+1) - l\,(\,l+1\,)}{2\,j\;(\;j+1\;)}. \tag{2.14}$$

A transition must occur to observe a spectral line, either an absorption or an emission. The shift of energy in a magnetised medium ν_{B}, with respect to the transition in a not-magnetised medium, depends on the upper and lower energy levels. Therefore from Eq. 2.13, and expressed in wavelength,

$$\begin{aligned} \Delta\,\nu_{\mathrm{B}} &= (m_{\mathrm{u}}\,g_{\mathrm{u}} - m_{\mathrm{l}}\,g_{\mathrm{l}})\,\nu_{\mathrm{L}} \\ \Delta\,\lambda_{\mathrm{B}} &= (m_{\mathrm{u}}\,g_{\mathrm{u}} - m_{\mathrm{l}}\,g_{\mathrm{l}})\,\lambda_{\mathrm{B}}, \end{aligned} \tag{2.15}$$

where the Zeeman splitting for the normal Zeeman triplet is defined, in units of Angstrom and Gauss, as

$$\lambda_{\mathrm{B}} \equiv \frac{\lambda_0^2\,\nu_{\mathrm{L}}}{c} = 4.67\,\times\,10^{-13}\lambda_0^2\,B. \tag{2.16}$$

Atomic transitions follow the selection rules of electric dipole transitions. A permitted transition complies with $\Delta L = 0, \pm 1$, $\Delta S = 0$, $\Delta J = 0, \pm 1$ (except for $j_{\mathrm{u}} = j_{\mathrm{l}} = 0$), which implies that

$$\Delta\,m \equiv m_{\mathrm{u}} - m_{\mathrm{l}} = 0, \pm 1. \tag{2.17}$$

Zeeman components are classified according to the Δm produced in the transition. Figure 2.3 illustrates the classification summarised below:

- **$\boldsymbol{\pi}$ transitions:** $\Delta m = 0$. They emit linearly polarised light.
- **$\boldsymbol{\sigma}$ transitions:** $\Delta m = \pm 1$. They emit circularly polarized light in the plane perpendicular to the direction of the π-linear polarization.

$$\begin{cases} \boldsymbol{\sigma_{+}} \text{ or } \boldsymbol{\sigma_{\mathrm{b}}} : \Delta m = +1. \text{ The blue component of the split.} \\ \boldsymbol{\sigma_{-}} \text{ or } \boldsymbol{\sigma_{\mathrm{r}}} : \Delta m = -1. \text{ The red component of the split.} \end{cases}$$

The so-called longitudinal Zeeman effect refers to observations made with a LOS parallel to the direction of the magnetic field. As a result, the observed light is circularly polarized, as illustrated in Fig. 2.3. When dealing with emission and a magnetic field vector (**B**) directed towards the observer, σ_{+} component is left-handed, and σ_{-} component is right-handed. Reversing the polarity of the magnetic field reverses the direction of the circular polarization of the components. This effect is visible in the V-stokes profile, where the positive and negative peaks switch according to the polarity of **B**. In the case of absorption transitions, the situations are reversed.

Conversely, the transversal Zeeman effect involves observations made with a LOS that is perpendicular to the direction of the magnetic field. Here, the π-components are seen as linearly polarized in the direction of the vector magnetic field, while the σ-components are linearly polarized perpendicular to the magnetic field vector. This type of radiation is quantified by the Stokes Q and U parameters.

In the analysis of sunspots and pores, the inclination of the $\boldsymbol{B}$ varies depending on the pixel position: $\boldsymbol{B}$ is close to vertical with respect to the local perpendicular at the centre of the umbra, and close to horizontal at the penumbra. Therefore, most of the observed beam-light combines the longitudinal and transversal Zeeman effects that help to confine the **B** direction and strength.

2.2 Radiative Transfer Equation

The radiative transfer equation (RTE) describes the propagation of light along a medium. The composition of the medium, the presence of a magnetic field or the

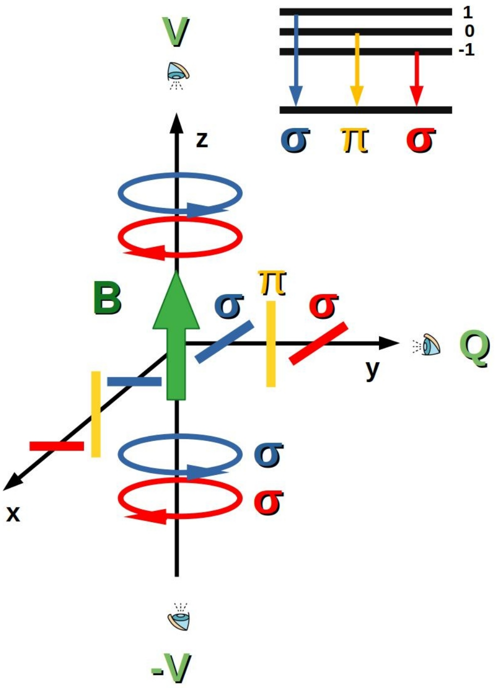

Figure 2.3 Illustration of the formation of the Zeeman components ($\sigma_{\rm r}$ in red, $\sigma_{\rm b}$ in blue, and π in yellow) and their polarization state according to the angle between the $\boldsymbol{B}$ and the line-of-sight (LOS) for a Normal Zeeman effect. The circular polarization is represented with closed curves with an arrow indicating the rotation direction, and the two perpendicular linear polarizations are represented with horizontal (σ) and vertical (π) lines. An observer detects signal in Stokes V in the direction parallel to $\boldsymbol{B}$ and Stokes Q (or U, depending on the LOS) in the direction perpendicular to $\boldsymbol{B}$. Figure adapted from Trujillo Bueno (2006).

thermodynamic conditions, among others, alter the initial beam by absorption, emission, scattering and magnetic effects, and the RTE accounts for them. Consequently, the RTE is a function of the wavelength. The first person to derive the RTE for the Stokes parameters of a Zeeman triplet, but neglecting the anomalous dispersion effects, was Unno (1956). A few years later, Rachkovsky (1962) introduced these effects with a classical approach.

In the following formalism, we assume that the radiation field is independent of time and that the absorption, emission and dispersion are independent of the incident beam. Moreover, the medium is stratified and hence it is anisotropic. Then the RTE is

$$\frac{\mathrm{d}\mathbf{I}_\lambda}{\mathrm{d}z} = -\mathbf{K}_\lambda\,\mathbf{I}_\lambda + \mathbf{j}_\lambda, \tag{2.18}$$

where $\mathbf{I}$ is the Stokes vector (2.2), z is the path along the medium, $\mathbf{j}$ refers to the emissivity processes, and $\mathbf{K}$ is the propagation matrix,

$$\begin{aligned}\mathbf{K} &= \begin{pmatrix} \eta_{\rm I} & \eta_{\rm Q} & \eta_{\rm U} & \eta_{\rm V} \\ \eta_{\rm Q} & \eta_{\rm I} & \rho_{\rm V} & -\rho_{\rm U} \\ \eta_{\rm U} & -\rho_{\rm V} & \eta_{\rm I} & \rho_{\rm Q} \\ \eta_{\rm V} & \rho_{\rm U} & -\rho_{\rm Q} & \eta_{\rm I} \end{pmatrix} \\ &= \begin{pmatrix} \eta_{\rm I} & 0 & 0 & 0 \\ 0 & \eta_{\rm I} & 0 & 0 \\ 0 & 0 & \eta_{\rm I} & 0 \\ 0 & 0 & 0 & \eta_{\rm I} \end{pmatrix} + \begin{pmatrix} 0 & \eta_{\rm Q} & \eta_{\rm U} & \eta_{\rm V} \\ \eta_{\rm Q} & 0 & 0 & 0 \\ \eta_{\rm U} & 0 & 0 & 0 \\ \eta_{\rm V} & 0 & 0 & 0 \end{pmatrix} + \begin{pmatrix} 0 & 0 & 0 & 0 \\ 0 & 0 & \rho_{\rm V} & -\rho_{\rm U} \\ 0 & -\rho_{\rm V} & 0 & \rho_{\rm Q} \\ 0 & \rho_{\rm U} & -\rho_{\rm Q} & 0 \end{pmatrix},\end{aligned} \tag{2.19}$$

where **K** has been divided into three matrices. The first term, the absorption matrix, accounts for the opacity, that is, it refers to the attenuation of the total intensity and all Stokes parameters are absorbed in the same way. On the other hand, the second term, the dichroism matrix, accounts for the selective absorption of the different polarization states. The last term, the dispersion matrix, accounts for the magneto-optical effects, that is, the transition of linear polarization states between them and to circular polarization.

The propagation matrix accounts for the whole spectra but we can reformulate it by separating the processes that affect the continuum and the processes that lead to line formation. The new formulation of the propagation matrix is

$$\mathbf{K} = \mathbf{K}_{\text{cont}} + \mathbf{K}_{\text{line}}. \tag{2.20}$$

The continuum radiation can be characterised by isotropic absorption and dispersion, and this is only present in isotropic mediums. The continuum radiation is assumed to be unpolarized. This implies that the dichroism matrix must be null, $\eta_{\text{U}} = \eta_{\text{Q}} = \eta_{\text{V}} = 0$. Therefore, the propagation matrix of continuum radiation is

$$\mathbf{K}_{\text{cont}} = \chi_{\text{cont}} \mathbf{1}, \tag{2.21}$$

where χ_{cont} is the absorption coefficient. Since it describes the continuum, it is wavelength-independent.

Due to the complex composition of the solar atmosphere that affects radiation differently depending on the wavelength, it is common to refer to the optical depth rather than to the actual atmospheric height. The continuum optical depth ($\tau_{\mathbf{c}}$) accounts for the extinction in the continuum of a beam along a certain height $z_0 - z$ in a medium,

$$\tau_{\text{c}} \equiv - \int_{z}^{z_0} \chi_{\text{cont}} \, \mathrm{d}z, \tag{2.22}$$

where z is the direction of propagation of the light.

Regarding the propagation matrix of spectral lines,

$$\mathbf{K}_{\text{lin}} \equiv \frac{N \pi e_0^2 f}{mc} \mathbf{\Phi}, \tag{2.23}$$

where f is the oscillator strength, $\mathbf{\Phi}$ is the matrix that contains the normalized dispersion (ϕ_α) and absorption (ψ_α) profiles, and N is the wavelength distribution of velocities. From Eqs. 2.20, 2.21, and 2.23 we obtain

$$\mathbf{K} = \chi_{\text{cont}} (\mathbf{1} + \eta_0 \mathbf{\Phi}), \tag{2.24}$$

where we have included the line-to-continuum absorption coefficient ratio,

$$\eta_0 \equiv \frac{\chi_{\text{lin}}}{\chi_{\text{cont}}} = \frac{N \pi e_0^2 f}{mc \chi_{\text{cont}}}. \tag{2.25}$$

2.2.1 Local Thermodynamic Equilibrium

Some layers of stellar atmospheres have the proper conditions to be approximated by the local thermodynamic equilibrium (LTE). The LTE means that the thermodynamic properties of matter are described by the thermodynamic equilibrium equations with the local values of temperature (T) and density (ρ). However, the radiation is allowed to deviate from the thermodynamic equilibrium. Frequent collisions between particles decouple radiation and matter, and the number of collisions is directly related to the medium ρ. Hence, layers with large ρ would be close to the LTE.

The LTE implies that the local number of emitters and absorbers in the different quantum states obeys Saha and Boltzmann's equations and that the distribution of velocities is Maxwellian. Emission and absorption profiles are the same, as natural excitation dominates in LTE. Moreover, we can use the complete redistribution approximation, where the frequencies of the incoming photons and the scattered photons are unrelated. Hence the pure scattering processes do not modify the absorption or emission profiles. Finally, the Kirchhoff's law is also valid,

$$\mathbf{j}_\lambda \equiv \begin{pmatrix} j_\mathrm{I} \\ j_\mathrm{Q} \\ j_\mathrm{U} \\ j_\mathrm{V} \end{pmatrix} = B_\lambda(T) \begin{pmatrix} \eta_\mathrm{I} \\ \eta_\mathrm{Q} \\ \eta_\mathrm{U} \\ \eta_\mathrm{V} \end{pmatrix}, \tag{2.26}$$

where B_λ is the Planck function,

$$B_\lambda(T) = \frac{2hc^3}{\lambda^5} \frac{1}{e^{hc/\lambda k_\mathrm{B} T} - 1}, \tag{2.27}$$

and k_B is the Boltzmann constant.

We can introduce a new variable, the source function $\mathbf{S}$, which is generally defined as the ratio between the emission coefficient and the absorption coefficient. Under LTE conditions, the source function equals

$$\mathbf{S}_\lambda \equiv \begin{pmatrix} B_\lambda(T) \\ 0 \\ 0 \\ 0 \end{pmatrix}. \tag{2.28}$$

We can finally rewrite the general RTE (Eq. 2.18) in terms of Eq. 2.20 under the LTE approximation. Therefore we introduce the newly defined source function (Eq. 2.28) and Kirchhoff's law (Eq. 2.26). Additionally, we exchange the height variations along the z axis for the continuum optical depth τ_c,

$$\frac{\mathrm{d}\mathbf{I}_\lambda}{\mathrm{d}\tau_\mathrm{c}} = \mathbf{K}_\lambda \, \mathbf{I}_\lambda - \mathbf{S}_\lambda. \tag{2.29}$$

In this formulation, the absorption-related elements of the propagation matrix are

$$\begin{aligned} \eta_\mathrm{I} &= \frac{\eta_0}{2}\Big\{ \phi_0 \sin^2\theta + \frac{1}{2}\left[\phi_{+1} + \phi_{-1}\right]\Big(1 + \cos^2\theta\Big)\Big\} + 1 \\ \eta_\mathrm{Q} &= \frac{\eta_0}{2}\Big\{ \phi_0 - \frac{1}{2}\left[\phi_{+1} + \phi_{-1}\right]\Big\} \sin^2\theta \, \cos^2 2\varphi \\ \eta_\mathrm{U} &= \frac{\eta_0}{2}\Big\{ \phi_0 - \frac{1}{2}\left[\phi_{+1} + \phi_{-1}\right]\Big\} \sin^2\theta \, \sin^2 2\varphi \\ \eta_\mathrm{V} &= \frac{\eta_0}{2}\left[\phi_{-1} - \phi_{+1}\right] \cos\theta, \end{aligned} \tag{2.30}$$

and the dispersion-related elements,

$$\begin{aligned} \rho_\mathrm{Q} &= \frac{\eta_0}{2}\Big\{ \psi_0 - \frac{1}{2}\left[\psi_{+1} + \psi_{-1}\right]\Big\} \sin^2\theta \, \cos^2 2\varphi \\ \rho_\mathrm{U} &= \frac{\eta_0}{2}\Big\{ \psi_0 - \frac{1}{2}\left[\psi_{+1} + \psi_{-1}\right]\Big\} \sin^2\theta \, \sin^2 2\varphi \\ \rho_\mathrm{V} &= \frac{\eta_0}{2}\left[\psi_{-1} - \psi_{+1}\right] \cos\theta, \end{aligned} \tag{2.31}$$

where θ and φ are the inclination and azimuth of the $\boldsymbol{B}$ respect to the direction of propagation of the light. From Eq. 2.30 and Eq. 2.31 we note that φ cannot be unambiguously retrieved during the solving of the RTE.

We have introduced the absorption ϕ_α and dispersion ψ_α profiles, of each of the Zeeman components σ_+, σ_- and π (see Subsect. 2.1.2), for which $\alpha = +1, -1, 0$, respectively,

$$\begin{aligned} \phi_\alpha(u_{0,\alpha}, a_\alpha) &= \frac{1}{\sqrt{\pi}} H(u_{0,\alpha} - u_{\mathrm{LOS}} + \alpha\, u_{\mathrm{B}}, a_\alpha) \\ \varphi_\alpha(u_{0,\alpha}, a_\alpha) &= \frac{1}{\sqrt{\pi}} F(u_{0,\alpha} - u_{\mathrm{LOS}} + \alpha\, u_{\mathrm{B}}, a_\alpha). \end{aligned} \tag{2.32}$$

The absorption and dispersion profiles are calculated for a moving system with a v_{LOS} with respect to the observer (u_{LOS} in its reduced form) in the presence of a magnetic field. Additionally, every particle has a velocity due to the thermal agitation, and the distribution of velocities is Maxwellian as mentioned above. The various movements of the system induce shifts with respect to the λ_0 of the system in rest. Therefore, the shape of the absorption and dispersion profiles are mostly influenced by the magnetic field and the induced Zeeman component, the thermal agitation and the LOS movement of the medium.

The width of the velocities, the Doppler width v_{D}, accounts for the temperature-related shifts. It introduces a term of microturbulence, ξ_{mic}, that comprises small-scale motions (smaller than the mean free path of photons) that are not included in the thermal agitation parameter,

$$v_{\mathrm{D}} \equiv \sqrt{\frac{2k_{\mathrm{B}}T}{m} + \xi_{\mathrm{mic}}^2}, \tag{2.33}$$

and it can also be formulated in terms of the wavelength shift produced,

$$v_{\mathrm{D}} = \frac{\Delta\lambda_{\mathrm{D}}\, c}{\lambda_{0,\alpha}}. \tag{2.34}$$

Since all the particles are in motion, the movement of a particle with respect to the others produces another wavelength displacement,

$$v = \frac{\Delta\lambda\, c}{\lambda_{0,\alpha}} = \frac{(\lambda - \lambda_{0,\alpha})c}{\lambda_{0,\alpha}},$$

from where we finally get the reduced form of the velocity, as employed in Eq. 2.32. A similar formulation is used for u_{LOS} and for the displacement produced by the presence of a magnetic field,

$$u_{0,\alpha} \equiv \frac{\Delta\lambda}{\Delta\lambda_{\mathrm{D}}} \qquad u_{\mathrm{LOS}} \equiv \frac{\Delta\lambda_{\mathrm{LOS}}}{\Delta\lambda_{\mathrm{D}}} \qquad u_{\mathrm{B}} \equiv \frac{\lambda_{\mathrm{B}}}{\Delta\lambda_{\mathrm{D}}}. \tag{2.35}$$

The parameter a_α included in Eq. 2.32, where Γ_α is the damping constant of each Zeeman component, is defined as

$$a_\alpha \equiv \frac{\Gamma_\alpha \lambda_{0,\alpha}^2}{c\Delta\lambda_{\mathrm{D}}}. \tag{2.36}$$

Finally, the Voigt (H) and Faraday-Voigt F functions, to which the absorption and dispersion profiles are proportional, are

$$
\begin{aligned}
H(u,a) &\equiv \frac{a}{\pi}\int_{-\infty}^{\infty} e^{-y^2}\frac{1}{(u-y)^2+a^2}\mathrm{d}y \\
F(u,a) &\equiv \frac{1}{\pi}\int_{-\infty}^{\infty} e^{-y^2}\frac{u-y}{(u-y)^2+a^2}\mathrm{d}y.
\end{aligned}
\tag{2.37}
$$

In the end, the formal solution of the RTE (Eq. 2.29) is

$$
\mathbf{I}(0) = \int_0^{\infty} \mathcal{O}(0,\tau_\mathrm{c})\mathbf{K}(\tau_\mathrm{c})\mathbf{S}(\tau_\mathrm{c})\mathrm{d}\tau_\mathrm{c}. \tag{2.38}
$$

This solution was first derived by Landi Degl'Innocenti et al. (1985), where they introduced the (linear) evolution operator $\mathcal{O}(\tau)$. This operator transforms the solution from two points at different optical depths,

$$
\mathbf{I}(\tau_\mathrm{c}) = \mathcal{O}(\tau_\mathrm{c},\tau_\mathrm{c}')\mathbf{I}(\tau_\mathrm{c}'). \tag{2.39}
$$

As long as the evolution operator is unknown, the RTE is solved using numerical methods. Nonetheless, some approximations allow for an analytical solution.

2.2.2 Milne-Eddington approximation

Since the solution of the RTE is not trivial, approximations are allowed under certain circumstances. This is the case of the M-E approximation, which assumes an M-E atmosphere to find an analytical solution of the RTE. This model atmosphere is characterised by atmospheric quantities that are constant along the optical depth. This means that the propagation matrix $\mathbf{K}$ is constant with optical depth and that the evolution operator has a known solution,

$$
\begin{aligned}
\mathbf{K}(\tau_\mathrm{c}) &= \mathbf{K}_0 \\
\mathcal{O}(0,\tau_\mathrm{c}) &= e^{-\mathbf{K}_0\tau_\mathrm{c}}.
\end{aligned}
\tag{2.40}
$$

Only the source function is allowed to change with optical depth and it does it linearly,

$$
\mathbf{S} = \mathbf{S}_0 + \mathbf{S}_1\,\tau_\mathrm{c}. \tag{2.41}
$$

By expressing Eq. 2.38 with the M-E atmospheric conditions and solving it,

$$
\mathbf{I}(0) = \int_0^{\infty} e^{-\mathbf{K}_0\tau_\mathrm{c}}\mathbf{K}_0(\mathbf{S}_0 + \mathbf{S}_1\,\tau_\mathrm{c})\mathrm{d}\tau_\mathrm{c} = \mathbf{S}_0 + \mathbf{K}_0^{-1}\mathbf{S}_1, \tag{2.42}
$$

we obtain the Unno-Rachkovsky solution (Unno, 1956; Rachkovsky, 1962), where the Stokes profiles are,

$$
\begin{aligned}
I(0) &= S_0 + \frac{\eta_\mathrm{I}}{\Delta}(\eta_\mathrm{I}^2 + \rho_\mathrm{Q}^2 + \rho_\mathrm{U}^2 + \rho_\mathrm{V}^2)S_1 \\
Q(0) &= -\frac{S_1}{\Delta}\left[\eta_\mathrm{I}^2\eta_\mathrm{Q} + \nu_\mathrm{I}(\nu_\mathrm{V}\rho_\mathrm{U} - \nu_\mathrm{U}\rho_\mathrm{V}) + \rho_\mathrm{Q}(\eta_\mathrm{Q}\rho_\mathrm{Q} + \eta_\mathrm{U}\rho_\mathrm{U}\eta_\mathrm{V}\rho_\mathrm{V})\right] \\
U(0) &= -\frac{S_1}{\Delta}\left[\eta_\mathrm{I}^2\eta_\mathrm{U} + \nu_\mathrm{I}(\nu_\mathrm{Q}\rho_\mathrm{V} - \nu_\mathrm{V}\rho_\mathrm{Q}) + \rho_\mathrm{U}(\eta_\mathrm{Q}\rho_\mathrm{Q} + \eta_\mathrm{U}\rho_\mathrm{U}\eta_\mathrm{V}\rho_\mathrm{V})\right] \\
V(0) &= -\frac{S_1}{\Delta}\left[\eta_\mathrm{I}^2\eta_\mathrm{V} + \nu_\mathrm{I}(\nu_\mathrm{U}\rho_\mathrm{Q} - \nu_\mathrm{Q}\rho_\mathrm{U}) + \rho_\mathrm{V}(\eta_\mathrm{Q}\rho_\mathrm{Q} + \eta_\mathrm{U}\rho_\mathrm{U}\eta_\mathrm{V}\rho_\mathrm{V})\right],
\end{aligned}
\tag{2.43}
$$

where the determinant of the propagation matrix, Δ is

$$\Delta = \eta_{\mathrm{I}}^2 \left(\eta_{\mathrm{I}}^2 - \eta_{\mathrm{Q}}^2 - \eta_{\mathrm{U}}^2 - \eta_{\mathrm{V}}^2 + \rho_{\mathrm{Q}}^2 + \rho_{\mathrm{U}}^2 + \rho_{\mathrm{V}}^2\right) - \left(\eta_{\mathrm{Q}}\rho_{\mathrm{Q}} + \eta_{\mathrm{U}}\rho_{\mathrm{U}} + \eta_{\mathrm{V}}\rho_{\mathrm{V}}\right)^2. \tag{2.44}$$

To calculate the Unno-Rachkovsky solution, the model atmosphere has to be properly characterised by the parameters introduced along Sect. 2.2. In the M-E approximation these parameters are reduced to only: the vector magnetic field strength B, azimuth θ, and inclination φ, the damping parameter a, the line-to-continuum absorption coefficient ratio η_0, the Doppler width of the line $\Delta\lambda_{\mathrm{D}}$, the LOS velocity, and the two source function parameters, S_0 and S_1. Since these parameters are considered constant along the optical depth, they account for their actual values averaged along the optical depth where the spectral line is most sensitive to those parameters. Complex observations, for example with asymmetric profiles, cannot be reproduced due to the lack of gradients. Therefore, in the presence of net circular polarization, which indicates the presence of a gradient of the physical properties along the LOS, the M-E approximation provides misleading results.

2.3 Inversion codes

An inversion code is a tool that uses spectropolarimetric observations to obtain estimated physical parameters of the atmospheric layers from where the radiation is emitted. These physical parameters are calculated by solving the RTE that takes into account plasma physics equations and atomic parameters for a spectral line from a medium in the presence of a magnetic field.

Forward modelling solves the RTE for a model atmosphere and calculates synthetic Stokes profiles. An inversion code compares the synthetic Stokes profiles to real observations and iteratively tunes the parameters of the initial model atmosphere to reproduce the real observations as accurately as possible through minimization algorithms. Figure 2.4 provides an example of observed and synthesized Stokes profiles.

As explained in Sect. 2.2, we can define the RTE more specifically by introducing the physics that characterises the atmospheric layer of our interest. Since the main aim of this work is to analyse photospheric magnetic structures (sunspots and pores) where the LTE can be assumed, we work with inversion codes that employ the LTE assumption. In every inversion code, the azimuth solution is ambiguated as a consequence of Eqs. 2.30 and 2.31. That is, a $\boldsymbol{B}$ with $\theta = \theta_0$ and $\theta = \theta_0 + 180°$ under the same model atmosphere produces the same Stokes profiles. Several minimization algorithms have been developed to disambiguate the azimuth, where each of them minimizes different quantities. As an example, AZAM minimizes the θ between neighbouring pixels, ME0, that used the Minimum Energy method, minimizes $\lambda|J_{\mathrm{z}}| + |\nabla \cdot \mathbf{B}|$, the "acute angle" method minimizes θ respect to reference field assuming a potential field, while the Non-Potential Field assumes the opposite. The accuracy of the different methods has been tested by different authors (e.g., Leka et al., 2009b) and the choice of one over another depends on the structure under study. In the case of sunspots and pores, due to the well-established radial orientation of the magnetic field, the disambiguation solution tends to be very solid for all the methods. Less accurate results arise in observations with large noise or with aleatory orientation of the magnetic field.

In the following subsections, we describe the inversion codes used to obtain the data analysed in this thesis. Vector magnetic fields calculated with the Very Fast Inversion of the Stokes Vector (VFISV) inversion code are analysed in the papers reproduced in Chapters 4, 6, and 5. Additionally, $\boldsymbol{B}$ inverted with the Milne-Eddington gRid Linear Inversion Network (MERLIN) and the SIR codes are included in the paper contained in Chapter 5.

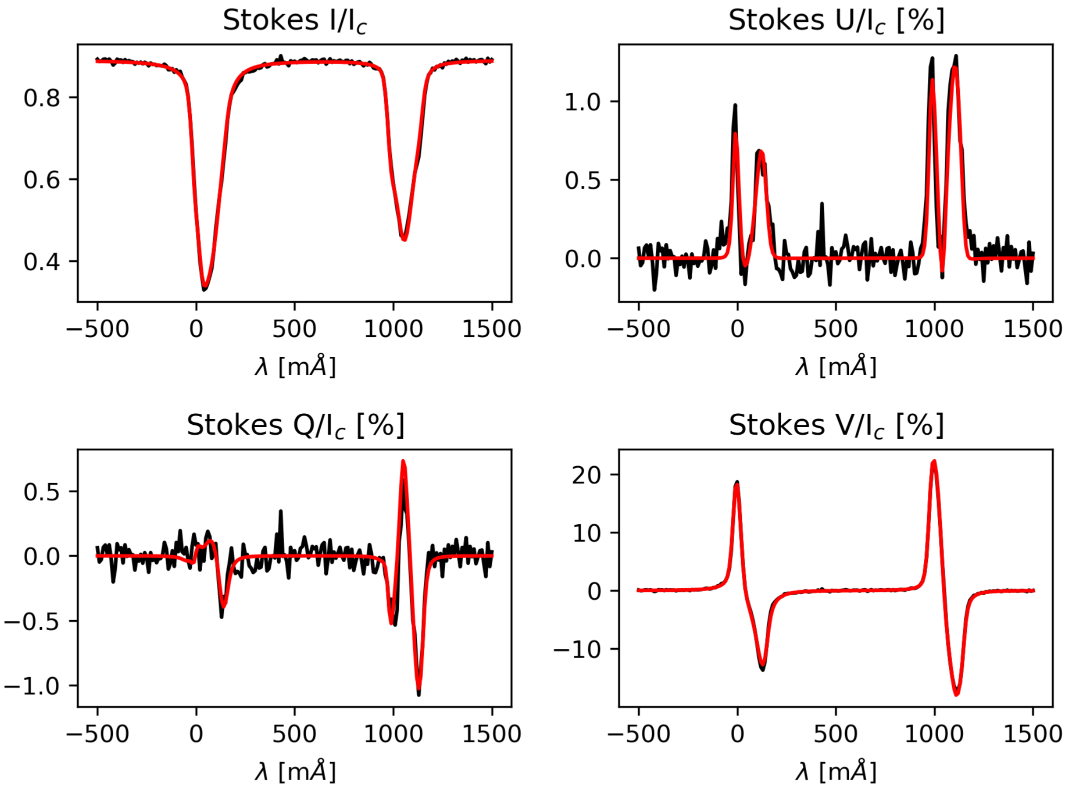

Figure 2.4 Visual comparison of observed Stokes profiles (black line) and the best fit obtained by SIR (red line).

2.3.1 VFISV

VFISV (Borrero et al., 2011b; Centeno et al., 2014) is an inversion code specifically designed to invert full-disc spectropolarimetric data from the HMI on board the Solar Dynamics Observatory (SDO). See Sect. 3.2.1 for further details of the instrument).

The code, written in FORTRAN, assumes a M-E atmosphere, where the number of free parameters to be inverted is very reduced. A small number of free parameters is key to completing the inversion of 2046 × 2046 pixels (HMI full field of view (FOV)) in a time inferior to the 12-minute temporal cadence of the observations. The atmospheric parameters to be calculated in a standard M-E atmosphere are $\mathcal{M}_{\rm M-E} = (\mathbf{B}, \mathbf{S}, \eta_0, \Delta\lambda_{\rm D}, a, v_{\rm LOS}, v_{\rm mac}, \alpha)$. The new parameter, the filling factor α, is a free parameter widely used by inversion codes and accounts for the fraction of the observed light within a pixel that comes from a magnetised atmosphere. Besides the use of the M-E approximation, VFISV realises several optimizations that allow for faster inversions. For instance, the filling factor and the damping parameter are kept constant ($\alpha = 1$, $a = 0.5$), and $v_{\rm mac}$ is removed from the free parameters because its effects can be mimicked by $\Delta\lambda_{\rm D}$. To restrict the number of iterations, large values of η_0 are penalized, and the parameters have physically feasible upper and lower limits, which –among other measures– translates into an average of 30 iterations per pixel. Moreover, the forward modelling only synthesises the inner wavelengths of the Fe I 617.33 nm absorption line, while the intensity of the outer wavelengths is calculated by integrating the contribution of the filter profiles and multiplying them by the continuum intensity obtained in the synthesis.

The strategy of the inversion is based on a non-linear least-squares minimization of a merit function, χ^2, that uses a Levenberg – Marquardt minimization algorithm. The signal levels are unequal for all the Stokes profiles, being I the most intense profile. The use of weights, W_S, strengthens or weakens the importance of each Stokes profile in the minimization process, giving more significance to U, Q and V. Furthermore, to keep the normalization of χ^2 as homogeneous as possible, and following MERLIN method, the weights are constant in the full-disc inversions. The weights were selected to optimise the inversions in ARs. Complementary to VFISV, the HMI Vector Magnetic Field pipeline provides solutions to disambiguate the azimuth through the Minimum Energy method, ME0 (Hoeksema et al., 2014) in pixels with a small-to-medium level of noise, and of three different methods (potential-acute, random, and radial-acute) in pixels with large level of noise.

Two versions of VFISV have been implemented to invert spectropolarimetric data from spectrographs and filtergraphs.

2.3.2 MERLIN

MERLIN is an inversion code designed to invert data from the SP/Hinode (see Sect. 3.2.2 for further details).

This code, written in C++, also assumes a M-E atmosphere. SP/Hinode observes two spectral lines, Fe I 630.15 nm and 630.25 nm, which help to constrain the free parameters due to the different physics behind each line; the same $\boldsymbol{B}$ alters the line differently because of their different magnetic sensitivity. The good spectral sampling and the number of spectral line points improve the quality of the inversions. The inversions are limited to the spectral range ±0.30 Å from the line centres. Opposite to VFISV, MERLIN does not require to reduce the inversion time as much as possible and therefore, less approximations are considered. For instance, neither α nor a are considered constant, and the v_{mac} is included as a constant (0.7083 km/s). Additionally, MERLIN includes a stray light factor that aims to remove the instrument-induced light contamination. The scattered light profile (I_{scatt}) is calculated by averaging the line profiles from pixels with low polarization. The observed intensity is then separated into two components, the intensity originated in magnetised plasma and the scattered light ($I_{\mathrm{obs}} = \alpha I_{\mathrm{mag}} + (1-\alpha) I_{\mathrm{scatt}}$). The initial values for the model atmosphere of the magnetic field strength, Doppler shift and filling factor are calculated with a genetic algorithm, which calculates a more accurate initial guess than other simpler methods.

The code maintains constant W_S in all the inversions, however, the weights are different to those considered in VFISV because of the different acquisition optics. MERLIN also employs a least-squares fitting using a Levenberg-Marquardt minimisation algorithm. Finally, the SP/Hinode pipeline uses the Minimum Energy method (Leka et al., 2009a) to calculate a solution for the disambiguated azimuth.

2.3.3 SIR

The SIR code (Ruiz Cobo et al., 1992) synthesises and inverts spectral lines assuming a stratified atmosphere. The code is able to work with any electric dipole transition and atomic species taking into account the Zeeman-induced polarization of the light under the LTE approximation. Moreover, it can invert the thermal, dynamic and magnetic atmospheric plasma properties for any arbitrary number of spectral lines by introducing the equation of state of an ideal gas to the solving process.

SIR introduces a new descriptor, the response function (RF). An example of RFs for Stokes I and V is given in Fig. 2.5. RFs account for the influence (or response) of small perturbations of the atmospheric parameters on the emitted Stokes profiles at different optical depths,

$$\delta \mathbf{I}(\lambda) = \int_0^\infty \mathbf{R}_x(\lambda, \tau)\delta x(\tau)\mathrm{d}\tau. \tag{2.45}$$

Mathematically, the RFs are a sort of partial derivative of the observed Stokes profiles with respect to the atmospheric parameters,

$$\mathbf{R}_x(\tau) = \mathcal{O}(0, \tau)\Big\{\mathbf{K}(\tau)\frac{\partial \mathbf{S}(\tau)}{\partial x} - \frac{\partial \mathbf{K}(\tau)}{\partial x}\left[\mathbf{I}(\tau) - \mathbf{S}(\tau)\right]\Big\}, \tag{2.46}$$

where $x(\tau)$ refers to the parameters of the model atmosphere. The evolution operator $\mathcal{O}(\tau)$, propagation matrix $\mathbf{K}(\tau)$ and source function $\mathbf{S}(\tau)$ have been already introduced in Sect. 2.2.

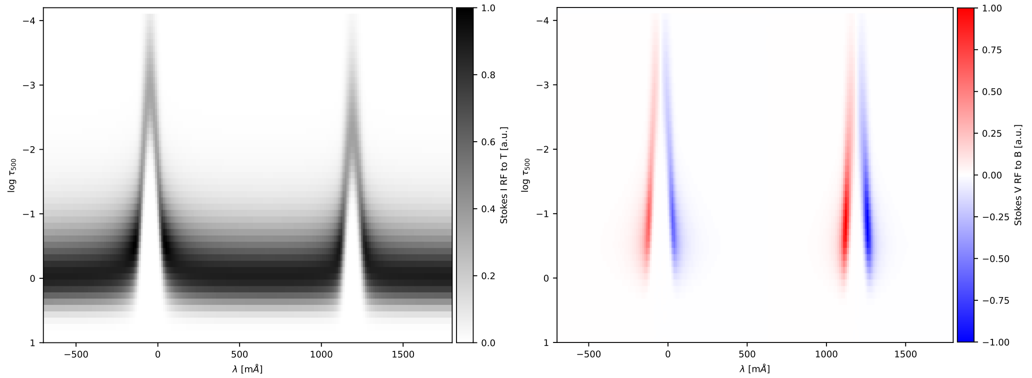

Figure 2.5 Examples of Response Functions of Stokes I and V to T and B, respectively. Stokes I in the continuum range of the spectrum is more sensitive to temperature fluctuations around $\log \tau = 0$ (which is the visual surface) while the lines are more altered at smaller τ values (that is, the lines are formed higher in the atmosphere and are more sensitive to temperature shifts up there). The RF for Stokes V shows that the right line is more sensitive to changes in B, while both of the lines are mostly affected by changes of B at around $\log \tau = -1$.

SIR calculates the perturbation of the initial model atmosphere needed to reproduce the observed Stokes profiles. In this code, the atmospheric parameters to be solved are $\mathcal{M}_{\mathrm{SIR}} = (\mathbf{B}(\tau), T(\tau), v_{\mathrm{LOS}}(\tau), v_{\mathrm{mic}}(\tau), v_{\mathrm{mac}}, \alpha)$. Several model atmospheres are available to use as an initial atmosphere, depending on where the pixel is located (umbra, penumbra, plage, etc). In order to accelerate the inversions, the code allows us to choose the amount of optical depths where to evaluate the synthetic profiles. These optical depths, called nodes, may differ for each x, and they are automatically positioned equidistantly along the optical depth range. The weights, unless specified otherwise, are automatically determined to give the same relative weights to all the Stokes profiles independently of their amplitudes. The minimization of χ^2 is executed by a Marquardt nonlinear least-squares algorithm. The importance of the newly introduced RFs is such that the Marquardt algorithm utilises the RFs instead of the derivatives of χ^2 with respect to the atmospheric parameters, therefore simplifying the calculations.

3 Observations

The study of the interactions between solar convection and magnetism requires spectropolarimeters. As seen in Fig. 2.1, it was the development of these instruments that provided a huge boost to the understanding of the magnetic configuration in the solar atmosphere. Spectropolarimeters can be attached to either space- or ground-based telescopes, and each of them has its own advantages. Space-based observations provide more homogeneous databases that are not influenced by the Earth's atmosphere. On the other hand, ground-based observations typically provide better resolutions (temporal, spatial and spectral) since the instruments and telescopes do not have such a strict small size, data volume or telemetry limitations. In the following sections, the instruments used in this PhD thesis are presented.

3.1 Ground-based observations

Even though large magnetic structures evolve gradually over hours or even days, their smaller structures are highly dynamic, changing within minutes or tens of minutes. Consequently, the study of the interaction between solar convection and magnetism greatly benefits from very high spatial resolution and temporal cadence. For this reason, a significant portion of our efforts has been dedicated to preparing observation proposals for ground-based telescopes.

During my PhD studies, we have been involved in a total of six observing campaigns:

1. 'Convection in magnetised plasma', GREGOR telescope (Tenerife, Spain), 17–24 October 2018. Visitor mode. PI: Jan Jurčák (Astronomical Institute of the CAS).
2. 'Effects of inclined magnetic fields on magnetoconvective modes: granulation characterization.', GREGOR telescope (Tenerife, Spain), 3–13 August 2019. Visitor mode. PI: Marta García Rivas (Astronomical Institute of the CAS, Astronomical Institute of Charles University).
3. 'Characterisation of solar granulation in terms of the vector magnetic field', Swedish Solar Telescope (SST; La Palma, Spain), 24–30 August & 10–16 October 2020. Service mode. PI: Marta García Rivas (Astronomical Institute of the CAS, Astronomical Institute of Charles University).
4. 'Observations of a photospheric and chromospheric response to flares', GREGOR telescope (Tenerife, Spain), 26 July–4 August 2021. Remote mode. PI: Lucia Mravcová (Astronomical Institute of the CAS, Astronomical Institute of Charles University).
5. 'Properties of convective cells at the penumbra/umbra boundary', Daniel K. Inouye Solar Telescope (DKIST; Maui, USA). Cycle 1. Service mode. PI: Philip Lindner (Institute for Solar Physics (KIS)).
6. 'Multi-wavelength observations of the atmospheric response to flares', GREGOR telescope (Tenerife, Spain), 2–20 May 2022. Visitor mode. PI: Marta García Rivas (Astronomical Institute of the CAS, Astronomical Institute of Charles University).

Except for the observing campaigns in service mode (3,6), I have been actively observing in all of the campaigns, both in visitor mode –at GREGOR telescope– or in remote mode –operating GREGOR telescope from the Astronomical Institute of the CAS in Ondřejov.

Big observatories are built in places with very favourable observing conditions. Yet, the success of a campaign is a matter of luck since it heavily depends on nature. Unfortunately, during most of our campaigns the atmospherical conditions (turbulence, calima, clouds, strong winds, etc), the solar atmosphere (lack of target of interest) or the local conditions (wildfires) were not favourable and no data of interest could be retrieved from campaigns 1 to 5. Nonetheless, the successful campaign (6) led to exceptional data. So far, a study related to the motions of penumbral grains has been published (Sobotka et al., 2024), and the first analysis of the unique GREGOR-IRIS co-observations of a M5.7 flare has been submitted. Since flares are not the main topic of this PhD thesis, a reproduction of the submitted paper (García-Rivas et al., 2024c) is included as a supplement (see Appendix A).

In the following section, we describe the telescopes and instruments employed to retrieve the data analysed in the papers reproduced in Chapter 6 (Vacuum Tower Telescope (VTT)) and Appendix A (GREGOR).

3.1.1 GREGOR telescope

GREGOR telescope is based at the Observatorio del Teide, Tenerife (Spain). Tenerife belongs to the Canary Islands archipelago, which, due to its volcanic origin, has reached considerable heights. The Observatorio del Teide is located 2400 meters above sea level, and only a few kilometres away from the third highest volcano measured from its base in the world, the peak of Teide. The local conditions produce a quasi-permanent vertical inversion line, on average between 800 and 1600 meters above sea level, that maintains the low clouds and humidity below the observatory. The exceptional stability, transparency and dryness of the atmosphere have been acknowledged by many studies (see e.g., Varela et al., 2002; Hidalgo et al., 2021).

The solar GREGOR telescope (W. Schmidt et al., 2012) is nowadays the largest solar telescope in Europe. Figures 3.1–3.2 present the building where it is installed, and the mechanical structure at the dome. GREGOR is a double Gregory system with three imaging mirrors. The 1.5-m primary mirror permits to observe structures on the Sun as

Figure 3.1 GREGOR telescope at the Observatorio del Teide, with the sea of clouds below.

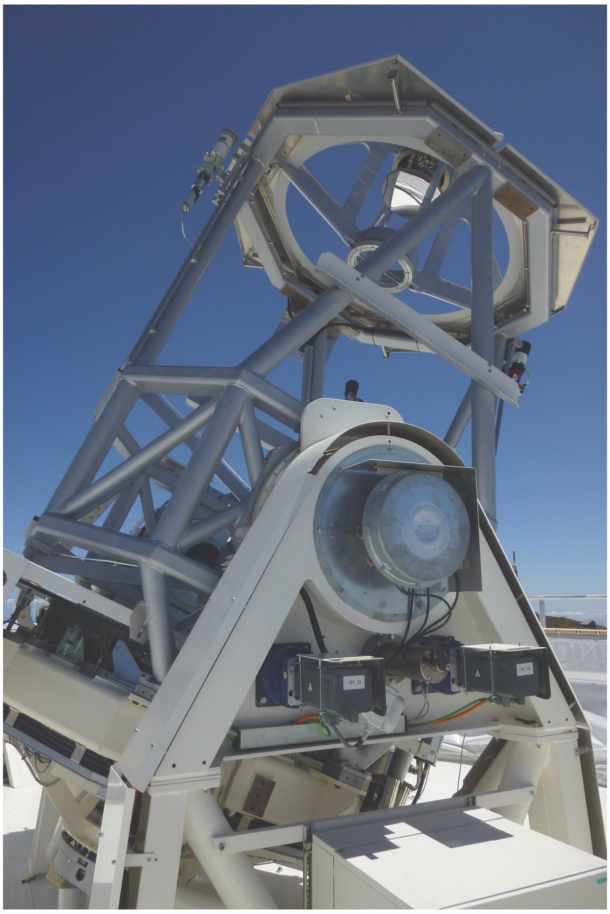

Figure 3.2 GREGOR secondary mirror and the mechanical structure at the dome.

small as 100 km wide. The FOV diameter is 150″ and it can observe a wide spectral range, from the near ultraviolet (UV) to almost 5 microns. In order to counteract the seeing effects, the telescope has an adaptive optics system (Berkefeld et al., 2012) with a deformable mirror with 256 actuators and a 10-cm sub-aperture size.

Since its inauguration in 2012, several instruments have been in use. We proceed to describe the instruments employed in the observing campaign that led to the paper reproduced in Appendix A.

GRIS

The GREGOR Infrared Spectrograph (GRIS, Collados et al., 2012) is an instrument composed of a grating spectrograph with a Czerny-Turner configuration and a polarimeter adapted from the Tenerife Infrared Polarimeter II (TIP-II Collados et al., 2007). GRIS can be used both in spectropolarimetry and spectroscopy modes. It can observe in the near-infrared (NIR) range (1.0–2.3 μm), however, since the polarimeter includes two sets of ferroelectric liquid crystals, the spectropolarimetric observations are limited to the wavelength ranges where each set better works: one in the range 1.0–1.3 μm, and the other in the range 1.5–1.8 μm.

GRIS currently provides two observing settings, a slit and an integral field unit (IFU). The slit has a $\sim 60''$ length and a $0.26''$ width, it moves along one direction up to $0.64''$. Consequently, 2D maps of up to $60'' \times 64''$ are recorded non-simultaneously as a composition of 1D spectropolarimetric observations. The IFU is based on image slicers that slice an image into several smaller rectangles that are arranged in the shape of a long slit. The IFU (Dominguez-Tagle et al., 2022) has eight slices with a width of $0.375''$

and, in total, it covers a $\sim 6'' \times 3''$ FOV. In this case, small 2D spectropolarimetric maps are retrieved simultaneously. Moreover, the IFU can scan the solar surface along two directions and acquire a bigger FOV of up to $60'' \times 60''$. The spatial sampling can be reduced to $0.135''$ using the double sampling mode. In both settings the pixel scale is $0.13''$. Additionally, context images are provided by the slit-jaw imaging system.

HiFI+

The Improved High-resolution Fast Imager (HiFI+ Denker et al., 2023) is the upgraded version of the High-resolution Fast Imager. This instrument comprises three pairs of synchronized cameras. HiFI+1 includes two sCMOS cameras with a FOV of $70.7'' \times 59.6''$ and a pixel scale of $0.028''\mathrm{pixel}^{-1}$. It is equipped with interference filters at G-band (4307 Å) and blue continuum (4506 Å), each with a passband of 11 Å. HiFI+2 consists of two Imager M-lite 2M CMOS cameras, featuring an FOV of $76.5'' \times 60.5''$ and a pixel scale of $0.050''\mathrm{pixel}^{-1}$. This setup includes a broadband interference filter and a narrowband Lyot filter at H-alpha (6563 Å) with passbands of 7.5 and 0.6 Å, respectively. HiFI+3 is equipped with two Imager M-lite 2M CMOS cameras, providing FOVs of $48.2'' \times 30.8''$ and $76.5'' \times 60.5''$ with pixel scales of $0.025''\mathrm{pixel}^{-1}$ and $0.050''\mathrm{pixel}^{-1}$, respectively. This configuration incorporates interference filters at Ca II H (3968 Å) and TiO molecular band (7058 Å), with passbands of 9 and 11 Å, respectively.

The sCMOS and CMOS cameras facilitate high-speed image acquisition: HiFI+1 operates at 49 Hz, while HiFI+2 and HiFI+3 operate at 100 Hz. Therefore, this instrument offers a unique combination of high-speed acquisition of photospheric and chromospheric images. The acquisition rates permit the restoration of images with a still very good cadence of ~ 12 s for HiFI+1 and ~ 6 s for HiFI+2 and HiFI+3. Additionally, a specific data reduction pipeline is available (`sTools`; Kuckein et al., 2017).

3.1.2 VTT telescope

Figure 3.3 The solar Vacuum Tower Telescope (VTT) at the Observatorio del Teide at sunset.

The VTT (Schroeter et al., 1985) is a solar telescope situated at the Observatorio del Teide (Fig. 3.3), right next to GREGOR. The solar beam is directed towards the interior of the tower, where the fixed telescope is situated, by a coelostat composed of two movable 80-cm flat mirrors. The coelostat is pictured in Fig. 3.4. The beam light is directed through a 75 cm entrance window towards a (not currently) evacuated tank. The tank is about 25 m high and about 2 m wide, and it used to be evacuated to less than 133 Pa to avoid internal seeing (the heating of the air inside the telescope by the solar radiation). The spherical 70 cm f/86 main mirror is located at the end of the tank. In addition, the Kiepenheuer Institut Adaptive Optics System (KAOS, van der Luehe et al., 2003) was installed to improve the quality of the observations by correcting the distortion of the images produced by the Earth's atmosphere.

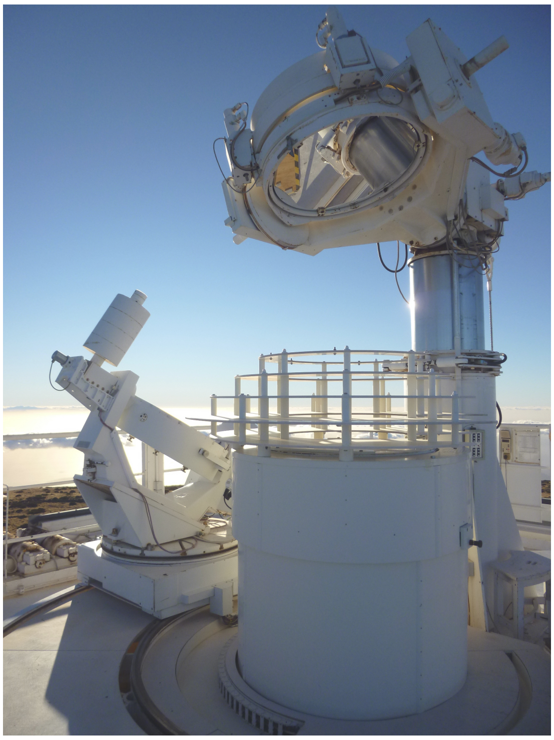

Figure 3.4 Coelostat on VTT that directs the light beam towards the interior of the building.

The VTT was designed in the 1970s and it has been operating since 1988. During this period, several permanent and temporal instruments have been observing the Sun from VTT. Moreover, some instruments have been tested at VTT and, afterwards, they have been moved to more powerful telescopes like GREGOR. Below, we describe the instrument used to acquire the dataset analysed in the paper reproduced in Chapter 6.

GFPI

The GFPI is a spectrometer developed in the 1990s (Bendlin et al., 1992; Puschmann et al., 2006a) that was mounted at VTT for several years. A series of upgrades transformed it into an instrument capable of recording 2D maps of full Stokes parameters. The final optical design upgrade was conducted to install GFPI at the GREGOR telescope, where it was moved in 2009. Thereafter, GFPI was known as the GREGOR FPI and it was one of the three first-light instruments at GREGOR.

The original GFPI observed in broad- and narrowbands to restore images from the atmospheric distortion and achieve better quality datasets. GFPI recorded the data with two CCD cameras with a FOV of $50'' \times 38''$ and a pixel size of $0.036''$. The FOV could be reduced to increase the temporal cadence of the line scanning. Around 5% of the light was directed towards the broadband channel, which contained an interference filter with a full width at half maximum (FWHM) of 50–100 Å. The image reconstruction could be carried out with speckle interferometry (Puschmann et al., 2006b) or with deconvolution techniques (Löfdahl, 2002). The remaining 95% of the light was directed towards the narrowband channel, where the Fabry-Pérot interferometers performed spectropolarimetric observations. The spectral resolution of this channel was $\mathcal{R} = \lambda/\Delta\lambda = 250\,000$. The FPIs spectrally scanned the line of interest at several positions determined by the requirements of the observed line and of the goal of the campaign. Broad- and narrowband images were acquired simultaneously for reconstruction purposes: since the distortion produced by the atmosphere in the broad- and narrowband images were the same, the speckle deconvolution method for polarimetric data developed by Keller et al. (1992) could estimate the instantaneous object transfer function from the broadband reconstructed images. Since the speckle broadband restoration demanded very short exposure times ($\sim 20 - 30$ ms) that were not enough for polarimetric observations, several frames at each line position were registered to reduce the noise level. Finally, the reconstruction methods could provide diffraction-limited observations.

3.2 Space-based observations

Space-based observations are a very rich source of data with great advantages, such as stability, homogeneity in the observations, the lack of atmospheric effects on the final data and a great volume of publicly available data. Even though, in general, space-based instruments do not provide such a big spatial and temporal resolution as ground-based telescopes, they are very useful tools to retrieve general magnetic properties and evolution tendencies of atmospheric structures and dynamic events.

Several space-based observatories aim to study the Sun. However, only the Hinode satellite (Kosugi et al., 2007), SDO (Pesnell et al., 2012), and Solar Orbiter (SO) (Müller et al., 2020) have a spectropolarimeter on board (see Fig. 2.1) that allow analysing the vector magnetic field. While SDO and Hinode keep a stable orbit, SO follows a complex trajectory "in resonance" with Venus that allows it to tilt the plane of the orbit to study the solar poles.

In the thesis, we have only exploited datasets from missions with stable orbits. We proceed to describe the specific instruments in the following subsections.

3.2.1 SDO

The SDO, illustrated in Fig. 3.5, is a NASA mission launched in February 2010 as part of the Living With a Star (LWS) program. For the last 13 years, this solar satellite has been providing observations of the full solar disc thanks to its inclined geosynchronous orbit at $\sim 35\,800$ km. This orbit produces two three-week eclipse seasons per year, during which solar observations are interrupted by the shadow of the Earth.

The goal of the mission is to better understand solar variability and to be able to predict the consequences that may influence life on Earth. SDO is equipped with three instruments that observe the Sun at different wavelengths that supply information on the plasma characteristics at different atmospheric layers, from the photosphere up to the corona: Atmospheric Imaging Assembly (AIA) (Lemen et al., 2012), EUV Variability Experiment (EVE) (Woods et al., 2012) and HMI (Schou et al., 2012).

AIA

The instrument AIA includes four telescopes that capture full-disc images of the solar atmosphere using 10 wavelength channels, seven filters in the extreme-ultraviolet (EUV)

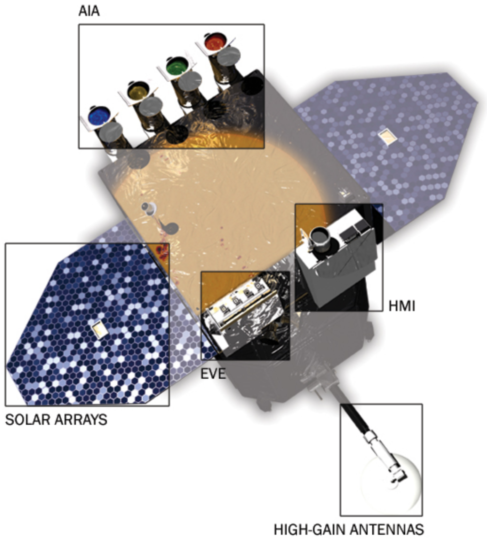

Figure 3.5 Illustration of the Solar Dynamics Observatory. Credits: NASA/Goddard Space Flight Center Conceptual Image Lab.

and three filters in the UV-visible spectral range. The wavelength coverage is meant to yield diagnostics over temperatures between 6000 K and 3×10^6 K. The CCD detectors are composed by 4096 $\times$4096 pixels with a pixel scale of $0.6''$that cover a FOV of $41'$, that is, the equivalent to $\sim 1.28\mathrm{R}\odot$. A summary of AIA channels and their parameters is presented in Table 3.1.

Channel	Primary ions	Char. emission $\log(T)$	Region of the atmosphere
White light	Continuum	3.7	Photosphere
1700 Å	Continuum	3.7	Temperature minimum Photosphere
304 Å	He II	4.7	Chromosphere Transition region
1600 Å	C IV, continuum	5.0	Transition region Upper photosphere
171 Å	Fe IX	5.8	Quiet corona Upper transition region
193 Å	Fe XII, XXIV	6.1, 7.3	Corona Hot flare plasma
211 Å	Fe XIV	6.3	Active-region corona
335 Å	Fe XVI	6.4	Active-region corona
94 Å	Fe XVIII	6.8	Flaring regions
131 Å	Fe VIII, XX, XXIII	35.6, 7.0, 7.2	Flaring regions

Table 3.1 AIA wavelength bands, the primary ions emitting in that passband, the ion characteristic emission temperature ($\log T$) and the solar region aimed to be detected.

The aim of AIA is to study the characteristics of the solar magnetic field by tracking its dynamism along the atmosphere, from the photosphere to the corona. Moreover, some passbands are specially implemented to observe flaring regions produced by magnetic reconnection (see Table 3.1). In order to achieve it, AIA EUV, UV and visible data are retrieved with a temporal cadence of 24 s, 12 s and 3600 s, respectively.

AIA data are employed in the flare analysis included in the Appendix A.

HMI

HMI instrument is a filtergraph that retrieves full Stokes parameters of the Fe I 6173 Å line by scanning the line at six positions with a 69 mÅ spectral distance. A summary of HMI parameters is contained in Table 3.2. The filtergraph contains of a five-stage Lyot filter with one tunable element, two tunable Michelson interferometers, a set of wave plates, and two cameras. The CCD cameras cover the full solar disc with 4096×4096 pixels with a size of $0.5''$. Each narrow-band filtergram is recorded every 3.75 s but the final temporal cadence depends on the data product.

Until April 2016 each camera worked independently following the Mod-C observing scheme: the front camera provided continuum intensity, v_{LOS} (Dopplergram), and LOS magnetograms every 45 s by recording the circular polarization, and the side camera provided $\boldsymbol{B}$ maps every 135 s by capturing circular and linear polarization (that leads to full Stokes parameters). After verifying that datasets from both cameras could be combined (Y. Liu et al., 2016), the Mod-L observing scheme was implemented. Under this scheme, the front camera keeps capturing the circular polarization and the side camera only collects linear polarization. Mod-L allows to obtain $\boldsymbol{B}$ maps with a faster cadence of 90 s.

Channel	Target line	Char. $\log(T)$	Region of the atmosphere
6173 Å	Fe I	3.7	Photosphere

Table 3.2 Similar to Table 3.1 but with HMI parameters.

Since HMI only scans the Fe I line at six positions, the data products are calculated by approximating the line profile to a Gaussian profile and assuming that the HMI transmission profile is a δ-function. The parameters line width, line depth and v_{LOS} for right- and left-handed circular polarization are calculated with the first and second Fourier coefficients that are obtained with an MDI[1]-like algorithm (Couvidat et al., 2016). Corrections from look-up tables with realistic, continuous line profiles and non-δ transmission functions are included. The 45 s data products (continuum intensity, Dopplergrams, and LOS magnetograms) are finally estimated from the corrected parameters.

The standard 720 s $\boldsymbol{B}$ full disc maps are an average of the 135 s full disc Stokes parameters and they are processed by their own Vector Magnetic Field Pipeline (Hoeksema et al., 2014).

HMI vector magnetic fields and intensity maps are analysed in the papers reproduced in Chapters 4, 5 and in Appendix A.

3.2.2 Hinode

Hinode satellite (Kosugi et al., 2007) is a Japanese mission developed in collaboration with the United States of America, and the United Kingdom. An illustration of the

---

[1] Michelson Doppler Imager

mission with its instruments is presented in Fig. 3.6. It was launched in September 2006 to a Sun-synchronous polar orbit with an altitude of $\sim$ 680 km, where it offers continuous observations of the Sun for nine months per year. During the eclipse season (from May to July), the Earth eclipses the Sun for a maximum of ten minutes in each 98-minute orbit.

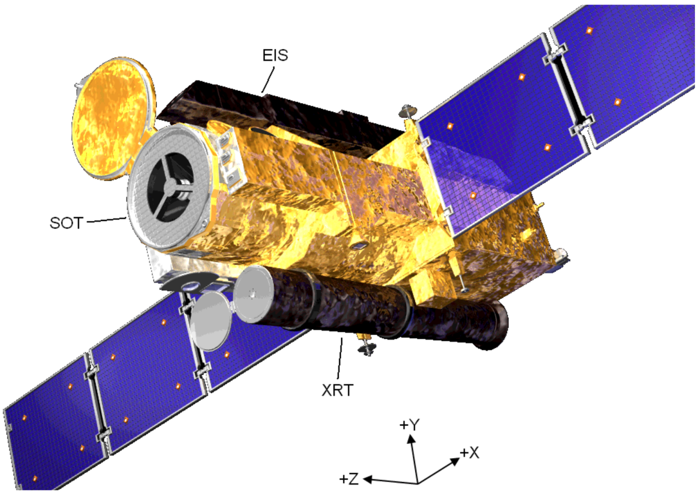

Figure 3.6 Illustration of the Hinode satellite with the instruments onboard marked. Figure retrieved from Kano et al. (2008).

The goal of the mission is to analyse the photospheric magnetic behaviour and to understand its consequences in the corona, such as solar eruptions. In order to achieve its scientific goals, Hinode contains three instruments that are specialised in different wavelength ranges emitted at different temperatures and atmospheric layers: the EUV Imaging Spectrometer (EIS), the X-Ray Telescope (XRT) and the Solar Optical Telescope (SOT). While EIS (Culhane et al., 2007) and XRT (Golub et al., 2007) aim to shed light on the heating mechanism and dynamics of the active solar corona, SOT (Tsuneta et al., 2008) focuses on the photospheric vector magnetic field and on photospheric and chromospheric dynamics.

SOT, a Gregorian-type telescope with a 50-cm aperture, contains the Broadband Filter Imager (BFI), Narrowband Filter Imager (NFI) and SP/Hinode. Until February 2016, BFI and NFI delivered diffraction-limited images with high spatial and temporal resolution and under very stable conditions thanks to an active image stabilization performed by the Correlation Tracker. While BFI produced photometric broadband images in six bands covering the photosphere and chromosphere, NFI produced intensity, Doppler and full Stokes polarimetric imaging in 10 spectral lines from the photosphere to the lower chromosphere. Unfortunately, due to a camera anomaly, BFI and NFI are no longer available.

SP

The SP/Hinode (Lites et al., 2013a) is the first space-based precision spectropolarimeter. It is composed of a $0.16'' \times 164''$ slit oriented in the solar North-South direction that scans a region of interest in the East-West direction. At each slit position, SP/Hinode records full Stokes profiles with a spectral sampling of 21.5 mÅ in the spectral range 630.08–630.32 nm, where two magnetically sensitive Fe I lines at 630.15 nm and 630.25 nm are located. Because these lines originate in the same multiplet, they have similar formation properties. Yet, they have different magnetic sensitivity which helps for more accurate inversions. They are also a good diagnostic tool for simpler inversions (e.g., M-E approximation) because of their not-high temperature sensitivity.

Spectra are read out continuously several times per rotation of the retarder Polarization Modulator. The full FOV of the scan depends on the scientific goal and on the telemetry limitations. The capability of data binning and the flexibility of the slit scanning allow to adapt the observing specifications. The CCD square pixels have the same dimension as the slit width ($0.16'' \times 0.16''$), however, pixels can be binned along the slit direction and data can be binned along the scanning direction, providing spatial scales of $0.32'' \times 0.32''$ instead. The versatility of the instrument allows for a number of pre-defined observing modes that are to be chosen depending on the scientific goal of the observations (Normal map, Fast map, Dynamics or Deep magnetogram. For more details see Sect. 6 in Lites et al., 2013a).

The raw spectra, Level 0, are calibrated and prepared for scientific use Level 1 (Community Spectropolarimetric Analysis Center (CSAC), 2006a) with the `sp_prep.pro` routine (Lites et al., 2013b). Additionally, Hinode/SP data pipeline provides Level 2 (Community Spectropolarimetric Analysis Center (CSAC), 2006b) and Level 2.1 datasets with inverted and disambiguated $\boldsymbol{B}$ scans, respectively.

SP/Hinode vector magnetic fields and intensity maps are analysed in the paper reproduced in Chapter 5.

3.2.3 IRIS

Interface Region Imaging Spectrograph (IRIS) is a NASA solar observation satellite that was launched in June 2013 into a Sun-synchronous, low-Earth inclined orbit at ~ 645 km of altitude. The eclipse season, when the shadow of Earth blocks the solar observations for part of the orbit, spans from November to February.

The goal of the mission is to understand how the solar atmosphere is energised by flows of mass and energy from the photosphere to the corona through the "interface region" formed by the chromosphere and the transition region. The analyses are performed with spectra obtained by a $175'' \times 0.33''$ slit spectrograph in the far UV (FUV) range (133.2–135.8 nm and 138.9–140.7 nm) and in the near UV (NUV) (278.3–283.5 nm) with high spatial (0.33–0.4$''$) and temporal resolution (~ 1.5 s). The temporal resolution is highly dependent on the observing mode (raster or sit-and-stare), on the spectral/spatial binning, and on the width of the spectral readout. Simultaneously, slit-jaw images at four possible passbands are recorded with a FOV up to $130'' \times 175''$.

IRIS NUV spectra are included in the paper reproduced in Appendix A.

4 Magnetic properties on the boundary of an evolving pore

Reproduction of García-Rivas et al. (2021) with permission © ESO
Published in *Astronomy & Astrophysics*
DOI: 10.1051/0004-6361/202039661

Received 12 October 2020 / Accepted 8 February 2021

Authors:
M. García-Rivas [1,2], J. Jurčák [1], and N. Bello González [3]

Affiliations:
[1]Astronomical Institute of the Czech Academy of Sciences, Fričova 298, 25165 Ondřejov, Czech Republic
[2] Astronomical Institute, Charles University, V Holešovickách 2, 18000 Praha, Czech Republic
[3] Leibniz-Institut für Sonnenphysik (KIS), Schöneckstrasse 6, 79104 Freiburg, Germany

ABSTRACT

Context: Analyses of the magnetic properties on umbrae boundaries have led to the Jurčák criterion, which states that umbra-penumbra boundaries in stable sunspots are equally defined by a constant value of the vertical magnetic field, $B_{\rm ver}^{\rm crit}$, and by a 50% continuum intensity of the quiet Sun, $I_{\rm QS}$. Umbrae with vertical magnetic fields stronger than $B_{\rm ver}^{\rm crit}$ are stable, whereas umbrae with vertical magnetic fields weaker than $B_{\rm ver}^{\rm crit}$ are unstable and prone to vanishing.

Aims: We aim to investigate the existence of a critical value of the vertical magnetic field on a pore boundary and its role in the evolution of the magnetic structure.

Methods: We analysed SDO/HMI vector field maps corrected for scattered light and with a temporal cadence of 12 min during a 26.5-hour period. A continuum intensity threshold ($I_{\rm c} = 0.55\,I_{\rm QS}$) is used to define the pore boundary and we study the temporal evolution of the magnetic properties there.

Results: We observe well-defined stages in the pore evolution: (1) during the initial formation phase, total magnetic field strength (B) and vertical magnetic field ($B_{\rm ver}$) increase to their maximum values of $\sim$ 1920 G and $\sim$ 1730 G, respectively; (2) then the pore reaches a stable phase; (3) in a second formation phase, the pore undergoes a rapid growth in terms of size, along with a decrease in B and $B_{\rm ver}$ on its boundary. In the newly formed area of the pore, $B_{\rm ver}$ remains mostly below 1731 G and B remains everywhere below 1921 G; (4) ultimately, pore decay starts. We find overall that pore areas with $B_{\rm ver} < 1731$ G, or equivalently $B < 1921$ G, disintegrate faster than regions that fulfil this criteria.

Conclusions: We find that the most stable regions of the pore, similarly to the case of umbral boundaries, are defined by a critical value of the vertical component of the magnetic field that is comparable to that found in stable sunspots. In addition, in this case study, the same pore areas can be similarly well-defined by a critical value of the total magnetic field strength.

—

Key words. Sun: photosphere – Sun: magnetic fields – sunspots

4.1 Introduction

When observed by telescope, the solar surface appears covered in a granular pattern. These granules are the tops of convective cells transporting hot plasma from the solar interior to the solar surface, thus heating the photospheric layer of the solar atmosphere. Hale (1908) discovered that sunspots are caused by strong magnetic fields. These strong magnetic fields inhibit the convective motions in the sub-surface layers of the sun resulting in cooler (darker) spots on the solar surface. There are also smaller dark structures observed on the solar disc called pores. Since these discoveries were made, an ongoing effort has been underway to investigate the properties of magnetic fields and dynamics in sunspots and pores (see e.g. Keppens et al., 1996; Solanki, 2003; Schlichenmaier, 2009; Borrero et al., 2011a).

Sunspots are structures composed of two distinctive areas: umbra and penumbra. Magnetic fields within umbrae are stronger and more vertical compared to the penumbra and the magneto-convection within them leads to the formation of umbral dots (e.g. Schüssler et al., 2006; Ortiz et al., 2010). Magnetic fields within penumbral regions are weaker and more horizontal than in umbrae, and magneto-convection in penumbrae leads to highly elongated cells that form the penumbral filaments (e.g. Rempel, 2011; Tiwari et al., 2013). Pores, on the other hand, are composed of only one distinctive area that morphologically resembles sunspot umbrae. The non-existence of penumbra around pores has been explained by a simple magnetic flux tube model with a prevailing vertical field (e.g. Simon et al., 1970). Subsequent high spatial resolution observations showed that some pores contain fine bright features, such as light bridges or umbral dots, that reveal magneto-convection (e.g. Sobotka et al., 1999b; Hirzberger, 2003; Giordano et al., 2008; Sobotka et al., 2009a).

Since there were no known magnetic properties to define them, umbra–penumbra (UP) boundaries were traditionally defined by a continuum intensity (I_{c}) threshold. In Jurčák (2011), the spectropolarimetric analysis of ten sunspots provided the first hint at the invariance of B_{ver} on UP boundaries. In an extended analysis of 79 active regions observed with Hinode/SOT-SP, Jurčák et al. (2018b) gave statistical proof of the magnetic nature of stable UP boundaries with a critical vertical magnetic field of $B_{\mathrm{ver}}^{\mathrm{crit}} = 1867 \pm 18$ G. The analysis of a long-lived sunspot during its stable phase observed with SDO/HMI resulted in a value of $B_{\mathrm{ver}}^{\mathrm{crit}} = 1693 \pm 15$ G (Schmassmann et al., 2018). The difference between Jurčák et al. (2018b) and Schmassmann et al. (2018) has been explained by the different instrument resolutions and analysis methods employed.

Additionally, unstable sunspots have also been investigated. During the formation of a sunspot, it was found that penumbra partially colonises umbral areas; over several hours, the UP boundary migrates to regions with a stronger B_{ver} until $B_{\mathrm{ver}}^{\mathrm{crit}}$ is reached and the position of the boundary stabilises (Jurčák et al., 2015). On the other hand, during the decay of a sunspot, B_{ver} is neither constant nor strong enough on the UP boundary; the umbra is prone to be disintegrated by convection or magnetic diffusion and this process takes place over several days (Benko et al., 2018).

The previously described observational studies have led to the so-called Jurčák criterion (first introduced in Schmassmann et al., 2018). This empirical law not only states that stable UP boundaries can be described either by 50% continuum intensity of the quiet Sun, $I_{\mathrm{c}} = 0.5\, I_{\mathrm{QS}}$, or by a critical vertical magnetic field $B_{\mathrm{ver}}^{\mathrm{crit}}$, it also states that $B_{\mathrm{ver}} \geq B_{\mathrm{ver}}^{\mathrm{crit}}$ only allow for umbral modes of magneto-convection, while umbral areas with $B_{\mathrm{ver}} < B_{\mathrm{ver}}^{\mathrm{crit}}$ are unstable and prone to vanish under more vigorous convective modes.

These observational results are in agreement with simplified theoretical studies of convective motions in the presence of magnetic fields. In 1961, Chandrasekhar derived the effects of inclined magnetic fields on convection; he showed that the convective mode is sensitive to the vertical magnetic field, B_{ver}, whereas the convective cells shape is sensitive to the horizontal component, B_{hor}. This was further supported by the theoretical study of Gough et al. (1966) on the stabilising effect against overturning convection of the vertical component of the magnetic field, thus expanding the Schwarzschild criterion for convective instability. Stability within this criterion is defined as the hindering of an instability or perturbation to develop overturning convection: Schwarzschild stated that convection sets in when the temperature gradient is steeper than the adiabatic gradient ($\nabla > \nabla_{\mathrm{ad}}$, where $\nabla \equiv d \ln T/d \ln p$, and T, p are the local temperature and pressure, respectively). Gough et al. (1966) derived an extra parameter to expand the Schwarzchild criterion; this new constraint to keep stability depends not only on the pressure, but also on the vertical component of the magnetic field, B_{ver}. This is a simplistic criterion that does not take into account other processes that influence the triggering of convective motions, such as rotation.

Analyses of the relevant observations focusing on the role of B_{ver} (Jurčák, 2011; Jurčák et al., 2015; Jurčák et al., 2017a; Jurčák et al., 2018b; Schmassmann et al., 2018; Benko et al., 2018; Lindner et al., 2020) suggest the validity of the theoretical studies by Chandrasekhar (1961) and Gough et al. (1966). Although it is not specifically mentioned in any of these observational studies, we understand the $B_{\mathrm{ver}}^{\mathrm{crit}}$ value as the photospheric counterpart of the critical vertical field stabilising the sub-photospheric layers against more vigorous modes of (magneto-) convection.

Magnetic properties have so far been studied exclusively on umbral boundaries. In this paper, we investigate the magnetic properties on the boundary of an evolving pore to study the applicability of the Jurčák criterion to the stability of pores against more vigorous modes of magneto-convection.

4.2 Data analysis

In this study, we analyse a pore observed in the active region NOAA 11175 from 09:24 UT on 18 March 2011 ($\mu = 0.94$, with $\mu = cos\theta$, where θ is the heliocentric angle) to 12:00 UT on 19 March 2011 ($\mu = 0.90$).

An analysis of the magnetic properties of an evolving pore requires spectropolarimetric data with a temporal cadence that is much higher than the evolutionary timescales of a pore, that is, we require abundant measures during the lifetime of a pore, which typically spans from hours to days. We also require observations with enough spatial resolution to resolve the magnetic structure.

The Helioseismic and Magnetic Imager (HMI Schou et al., 2012) on-board the Solar Dynamics Observatory (SDO Pesnell et al., 2012) fulfils our requirements. HMI provides full-disc Stokes parameters every 12 minutes, with a pixel scale of $\approx 0,5''$ and stable conditions. However, the observations are limited by a moderate spatial resolution of $\approx 1''$. As in any optical setting, spatial resolution is diminished by the convolution of a real image with the point spread function (PSF) of the instrument. Therefore, a proper characterisation of the HMI's PSF could improve the quality of the images. Couvidat et al. (2016) have modelled HMI's PSF as an Airy function convolved with a Lorentzian; they correct images from both large-scale wave-front errors and long-distance scattering based on tests prior to the launch of SDO (Wachter et al., 2012), and in-flight Venus-transit and Lunar-eclipse observations. Deconvolved HMI maps, that is, regular HMI maps corrected for scattered light using the described PSF model, are in qualitative agreement with sub-arcsecond spatial resolution observations (e.g. Criscuoli et al., 2017). Deconvolved maps exhibit a better spatial resolution, which implies a higher continuum intensity contrast in granulation and darker magnetic structures such as umbrae.

Figure 4.1 compares a sub-arcsecond spatial resolution scan from the spectropolarimeter on-board Hinode satellite (Tsuneta et al., 2008; Kosugi et al., 2007) to regular and deconvolved HMI maps. The deconvolved image not only exhibits a better spatial resolution, but a more consistent intensity map. Consequently, our analysis of the temporal evolution of a pore was performed using deconvolved HMI maps, specifically HMI data sets `hmi.B_720s_dconS` and `hmi.Ic_720s_dconS` kindly processed for us by A. Norton. Henceforth, every time we mention HMI maps, we are referring to the HMI deconvolved maps.

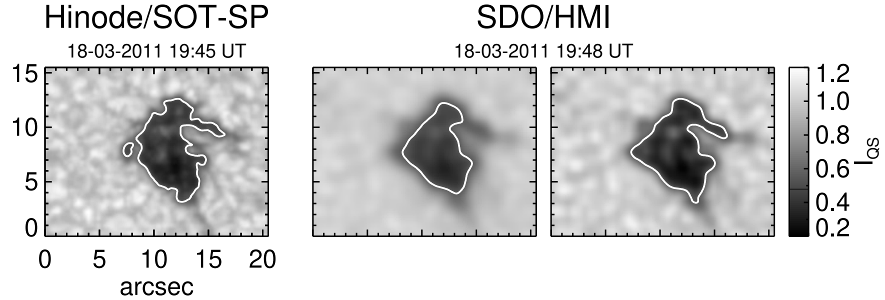

Figure 4.1 Comparison of continuum intensity maps of the pore on 18 March 2011 observed with Hinode/SOT-SP at 19:45 UT (left) and regular (middle) and deconvolved (right) HMI/SDO maps at 19:48 UT. Isocontours at $I_{\mathrm{c}} = 0.55\,I_{\mathrm{QS}}$ are marked with a white curve.

The HMI measures the Stokes parameters at six wavelength positions along the Fe I 617.3 nm line on the full-solar disc. The HMI Vector Magnetic Field Pipeline (Hoeksema et al., 2014) automatically computes the photospheric vector magnetic field using the Very Fast Inversion of the Stokes Vector code (VFISV, Borrero et al., 2011b; Centeno et al., 2014). For our purposes, we use three inferred parameters: magnetic field strength, inclination, and azimuth, which are in a line-of-sight reference frame (LOS). We transfer the magnetic field vector to the local reference frame (LRF) by solving the azimuth ambiguity first. In pores, we can use the solution provided by the ME0 method, a variation of the Minimum-Energy method (Metcalf, 1994; Leka et al., 2009b), available for all HMI data sets. In 180°-rotated HMI maps, 180° must be added to the azimuth. The transformation of the angular parameters of the magnetic field from LOS to LRF is then performed with the routine `r_frame_sphduo.pro` from the AZAM package (Lites et al., 1995). Thus, we obtain the magnetic parameters necessary for our analysis: magnetic field strength (B), magnetic field inclination in LRF (γ), and the vertical component of the magnetic field ($B_{\mathrm{ver}} = B\,cos\gamma$). The 24-hour orbital induced variation on the magnetic parameters was calculated on the umbral boundary of a stable sunspot during a period of about ten days by Schmassmann et al. (2018). They found that B and B_{ver} oscillated less than $20\,G$ and γ oscillated $0.2\,°$. Our analysis of the pore does not allow us to study the orbital induced variations in full, however, based on the analysis by Schmassmann et al. (2018), the difference is almost negligible compared to the evolutionary changes in B, B_{ver}, and γ.

Continuum intensity maps are normalised to local quiet Sun intensity (I_{QS}). In order to discard the centre-to-limb and orbital induced variations, local quiet Sun intensity is calculated as the mean continuum intensity of a quiet Sun sub-region close to the studied pore for each frame.

For the purpose of defining the boundary of the pore in terms of the continuum intensity, we investigate isocontours in the range $(0.4 - 0.6)\,I_{\mathrm{QS}}$. In order to carry out a systematic study of the evolution of magnetic properties on the pore boundary, we need to select a unique intensity isocontour. We are aware that in some cases a unique isocontour does not completely match the boundary of the pore. The dimmer regions of the pore that are not included in the selected isocontour evolve more rapidly than the main structure of the pore. Therefore, we believe that using a higher value of intensity threshold would only contaminate our results by adding rapid variations of the magnetic properties. The chosen isocontour at $I_{\mathrm{c}} = 0.55\, I_{\mathrm{QS}}$ provides a good visual match to the pore's boundary while avoiding the introduction of strong variations on the magnetic properties.

Due to the difference between the formation heights of the continuum intensity and the derived magnetic properties (the Fe I 617.3 nm line is more sensitive to magnetic fields around $\log \tau = -1$, Bello González et al., 2009), there are projection effects that can influence our analysis. In the case of sunspots, observations in areas away from the disc centre resulted in shifts between intensity and magnetic isocontours (Jurčák et al., 2018b; Schmassmann et al., 2018) or analogically systematic variation of magnetic properties along intensity boundaries (Jurčák, 2011). Schmassmann et al. (2018) calculated a shift of 1.3 pixel on a UP boundary at the limb, therefore, the projection effects are negligible in our case study, since the observed pore is located close to the disc centre ($\mu \in [0.90 - 0.94]$).

4.3 Results

We investigate the properties of the magnetic field on the boundary of an evolving pore. The analysis begins when the pore area, defined by $I_c \leq 0.55\, I_{\mathrm{QS}}$, exceeds five square pixels, which corresponds roughly to 0.72 Mm^2. The pore completely disintegrates into multiple areas smaller than 0.72 Mm^2 around 18:00 UT on March 19. From 12:00 UT on March 19, the pore is divided into multiple patches, which alternatively fulfil and do not fulfil the size requirement. Hence, in order to have a coherent analysis of the same magnetic structures during the whole evolution of the pore, we stopped the analysis at 12:00 UT.

In each frame, we average the values of γ, B, and B_{ver} along the intensity isocontour and calculate the standard deviations of these magnetic parameters. We note that when the analysed pore splits into multiple parts, the presented values correspond to the average along all boundaries encircling areas larger than 0.72 Mm^2. Temporal evolutions of the averaged B, γ, and B_{ver} along the pore boundary are shown in Fig. 4.2. It reveals that the temporal evolution of B_{ver} on the pore boundary behaves similarly to what has been observed on UP boundaries: B_{ver} on UP boundaries increases during the formation of the sunspot until it reaches a maximum stable value (Jurčák et al., 2015), leading to a stage of stability characterised by a critical B_{ver} (Jurčák, 2011) and followed by the decay of the sunspot, during which B_{ver} is weaker until the disappearance of the sunspot (Benko et al., 2018).

Continuum intensity maps show a stage where the pore does not change significantly. It matches the period in which B_{ver} reaches its maximum value in Fig. 4.2. The combination of both the temporal evolution and continuum intensity maps suggests the existence of a stable stage in the lifetime of the pore with a constant B_{ver} that corresponds to the maximum value during its lifetime. Most importantly, this maximum B_{ver} value is comparable to the $B_{\mathrm{ver}}^{\mathrm{crit}}$ value found on UP boundaries of stable sunspots (see Sect. 4.4).

In Fig. 4.3, we show the evolution of the pore area defined by the intensity threshold ($I_c \leq 0.55\, I_{\mathrm{QS}}$; red symbols) next to the evolution of areas of the pore limited by magnetic thresholds ($B = 1921$ G; orange symbols. $B_{\mathrm{ver}} = 1731$ G; blue symbols). We define the evolutionary stages of the pore based on its size, morphology, and magnetic properties on its boundary. The phases, along with the definition of the magnetic thresholds, are described below.

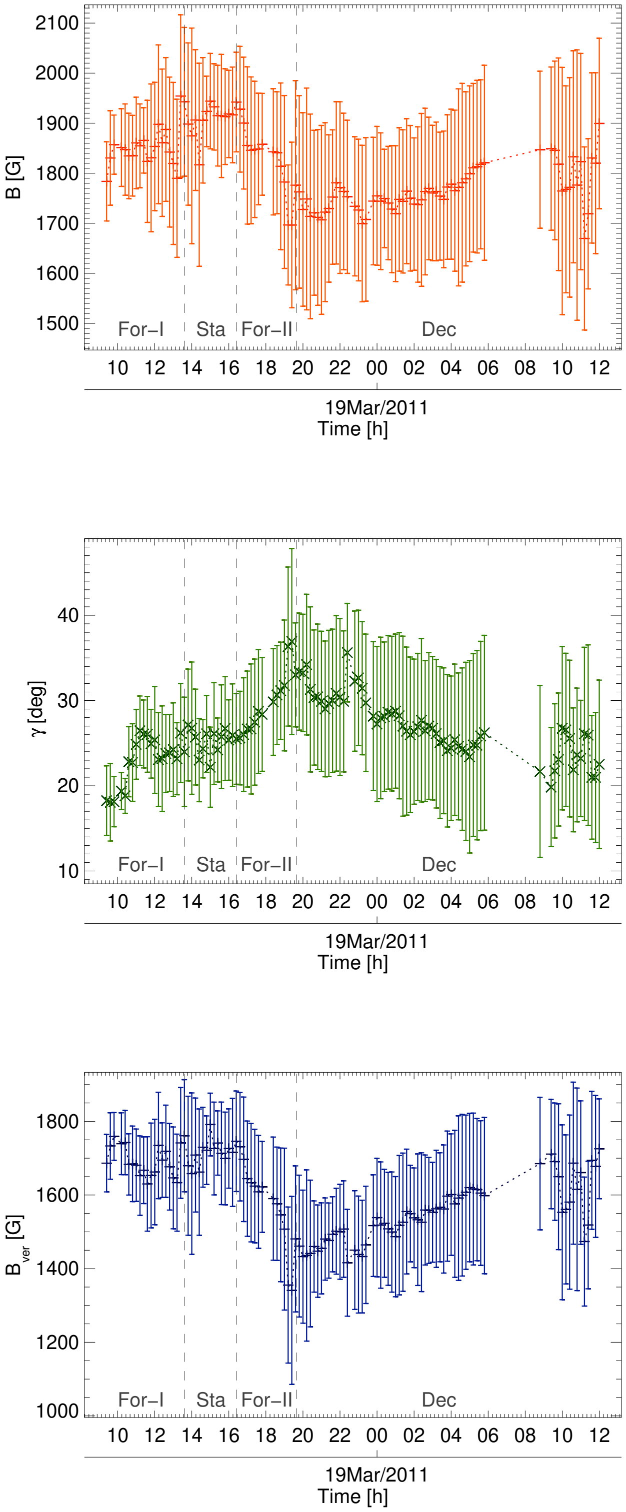

Figure 4.2 Temporal evolution of the averaged magnetic parameters on the boundary of the pore ($I_c = 0.55\,I_{\rm QS}$). From top to bottom, we show B, γ, and $B_{\rm ver}$. The uncertainties are given by the standard deviation of these physical parameters for each observation. The plot is divided in evolutionary stages: first period of formation (For-I), stability (Sta), second period of formation (For-II), and decay (Dec).

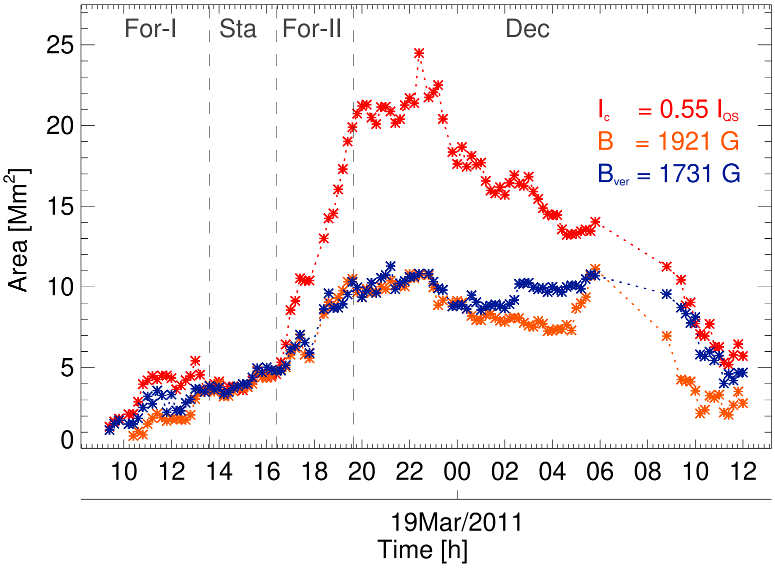

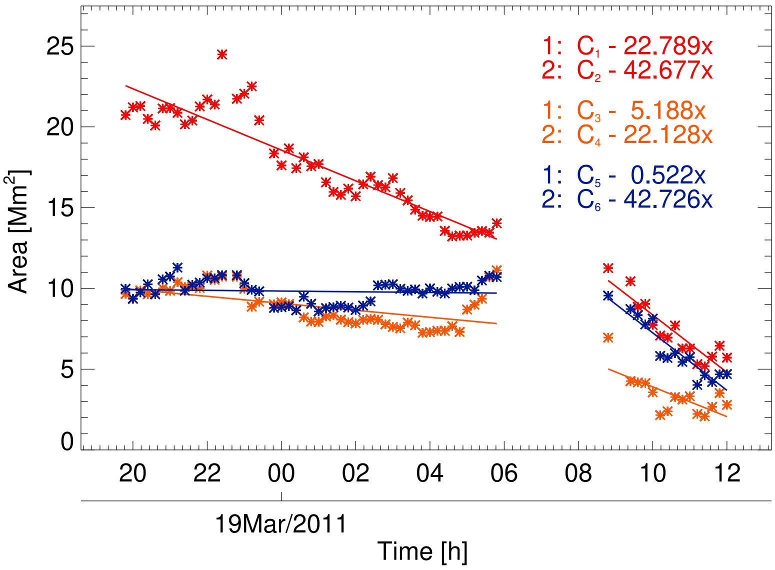

Figure 4.3 Temporal evolution of the areas of the pore encircled by both intensity and magnetic thresholds. *Top:* Comparison of the area of the pore encircled by the isocontours $I_c = 0.55\, I_{QS}$ (red), $B = 1921$ G (orange), and $B_{\rm ver} = 1731$ G (blue). Vertical lines divide the evolutionary stages of the pore as in Fig. 4.2. *Bottom:* Detail of the decaying stage. The straight lines are linear fits of the decay for each of the sub-periods (*1, 2*) with the continuous data available.

Formation I. After we started to analyse the pore on the solar surface at 09:24 UT, the pore area increased slowly from 1 Mm^2 to 2 Mm^2 until approximately 10:30 UT. This phase was accompanied by a strengthening of B on its boundary along with an invariable γ, that is, the field became, on average, stronger on the pore boundary. We note that B_{ver} reached values around 1730 G during this short period of time. These values are comparable to the later identified critical value of B_{ver}. This initial phase was followed by a sharp increase in the pore area (from 2 Mm^2 to 4 Mm^2) between 10:30 UT and 11:00 UT, when we found a local maximum of the pore size. During this rapid increase in the pore area, we found, on average, a weaker and more inclined field on the boundary, caused by the newly accumulated magnetic field. Between 11:30 UT and 13:30 UT, the pore area decreased slowly while, on average, B increased and γ decreased, resulting into an increase in B_{ver}, on the boundary of the pore. We call this period of time the Formation I phase, marked as For-I in Figs. 4.2 and 4.3. In Fig. 4.4, the left-most panels show the pore during this phase. The magnetic thresholds do not generally match the intensity boundary of the pore during this phase.

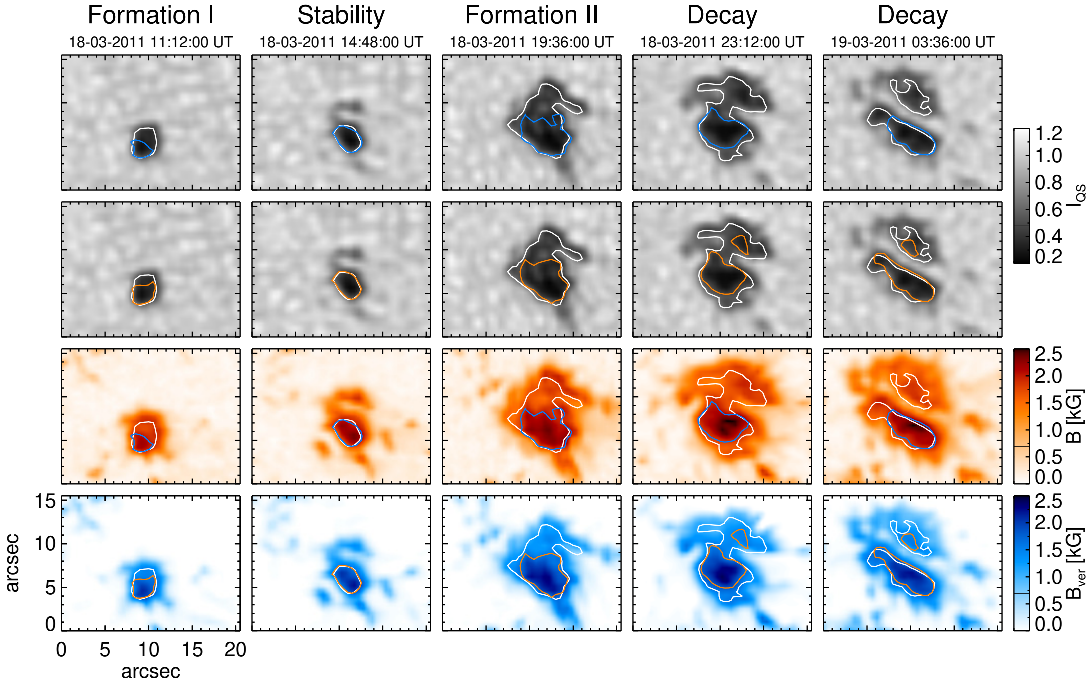

Figure 4.4 SDO/HMI samples of the evolutionary stages during the lifetime of the pore. *Top row*: Intensity maps with intensity ($I_c = 0.55\, I_{\mathrm{QS}}$; white) and magnetic field strength contours ($B = 1921$ G; blue). *Second row*: Intensity maps with intensity ($I_c = 0.55\, I_{\mathrm{QS}}$; white) and B_{ver} contours ($B_{\mathrm{ver}} = 1731$ G; orange). *Third row*: Maps of magnetic field strength with contours identical to those in top row. *Bottom row*: Maps of B_{ver} with contours identical to those in second row.

Stability. Between 13:30 UT and 16:30 UT, the pore size was not changing initially and then it slowly increased. We define this as the Stability stage. Within it, both B and B_{ver} fluctuate around their maximum value over the pore lifetime. During this phase, the mean values weighted by their standard deviations are $B = 1921$ G and $B_{\mathrm{ver}} = 1731$ G. These values are used as thresholds of the magnetic parameters in our analysis based on the similar behaviour and strength of the B_{ver} found on the pore boundary and on UP boundaries, as explained above. As a result, the areas of the pore defined by the intensity and magnetic thresholds evolve consistently during the stable phase as shown in Fig. 4.3. Accordingly, in Fig. 4.4, the second column shows the pore in this phase, where we find a match between isocontours of intensity, B, and B_{ver}.

Formation II. The stable phase was terminated by a rapid growth of the pore caused by an accumulation of new flux in the northern part of the pore. This Formation II phase lasted from 16:30 UT until 19:30 UT. During this time period, the pore size, defined by the intensity threshold, increased to 20 Mm^2. In the first 30 min, the pore expanded to an area with pre-existing magnetic field that strengthened and became more vertical, namely, it is also the areas outlined by $B_{\mathrm{ver}} = 1731$ G and $B = 1921$ G that increased sharply (Fig. 4.3, top plot). However, the newly gathered magnetic field is significantly weaker and more horizontal than the original magnetic field and leads to the decrease in the average B and B_{ver} (and increase in γ) on the intensity boundary during the whole Formation II period (Fig. 4.2). During the whole period, the areas of the pore with $B_{\mathrm{ver}} > 1731$ G and $B > 1921$ G increased, but significantly more slowly than the area encircled by the isocontour $I_{\mathrm{c}} = 0.55\, I_{\mathrm{QS}}$ (Fig. 4.3, top plot). In Fig. 4.4, we show the pore in the Formation II phase in the third column. The magnetic thresholds show two distinctive regions: the original magnetic field with $B > 1921$ G and $B_{\mathrm{ver}} > 1731$ G in the southern part and the newly formed northern region with $B < 1921$ G and $B_{\mathrm{ver}} < 1731$ G. We note that the southern part of the pore boundary –where there was no accumulation of new flux– is mostly outlined by the magnetic thresholds.

Decay. At $\sim$ 19:30 UT, the decay phase of the pore began. Initially, between 19:30 UT and 23:00 UT, the pore size fluctuated around 21 Mm^2 and the areas with $B_{\mathrm{ver}} > 1731$ G and $B > 1921$ G slightly increased. Afterwards, between 23:00 UT and 06:00 UT, the pore decreased in size while regions with $B > 1921$ G tend to diminish. However, during this period, areas of the pore with $B_{\mathrm{ver}} > 1731$ G fluctuated around 10 Mm^2. Then both the areas defined by intensity and magnetic thresholds decreased. Decay rates were studied separately during the two sub-periods with the continuous data available (bottom plot in Fig. 4.3). We note that during the whole decay process, we observed slight fluctuations of the pore areas as defined both by intensity and magnetic thresholds. These fluctuations are partly caused by relatively fast evolution of outermost structures of the pore with intensities comparable to the intensity threshold and partly caused by the size increase due to occasional small accumulations of magnetic flux.

The first sub-period spans from 18 March, 19:30 UT to 19 March, 06:00 UT. During this interval, the pore defined by the intensity isocontour decays at a rate of 0.95 Mm^2/h. Regions with $B > 1921$ G decay at a rate of 0.22 Mm^2/h on average. This implies that regions with $B < 1921$ G decay at a rate of 0.73 Mm^2/h, which is 3.4 times faster than regions with a stronger total magnetic field. Regions with $B_{\mathrm{ver}} > 1731$ G decay at a rate of 0.02 Mm^2/h. This implies, as observed in Fig. 4.3, that only regions with a weak vertical magnetic field disappear from the solar surface while regions with a strong vertical magnetic field remain almost invariant. Short-term fluctuations of the pore size as defined by intensity and magnetic thresholds are small compared to the overall trend observed in this sub-period. At the end of the first sub-period, we observe a newly accumulated magnetic flux in the northern region that has more significant impact on the size of regions defined by the total magnetic field strength threshold. This indicates an accumulation of a strong but inclined magnetic field.

The second sub-period spans from 19 March, 08:48 UT to 12:00 UT. During this interval, the pore size defined by the intensity isocontour decays at a rate of 1.78 Mm^2/h and it is an identical decay rate as for regions with $B_{\mathrm{ver}} > 1731$ G, while regions with $B > 1921$ G decay at a rate of 0.922 Mm^2/h. During this sub-period, the patches of the pore defined by the intensity and B_{ver} thresholds are nearly identical, and therefore we observe B_{ver} values close to 1731 G during this period (see Fig. 4.2). It means that the dissipation of the pore is strictly connected to the disappearance of strong vertical fields. The flux tube is mostly vertical and the total magnetic field strength is, in general, weaker than in previous stages. Fluctuations of the pore regions defined by intensity and magnetic thresholds are significant compared to the mean values during the second sub-period of the decay. Towards the end of the lifetime of the pore, the pore is split into multiple segments. These segments alternately fulfil or do not fulfil the conditions to be included in the analysis and, thus, they cause rapid changes in the pore areas defined by the intensity and magnetic thresholds, which significantly influences the evolving properties and the decay rates, therefore, we have not included this last sub-period in the analysis.

In Fig. 4.4, the fourth and fifth columns show the pore in the Decay phase. We observe a division of the pore by a light bridge through a region with weak magnetic field. A comparison of the two frames also indicates that the area of the pore with $B_{\mathrm{ver}} < 1731$ G ($B < 1921$ G) is more unstable. We also want to note that during the Decay phase, we find a better match between I_c and B_{ver} contours, rather than between I_c and B contours on the southern segment of the pore, which is the most stable region.

4.4 Discussion and conclusions

In this work, we analyse the magnetic properties on the boundary of an evolving pore with the aim of investigating the role of the vertical component of the magnetic field on the pore stability. More specifically, we study the similarity between the umbra-penumbra (UP) boundaries in sunspots and pore-quiet Sun boundaries in terms of $B_{\mathrm{ver}}^{\mathrm{crit}}$ values. The pore stability refers to the effective damping of more vigorous magneto-convective motions and, conversely, the pore instability refers to the ineffective attenuation of vigorous magneto-convective motions within the pore, leading to its dissipation. We use 113 observations of a pore in active region NOAA 11175 taken by SDO/HMI that cover ~ 26.5 hours of the pore evolution. A morphological characterisation of the evolution of the pore, determined from the development of the pore area (Fig. 4.3) and from the behaviour of the averaged magnetic parameters along the pore boundary (Fig. 4.2), lead us to define four evolving phases: a first formation period (Formation I), a stable period (Stability), a second formation period (Formation II), and a disintegration period (Decay).

During the first formation phase, we find that both B and B_{ver} are generally increasing on the visual boundary of the pore defined at $I_c = 0.55\,I_{\mathrm{QS}}$. In the later phase of the Formation I period, the pore area decreases until the maximum values of B and B_{ver} are reached on the boundary (Fig. 4.2). During the Stability phase that follows, the pore boundaries defined by $0.55\,I_{\mathrm{QS}}$, $B = 1921$ G and $B_{\mathrm{ver}} = 1731$ G are nearly identical and encircle the same area (Fig. 4.3). This stability is disrupted by the accumulation of new magnetic flux of weaker and more horizontal field that causes a sharp increase in the pore size and the subsequent decrease in B and B_{ver} on the pore boundary. The pore does not stabilise again and starts to decay immediately after the supply of new magnetic flux is depleted.

The mean value of B_{ver} found on the pore boundary during the Stability phase is 1731 G. This value is comparable to 1639 G, B_{ver} found by Schmassmann et al. (2018) on the UP boundary of a long-lived sunspot, where the authors analysed standard SDO/HMI data at 53% I_{QS}. The dissimilarity can be attributed to the use of deconvolved data, which should lead to stronger B_{ver} values. The similarity of the B_{ver} value on the pore boundary with those found on UP boundaries of stable sunspots (1867 G, 1693 G, 1787 G by Jurčák et al., 2018b; Schmassmann et al., 2018; Lindner et al., 2020, respectively) indicates that it is also in pores that the magneto-convection is effectively and stably hindered by the vertical component of the magnetic field. In the analysed pore, we find this critical value to be $B_{\mathrm{ver}}^{\mathrm{crit}} \sim 1730$ G.

Furthermore, in the studied pore, we find that the same applies for a magnetic field strength of 1921 G, the mean value on the pore boundary during the Stability phase. During this phase, the isocontours of intensity and B are in equally good agreement as isocontours of intensity and B_{ver}. Also, the areas encircled by isocontours of $B = 1921$ G and $B_{\mathrm{ver}} = 1731$ G, shown in Fig. 4.3, exhibit a comparable evolution.

During the Decay phase, we initially observe a much faster disappearance of the pore areas with $B_{\mathrm{ver}} < 1731$ G, namely, granular magneto-convection takes over pore areas with $B_{\mathrm{ver}} < B_{\mathrm{ver}}^{\mathrm{crit}}$. This provides us with a further indication of the important role of $B_{\mathrm{ver}}^{\mathrm{crit}}$ in hindering magneto-convection, as stated by the Jurčák criterion for stable sunspots. The decay process takes hours and is thus comparable to other case studies. For example, Jurčák et al. (2017a) analysed the 12-hour formation of a penumbra at the expense of a pore, which had $B_{\mathrm{ver}} < B_{\mathrm{ver}}^{\mathrm{crit}}$ over the whole process; and Benko et al. (2018) described the decay of a sunspot umbra that spans over several days. We do not know why the decay process is not comparable to the granular life-time or life-time of penumbral filaments.

For the first time, we try to directly estimate, the stabilising role of the critical value of the vertical component of the magnetic field by comparing the decay rates of the areas that have $B_{\mathrm{ver}} > 1731$ G and $B_{\mathrm{ver}} < 1731$ G. During the initial sub-period of the pore's decay, we find that areas with $B_{\mathrm{ver}} > 1731$ G do not decay, while areas with $B_{\mathrm{ver}} < 1731$ G progressively disappear until, after the gap in the observations, the areas of the pore defined by the intensity and B_{ver} thresholds are nearly identical. Therefore, we observe an increase in the B_{ver} value averaged over the intensity boundary of the pore towards the end of the analysed period (see Fig. 4.2).

As pointed out earlier in this work, we can also use B as a determining parameter for stability in the studied pore. Areas with $B > 1921$ G decay 3.4 times slower than pore areas with $B < 1921$ G. We note that during the second sub-period of the pore's decay, the decay rates for areas with $B_{\mathrm{ver}} > 1731$ G and $B > 1921$ G increased significantly, and regions with $B_{\mathrm{ver}} > 1731$ G decay at the same rate as areas defined by the intensity threshold. This means that the pore decays at a fast rate while having an intense vertical magnetic field, and we do not know the reason for this behaviour.

This case study highlights the importance of the $B_{\mathrm{ver}}^{\mathrm{crit}}$ value found for sunspots to the stability of pores as well. However, an analysis of a larger sample of pores is necessary in order to investigate if the found $B_{\mathrm{ver}}^{\mathrm{crit}} \sim 1730$ G is a unifying parameter for stable boundaries of all pores and if the same unifying parameter could also be $B^{\mathrm{crit}} \sim 1920$ G. Statistical analyses of pore lifetimes and decay rates with respect to their magnetic properties is also necessary in order to investigate the stabilising effect of $B_{\mathrm{ver}}^{\mathrm{crit}}$.

Acknowledgments:

We would like to thank the referee for the valuable comments that helped to improve this paper. We also would like to thank A. Norton for providing us deconvolved full-disc vector field maps. This work was supported by project 204119 from the Grant Agency of Charles University and by the Czech Science Foundation grant project 18-06319S. The data is courtesy of NASA/SDO and the HMI science teams. Hinode is a Japanese mission developed and launched by ISAS/JAXA, with NAOJ as domestic partner and NASA and STFC (UK) as international partners. It is operated by these agencies in co-operation with ESA and NSC (Norway).

5 Magnetic properties of the umbral boundary during sunspot decay. Comparative study of multiple datasets.

Reproduction of García-Rivas et al. (2024a)
To be published in *Astronomy & Astrophysics*
DOI: 10.1051/0004-6361/202348068

Received 26 September 2023 / Accepted 14 June 2024

Authors:
M. García-Rivas[1,2], J. Jurčák[1], and N. Bello González[3]

Affiliations:
[1]Astronomical Institute of the Czech Academy of Sciences, Fričova 298, 25165 Ondřejov, Czech Republic
[2] Astronomical Institute, Charles University, V Holešovickách 2, 18000 Praha, Czech Republic
[3] Institut für Sonnenphysik (KIS), Georges-Köhler-Allee 401a, 79110 Freiburg, Germany

ABSTRACT

Context: In recent years, the magnetic properties of the umbra-penumbra boundary of sunspots and the boundary of pores at various evolutionary stages have been characterised using datasets from different instruments.

Aims: We aim to study the intrinsic differences between the intensity and vector magnetic field properties derived from Hinode/SP and SDO/HMI observations of a decaying sunspot.

Methods: We analysed the sunspot embedded in active region NOAA 12797 during six days in 30 SP/Hinode scans and 704 HMI/SDO for both regular maps and maps corrected for scattered light, $\mathrm{HMI_{dcon}}$. We studied the correlation of the magnetic properties and continuum intensity in the datasets within the spot, and we investigated the differences at the umbra-penumbra boundary. We examined the decaying process in detail using the full temporal resolution of the $\mathrm{HMI_{dcon}}$ maps.

Results: We find a good one-to-one correspondence between the magnetic properties in the SP and $\mathrm{HMI_{dcon}}$ maps, but the continuum intensity of the spots in the SP maps is found to be $0.04\,I_{\mathrm{QS}}$ brighter than in the $\mathrm{HMI_{dcon}}$ maps. The considerable influence of scattered light in the HMI maps makes it the least ideal dataset for studying the boundary of spots without a penumbra. The properties at the umbra-penumbra boundary evolve slowly during the sunspot decay stage, while the penumbra still provides some stability. In contrast, they respond more abruptly to areal changes in the naked-spot stage. During the sunspot decay, we find linear decay in the area and in the magnetic flux. Moreover, the umbra shows two characteristic decaying processes: a slow decay during the first three days, and a sudden fast decay during the final dissipation of the penumbra. We find indications of a 3.5 h lag between the dissipation of the vertical fields in the umbral region and the photometric decay of the umbral area.

Conclusions: The differences found in the continuum intensity and in the vertical component of the magnetic field, B_{ver}, between the analysed datasets explain the discrepancies among the B_{ver} values found at the boundaries of umbrae in previous studies. —

Key words. Sun: photosphere – Sun: magnetic fields – sunspots - Sun: evolution

5.1 Introduction

Sunspots are the largest structures seen on the surface of the Sun. They are produced by the interaction of strong magnetism and convective motions. It is well known that sunspots consist of a dark inner part, the umbra, which is surrounded by lighter radial filaments, the penumbra. The umbra is produced by strong, vertical magnetic fields, while the penumbra is characterised by weaker and more horizontal magnetic fields. Chandrasekhar (1961) studied the effects of magnetism on convection and stated that vertical fields (B_{ver}) affect the convective mode, whereas horizontal fields shape the convective cells.

Different methods have been used to characterise the boundary between umbrae and penumbrae (UP boundaries) in terms of a continuum intensity threshold, such as intensity distributions, cumulative histograms, or maximum intensity gradients (e.g. Grossmann-Doerth et al., 1981; Pettauer et al., 1997; Beck et al., 1993). These methods have been applied, for example, to establish the relation between the sunspot area and brightness and the (in)variability of the area with the cycle phase (e.g. Mathew et al., 2007). Although this is useful for automatic sunspot detection analyses, each method has limitations. Many authors therefore rather select the intensity thresholds based on visual investigation and keep them constant during the evolution of the spot (e.g. Q. Li et al., 2021; Q. Li et al., 2022; Schmassmann et al., 2018; Benko et al., 2018).

Sunspots are very dynamic structures. Despite this dynamism, Jurčák et al. (2018b) found a critical value of the vertical magnetic field ($B_{\mathrm{ver}}^{\mathrm{crit}} = 1867 \pm 18\,\mathrm{G}$) at the UP boundaries of stable sunspots defined at 50% of the continuum intensity of the local quiet Sun, I_{QS}, based on a statistical study of maps from the Spectro-Polarimeter of the Solar Optical Telescope onboard the Hinode satellite (Hinode/SP). Further studies of stable sunspots and pores observed with different instruments have also found a $B_{\mathrm{ver}}^{\mathrm{crit}}$ value at the boundary (e.g., 1693 G in SDO/HMI[1] maps, 1787 G in GRIS[2]/GREGOR maps, and 1731 G in SDO/HMI$_{\mathrm{dcon}}$[3], were respectively found by Schmassmann et al., 2018; Lindner et al., 2020; García-Rivas et al., 2021). In contrast, Löptien et al. (2020) claimed that the invariable $B_{\mathrm{ver}}^{\mathrm{crit}}$ value is due to the use of a fixed continuum intensity threshold that falls at different positions of the UP boundary with sunspot sizes. That is, the intensity contour falls at different magnetic structures (spines and penumbral filaments) whose B_{ver} counteracts with each other and maintains a constant averaged vertical field.

The question then is what happens when the magnetic structures undergo an unstable phase in their evolution. Jurčák et al. (2015) investigated the process of the formation of a penumbra: The penumbra formed by invading the umbral regions with weak B_{ver} values until the incursion stabilised, leading to a UP boundary with a constant B_{ver} of the maximum observed value. During the formation of a penumbra around a pore of reduced B_{ver}, the penumbra in contrast completely colonised the pore region, resulting in an orphan penumbra (Jurčák et al., 2017a). This line of investigation led to the

---

[1] Helioseismic and Magnetic Imager on board the Solar Dynamics Observatory.

[2] GREGOR Infrared Spectrograph.

[3] HMI maps corrected for scattered light

Jurčák criterion, an empirical law that states that UP boundaries of stable sunspots are not only defined by 50% of the I_{QS}, but also by a $B_{\mathrm{ver}}^{\mathrm{crit}}$ value. This criterion implies that umbral magnetoconvection settles in regions with $B_{\mathrm{ver}} > B_{\mathrm{ver}}^{\mathrm{crit}}$. However, areas with $B_{\mathrm{ver}} < B_{\mathrm{ver}}^{\mathrm{crit}}$ are unstable and prone to vanish against other more vigorous modes of (magneto)convection. The analysis of the Gough-Tayler stability criterion (Gough et al., 1966) in MURaM[4] sunspot simulations by Schmassmann et al. (2021) supports the importance of the role of B_{ver} in the stability of different modes of magneto-convection.

The magnetic properties of a decaying sunspot observed by Hinode/SP were studied by Benko et al. (2018). They did not find a constant B_{ver} at the UP boundary, but rather a value that tended to weaken in the first stages and strengthened in the last stages of the decay. Moreover, the $B_{\mathrm{ver}}^{\mathrm{crit}}$ value found by Jurčák et al. (2018b) was only measured well inside the umbra during the seven-day process. In contrast, Löptien et al. (2020) presented a decaying sunspot with a constant B_{ver} at the UP boundary, equivalent to the value found by Jurčák et al. (2018b) during a five-day analysis of Hinode/SP maps.

The physical processes leading to the disappearance of a penumbra are still not well understood. Moving magnetic features (MMFs) remove flux from the active region, but this is not always equivalent to the decay rate of the sunspot (e.g., Martínez Pillet, 2002). This means that other processes must play an important role as well, for instance, a change in the configuration of the magnetic canopy, similar to the process of the formation of the penumbra, but bottom-up instead (Romano et al., 2020), or the erosion by convective motions (Rempel, 2015; Strecker et al., 2021). A difference in the decay rates may explain why some decaying sunspots fulfil the Jurčák criterion.

In this work, we analyse the properties on the UP boundary of a decaying sunspot that transforms into naked spots. We aim to study the differences with respect to other studies of decaying sunspots. We use $\mathrm{HMI}_{\mathrm{dcon}}$ data, following the methods used in García-Rivas et al. (2021). Complementary, since this spot was observed with Hinode/SP during its passage across the solar disc, we compare the magnetic properties derived from Hinode/SP, SDO/HMI and SDO/$\mathrm{HMI}_{\mathrm{dcon}}$ to better understand the differences of $B_{\mathrm{ver}}^{\mathrm{crit}}$ in the studies that were based on these datasets.

5.2 Data

In order to compare the magnetic properties derived from the Hinode/SP (Kosugi et al., 2007; Tsuneta et al., 2008) and SDO/HMI (Pesnell et al., 2012; Schou et al., 2012) observations, we selected a long-lasting active region that traversed the solar disc and contained a decaying sunspot. The transition from sunspot to naked spots allows a comparison between the targets at different evolutionary stages.

5.2.1 Decaying sunspot

We studied a sunspot in active region (AR) NOAA 12797. This is an α-active region with negative polarity, followed closely ($\sim 100''$) by the β-active region NOAA 12798. The sunspot appeared on the eastern limb of the southern hemisphere on 17 January 2021. Initially, the umbra was divided by a light bridge and one penumbra surrounded both umbrae. During the following days, the penumbra around the light bridge vanished, while the two umbral cores grew apart. The complete dissipation of the penumbrae on 24 January led to two small naked spots. Instead of completely disappearing, they gathered more magnetic flux and grew larger before they completely disappeared from

---

[4] Max-Planck-Institute for Solar System Research/University of Chicago Radiation Magneto-hydrodynamics.

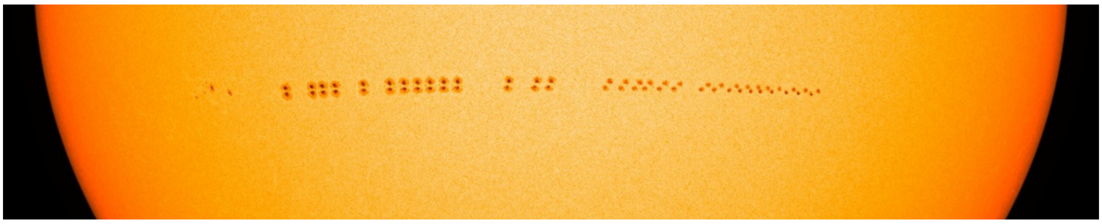

Figure 5.1 HMI composition of the transition in AR NOAA 12797 from a decaying sunspot to naked spots. The 30 snapshots correspond to the scanning times of the analysed SP scans. AR NOAA 12798 on the left was magnetically connected to AR 12797 during most of the passage across the solar disc.

the solar surface close to the western limb on 28 January. The evolution of the spots is summarised in Fig. 5.1 with a composition of 30 HMI maps at the times of the analysed SP scans.

Despite having the spots on sight for several days, we limited the data to the period from 20 January at 18:36 UT to 26 January at 21:24 UT, which corresponds to the positions on the solar disc with $\mu > 0.75$, where $\mu = cos(\theta)$ and θ is the heliocentric angle. This constraint aimed to minimise the errors induced by the projection effects and to have a continuous dataset in HMI observations by avoiding data gaps. We also intended the overlap between the HMI and SP observations to be as long as possible.

The first observation of a coronal mass ejection ever captured by the coronagraph Metis (Antonucci et al., 2020) on board Solar Orbiter (Müller et al., 2020) occurred on 16 and 17 January 2021. The source region was declared consistent with the location of the active region of this study, AR 12797, on the eastern limb (Andretta et al., 2021). AR 12797 and mostly AR 12798 produced several B- and even C-class flares between the appearance on the eastern limb and the beginning of our study. Only weaker B-class flares continued to erupt in the neighbouring region AR 12798 from the beginning of our analysis until 23 January. Since the active regions were magnetically connected, these eruptions could have induced changes in the magnetic structure of the studied spots and, as a consequence, in the decay.

5.2.2 SDO/HMI data

In order to study the magnetic properties of the decaying sunspot, we required a homogeneous dataset with good temporal resolution, that is, a temporal cadence that allows for several observations during the fastest stages of the structural transitions. This requirement was largely fulfilled by HMI. It provides full-disc spectropolarimetric data every 12 minutes with a pixel scale of $\sim 0,5''$. The filtergraph scans the Fe I photospheric line at 617.3 nm along six positions with a spectral step of 7.6 pm. Ready-to-use data are provided by the Joint Science Operation Center (JSOC[5]), where the standard full-disc vector magnetic field (`hmi.B_720s`) and continuum intensity (`hmi.Ic_720s`) maps can be downloaded. We required the best available spatial resolution to study the magnetic properties at the boundary of the spots. For this reason, we used the $\mathrm{HMI_{dcon}}$ series: regular HMI maps corrected for scattered light (`hmi.B_720s_dconS` and `hmi.Ic_720s_dconS`), as described in García-Rivas et al. (2021). The $\mathrm{HMI_{dcon}}$ maps agree qualitatively with sub-arcsecond spatial resolution observations (e.g. Criscuoli et al., 2017), and they show a higher continuum intensity contrast in granulation and darker magnetic structures such as umbrae.

The two sets of Stokes parameters, standard HMI and $\mathrm{HMI_{dcon}}$, were processed similarly by the HMI vector magnetic field pipeline (Hoeksema et al., 2014): Full-

---

[5] `http://jsoc.stanford.edu/`

disc photospheric vector magnetic field maps were inferred using the Milne-Eddington inversion code called Very Fast Inversion of the Stokes Vector (VFISV, Borrero et al., 2011b; Centeno et al., 2014). The Zeeman-induced 180-azimuth ambiguity was solved using the ME0 method, which is a variation of the minimum energy method (Metcalf, 1994; Leka et al., 2009b), and the disambiguation solution was applied using `hmi_disambig.pro`. We transformed the components of the magnetic field vector referred to the line of sight (LOS) (total magnetic field strength, LOS inclination, and azimuth) to components referred to a local reference frame (LRF) (vertical and transversal components) using the `hmi_b2ptr.pro` routine. Following García-Rivas et al. (2021), we analysed the total magnetic field strength (B), the vertical magnetic field ($B_{\rm ver}$), and the LRF inclination ($\gamma = {\rm acos}[B_{\rm ver}/B]$) of 704 HMI and $\rm HMI_{dcon}$ cutouts.

Even though we analysed the sunspot for several days, the decaying process did not allow us to calculate the 24-hour orbital-induced magnetic variations reliably. Nonetheless, these variations were calculated by Schmassmann et al. (2018) at the umbral boundary of a stable sunspot during ~ 10 days, where B and $B_{\rm ver}$ oscillated by less than 20 G and γ oscillated by $0.2\,^{\circ}$. Therefore, we can neglect the 24-hour oscillations as their magnitude is significantly lower than the actual change in the magnetic parameters caused by the sunspot decay.

5.2.3 Hinode/SP data

The SOT incorporates the SP (Ichimoto et al., 2008), which is a slit spectropolarimeter that provides high-resolution solar observations with spatial samplings along the slit and in the scanning direction, and temporal cadences that depend on the mapping mode. The current dataset was recorded with a spatial scale of $0.30'' \times 0.32''$ and a temporal cadence of 1.6 s per slit position, that is, in fast mode. The SP spectral range is centred on two Zeeman-sensitive Fe I photospheric lines (at 630.15 and 630.25 nm), including the nearby continuum, and has a spectral sampling of 2.15 pm. The different magnetic sensitivities of the spectral lines permit a better accuracy in the determination of the vector magnetic field. Even though different types of data are publicly available (e.g. `Level 0` raw non-calibrated Stokes profiles from one slit position; `Level 1` calibrated Stokes profiles from a full scan), we used already inverted data (`Level 2` and `2.1`) provided by the Community Spectro-polarimetric Analysis Center (CSAC[6]).

The inversion, that is, inferring the magnetic and thermodynamical properties at the line formation height, was made with the Milne-Eddington gRid Linear Inversion Network (MERLIN, Lites et al., 2007). Among other parameters outside of our current interest, Level 2 data provide the vector magnetic field with respect to the LOS reference frame (magnetic field flux (B_f), LOS inclination, non-disambiguated azimuth, and filling factor (α)). `Level 2.1` data contain the vector magnetic field (vertical and transversal) with respect to the LRF and the disambiguated azimuth used to transform the reference frame. The disambiguation was carried out using the same algorithm as was used in HMI data, ME0. In contrast to HMI inversions, where the filling factor is constant (α=1), α is variable in SP inversions. Therefore, the total magnetic field strength was calculated by multiplying the inverted field flux by the filling factor ($B = \alpha B_f$). The LRF inclination was obtained from the ratio of the total magnetic field strengths and vertical fields as for HMI datasets.

As a result, a combination of `Level 2` and `Level 2.1` data allows us to retrieve the same parameters as were analysed from HMI (B, $B_{\rm ver}$, and γ) from 30 scans. Six observations were removed from the dataset due to interruptions in the scanning. Since a full scan takes approximately 45 min and scans are not taken consecutively, the

---

[6] `https://csac.hao.ucar.edu/sp_data.php`

temporal resolution is poor for our purposes. However, the high spatial resolution allows a more precise analysis of the UP magnetic properties than HMI maps.

This is the first analysis that uses `Level 2` and `Level 2.1` SP data to assess the B_{ver} evolution. Previous analyses, namely Jurčák et al. (2018b) and Benko et al. (2018), used the Stokes Inversion based on Response functions code (SIR, Ruiz Cobo et al., 1992) with constant magnetic parameters in the modelled atmosphere. This inversion scheme of the SIR code, as well as any inversion code based on the Milne-Eddington approximation, provides us with an average value of the magnetic field parameters at optical depths where the line is most sensitive to these parameters. According to Cabrera Solana et al. (2005), the spectral lines observed by SP and HMI are most sensitive to magnetic field parameters between $\log \tau_{\mathrm{c}} = -1$ and -2. The results from a similar range of optical depths were used by Jurčák (2011), who used the SIR code with height-dependent stratifications of the magnetic parameters.

With the decay of the sunspot, we expect changes in the Wilson depression (Löptien et al., 2018), and thus, the geometrical height of the region in which we obtain the magnetic parameters increases during the decaying process. As summarised by Balthasar (2018), the magnetic field strength and also its vertical component decrease with height in the atmosphere. Combining the results of Löptien et al. (2018) and Balthasar (2018), we estimate that B and B_{ver} decrease up to 100 G due to the increase in the geometrical height during the decay process. However, we cannot determine this value exactly with the applied data analysis methods.

The methods for comparing the magnetic properties derived from the HMI, $\mathrm{HMI}_{\mathrm{dcon}}$, and SP maps at the decaying spot and at the umbral boundary are described in Sect. 5.3. The results are summarised in Sect. 5.4, and a discussion is provided in Sect. 5.5.

5.3 Analysis of the method

Since the aim of our current research is to study the evolution of the magnetic properties at the boundary of dark structures (sunspots or pores), and because different studies have been carried out using a variety of instruments (e.g., Hinode/SP, SDO/HMI, SDO/$\mathrm{HMI}_{\mathrm{dcon}}$ by Jurčák et al., 2018b; Schmassmann et al., 2018; Benko et al., 2018; Campos Rozo et al., 2023; García-Rivas et al., 2021), we find it necessary to study the differences between these datasets in more detail. We only investigated the magnetic parameters in spots areas and disregarded the rest of the field of view (FOV). In the case of a decaying sunspot, the first step is to examine side by side the magnetic properties of the whole spot from the SP, HMI, and $\mathrm{HMI}_{\mathrm{dcon}}$ observations. To do this, the outer boundary has to be defined. Moreover, the umbra-penumbra (UP) boundary has to be characterised with the aim of studying the temporal evolution of the magnetic properties in it and comparing the different datasets. These two boundaries are defined in terms of continuum intensity thresholds.

As described above, the temporal and spatial sampling of SP and HMI is not identical. In order to directly compare the magnetic properties derived from the two instruments, the data with the best pixel scale (SP, $\sim 0.30'' \times 0.32''$) must be degraded to match the lowest spatial sampling (HMI, $0.5'' \times 0.5''$). SP maps were aligned and resampled to HMI maps using `auto_align_images.pro`, a routine that minimises the cross-correlation between images while allowing for image warping, if needed. The warping is allowed as a way to remove possible effects of irregular slit movements in SP scans (Centeno et al., 2009). First, reference points in the two images provide rough transformation parameters via `caltrans.pro`. These serve as initial transformation parameters for a first run of `auto_align_images.pro`, using the minimisation algorithm Amoeba. The obtained transformation parameters are used as the initial transformation parameters of the final run of `auto_align_images.pro`, now allowing for image warping and allowing the more robust minimisation algorithm Powell. The result is PQ parameters (shifts, scales, rotations, etc.) that transform each SP scan into a reference HMI map. Since SP scans are a combination of several slit positions at different times, we must find the time at which the slit was in the middle of the spots, and align this to the HMI map closer to that time (see Table 5.1). On average, SP spends around 5 min to cover the whole spot area, while HMI data are a sum of 12 min full-disc observations. Therefore, we expect evolutionary differences in the compared maps that affect the alignment procedure and our results, but these cannot be removed. As a way to minimise the effects of granular evolution in the alignment procedure, the transformation was carried out by masking pixels with a continuum intensity brighter than 95 % of the continuum intensity of the local quiet Sun ($I_{\mathrm{c}}>0.95\,I_{\mathrm{QS}}$).

The PQ parameters are not only a tool for transforming SP scans into HMI maps,

No.	Time (UT) SP scan	Time (UT) SP slit on spots	Time (UT) HMI map	μ
1	21 Jan 06:41:28	07:04:00	07:00:00	0.83
2	21 Jan 13:00:03	13:23:00	13:24:00	0.86
3	21 Jan 15:35:04	15:58:00	16:00:00	0.87
4	21 Jan 18:36:28	18:59:00	19:00:00	0.88
5	22 Jan 01:00:04	01:23:00	01:24:00	0.90
6	22 Jan 07:05:05	07:28:00	07:24:00	0.92
7	22 Jan 10:20:03	10:43:00	10:48:00	0.93
8	22 Jan 13:30:03	13:53:00	13:48:00	0.94
9	22 Jan 16:10:03	16:33:00	16:36:00	0.95
10	22 Jan 19:11:27	19:35:00	19:36:00	0.95
11	22 Jan 22:13:03	22:36:00	22:36:00	0.96
12	23 Jan 09:17:03	09:40:00	09:36:00	0.97
13	23 Jan 15:11:33	15:35:00	15:36:00	0.97
14	23 Jan 18:14:26	18:37:00	18:36:00	0.97
15	24 Jan 06:41:26	07:03:00	07:00:00	0.97
16	24 Jan 10:00:02	10:22:00	10:24:00	0.96
17	24 Jan 13:00:02	13:22:00	13:24:00	0.96
18	24 Jan 15:30:02	15:51:00	15:48:00	0.96
19	24 Jan 18:35:01	18:56:00	19:00:00	0.95
20	24 Jan 21:50:01	22:11:00	22:12:00	0.94
21	25 Jan 04:00:01	04:20:00	04:24:00	0.93
22	25 Jan 07:16:25	07:37:00	07:36:00	0.92
23	25 Jan 10:34:01	10:55:00	11:00:00	0.91
24	25 Jan 13:15:01	13:35:00	13:36:00	0.90
25	25 Jan 15:45:01	16:05:00	16:00:00	0.89
26	25 Jan 17:50:01	18:10:00	18:12:00	0.88
27	25 Jan 20:45:01	21:05:00	21:00:00	0.87
28	26 Jan 00:00:01	00:20:00	00:24:00	0.86
29	26 Jan 03:00:01	03:20:00	03:24:00	0.84
30	26 Jan 06:33:25	06:53:00	06:48:00	0.83

Table 5.1 Summary of the SP scans. Second column: SP scan time, corresponding to the beginning of the scan. Third column: Time when the SP slit observed the middle of the spots. Fourth column: Time of the HMI maps closest to the SP observations in the middle of the spots.

but also for transforming the boundary contours from HMI and $\mathrm{HMI_{dcon}}$ into SP maps and vice versa by means of `pq2xy.pro` and `pqinvert.pro`. This approach permits us to compare the one-to-one correspondence between magnetic and intensity maps and to establish a relation between the UP boundary properties in the different non-transformed datasets.

The continuum intensity thresholds were delimited from $\mathrm{HMI_{dcon}}$ maps. The $\mathrm{HMI_{dcon}}$ data suit our goals better because they provide a very good temporal cadence and improved sharpness. We therefore used them as the reference maps. The external boundary of the spots was defined at $I_\mathrm{c} = 0.90 I_\mathrm{QS}$ based on visual inspection. In the early stages of the decay, this threshold traces the penumbral outer boundary, while in the later stages, it outlines weakly magnetised regions of the naked spots. Following the method used by Jurčák et al. (2018b), the internal boundary was defined at $I_\mathrm{c} = 0.50 I_\mathrm{QS}$, which in the early stages delimits the UP boundary, and in the later stages, it outlines the darker umbral cores. We recall that the sunspot occasionally contains small darker regions that are embedded in the penumbra, while the naked spots are formed by various darker umbral cores that are surrounded by dark areas that are slightly brighter. Only the larger dark regions were considered in the investigation; contours that encircled regions smaller than 0.75 Mm^2 were neglected. Figure 5.2 shows two stages of the transition, the sunspot on the left and naked spots on the right, with the mentioned contours. The better spatial resolution of SP is perceived in the more corrugated boundary contours that show intrusions into the umbral region of the sunspot and a division into multiple darker cores in the naked spots. The discarded small umbral cores are visible as the regions with an $\mathrm{HMI_{dcon}}$ blue contour without an SP red contour. On the other hand, the yellow HMI contours fail to reach the full extent of the spots and the corrugation of the UP boundary. To conclude, the temporal evolution of the magnetic properties at the internal boundaries was studied by averaging B, B_ver, and γ along the $I_\mathrm{c} = 0.50 I_\mathrm{QS}$ threshold based on $\mathrm{HMI_{dcon}}$ intensities.

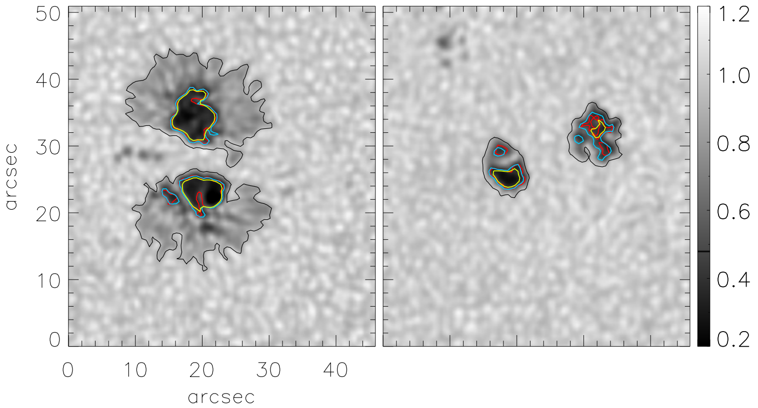

Figure 5.2 Examples of continuum intensity $\mathrm{HMI_{dcon}}$ maps. The black lines outline the $I_\mathrm{c} = 0.90 I_\mathrm{QS}$ threshold. The colour lines mark the $I_\mathrm{c} = 0.50 I_\mathrm{QS}$ location in the SP (red), HMI (yellow) and $\mathrm{HMI_{dcon}}$ (blue) co-temporal maps. Left: Sunspot stage on 22 January at 10:48 UT. Right: Naked-spots stage on 26 January at 06:48 UT.

5.4 Results

5.4.1 Comparison between datasets within the spot

To better understand the differences between SP, HMI, and HMI$_{\rm dcon}$, a one-to-one comparison is required. Only pixels within the spot (90% of $I_{\rm QS}$ in HMI$_{\rm dcon}$ maps, or from now on, $I_{\rm c,dcon} = 0.90 I_{\rm QS}$) were considered. Figure 5.3 displays the two-dimensional density functions of the compared datasets. Additionally, Fig. 5.4 compares the SP vector fields inferred with the MERLIN (the default dataset used in this work) and SIR codes. Unless specified otherwise, any reference to SP data refers to the vector field retrieved from `Level 2` and `Level 2.1` datasets, which were inferred with MERLIN.

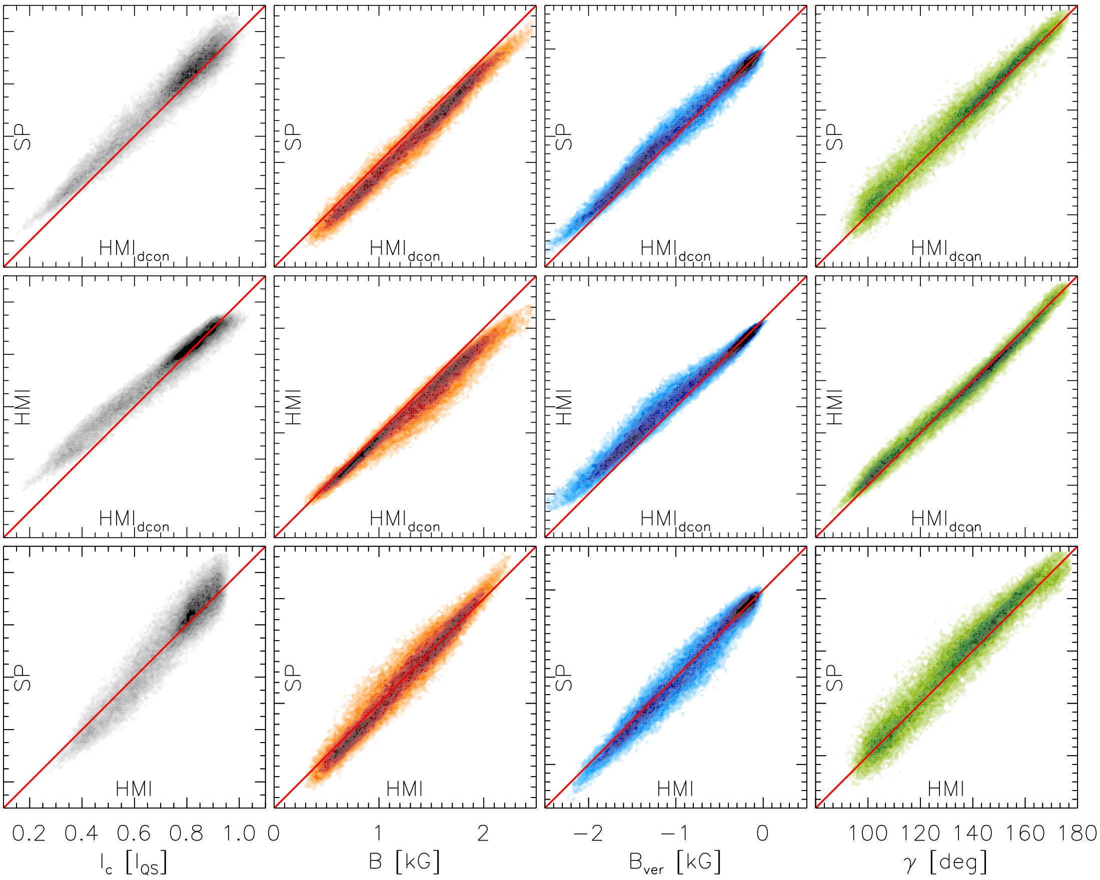

Figure 5.3 Density functions comparing the continuum intensity ($I_{\rm c}$, grey), total magnetic field (B, orange), vertical magnetic field ($B_{\rm ver}$, blue), and magnetic field inclination (γ, green) between the SP, HMI, and HMI$_{\rm dcon}$ datasets. Top row: SP vs. HMI$_{\rm dcon}$. Middle row: HMI vs. HMI$_{\rm dcon}$. Bottom row: SP vs. HMI. The red line marks the one-to-one correspondence. The spans of the y-axes are identical to those of the x-axes.

For SP versus HMI$_{\rm dcon}$ (top row in Fig. 5.3), the continuum intensity is ~ 5 % darker in HMI$_{\rm dcon}$ maps than in SP on average. The one-to-one correspondence is better for the total magnetic field strength, but there is a ~ 100 G offset where HMI$_{\rm dcon}$ values are stronger than those in SP. On the other hand, $B_{\rm ver}$ values are comparable at the lowest values of the magnetic field, but the HMI$_{\rm dcon}$ values we retrieved are stronger on average, with a ~ 70 G offset with respect to SP. The inclination, γ, has a linear trend in the whole range and an offset of $\sim (1–2)^\circ$ in the umbral region. Penumbral regions are retrieved to be more vertical in SP, and the scattering is stronger than in umbral regions.

For HMI versus HMI$_{\rm dcon}$ (middle row in Fig. 5.3), we limited the 704 available maps

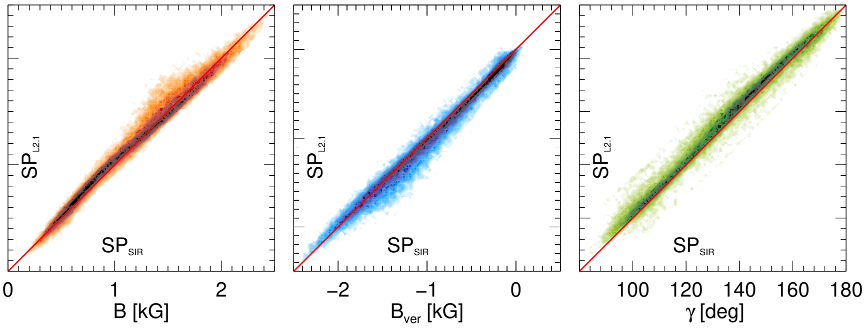

Figure 5.4 SP density functions comparing the total magnetic field (B, orange), vertical magnetic field (B_{ver}, blue), and inclination (γ, green) inverted with SIR ($_{\mathrm{SIR}}$) and MERLIN ($_{\mathrm{L2.1}}$).

to the 30 maps used for SP in order to obtain similar statistics. The continuum intensity does not have a one-to-one correlation; while bright areas are darker in HMI than in HMI$_{\mathrm{dcon}}$, the dark areas are brighter in HMI than in HMI$_{\mathrm{dcon}}$. B and B_{ver} are similar in their magnetic properties in HMI compared to HMI$_{\mathrm{dcon}}$ for the weaker values, and the differences increase linearly with the parameter amplitudes. The inclinations are comparable in the whole range of obtained values.

We also compared SP and HMI (bottom row in Fig. 5.3) because previous studies related to the magnetic nature of UP boundaries have used both datasets. The SP versus HMI density plots exhibit the greatest dispersion in all the parameters. Regarding I_{c}, bright pixels are brighter in SP than in HMI, while dark pixels are darker in SP maps. B is retrieved to be weaker in SP maps, where the field is lower, and it is stronger in the strongest fields. Similarly, B_{ver} is retrieved to be stronger in SP than in HMI in the regions with stronger fields, but the weaker fields are retrieved to be similar. The inclination has a good one-to-one correspondence in the more horizontal fields and an offset of $\sim 3^\circ$ in the umbral region, where the SP values are more vertical than the HMI values.

We note that the B_{ver} parameter has the best correlation of all the datasets and the best one-to-one correspondence between SP and HMI$_{\mathrm{dcon}}$. Complementary, γ has the best one-to-one correspondence between SP and HMI maps and between HMI and HMI$_{\mathrm{dcon}}$ maps. On the other hand, the I_{c} maps have the worst one-to-one correlation of all the parameters in all the compared datasets. Therefore, a magnetic field threshold, that is, a fixed B_{ver} value, would outline more similar umbral regions between different datasets than a fixed I_{c} threshold.

We additionally compared the default dataset analysed in this work (the vector field components inferred with MERLIN) to the vector field obtained with SIR. Figure 5.4 shows a relatively good correspondence in the B, B_{ver}, and γ maps for SIR and MERLIN datasets. Based on the regions with the highest density function, MERLIN retrieves ~ 40 G higher values of B and B_{ver} in weaker magnetic fields (<1.4 kG), while SIR retrieves higher values of B ($\sim$ 30 G) in stronger magnetic fields (>1.4 kG). Strong B_{ver} fields have a good one-to-one correspondence. A region with stronger scattering in B ([1.2–1.8] kG) and in B_{ver} ([-1.0,-1.6] kG) corresponds to the naked-spot stage, which shows that during the absence of a penumbra, the MERLIN magnetic fields can be retrieved to be up to $\sim$ 150 G stronger than SIR magnetic fields. γ is $1-2^\circ$ more vertical in vector fields obtained with MERLIN than with SIR on average, independently of the spot stage.

5.4.2 Comparison between datasets at the UP boundary

After the general comparison of the spot properties inferred from interpolated SP, HMI, and HMI$_{\mathrm{dcon}}$ maps, we investigated the differences of the physical parameters among different datasets specifically at the UP boundary.

As already mentioned, HMI$_{\mathrm{dcon}}$ is the main dataset of interest in this study. Therefore, we used the $I_c = 0.50 I_{\mathrm{QS}}$ threshold defined in HMI$_{\mathrm{dcon}}$ maps ($I_{\mathrm{c,dcon}} = 0.50 I_{\mathrm{QS}}$) as a reference and projected it onto SP and HMI maps. Since HMI and HMI$_{\mathrm{dcon}}$ have the same pixel scale, the boundary coordinates are the same. On the other hand, the boundary coordinates in the original SP maps are obtained thanks to the PQ transformation parameters. We emphasize that the UP boundaries were studied on the original maps, not in transformed maps, as was done in subsection 5.4.1. The evolution of the physical properties averaged along the $I_{\mathrm{c,dcon}} = 0.50 I_{\mathrm{QS}}$ contour is shown in Fig. 5.5.

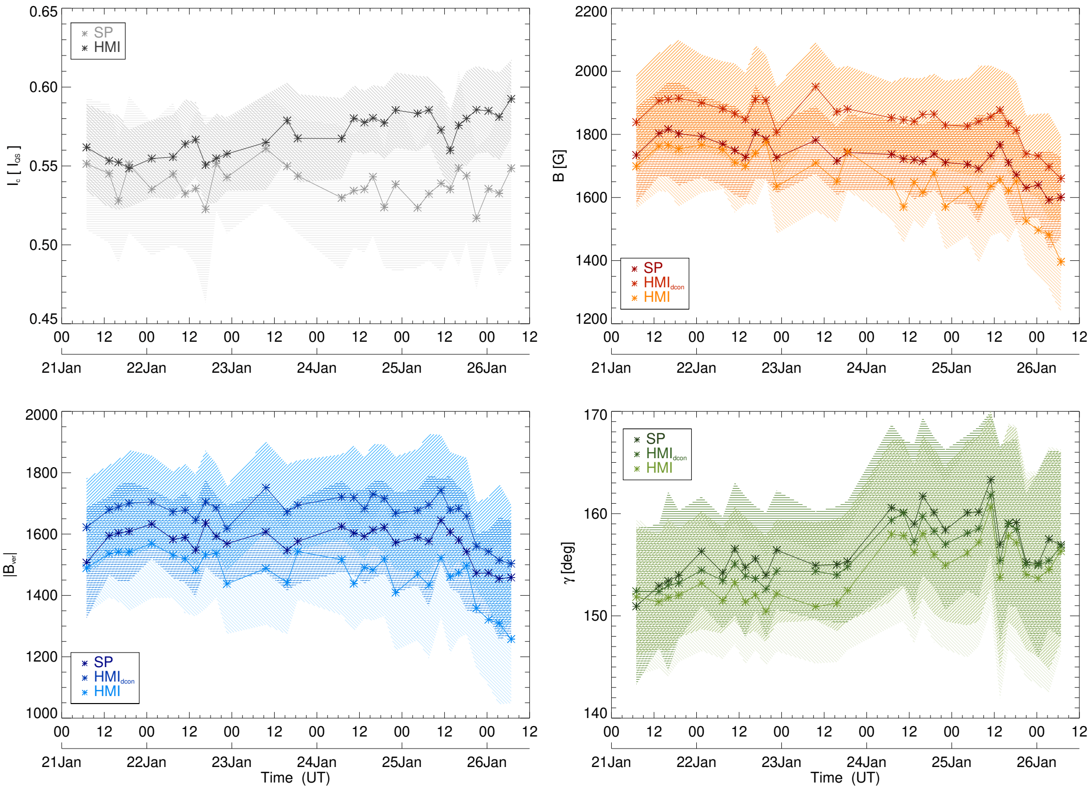

Figure 5.5 Temporal evolution of the properties averaged along the HMI$_{\mathrm{dcon}}$ threshold $I_c = 0.50\, I_{\mathrm{QS}}$ in the SP, HMI, and HMI$_{\mathrm{dcon}}$ maps. The striped areas illustrate the standard deviation of the averaged properties ($\beta = 0°$: SP, $\beta = 45°$: HMI$_{\mathrm{dcon}}$, and $\beta = 135°$: HMI). Top left: Continuum intensity (I_{qs}). Top right: Total magnetic field strength (B). Bottom left: Vertical magnetic field (B_{ver}). Bottom right: LRF inclination (γ).

In the case of I_c (upper left, grey in Fig. 5.5), the UP boundary crosses brighter regions in SP and HMI maps on average. In order to address the significance of the magnetic structure (spot or naked spot), we compared I_c averaged during the first day (21 January; sunspots with a developed penumbrae) and last day (26 January; naked spots). In the SP maps, the UP boundary crosses structures with an averaged intensity of $I_c = 0.54 I_{\mathrm{QS}}$ independently of the observed structure. Even though this result was expected from Fig. 5.3, the significant standard deviation in the SP maps suggests that another factor affects the brightness at the contour. The larger HMI$_{\mathrm{dcon}}$ pixel scale translates into maps with fewer small-scale details. Small light bridges, for instance, are not well resolved. However, as shown in Fig. 5.2, SP contours are more intricate, and as a result, $I_{\mathrm{c,dcon}} = 0.50 I_{\mathrm{QS}}$ crosses the SP UP boundary, the brighter light-bridge ends, and even penumbral filaments, increasing both the averaged I_{c} and the standard deviation values.

In the HMI maps, the average I_{c} at the UP boundary is $I_{\mathrm{c}} = 0.57 I_{\mathrm{QS}}$. The tendency of increasing I_{c} with time is clear in this case. The last-day observations are 3% brighter than the first-day observations, that is, $I_{\mathrm{c}} = 0.58 I_{\mathrm{QS}}$ on the last day compared to $I_{\mathrm{c}} = 0.55 I_{\mathrm{QS}}$ on the first day. The scattered light from the neighbouring granulation in naked spots or pores affects the characterisation of the spot boundary in terms of a I_{c} threshold up to $\sim$ 3% compared to the phase when the UP boundary is influenced by the scattered light from a darker penumbra.

In the case of the total field strength, B (upper right, orange in Fig. 5.5), three temporal evolutions are depicted (for SP, HMI$_{\mathrm{dcon}}$, and HMI data). Overall, a decrease in the total magnetic field strength is observed in all the datasets due to the decaying process. The total magnetic field is derived to be weaker by $\sim$ 6% in the SP than in the HMI$_{\mathrm{dcon}}$ datasets during the whole period on average, even though their difference varies by $\sim$ 2% with the position of the spot on the solar disc: the larger μ, the smaller the difference between datasets. On the other hand, the evolutionary state of the spot causes no difference.

As for B in HMI maps, the evolution of the divergence is more obvious. The effects of μ are not evident since both types of observations are processed in the exact same way. We only see a slowly increasing divergence between datasets. HMI is weaker by 10% than HMI$_{\mathrm{dcon}}$ on average, starting at 8% weaker during 21 January, and increasing up to 16% at the end of the observations. This increase is related to the size of the structure, and thus, to the increasing influence of the scattered light towards the end of the analysed period.

The magnetic field inclination, γ (lower right, green in Fig. 5.5) increases (it becomes more vertical with respect to the solar surface) during the first three days, followed by a decrease (it becomes more horizontal) in the later stages of the naked spots. The inclination is inferred to be more vertical in SP maps than in the two HMI maps, except for the first observation. The inclination in the SP maps is lower than 1 % and more vertical than in HMI$_{\mathrm{dcon}}$ maps, while the inclination in HMI maps is 1 % more horizontal than in HMI$_{\mathrm{dcon}}$ maps on average. The difference between HMI and HMI$_{\mathrm{dcon}}$ varies with μ, and it is smaller than 1 % close to the limb and around 2 % close to disc centre. Fig. 5.3 also shows that the retrieved inclinations are comparable in all the datasets.

The vertical magnetic field (lower left, blue in Fig. 5.5) shows a combination of the results from B and γ. During most of the observations, B_{ver} oscillates around a fixed value in SP and HMI$_{\mathrm{dcon}}$ during the decay of the penumbra, and it decreases during the last stages of the naked spots, which correspond to the emergence of new flux, as discussed in sect. 5.4.3. The values of B_{ver} in HMI$_{\mathrm{dcon}}$ maps are stronger by 6% on average than in SP maps. The difference between the two datasets varies slightly with μ. It reaches a minimum difference at the western limb ($\sim$4%) and a maximum difference close to the disc centre ($\sim$6%).

B_{ver} in HMI weakens constantly, with fluctuations, during the whole observation period. The difference between HMI and HMI$_{\mathrm{dcon}}$ B_{ver} values mostly depends on the spot size: On 21 January, B_{ver} in HMI is 9 % weaker than in HMI$_{\mathrm{dcon}}$, and it continuously decreases by 15 % on 26 January.

5.4.3 Evolution of the decaying sunspot in HMI$_{\mathrm{dcon}}$

In this section, we focus on the detailed study of the transition from a decaying sunspot to naked spots. This case study is interesting enough on its own, and it allows us to compare it to other studies of decaying sunspots. Since we aim to investigate the magnetic properties as accurately as possible, we used $\mathrm{HMI}_{\mathrm{dcon}}$ maps with the full 12 min temporal cadence (704 maps from 20 January at 18:36 UT to 26 January at 21:24 UT). The magnetic properties averaged along $I_{\mathrm{c,dcon}} = 0.50 I_{\mathrm{QS}}$ are shown in Fig. 5.6. We included the flaring times of the neighbouring region (AR 12798), to which the analysed AR was magnetically connected. Due to the weak nature of the flares, we did not observe any clear change due to the flaring activity. Additionally, we marked interesting times of the decay, such as the beginning and end of the fast decay during the last stages of the sunspot, the accumulation of magnetic flux, and the area reduction of the naked spots.

The magnetic field inclination (green in Fig. 5.6) remained stable from the beginning of the observations. It oscillated around $154\,^{\circ}$ until 23 January at midday. During the rapid decay of the umbral areas and the dissipation of the penumbrae, the inclination became increasingly vertical. Subsequently, during the first stages of naked spots, γ oscillated around $\sim 158\,^{\circ}$. The accumulation of new flux led to an increase in horizontal fields along the intensity boundary on average. During the naked-spot stage, γ became more vertical on average, diminished, and became more horizontal when the area increased. The same behaviour was observed in our previous case study of the evolution of a pore (García-Rivas et al., 2021).

The magnetic field strength (orange in Fig. 5.6) was weaker than B^{crit}=1979 G (found at the boundary of a stable pore; García-Rivas et al., 2021) during the whole decaying process. From the beginning of the observations until 23 January midday, B oscillated around 1880 G. The oscillations were due to the slow changes that affected the umbral structure. The combination of penumbral fast dissipation and umbral shrinking on 23 January at midday translated into a weakening of B. From this moment, B oscillated around a weaker value of 1850 G with fluctuations that were shorter in time. This period corresponds to the first stages of naked spots, while the penumbra completely disappeared. Due to the accumulation of new flux and the consequent increase in the umbral area, B weakened down to its minimum, $\sim$ 1730 G, after 25 January at 18 UT. Even though there is a tendency to recover the strength of B at the naked-spot boundary and it even reached 1850 G again, the rapid areal changes did not allow for a stable naked-spot stage. In general, B strengthens when the naked-spots area diminishes, and it weakens when the area increases. This again agrees with our previous case study of an evolving pore (García-Rivas et al., 2021).

The vertical field, B_{ver} (blue in Fig. 5.6) behaves very similarly as B, although B_{ver} shows weaker fluctuations; it is only a scale effect. Similarly to B, the magnetic vertical component was weaker in general than $B_{\mathrm{ver}}^{\mathrm{crit}} = 1821$ G, a maximum B_{ver} value found by (García-Rivas et al., 2021) at the boundary of a stable pore. It punctually reaches the critical value, however. During the first three days, that is, during the slow decay, B_{ver} oscillated around 1670 G. Afterwards, the fast penumbral decay began. In the case of B_{ver}, this induced a strengthening of the vertical field component that led to oscillations around 1690 G during the first stages of naked spots. The highest B_{ver} was reached when the northern spot was close to complete dissipation and the southern spot was dark and compact. In these periods, the vertical field reached maximum values. Nonetheless, the accumulation of new flux during the last hours of 25 January caused a sudden drop of B_{ver} to below $\sim$ 1550 G. As for B, B_{ver} tends to weaken with areal growth and to increase with areal stability or reduction.

The differences between the temporal trends in B and B_{ver} are noteworthy. Both magnetic properties behave in a comparable way, but with a 200 G offset (with B being stronger) during the first observation days. However, this behaviour is only observed when the umbra is surrounded by penumbra. After 24 January at midnight, when the first stages of the naked spot begin and the relative areal changes increase, B_{ver}

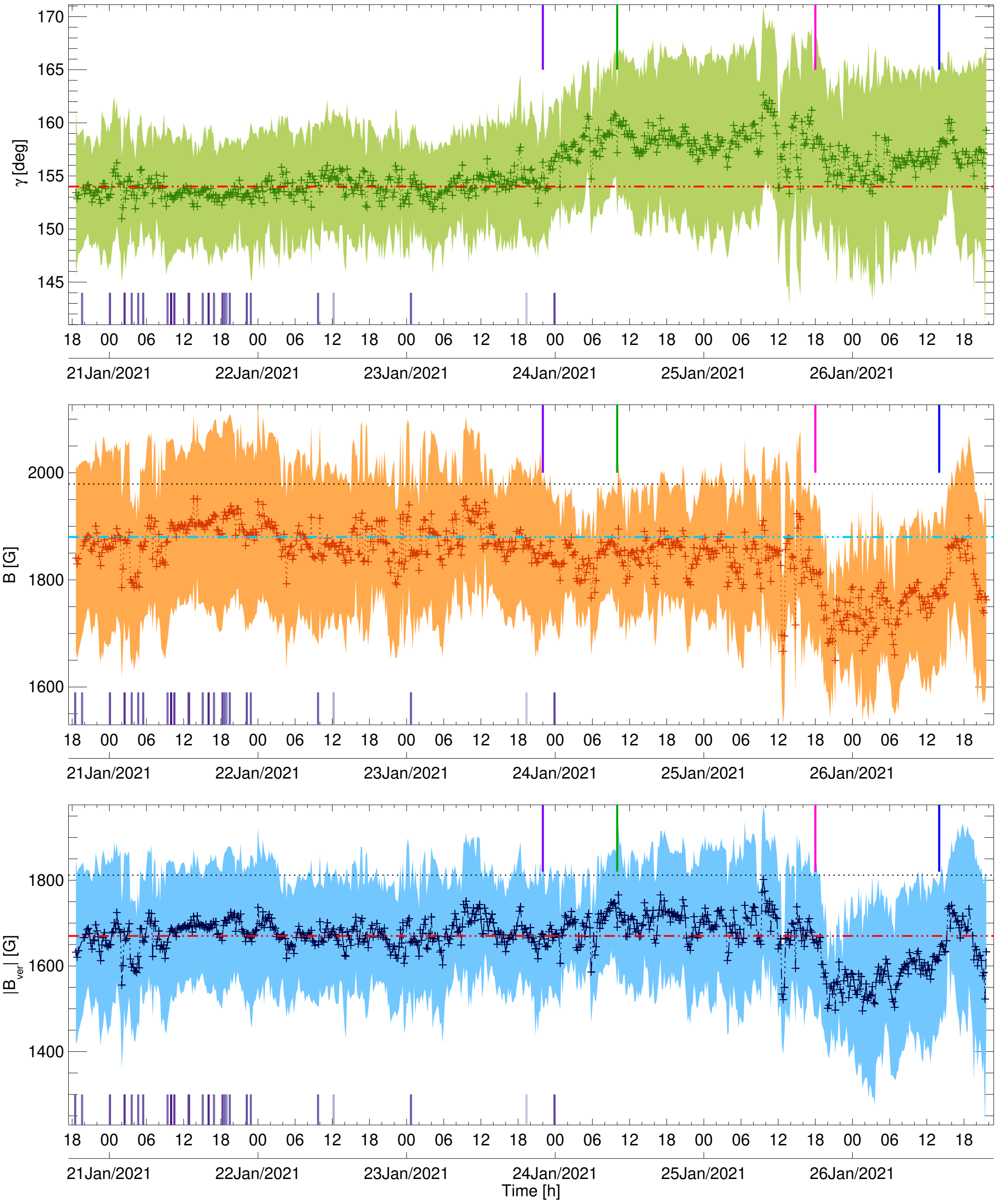

Figure 5.6 Temporal evolution of the magnetic properties: γ (in green, top), B (in orange, middle), and $B_{\rm ver}$ (in blue, bottom) averaged along the UP boundary in HMI$_{\rm dcon}$ maps. The filled areas stand for the standard deviation of the averaged properties. The dotted horizontal lines (1821 G and 1979 G) mark the maximum B and $B_{\rm ver}$ found in an evolving pore in HMI$_{\rm dcon}$ maps in García-Rivas et al. (2021), but retrieved from the $I_{\rm c,dcon} = 0.50 I_{\rm QS}$ contour instead of the $I_{\rm c,dcon} = 0.55 I_{\rm QS}$ reported in the study. The coloured horizontal lines mark the average value during the sunspot stage. The upper vertical lines indicate the times of specific evolutionary stages: The beginning of the fast decay (purple), the end of the fast decay (green), the accumulation of new flux (pink), and the decrease in the spot area (blue). The bottom vertical lines indicate the flaring times of AR 12798. The colour relates to the GOES flare class, from lighter purple (weakest: A5.6) to darker purple (strongest: B5.4).

strengthens while B weakens; their offset rises to 250 G on average. The accumulation of new flux again balances the magnetic parameters, but the following decays again increase their offset. We conclude that the presence of a penumbra stabilises the evolution of the magnetic properties at the umbral boundary. After the penumbra has completely disappeared, any change in the spot area translates into significant changes in B, γ, and B_{ver}.

The behaviour of B_{ver} in the naked spot resembles the evolving pore investigated in García-Rivas et al. (2021). When the area increases, B_{ver} diminishes, and when the area of the spot diminishes, the boundary B_{ver} strengthens. In this case study, we do not observe a stable phase nor a critical maximum B_{ver}, however. During the first days, the sunspot B_{ver} oscillates around 1670 G, while the naked-spot flux tube becomes more vertical and punctually reaches $B_{\mathrm{ver}} = 1820$ G. Because of this wide span of values, we explored the evolution of a range of B_{ver} thresholds (1600–1850 G) by calculating the areas within the contours, and we compare the evolution of the areas within $I_{\mathrm{c,dcon}} = 0.50 I_{\mathrm{QS}}$ in Fig. 5.7.

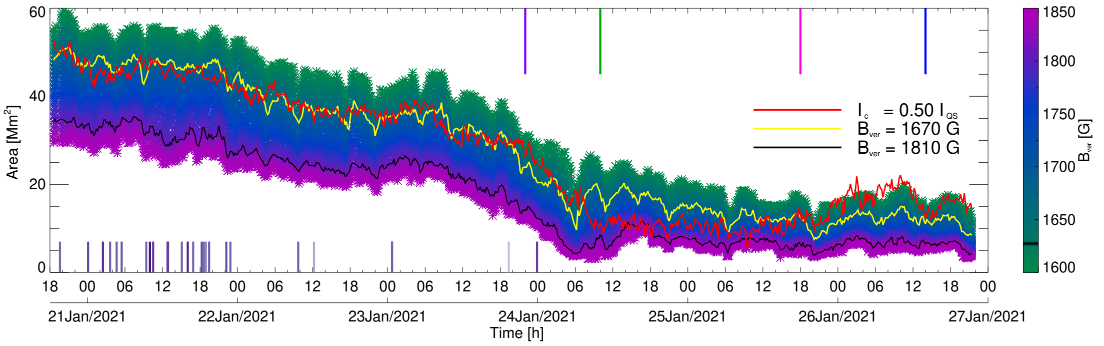

Figure 5.7 Temporal evolution of the areas encircled by B_{ver} thresholds (1600–1850 G) compared to the areas encircled by the threshold $I_{\mathrm{c,dcon}} = 0.50 I_{\mathrm{QS}}$ (yellow). The contours $B_{\mathrm{ver}} = 1810$ G and $B_{\mathrm{ver}} = 1670$ G are highlighted (black and yellow, respectively). The upper and lower vertical lines are the same as in Fig. 5.6.

The areas encircled by the intensity contour (red in Fig. 5.7) show a slow but steady decrease during the first three days when the sunspots area decreases from 50 Mm^2 to 30 Mm^2. An isolated short and sudden decrease is visible on 23 January between approximately 6 and 12 UT, however, which corresponds to the beginning of the fast penumbral decay in the southern spot. The small area variations within the three-day period are due to the evolution of the umbra-penumbra boundary and to small dark patches embedded in the penumbrae that were only taken into consideration when they were larger than ~ 5 pixel^2. This condition changed fast.

Subsequently, the decay rate of the umbral area suddenly changed during the first hours of 24 January from the previous trend. The umbrae shrink from 30 Mm^2 to 10 Mm^2 in less than 10 hours. This fast decay coincided with the dissipation of most of the penumbrae in the northern and southern spots, even though penumbral filaments continued to appear and disappear around the northern spot (details of the decay rates are discussed in Sect. 5.4.4). The southern spot dimmed, and the umbral area held multiple darker cores. The penumbra completely disappeared during the first hours of 25 January in the northern spot, and the southern pore recovered a compact and darker umbral area. Even though it seemed that the naked spots would completely dissipate, they maintained an area of ~ 10 Mm^2 until an accumulation of new flux during the latest hours of 25 January. The areas increased up to ~ 20 Mm^2 in approximately 10 hours, but they immediately evolved again, with a final decay at the end of the analysed period.

Fig. 5.7 does indeed not show a preferred B_{ver} on the $I_{\mathrm{c,dcon}} = 0.50 I_{\mathrm{QS}}$ during the whole period. As expected, the slow-decay process of the umbra is closer to the areas encircled by B_{ver}=1670 G, and the naked spots stages are characterised by stronger vertical fields before the accumulation of new flux. In Fig. 5.7, we visually identify an indication that the fast decay of the area defined by the $B_{\mathrm{ver}} = 1670$ G precedes the fast decay of the area defined by the intensity threshold by ~ 3.5 hours, as seen between 23 January 18:00 UT and 24 January 6:00 UT. A cross-correlation between the areas encircled by each of the B_{ver} thresholds and the area encircled by the intensity contour shows that the areas encircled by B_{ver}=[1640–1800] G have a unique maximum correlation (above 0.975) between 3 and 4 hours, suggesting that the areas that are defined by the vertical field decay 3.5 h on average before the areas that are defined by the continuum intensity boundary.

The cross-correlations of the areas that are defined by the intensity threshold and by $B_{\mathrm{ver}} < 1640$ G have local maxima in their correlation at a lag of 3.5 h and also for a lag 0 h or even for negative lags. The reason might be that the fluctuations in the areas defined by smaller B_{ver} are larger since the thresholds are embedded outside the umbral region, and they affect the reliability of the correlation.

We note that the cross-correlation was made from the beginning of the observations until 25 January at 5 UT in order to avoid the process of flux accumulation. The variations in the cross-correlation coefficient are low with the time lag (the minimum is 0.96 for positive lags). We recall that the encircled areas are the sum of the two spots that evolve at different paces, and therefore, we combined information that may dilute stronger evidence. In García-Rivas et al. (2021) we did not find any delay between the decay in the areas defined by B_{ver} and intensity.

5.4.4 Sunspot decay rates

In this subsection, we focus on the decay rates of the sunspot, that is, the time at which the penumbra disappears. To do this, we analysed the two components of the sunspot, umbra, and penumbra separately.

Umbral areas are limited by a $I_{\mathrm{c,dcon}} < 0.50 I_{\mathrm{QS}}$ threshold, while penumbral areas are defined by $0.50 I_{\mathrm{QS}} < I_{\mathrm{c,dcon}} < 0.90 I_{\mathrm{QS}}$. The decay rates were investigated from the beginning of the observations until 24 January at 10 UT, when the spots reached their minimum umbral area during the complete dissipation of the penumbra. We note that the disappearance of the penumbra does not imply a lack of spot areas with $0.50 < I_{\mathrm{QS}} < 0.90$. That is, in the later stages of the decay, the term penumbral area refers to the brighter regions around the darker umbral areas without penumbral filaments. Figure 5.8 summarises the temporal evolution of the umbral and penumbral area (red, A) and magnetic flux (purple, Φ).

The penumbra (light red, Fig. 5.8, top) shows a constant linear decay during the whole period at a rate of 45.9 $\mathrm{Mm^2 day^{-1}}$. The umbra (red) decays linearly as well, although it shows two stages: (1) a slow decay with a rate of 6.4 $\mathrm{Mm^2 day^{-1}}$ from the beginning of the observations to 23 January at ~ 20 UT, and (2) a fast decay with a rate of 35.0 $\mathrm{Mm^2 day^{-1}}$ until the complete disappearance of the penumbrae. The whole sunspot decay is the sum of the decay in the umbra and penumbra.

The type of decay law depends on the decaying mechanism. For example, the quadratic law is related to the turbulent erosion model, where the dissipation is due to the erosion of the external boundary of the sunspot, and it therefore varies with the length of the boundary. On the other hand, the linear decay law is related to turbulent magnetic diffusion within the whole area of the sunspot (for a wider review see Solanki, 2003). These types of decaying laws have been studied in sunspot groups and in individual sunspots, and the decay rates have been found to be dependent on the

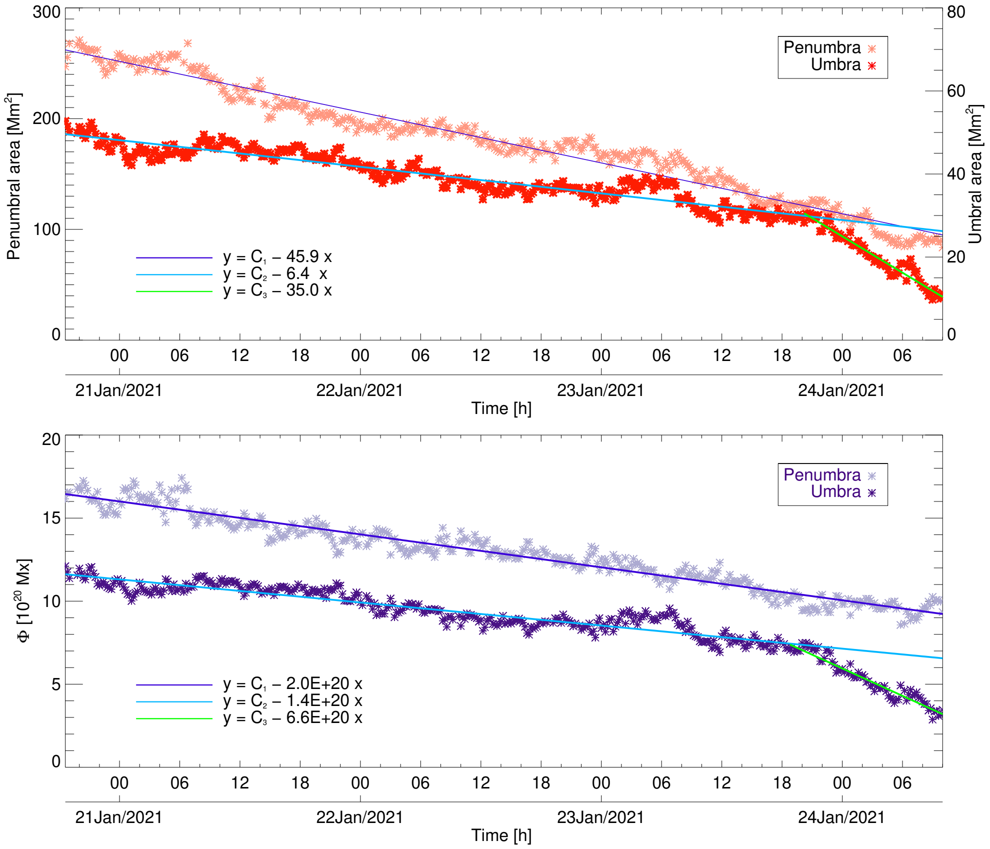

Figure 5.8 Temporal evolution of the photometric and magnetic sunspot during the dissipation of the penumbra, which includes the slow and fast umbral decay. Top: Umbral and penumbral areas (red and light red, respectively). Bottom: Umbral and penumbral magnetic flux (dark and light purple, respectively).

sunspot area, the latitude, the solar cycle, or the leading or following sunspot, among others, or to have a lognormal distribution (e.g. Martinez Pillet et al., 1993; Muraközy, 2020; Petrovay et al., 1997b; Hathaway et al., 2008).

Although statistical analyses are very useful for general rules, they can omit rarer or less noticeable events, such as the detection of different decay rates in one decaying spot. For example, Verma et al. (2016) studied the case of a small active region that first decayed fast (23 Mm^{2}day^{-1}) and then decayed slowly (14 Mm^{2}day^{-1}). Neither the decay processes nor the decay rates agree with the results presented here. A similar result was found by Q. Li et al. (2021) in one of the eight α-sunspots they analysed, while seven sunspots decayed slowly, followed by a fast linear decay, like in our study. The sunspot decay we studied first decayed slowly and then fast only due to a change in the umbral decay, but Q. Li et al. (2021) reported diverse scenarios (constant umbral decay and two-stage penumbral decay; two-stage umbral decay and two-stage penumbral decay). Even their reported decay rates (slow umbral decay: 3.3 Mm^{2}day^{-1}, fast umbral decay: 29 Mm^{2}day^{-1}, and fast penumbral decay: 38 Mm^{2}day^{-1}) are lower than ours, perhaps due to the difference in the sunspot areas.

The ratio of the umbra-to-penumbra area (U/P), the umbra-to-total area, or the penumbra-to-umbra area were used in the literature to describe sunspot decay that take the evolution of their components into account. It has been found to be constant (Martinez Pillet et al., 1993, e.g.) and variable, depending on the sunspot decay rate. Carrasco et al. (2018) found higher U/P values during faster sunspot decays, for instance, while Chapman et al. (2003) found higher U/P ratios with slower sunspot decays. The sunspot we studied has a variable U/P ratio that varies with the velocity of the umbral decay. During the slow umbral decay, the U/P ratio oscillates around 0.21, while during the fast umbral decay, it reaches its minimum (0.13). However, the sunspot decay rate remains constant, and therefore, the U/P ratio is lower during a constant sunspot decay. Similar results were found by Q. Li et al. (2021) in certain sunspots, where the significant drop of the U/P ratio was connected to sudden drops of the umbral area and not to sudden changes in the evolution of the whole sunspot.

The flux trend is parallel to the decaying areas: The penumbral flux (light purple in Fig. 5.8, bottom) decays linearly during the whole period we studied at a rate of $2 \times 10^{20}\,\mathrm{Mx\,day^{-1}}$, and the umbral flux (dark purple) decays in two stages, $1.4 \times 10^{20}\,\mathrm{Mx\,day^{-1}}$ at the beginning, and $6.6 \times 10^{20}\,\mathrm{Mx\,day^{-1}}$ during the fast decay. Compared to Q. Li et al. (2021), our umbral flux decay rates are twice higher, but their penumbral flux decreases faster. Our slow-decay rate is similar to the rate derived by Deng et al. (2007) ($2.8 \times 10^{20}\,\mathrm{Mx\,day^{-1}}$), while our fast-decay rate is closer to the decay rate of a naked spot simulated by Rempel (2015). Overall, Benko et al. (2018) reported a similar flux disappearance to the values we find during the slow umbral and penumbral decay.

5.5 Discussion and conclusions

We presented the analysis of a decaying sunspot that turned into naked spots while transiting from the eastern to the western solar limb. The aim of this work was to analyse the evolution of the magnetic properties on the UP boundary during the decay phase. Moreover, this sunspot enabled us to compare the differences between datasets that were previously used in the study of UP boundaries, that is, SP maps inferred with SIR and MERLIN, regular HMI maps, and $\mathrm{HMI_{dcon}}$ maps. Not only can we compare the dissimilarities among the derived properties inside the spot, but we can concentrate on the divergences at the UP boundary in particular.

Due to the choice of a unique continuum intensity threshold for our study, we find that UP boundaries are better defined by the $0.50\,I_{\mathrm{QS}}$ threshold than the naked spots. As reported in García-Rivas et al. (2021), pores are more precisely defined by a $0.55\,I_{\mathrm{QS}}$ threshold, especially when the pore structure is compact.

From a comparison of the intensity thresholds defined individually for each dataset at $0.50\,I_{\mathrm{QS}}$ (Fig. 5.2), we see that HMI outlines only the larger structures without fine details and fails to characterise the smaller structures. During the naked-spot stage, the HMI $0.50\,I_{\mathrm{QS}}$ threshold falls well inside the spot. On the other hand, the $\mathrm{HMI_{dcon}}$ and SP $0.50\,I_{\mathrm{QS}}$ contours are more similar, even though the SP contours have more finely detailed structures. The lower spatial resolution of $\mathrm{HMI_{dcon}}$ translates into the apparent fusion of structures that SP considers as separated structures. As proposed in García-Rivas et al. (2021) and proven in this study, $\mathrm{HMI_{dcon}}$ and SP are a more accurate source for studying the UP and pore boundaries.

From a general comparison of the spot properties shown in Fig. 5.3 and from the detailed comparison of the physical properties found on the UP boundary shown in Fig. 5.5, we find the best agreement between the studied datasets in the B_{ver} parameter, while the continuum intensity lacks a good one-to-one correspondence like this and shows larger scatter. This implies that a fixed B_{ver} threshold would define the areas in all the datasets more accurately than a fixed I_{c} threshold.

The UP boundary defined in the $\mathrm{HMI_{dcon}}$ dataset at $I_{\mathrm{c}} = 0.50 I_{\mathrm{QS}}$ is characterised in SP maps by $I_{\mathrm{c}} = 0.54 I_{\mathrm{QS}}$ (8% brighter). This intensity value fluctuates from one map to the next, but it is not dependent on the spot structure, size, or location. On the other hand, the I_{c} value found in HMI maps brightens with a smaller spot size, that is, when more scattered light from the brighter granulation contaminates the darker structures. The intensities found at the boundaries in HMI maps increase from $I_{\mathrm{c}} = 0.55 I_{\mathrm{QS}}$, 10% brighter, to $I_{\mathrm{c}} = 0.58 I_{\mathrm{QS}}$, 16% brighter (see Fig. 5.5).

Along with the differences of I_{c} between the analysed datasets, we also found differences in the B_{ver}, values as shown in Fig. 5.5. These differences explain the origin of the discrepancies in the B_{ver} values found at the umbral boundaries in previous studies.

The mean B_{ver} at the UP boundary in the SP maps is 5 % weaker on average than the value obtained in $\mathrm{HMI_{dcon}}$ maps. The fact that $\mathrm{HMI_{dcon}}$ maps provide the strongest B_{ver} values implies that the maximum vertical field found in the stable stage of an evolving pore ($B_{\mathrm{ver}}^{\mathrm{crit}}$=1821 G at 0.50 I_{QS}) by García-Rivas et al. (2021) is not comparable to the $B_{\mathrm{ver}}^{\mathrm{crit}}$ value obtained from a statistical analysis of stable sunspots in SP maps (1867 ± 18 G) by Jurčák et al. (2018b).

On the other hand, the difference of B_{ver} at the UP boundary between $\mathrm{HMI_{dcon}}$ and HMI maps largely depends on the spot size (it increases with smaller areas), and it varies from 8 % (sunspot) to 15 % (naked spots). The disagreement between the $B_{\mathrm{ver}}^{\mathrm{crit}}$ obtained by Schmassmann et al. (2018) in a stable sunspot in HMI maps with respect to the one obtained by García-Rivas et al. (2021) (1695 G and 1821 G at 0.50 I_{QS}, respectively) is 6 %, which agrees with the dissimilarities between the sunspot stage in this study. Complementary, the $B_{\mathrm{ver}}^{\mathrm{crit}}$ obtained by Schmassmann et al. (2018) is 9 % weaker than the value obtained by Jurčák et al. (2018b), which again agrees with the difference between B_{ver} at the UP boundary of HMI with respect to SP maps found during the sunspot stage in this study (5 %).

As reported in previous studies during the evolution of pores (García-Rivas et al., 2021), an increase in the naked-spots area translates into drops of the magnetic fields at the boundary. On the other hand, non-variable or decreasing areas yield increasing B_{ver} values at the I_{c} threshold during non-stable stages. The maximum B_{ver} values are achieved in the naked-spot stage, even though it never reaches the $B_{\mathrm{ver}}^{\mathrm{stable}}$ found in previous studies, nor is a stable period in terms of constant area observed.

An interesting result is that the areas encircled by B_{ver} thresholds between 1640 G and 1800 G seem to decay $\sim$ 3.5 h before the areas encircled by the intensity contour (Fig. 5.7). This result indicates that the magnetic field may decay before the photometric structure. However, the correlation coefficient that indicates the earlier decay of the magnetic field depends only weakly on the time lag.

The area and magnetic flux decay were studied separately in the umbra and in the penumbra. The photometric spot and the Φ decay linearly, which suggests magnetic diffusion in the whole area of the sunspot (e.g. Solanki, 2003). While the penumbra decays at a constant rate, the umbra first decays slowly, which is followed by a sudden fast decay in the later stages of the penumbral dissipation. This behaviour is not consistent with reported constant linear or quadratic decay rates (e.g. Benko et al., 2018; Deng et al., 2007; Petrovay et al., 1997b). Nonetheless, decaying processes divided into slow and fast stages have been observed as well (e.g. Q. Li et al., 2021; Verma et al., 2016; García-Rivas et al., 2021), even though the order (slow/fast or fast/slow) seems to depend on the case study.

Acknowledgements:

We would like to thank A. Norton for providing us with deconvolved full-disc HMI vector field maps. This work was supported by the Czech-German common grant, funded by the Czech Science Foundation under the project 23-07633K and by the Deutsche Forschungsgemeinschaft under the project BE 5771/3-1 (eBer-23-13412), and the institutional support ASU:67985815 of the Czech Academy of Sciences. The HMI data are courtesy of NASA/SDO and the HMI science teams. Hinode is a Japanese mission developed and launched by ISAS/JAXA, collaborating with NAOJ as a domestic partner, NASA

and STFC (UK) as international partners. Scientific operation of the Hinode mission is conducted by the Hinode science team organized at ISAS/JAXA. This team mainly consists of scientists from institutes in the partner countries. Support for the post-launch operation is provided by JAXA and NAOJ(Japan), STFC (U.K.), NASA, ESA, and NSC (Norway).

6 On the onset of penumbra formation

Reproduction of García-Rivas et al. (2024b)
Published in *Astronomy & Astrophysics*
DOI: 10.1051/0004-6361/202348764

Received 28 November 2023 / Accepted 08 March 2024

Authors:
M. García-Rivas[1,2], J. Jurčák[1], N. Bello González[3], J. M. Borrero[3], R. Schlichenmaier[3], and P. Lindner[3]

Affiliations:
[1]Astronomical Institute of the Czech Academy of Sciences, Fričova 298, 25165 Ondřejov, Czech Republic
[2] Astronomical Institute, Charles University, V Holešovickách 2, 18000 Praha, Czech Republic
[3] Institut für Sonnenphysik (KIS), Georges-Köhler-Allee 401a, 79110 Freiburg, Germany

ABSTRACT

Context: Fully fledged penumbrae have been widely studied both observationally and theoretically. Yet the relatively fast process of penumbra formation has not been studied closely with high spatial resolution.

Aims: We investigate the stages previous to and during the formation of penumbral filaments in a developing sunspot.

Methods: We analysed Milne-Eddington inversions from spectro-polarimetric data of the leading sunspot of NOAA 11024 during the development of its penumbra. We focused on selected areas of this protospot in which segments of penumbra develop.

Results: We find that few types of distinctive flow patterns develop at the protospot limb and centre sides previous to penumbra formation. The flow in the centre side is often characterised by a persistent (>20 min) inflow-outflow pattern extending radially over 4 arcsec at the direct periphery of the protospot umbra. This inflow-outflow system often correlates with elongated granules, as seen in continuum intensity maps, and is also coupled with magnetic bipolar patches at its edges, as seen in magnetograms. The field is close to horizontal between the bipolar patches, which is indicative of its possible loop configuration. All of these aspects are analogous to observations of magnetic flux emergence. In the protospot limb side, however, we observed a mostly regular pattern associated with small granules located near the protospot intensity boundary. Locally, an inflow develops adjacent to an existing penumbral segment, and this inflow is correlated with a single bright penumbral filament that is brighter than filaments containing the Evershed flow. All investigated areas at the centre and limb side eventually develop penumbral filaments with an actual Evershed flow that starts at the umbral boundary and grows outwards radially as the penumbral filaments become longer in time.

—

Key words. Sun: photosphere – Sun: magnetic fields – sunspots

6.1 Introduction

As discussed by Bello González et al. (2019), the basic necessary conditions of a minimum required flux and the presence of strong horizontal fields for the formation of penumbrae are known in general. However, there are a number of aspects that are still not known and/or understood. Observational analyses of pores and sunspots imply that a minimum magnetic flux on the order of 10^{20} Mx is necessary for the penumbra to form (Zwaan, 1987; Leka et al., 1998). This number is consistent with the theoretical model by Rucklidge et al. (1995), who investigated the stability of magnetic flux tubes and their properties based on their total flux. These models and observations describe pores and sunspots created by rather symmetrical magnetic flux tubes. As the magnetic flux within the flux tube increases, the magnetic field inclination on its edges increases, and the horizontal component of the magnetic field is strong enough to shape the rising convective cells to form the elongated penumbral filaments. The magnetohydrodynamic (MHD) simulations of sunspots by Rempel et al. (2009) as well as analysis of the observations by Jurčák et al. (2014b) suggest that the critical magnetic field inclination necessary for penumbra formation is around 45°. This value is also in agreement with the simpler models of Rucklidge et al. (1995).

Another property of penumbrae in sunspots that might play a role in sustaining horizontal fields resulting in penumbra formation is the presence of an overlaying magnetic field that traps the emerging horizontal field in the photosphere in the form of penumbral filaments. Solanki et al. (1993) proposed the uncombed structure of the magnetic field in sunspot penumbra where horizontal flux tubes or tops of elongated convective cells (as suggested by MHD simulations) are interleaved by a stronger and more vertical magnetic field known as the background magnetic field or intraspines. The actual configuration of the magnetic field is very similar to the proposed model, as confirmed by Tiwari et al. (2013), and it was shown by Borrero et al. (2007) and Borrero et al. (2008) that the background magnetic field closes above the penumbral filaments.

Another form of penumbra is the orphan penumbra. These are penumbrae not coupled to an umbra. Jurčák et al. (2014b) reported no background magnetic field present in these structures, while Zuccarello et al. (2014) found indications of it. Orphan penumbrae are in most aspects (e.g. Evershed flows and penumbral grains) similar to sunspot penumbrae (Jurčák et al., 2014b). Lim et al. (2013) and Zuccarello et al. (2014) found orphan penumbrae originating from an emerging magnetic field trapped at the photospheric level by the pre-existing overlying fields in areas of complex topology in active regions, typically near the polarity inversion lines.

Details of penumbra formation were studied by Schlichenmaier et al. (2010a), Schlichenmaier et al. (2010b), Schlichenmaier et al. (2011), and Schlichenmaier et al. (2012), who used unique observations of sunspot formation over a period of 4.5 h. The formation of penumbra was in this case caused by the accumulation of magnetic flux on one side of the protospot where a stable segment of a penumbra formed on the opposite side. Prior to the formation of a stable penumbra, Schlichenmaier et al. (2011) observed temporal filaments with what they introduced as counter-Evershed flows. Using the same data, Rezaei et al. (2012) found signatures of a low lying (observed in the Fe I 617.3 nm line) magnetic canopy in the regions where penumbra later formed. This scenario was subsequently confirmed by the numerical simulations of MacTaggart et al. (2016), who studied the flux emergence of a twisted magnetic flux tube and the magnetic canopy formed preferentially away from the emergence site. Indication of a chromospheric magnetic canopy was found also by Shimizu et al. (2012) and Romano et al. (2013), who observed a chromospheric halo in regions where penumbra later formed. The presence of a chromospheric halo preceding the formation of the penumbra was interpreted by Romano et al. (2013) and Romano et al. (2014), and Murabito et al. (2016) as a necessary configuration of the magnetic field that allows for downward bending of the chromospheric field lines and the creation of a shallow loop that is also associated with temporal counter-Evershed flows caused by siphon flows. The recent work by Lindner et al. (2023) favours a scenario in which emerging flux blocked by an overlying (chromospheric) canopy provides the strong horizontal fields necessary for penumbra formation.

Q. Li et al. (2018) investigated the formation of a penumbra sector and found that in a first stage, the area and magnetic flux of the forming penumbral sector and the umbra both increased and that in a subsequent second stage, the area and magnetic flux of the penumbra increased at the expense of the umbra area and the flux. They also found a persistent blueshift in the penumbra formation area that they interpreted as a signature of magnetic flux emergence. However, they did not find any chromospheric counterpart coupled to the penumbra formation unlike the annular region reported by Shimizu et al. (2012). Yet, they found a correlation between the penumbral sector formation and sunspot rotation. Q. Li et al. (2019) also found indications of penumbral areas formed by emerging flux trapped in the photosphere by the overlying pre-existing field in a complex active region.

Jurčák (2011) discovered the magnetic property defining the umbra-penumbra boundary of stable sunspots, a critical value of the vertical magnetic field (1.86 kG, Jurčák et al., 2018b). Jurčák et al. (2015) found this canonical value to be a natural inner boundary for the expansion of penumbral magneto-convection in umbral areas. Their result is in agreement with the findings of Q. Li et al. (2018), as umbral areas are originally occupied by developing penumbra. Therefore, penumbra can only set in and operate in regions with a vertical field below the critical value. The observation of such a vertical magnetic field boundary against vigorous modes of magneto-convection (e.g. the penumbral mode) is supported by the analysis of the Gough and Tayler criterion (Gough et al., 1966) of stability by vertical fields against overturning convection by Schmassmann et al. (2021).

From a modelling point of view, there are a number of realistic simulations of sunspots with penumbra (See, e.g., Rempel et al., 2009; Rempel, 2011; Rempel, 2012; Chen et al., 2017; Panja et al., 2021). Yet only a few works address the onset and formation of penumbra. In accordance with observations, Hurlburt et al. (2000), Simon et al. (1970), and Jahn et al. (1994) found that an increasing inclination (with respect to the normal to the solar surface) of the magnetic field and an increasing flux in sunspot models are key factors for the origin of penumbra. Wentzel (1992) proposed the 'fallen magnetic flux tubes' model for penumbra formation. There, the upwelling of a mass flow in the inner footpoint of the field lines within the umbra provokes the flux tubes to fall onto the photosphere and become submerged in the surroundings of the sunspot (i.e. the penumbra forms from top to bottom). On local scales, Rempel (2011) presented a more elaborated model where the flux tubes bend due to the mass loads originated from pressure-driven upflows (see Fig. 19 of the cited work). On the other hand, Chen et al. (2017) simulated the formation of an asymmetric sunspot formed by the coalescence of magnetic features with the same polarity from small-scale dipoles embedded in granular cells (i.e. the penumbra forms from bottom to top). Regarding penumbral radial flows (e.g. Evershed flow or counter-Evershed flow), Chen et al. (2017) found that penumbral filaments were dominated by inflows in the region where the flux emergence was more active (between the two main spots). More interestingly, some penumbral filaments developed intermittent outflows even when they were originally dominated and surrounded by inflows. Transient inflows embedded in outflows were obtained by Siu-Tapia et al. (2018) from simulations based on the MURaM radiative

MHD code.

In this work, we describe the observational properties of magneto-convection at the outskirts of a protospot before the onset of a penumbra and during the first stages of the penumbral formation process. The observations and data analysis are described in Sect. 6.2. Three distinct penumbral formation processes are respectively presented and discussed in Sect. 6.3 and Sect. 6.4. This work closes with conclusions obtained from the results.

6.2 Observations and data analysis

The data were recorded on 9 July 2009 with the 'Göttingen' Fabry-Pérot Interferometer (GFPI, Bendlin et al., 1992; Puschmann et al., 2006a) in the full-Stokes polarimetric mode (Bello González et al., 2008) at the VTT Telescope (Tenerife). The observations consisted of a time series of 4:40 h following the evolution of the leading sunspot in NOAA 11024 located at a heliocentric angle $\theta \sim 28°$. Here, we make use of the imaging data in the G-band and full-Stokes polarimetry in the Fe I 617.3 nm photospheric line. We note that these data were previously used in other investigations (Schlichenmaier et al., 2010a; Schlichenmaier et al., 2010b; Rezaei et al., 2012; Bello González et al., 2012; Jurčák et al., 2014a), and therefore we defer to the referenced works for further details about the observations.

We restricted our analysis to a 2 h time span (08:32 UT–10:32 UT) of uninterrupted observation of penumbra formation consisting of 109 GFPI scans. We focused on selected regions of the protospot periphery in which the formation of penumbral segments can be followed over time. We ran Milne-Eddington inversions of the Fe I 617.3 nm spectropolarimetric observations with the VFISV code (Borrero et al., 2011b), which provides the components of the magnetic field vector and line-of-sight (LOS) velocity maps. We used the code AMBIG (Leka et al., 2009b) to solve the 180° ambiguity in the component of the magnetic field perpendicular to the observer's LOS. We also made use of routines of the AZAM code (Lites et al., 1995) to transform the magnetic field vector from the LOS frame to the local reference frame (LRF). During the time series, the field of view varies. This resulted in a limited effective field of view.

6.3 Results

Figure 6.1 shows a snapshot of the field of view under analysis at the beginning of the observations. An animation of the development and evolution of the protospot can be found **online**. At this early stage, the protospot already shows segments of stable penumbra around (22″, 20″) and (16″, 11″). The penumbra around (11″, 19″) is highly distorted by the continuous emergence of the new flux in the developing active region (Rezaei et al., 2012). We note that the protospot is the leading polarity of NOAA 11024, and the following polarity is directed towards the east (not visible within the field of view).

We studied the magnetic field and velocity properties in regions where penumbrae later form. We note that the Milne-Eddington inversion scheme does not allow for disentangling of the different physical properties of the spot background component from the penumbral filaments. Instead, the Milne-Eddington inversion provides mean values of LOS velocity, magnetic field strength, and inclination (Borrero et al., 2014) from regions where the 617.3 nm line forms and is most sensitive to changes of the physical properties. This implies that the magnetic canopy affects the plasma properties inferred at the external boundary of the umbral core and beyond. In this case, the influence is asymmetric due to the heliocentric angle and the resulting projection effects. As seen in

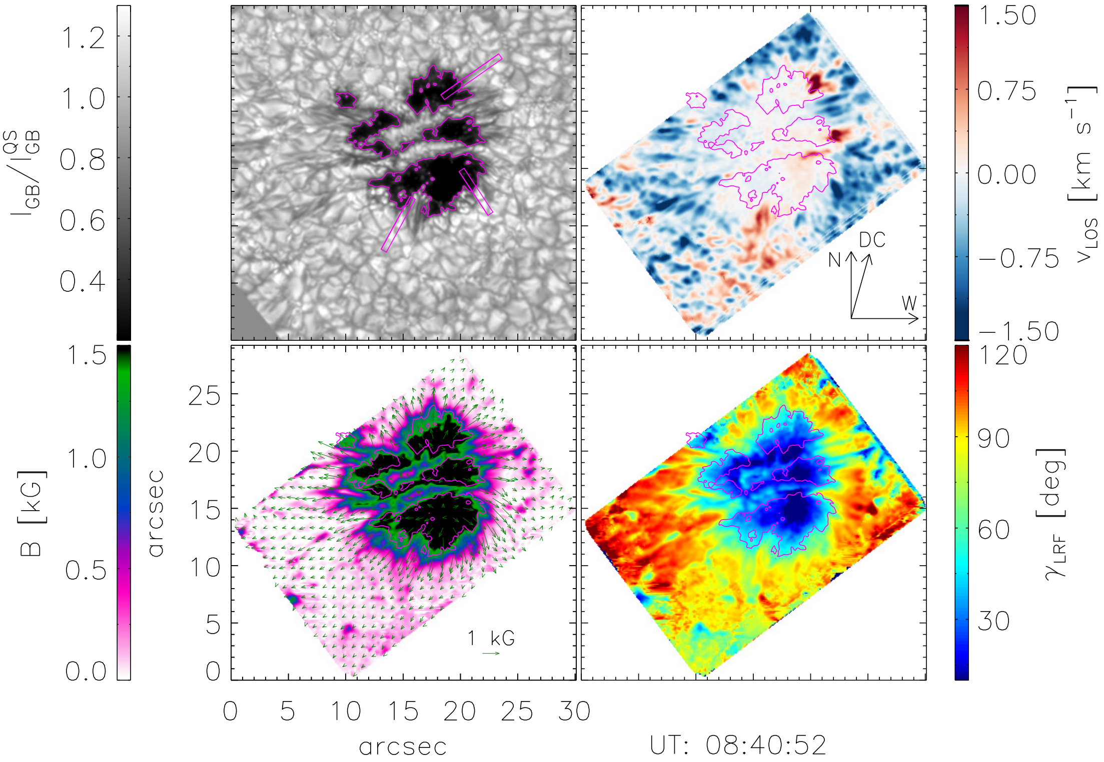

Figure 6.1 Snapshot of NOOA 11024 sunspot at the early stages of penumbra development (08:40:52 UT) as seen in G-band intensity (upper left), LOS velocity (upper right), total magnetic field strength (lower left), and magnetic field inclination in the LRF (lower right). The pink iso-contour outlines the umbral boundary using a threshold of 50% of the quiet-Sun intensity. The three pink boxes in the G-band intensity maps mark the regions studied in detail. The maps have been rotated according to the solar north-south direction. The temporal evolution is available **online**.

the bottom maps of Fig. 6.1 (B and γ_{LRF}), the magnetic boundary oriented towards the disc centre is sharper than the magnetic boundary oriented towards the solar limb (i.e. the magnetic radial gradient at the umbral boundary is larger at the centre side than at the limb side). Figure 6.2 illustrates how the projection of the magnetopause on the quiet-Sun regions induces a larger magnetic gradient at the centre side of the umbral boundary, while it induces a smaller magnetic gradient at the limb side, which translates into a sharper magnetic boundary at the centre side of the spot. We note that this is a simplified sketch where the complex nature of the magnetopause is not shown and the line formation region, spot size, and Wilson depression are not to scale.

In the following three subsections, we identify three distinct types of magneto-convection: a bi-directional flow in elongated granules located at the centre side of the spot, a transient filament with counter-Evershed flow, and a granular pattern located at the limb side. All of them are followed by the formation of the penumbra and the onset of the Evershed flow.

6.3.1 Bi-directional flow in elongated granules

On the centre-side region of the protospot, the penumbra starts to form at approximately 9:20 UT (i.e. some 50 min after the start of our observations). In Fig. 6.3, we show a 2 h time slice of a 5 pixel-wide selected region from 08:32 UT until 10:30 UT for intensity, inclination, field strength, and LOS velocity.

The time slice shows that from the start of the observations and for about 50 min, the velocity in the selected region at the very outskirts of the umbra is characterised by

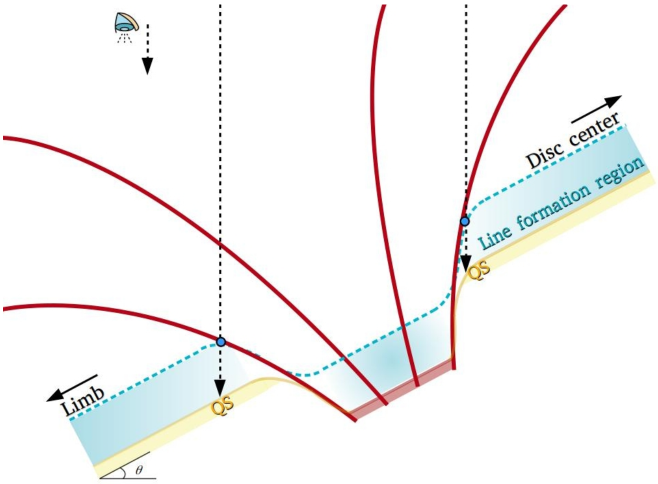

Figure 6.2 Sketch of the projection effects on the derived magnetic properties around a spot at $\theta = 28°$. The influence of the magnetopause (i.e. the most external red lines) on the derived magnetic properties reaches areas farther away from the umbral boundary at the limb side compared to the centre side.

a persistent redshift-blueshift pattern (i.e. the flow is directed towards the umbra in its close vicinity and outwards further out). This bi-directional velocity pattern occurs in regions with weak magnetic fields of less than 500 G. Only the innermost end of the redshifted region is rooted in regions with 1000 G field strength inside the umbra, as seen in the continuum intensity slices. The time slice shows that before the penumbra sets in, the (radial) red-blue pattern is associated with inclinations that go from positive polarity (blue-green) to horizontal (yellow) to opposite polarity (orange-red). The G-band intensity images show that the bi-directional flow pattern is associated with one intensity structure that resembles an elongated granule. The mean intensity of this granule is comparable to the quiet-Sun intensity.

We note that in the region under study, the LOS inclination of the magnetic field is around 30° and towards the centre of the solar disc. The strong magnetic field observed close to the umbral boundary is part of the magnetic body of the spot. Further away from the umbral boundary, the LOS does not cross the magnetic canopy of the protospot, as illustrated in Fig. 6.2 (centre side), and thus we observe the actual magnetic field configuration of the bi-directional flow pattern.

From about 9:10 UT onward, the red-blue patch is displaced away from the umbra, and the displacement increases in time. The reason for this displacement is the formation of a new convective cell featuring an outwards-oriented plasma motion (blueshifted region) that is initially most visible in the G-band continuum images as faint, bright filaments that do not have a strong enough LOS flow to be encircled by the red contour (i.e. $-130\ \mathrm{m\,s^{-1}}$). This outwards flow can be considered the first appearance of the Evershed flow. As time progresses, the length of the region occupied by the incipient Evershed flow expands. In the continuum intensity slices, one can see multiple bright structures whose inner footpoint, which is also the brightest, moves inwards into the umbra in a manner similar to penumbral grains in stable penumbrae (e.g. Sobotka et al., 1999a). From the intensity time slices it becomes obvious that the forming penumbra with Evershed flow does not heat the solar surface as effectively as the convection pattern characterised by the bi-directional flow. The mean G-band intensity in the forming penumbra decreases to 70 % of the quiet-Sun intensity ($0.7\,I_{\mathrm{QS}}$). This value is comparable to the average penumbral intensity measured in fully developed sunspot penumbrae.

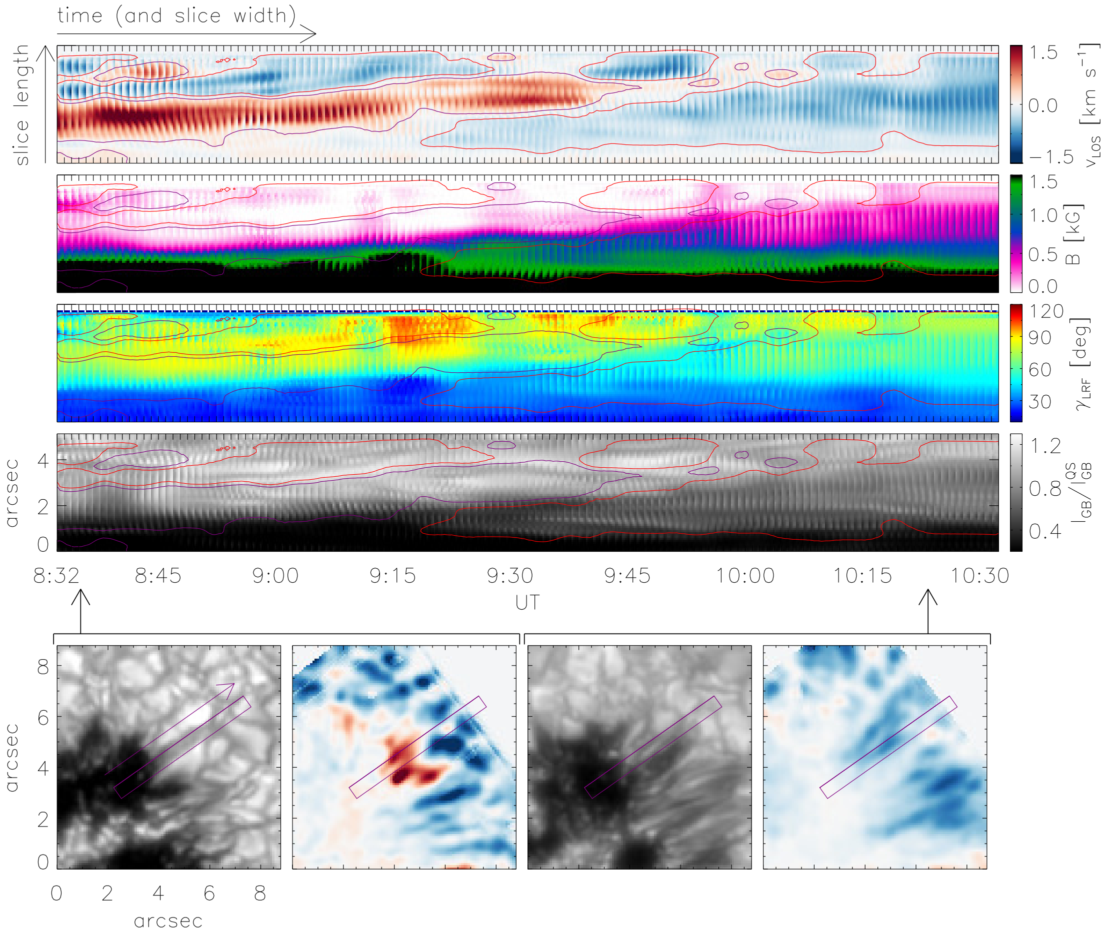

Figure 6.3 Bi-directional flow in elongated granules. Top panels: Time slices of selected penumbra-formation region on the sunspot centre side. From top to bottom: LOS velocities, magnetic field strength, inclination (LRF), and G-band intensity. Bottom panels: Context maps containing the areas (marked by purple boxes) selected for the time slices as seen in the G-band intensity and LOS velocity at 8:35 UT (two left panels) and at 10:24 UT (two right panels). The violet arrow points the direction along the slice length. The purple and red iso-contours highlight velocities of ±130 $\mathrm{m\,s^{-1}}$, respectively.

Along with the expansion of the region occupied by the Evershed flow, we observed an expansion of the region with a strong magnetic field. The initially sharp gradient of the magnetic field strength at the protospot boundary became more diffuse. At the end of the analysed period, the magnetic field strength increased to approximately 600 G at the outer edge of the slice. A similar trend was also observed for the magnetic field inclination and can be explained by the expansion of the magnetic field that is associated with the penumbra formation. In the beginning, we had a sharp boundary between the nearly vertical magnetic field at the protospot boundary and the horizontal field in the weakly magnetised bi-directional flow patch. Later on, we found LRF inclinations around 80° at the end of the slice, and such values are comparable to those found at the outer penumbral boundaries of stable sunspots.

6.3.2 Transient filament with counter-Evershed flow

On the limb-side boundary of the protospot, we observed one clear example of the formation of a transient filament carrying a counter-Evershed flow. In Fig. 6.4, we show the time slice evolution of this region. We note that the LOS inclination in this region is around 70° and points towards the limb. Therefore, the magnetic boundary of the

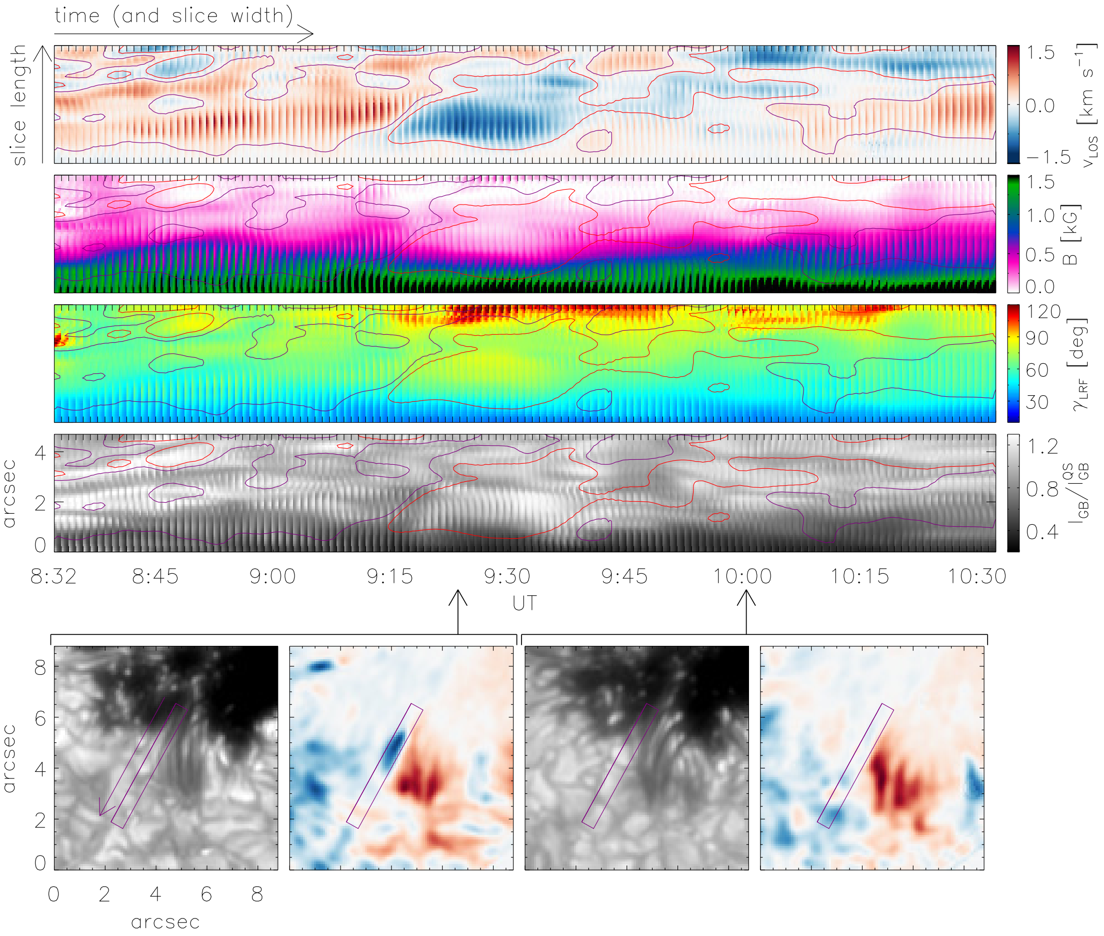

Figure 6.4 Analogous to Fig. 6.3 but showing the limb-side region where a transient filament with a counter-Evershed flow formed. The bottom panels correspond to observations at 9:23 UT (two left panels) and at 10:01 UT (two right panels).

protospot is not as sharp as on the centre side, and our results are influenced by looking through the magnetic canopy of the protospot. Also, the viewing angle is such that upflows located at the penumbral bright grains are seen as blueshifts, and a regular Evershed flow is therefore not represented only by redshifts.

Prior to the formation of the transient filament, we observed within the slice an edge of the region with a formed penumbra. The innermost part of the penumbra had intensities around 0.7 I_{QS}, but the second row of penumbral bright grains (located around 2″of the slice length) reached intensities around I_{QS}. As mentioned before, at this location, the bright grains are associated with blueshifts; these blue patches are visible until 8:52 UT. The magnetic boundary of the protospot was diffuse due to the presence of the penumbra, while the magnetic field strength and inclination steadily decreased and increased along the slice, respectively.

Around 9:18 UT, a filament with counter-Evershed flow developed. Within 10 minutes, it reached its full length and maximum LOS velocity and then decayed for approximately 15 minutes. It reached its maximum continuum intensity in later stages, around 9:34 UT. Its formation can also be identified in the time-slice plots of the magnetic field strength and inclination. The magnetic field is weaker and more horizontal than that of regular penumbra observed before and afterward. A similar behaviour has been reported for some of the cases in a statistical study of counter-Evershed flows by Castellanos Durán et al. (2021). After the disappearance of the transient filament, we observed a similar magnetic field configuration as before its formation. There are no strong LOS velocities observed, as the LOS inclination is close to 90° within the slice. We note that the Evershed flow observed before 9:12 UT is associated with LRF inclinations around 60°, and such inclinations are not found within the slice between minutes 9:42 UT and 10:02 UT. Starting at 9:52 UT, we observed weak blueshifts associated with bright penumbral grains of very short penumbral filaments that have LOS inclinations close to 90°. After 10:02 UT, the filaments became longer and more inclined, so the redshifted regions associated with Evershed flow appeared. As in the case of 6.3.1, we observed steady lengthening of the filaments carrying the Evershed flow in time.

6.3.3 Granular pattern

On a different segment of the limb-side boundary of the protospot, we analysed the granular pattern that precedes the formation of the Evershed flow. The evolution of this region is shown in Fig. 6.5. As in the case of 6.3.2, we were looking through the magnetic canopy of the protospot, and the physical parameters resulting from the inversion are influenced by this.

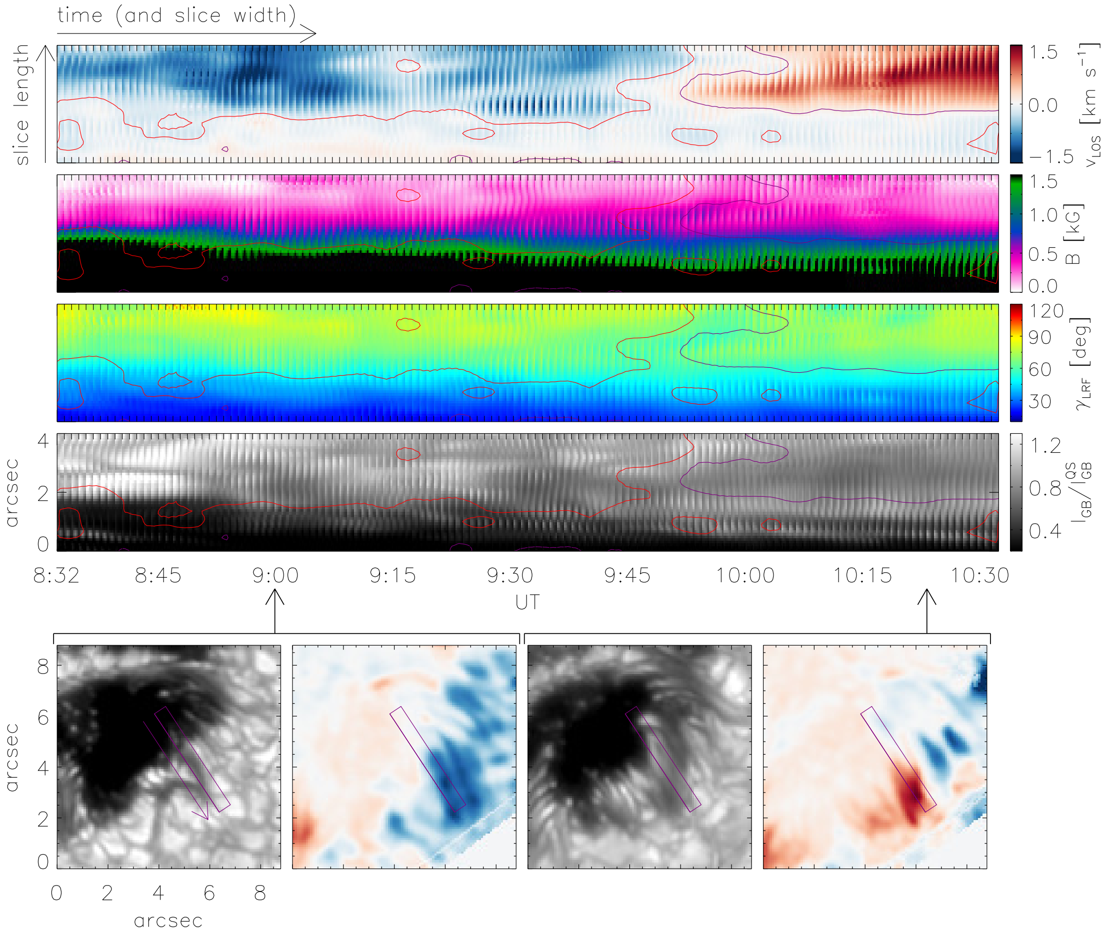

Figure 6.5 Analogous to Fig. 6.3 but showing the limb-side region where the granular pattern was observed before the penumbra formation. The bottom panels correspond to observations at 9:00 UT (two left panels) and at 10:24 UT (two right panels).

At the displayed segment of the protospot boundary, in the continuum intensity maps we observed for the first 80 minutes granular patterns with granules smaller than those observed in the quiet-Sun regions. Despite being smaller, the mean intensity is comparable to the I_{QS}. During this time, we observed blueshifts. The structure of the LOS motions does not correspond to the granular pattern seen in the continuum intensity. In the dopplergram, the motions have a filamentary structure, and their lifetimes are longer than those of granular upflows. Such flows would correspond to the counter-Evershed flow described in Sect. 6.3.2.

During the two studied hours, we did not detect any significant nor sudden changes in the configuration of the magnetic field along the slice in Fig. 6.5. The gradients of the magnetic field strength and inclination along the slice length steadily decreased in time. During the first 80 minutes until 9:52 UT, we did not detect any filaments with Evershed flows represented by redshifts. However, during the whole two hours, we observed short filaments on the protospot boundary that moved inwards and contained weak blueshifts. As explained in Sect. 6.3.2, these can be associated with upflows located in bright grains of such short filaments, where the outflow motion characterising the Evershed flow cannot be detected due to the viewing angle.

The filaments carrying the Evershed flow started to be apparent in the intensity slices around 09:44 UT as bright structures. We could not detect any LOS velocity due to the viewing angle. As the filaments lengthened in time, we started to detect redshifted LOS velocities around 09:52 UT in parts of the filaments where the flow is horizontal and oriented towards the limb side. It is noteworthy that the Evershed flow sets in rapidly, within five to ten minutes. Until the end of the analysed period, the filaments lengthened and the Evershed flow became stronger.

6.4 Discussion and conclusions

We have identified three distinct types of magneto-convection-related motions prior to penumbra formation. These have been reported previously in other solar contexts unrelated to penumbra formation.

The bi-directional flows observed on the centre side and contained in one elongated granule, as seen in the intensity maps, resemble in many aspects the flux emergence event described in detail by Centeno et al. (2017). In the case of the flux emergence described by Centeno et al. (2017), the transversal magnetic field strength reached a maximum of 800 G. In our case, the horizontal field component is, at maximum, around 200 G. Higher field strength values can be found at the footpoints of the flow pattern, but the inner footpoint is influenced by the magnetic canopy of the protospot (see Fig. 6.2), and the outer footpoint is situated in the vicinity of another patch of positive polarity. In our case, the bright elongated granule is not as long and thin as in the case described by Centeno et al. (2017). Based on this comparison and on the observations of orphan penumbra, where the horizontal field component is even higher (above 1000 G; Jurčák et al., 2014b) and where intensity structures are visually comparable to penumbral filaments, we surmise that the horizontal component of the magnetic field determines the width and length of the convective cell.

Counter-Evershed flows have already been reported on the boundaries of the studied protospot by Schlichenmaier et al. (2011). There are other studies that have described observations of counter-Evershed flows in penumbra since then (Louis et al., 2014; Siu-Tapia et al., 2017). The recent statistical analysis of Castellanos Durán et al. (2021) shows that counter-Evershed flows are common phenomena in the majority of active regions, although they are more frequently observed when the filaments carrying the counter-Evershed flow are related to sunspot light bridges (see also Kleint et al., 2013; Louis et al., 2020). However, the typical lifetimes found by Castellanos Durán et al. (2021) are significantly longer (most commonly around 7 hours) than the case studied in Sect. 6.3.2. Similar lifetimes in counter-Evershed flows have been found in sunspot MHD simulations (i.e. of a few hours) by Siu-Tapia et al. (2018). The big disparity between the counter-Evershed flow found in Sect. 6.3.2 that lasts only approximately

30 minutes and the observed and simulated inflows that last a few hours suggests that the penumbral formation process may benefit from the existence of short-lived counter-Evershed flows. Based on a more detailed analysis of the counter-Evershed flows reported by Schlichenmaier et al. (2011) at the centre side of the spot, we found that they actually correspond to the inner end of a bi-directional flow pattern.

It is well known that the magnetic boundaries of pores exceed those defined by intensity (Keppens et al., 1996) and that the size of the granules is influenced by the magnetic field strength (Hirzberger et al., 2002; Lagg et al., 2014; Jurčák et al., 2017b; Vigeesh et al., 2017). Therefore, it is common to observe small granules near the boundaries of pores and protospots. Moreover, Falco et al. (2017) showed that the effects of strong magnetic fields on inhibiting the convection are visible in the granules observed in light bridges and in umbral dots, where granular sizes are smaller than those reported in quiet-Sun regions and their mean continuum intensity is darker than in quiet-Sun granules. Yet granules spanning from small to quiet-Sun-like sizes are observed in plage regions with mean magnetic fields weaker than 700 G and quiet-Sun-like mean continuum intensities. As shown in Jurčák et al. (2017b), the intensity of granules is not influenced significantly by the magnetic field strength. We observed small but bright granules in regions with magnetic field strengths from 200 G to 700 G, depending on the distance from the protospot boundary, and with LRF inclinations of around 70° (the retrieved values are influenced by the LOS crossing the magnetic field canopy of the protospot; see Fig. 6.2). Thus, the horizontal component is not strong enough (yet) to shape the granules into more elongated convective cells. However, LOS velocity maps of the same regions show a filamentary blueshifted structure that does not match a typical granular motion. The disagreement between the granular structure and the filamentary flow is possibly caused by the height difference between the formation regions of the continuum intensity and the Fe I line. The lack of significant or sudden changes in the configuration of the magnetic field during the convective transformation from small granules to penumbral filament might be a combination of the effects of the LOS crossing the magnetic field canopy and the viewing angle.

Irrespective of the location where we observed the initial phases of the penumbra formation, the process always follows a similar pattern. We note that due to the viewing angle and LOS effects, the situation is best seen in Fig. 6.3, where the LOS is well aligned with the magnetic field on the umbral boundary, and we thus detected very weak flows along magnetic field lines. On the other hand, on the limb side, the LOS is close to being perpendicular to the magnetic field orientation, and the LOS velocities are thus hard to detect.

The process of penumbra formation starts within umbral areas with vertical fields below the critical threshold (Jurčák et al., 2015) and the appearance of short, bright filaments. Schmassmann et al. (2021) has described the role of vertical fields in the inhibition of vigorous modes of magneto-convection in umbrae. These filaments carry weak flows oriented outwards, and the bright penumbral grains (heads) of these filaments move further into the umbra. As time progresses, the newly appearing filaments become longer and extend radially from the original location of the umbra–quiet-Sun boundary. Thus the sunspot expands to become larger in size. To some extent, the umbra-penumbra boundary also moves inwards to the umbra, as explained in Jurčák et al. (2015). As the penumbra forms, the radial gradient of the magnetic field strength and inclination decreases, eventually reaching values typically observed in stable sunspots (i.e. field strength and inclination around 2500 G and 30°, respectively, on the inner penumbral boundary and around 600 G and 70° on the outer penumbral boundary).

The initial appearance of the penumbral filaments can be explained by the MHD simulation of Rempel (2011), which describes how the mass loading along inclined field lines bends the magnetic field and creates filaments. The length of the filaments is given by the magnetic field inclination, so the more inclined the field initially is, the longer are the filaments that can be produced. However, it has not yet been observed if the actual process of filament formation is identical to this scenario. It is also possible that the short filaments are created by small-scale flux emergence in which the horizontal field is carried up to the photosphere by convective motions, as obtained with a numerical model of a forming sunspot by Chen et al. (2017). Yet, these authors found that most of the penumbral filaments form in the flux emergence region, while we find that the penumbral filaments mostly form in the other side of the spot. The main difference between these scenarios is that in the simulations, the penumbral filaments form from the pre-existing field, while in the second scenario, the penumbral filaments form due to additional flux emergence. Only in the case of the first scenario would we observe the re-emergence of the bent field lines (sea-serpent configuration). Given the complex configuration of the sunspot magnetic field, we cannot be sure if such a sea-serpent structure is indeed related to the re-emergence of the field lines that were bent by the mass loading or if it is just an emerging flux loop and part of the so-called background magnetic field that is observed around filaments everywhere in sunspot penumbra. We note that we are comparing the observations of forming filaments in a developing penumbra to the Rempel (2011) MHD simulation of filaments in a stable penumbra.

According to Rempel (2011), Evershed flows develop from the deflection of the (convective) upflow into a radial outflow by the action of Lorentz forces in a thin layer right below the $\tau = 1$ surface. We surmise that in the observations presented here, the bi-directional flows result from the elongation of (magneto-) convective cells by horizontal fields building up at the outskirts of the protospot. At this stage, the Lorentz force is not strong enough to drive an Evershed flow. During the following flux accumulation process (Rezaei et al., 2012), the horizontal fields develop the necessary gradient (with height) to develop a Lorentz force that eventually deflects the emerging upflows into an Evershed flow.

We find that the Evershed flow onsets in the umbra, and as it develops, it expands outwards into actual penumbral filaments. Physical conditions allowing for bi-directional flows and their evolution into Evershed flows will be investigated in future sunspot simulations.

Acknowledgements:

This work was supported by the Czech-German common grant, funded by the Czech Science Foundation under the project 23-07633K and by the Deutsche Forschungsgemeinschaft under the project BE 5771/3-1 (eBer-23-13412), and the institutional support ASU:67985815 of the Czech Academy of Sciences. The Vacuum Tower Telescope is operated by the Leibniz-Institut für Sonnenphysik (KIS) in Freiburg, at the Spanish Observatorio del Teide of the Instituto de Astrofísica de Canarias.

7 Summary and conclusions

After the first hints about the invariability of the B_{ver} along the UP boundary of a stable sunspot performed by Jurčák (2011), several studies have focused on the analysis of UP boundaries of stable, forming and decaying sunspots (e.g. Jurčák et al., 2015; Jurčák et al., 2017a; Benko et al., 2018; Jurčák et al., 2018b; Schmassmann et al., 2018; Jurčák et al., 2020; Schmassmann et al., 2021). The interpretation of the obtained results has led to an empirical law that serves as a stability criterion: umbral areas with $B_{\mathrm{ver}} > B_{\mathrm{ver}}^{\mathrm{crit}}$ are stable, whereas areas with $B_{\mathrm{ver}} < B_{\mathrm{ver}}^{\mathrm{crit}}$ are unstable and prone to vanish against other more vigorous modes of magnetoconvection.

Pores, often merely defined as umbrae without surrounding penumbrae, are apparently simple magnetic structures that may hide more complex evolutions. While regular pores never develop a penumbra, some pores grow a penumbra and transform into a sunspot. Conversely, some umbrae lose their penumbra and remain as naked spots. Due to the similar magnetoconvective modes observed in pores and in umbrae, and to the obvious evolutionary inter-connection between these types of spots, in this PhD thesis, we aimed to investigate the stabilising role of B_{ver} against other modes of magnetoconvection in pores (regular pores and naked spots).

In the paper reproduced in Chapter 4, we analysed the magnetic properties averaged along the boundary of an evolving pore using HMI data corrected for scattered light ($\mathrm{HMI}_{\mathrm{dcon}}$). The pore's evolution was divided into four phases: Formation I, Stability, Formation II and Decay. From this work we can conclude that:

- **$\mathbf{B}_{\mathrm{ver}}$ evolves similarly in pores and in umbrae**: During the formation, the B_{ver} on the boundary of the pore strengthens until it reaches a maximum value. During the Stability phase, B_{ver} oscillates around this maximum value, but the emergence of weaker and more horizontal new flux decreases the B_{ver}. As previously observed in sunspots, the inclination gets more vertical during the Decay, hence showing an increase of the B_{ver}.

- **The pore exhibits a $\mathbf{B}_{\mathrm{ver}}^{\mathbf{crit}}$**: Analogous to sunspots, the B_{ver} value averaged during the Stability phase serves as a $B_{\mathrm{ver}}^{\mathrm{crit}}$ that defines the sectors that are more stable. In this case, pore regions with B_{ver}>1731 G are more stable and last longer while regions with B_{ver}<1731 G are divided by a light bridge and decay faster against granulation.

- **B behaves similar to $\mathbf{B}_{\mathrm{ver}}$**: In this pore, B and B_{ver} show similar behaviours. We define, following the same method, a B_{crit}=1921 G. We cannot uniquely identify B_{ver} as the stabiliser factor.

- **The area decays in a two-stage linear decay**: The whole decay process is linear, however, the decaying rates are substantially different with time. During the initial, slow decay only regions with $B_{\mathrm{ver}}<B_{\mathrm{ver}}^{\mathrm{crit}}$ decay while regions encircled by a $B_{\mathrm{ver}}=B_{\mathrm{ver}}^{\mathrm{crit}}$ threshold remain of the same size. After a period without observations, a fast decay that leads to the disappearance of the pore begins. During this stage, the areas of the pore defined by $B_{\mathrm{ver}}=B_{\mathrm{ver}}^{\mathrm{crit}}$ and by I_{c}=0.5continuum intensity of the local Quiet Sun (I_{QS}) are almost identical.

In the paper reproduced in Chapter 5, we aimed to inspect whether pores and naked spots have analogous magnetic behaviour on their boundary and whether the decay of a sunspot that leads to naked spots is comparable to the decay of a sunspot that quickly dissipates after losing its penumbra. For this purpose, we analysed $\mathrm{HMI}_{\mathrm{dcon}}$ data of a decaying sunspot that turned into naked spots during ~ 5 days. From this part of the paper, we conclude that:

- **The area decays in a two-stage linear decay**. Similar to the case of the pore discussed above, the umbral area decays linearly and in two stages: a slow decay followed by a fast decay. In this case, the fast decay corresponds to the late stages of penumbral dissipation. The umbral Φ decays with the same tendency.
- **Penumbral and umbral decaying processes are different**. Penumbra decays linearly, but only in one stage. The areal and magnetic flux decay rates do not change with time.
- **The inclination only increases during the fast decay**. During sunspot decay, γ tends to get more vertical. However, we do not see any increase in γ until the fast decay. The compensation between the weakening of B and the verticality of γ leads to an almost invariable B_{ver}.
- **Penumbra provides stability to the magnetic properties**. In the presence of a penumbra, magnetic properties tend to change smoothly. However, in the absence of a penumbra, small changes in the area of the naked spots have a large effect on the magnetic fields. Nonetheless, B and B_{ver} are always weaker than the critical values retrieved in the aforementioned pore.
- **$\mathbf{B}_{\mathrm{ver}}$ evolve similarly in naked spots and pores**. As seen in the pore, increases in the naked spots area translate into weakening of the magnetic fields on the boundary. Conversely, B_{ver} tends to strengthen in decreasing or non-variable areas. Also, the strongest values of B_{ver} appear during the naked spot stage.
- **There is a delay between the shrink of the umbral area and the areas encircled by a $\mathbf{B}_{\mathrm{ver}}$ threshold**. We find hints of a 3.5 h delay between the decay of the photometric umbra and the magnetic trunk. The correlations are however influenced by the two umbral cores not decaying synchronously.

The transition from sunspots to naked spots occurred during the transit of the spots across the solar disc. Since SP/Hinode also followed this AR during the whole transit, we compared the magnetic properties obtained from SP/Hinode, HMI and $\mathrm{HMI}_{\mathrm{dcon}}$ datasets. With this study, also included in the paper reproduced in Chatper 5, we aimed to investigate the intrinsic differences between the datasets previously used to study the stabilising factor of B_{ver} on sunspots and pores and to clarify the variety of values obtained. Our main conclusions are:

- **$\mathbf{B}_{\mathrm{ver}}$ is the most reliable threshold**. While magnetic fields have a good one-to-one correspondence between datasets, B_{ver} has the best. The typically used I_{c} is proven to fall at different regions of the spot for different instruments. Of all the data, I_{c} has the worst consistency between all datasets.
- **$\mathbf{HMI}_{\mathbf{dcon}}$ and SP maps are the best datasets to study pore boundaries.** Regular HMI maps are very contaminated by scattered light. The effect is not so severe in the case of UP boundaries, but it is acute in the case of pores, where the boundaries are contaminated by the surrounding granulation light.
- **$\mathbf{HMI}_{\mathbf{dcon}}$ retrieves the darkest I_{c} and the strongest B**. Therefore, the $B_{\mathrm{ver}}^{\mathrm{crit}}$ derived at the evolutionary pore is not comparable to the $B_{\mathrm{ver}}^{\mathrm{crit}}$ values observed in stable sunspots.

- **$\mathbf{B}_{\text{ver}}^{\text{crit}}$ derived from HMI and SP/Hinode are comparable**. The discrepancy between the $B_{\text{ver}}^{\text{crit}}$ values obtained by Jurčák et al. (2018b) with SP/Hinode observations and by Schmassmann et al. (2018) with HMI observations is consistent with the intrinsic instrumental and methodological differences found in the sunspot phase of the analysis.

Finally, we studied the development of penumbral filaments in a proto-spot from ground-based spectropolarimetric observations recorded by GFPI/VTT in July 2009. By selecting sections that developed penumbral filaments at different locations of the spot (centre- and limb-side) we can conclude that:

- **Penumbral filaments form in different types of magnetoconvection**. Penumbral filaments do not need a specific initial type of magnetoconvection to set it. In this study, they form in a bi-directional flow embedded in an elongated granule, in the location of a previous transient filament with counter-Evershed flow, and in a granular region with filamentary motions.
- **Penumbral filaments are formed close to the boundary and expand radially outwards**. Independently of the previously existing flows, penumbral filaments form close to the umbra, where $B_{\text{ver}} < B_{\text{ver}}^{\text{crit}}$, and expand radially.
- **The Evershed flow sets in rapidly**. As soon as the penumbral filament appears, the Evershed flow is visible.

In conclusion, the research presented in this thesis successfully meets the objectives of the PhD work. We have identified significant interconnections between the evolutions of umbrae and pores and found evidence suggesting the presence of a $B_{\text{ver}}^{\text{crit}}$ in pores. Although investigating the transition between modes of magnetoconvection is complex, we have demonstrated the diverse initial conditions that result in the formation of penumbral filaments. Additionally, this PhD thesis has led to other interesting results not mentioned here, such as the work on flare continuum enhancement included in the Appendix A.

Prospects include further ground-based campaigns, with the hope that the proximity to the solar maximum will raise the chances of recording interesting observations of the transformation between different types of magnetoconvection. Moreover, the very rich archive of data that HMI has provided during the last years will allow us to run systematic statistical analyses of different parameters on the boundary of evolving pores.

Appendix

A Flare heating of the chromosphere: Observations of flare continuum from GREGOR and IRIS

Reproduction of García-Rivas et al. (2024c)
Submitted to *Astronomy & Astrophysics*

Received 24 June 2024

Authors:
M. García-Rivas[1,2], J. Kašparová[1], A. Berlicki[1,3], M. Švanda[1,2], J. Dudík[1], D. Čtvrtečka[4], M. Zapiór[1], W. Liu[1], M. Sobotka[1], M. Pavelková[1], and G. G. Motorina[1,5]

Affiliations:
[1]Astronomical Institute of the Czech Academy of Sciences, Fričova 298, 251 65 Ondřejov, Czech Republic
[2] Astronomical Institute, Faculty of Mathematics and Physics, Charles University, V Holešovičkách 2, 180 00 Prague, Czech Republic
[3] Center of Scientific Excellence - Solar and Stellar Activity, University of Wrocław, Mikołaja Kopernika 11, 51-622 Wrocław, Poland
[4] Christian Doppler Grammar School, Zborovská 621/45, 150 00 Prague, Czech Republic
[5] Central Astronomical Observatory at Pulkovo of Russian Academy of Sciences, St. Petersburg, 196140, Russia

ABSTRACT

Context: On 2022 May 4 a M5.7 flare erupted in the active region NOAA 13004, which was the target of a coordinated campaign between GREGOR, IRIS, Hinode, and ground-based instruments at the Ondřejov observatory. A flare kernel located at the edge of a pore was co-observed by IRIS slit and GREGOR HiFI+ imagers.

Aims: We investigated the flare continuum enhancement at different wavelength ranges in order to derive the temperature of the chromospheric layer heated during the flare.

Methods: All datasets were aligned to IRIS slit-jaw images. We selected a pixel along IRIS slit where the flare kernel was captured and evaluated multi-wavelength lightcurves within it. We defined a narrow IRIS NUV band that comprises only continuum emission. The method, which assumes that the flare continuum enhancement is due to optically thin emission from hydrogen recombination processes, was applied to obtain a lower limit on the temperature in the layer where the continuum enhancement was formed.

Results: We determined a lower limit on the temperature and its time evolution in the chromospheric layer heated during the flare in the range of $(3–15)\times10^3$ K. The mean electron density in that layer was estimated to be $\sim 1 \times 10^{13}$ cm^{-3}.

Conclusions: Multi-wavelength flare co-observations are a rich source of diagnostics. Due to the rapidly evolving nature of flares, the sit-and-stare mode is key to achieving a high temporal cadence that allows us to analyse the same flare structure thoroughly.

—

Key words. Sun: flares - Sun: UV radiation - Sun: Atmosphere - Sun: Chromosphere - Sun: X-rays, gamma rays

A.1 Introduction

Solar flares (Fletcher et al., 2011) represent the most energetic processes within the solar system and are a consequence of the solar magnetic activity. The energy released by magnetic reconnection in solar flares is converted to other forms of energy, such as acceleration of charged particles, bulk plasma heating, plasma motions that include coronal mass ejections, and others. Much of the released magnetic energy is deposited by beams of accelerated particles into the solar chromosphere, which is heated and evaporates (e.g., Young et al., 2013; Graham et al., 2015; Polito et al., 2016b), leading to the creation of hot (several ten million K) flare loops higher in the atmosphere, and bright flare ribbons at the chromospheric footpoints of the flare loops. These structures containing heated plasma then emit radiation in many portions of the electromagnetic spectrum (e.g., Fletcher et al., 2011). Since the energy deposit into the solar chromosphere by necessity precedes the creation of the hot flare loops, observations of the heating of the chromosphere are indispensable for understanding the energy release in solar flares.

Due to its relatively low temperatures around 10^4 K, the chromosphere contains large amounts of neutral hydrogen (e.g., Anzer et al., 2005; Leenaarts et al., 2007). The heating of the chromosphere can produce multiple well-known spectral lines as well as continuum emission. Although line emission in chromospheric or transition region lines is prominent during solar flares and can be enhanced by orders of magnitude, continuum emission also contributes significantly to the amount of energy radiated away, see for example indications from observations (Kretzschmar, 2011) and modelling (Allred et al., 2005).

Several mechanisms have been proposed for the enhancement of the continuum during solar flares, namely hydrogen bound-free and free-free transitions, Thomson scattering, and H^- emission (e.g., Heinzel et al., 2014; Heinzel et al., 2017). They emit in the wavelength range from near ultraviolet (NUV) to near infrared (IR). Each mechanism may dominate in different atmospheric layers, from the photosphere to the chromosphere.

These mechanisms require not only an increase of temperature in the emitting layers, but also an increase of electron density. Yet, it is still not fully understood which processes increase them. Some of the proposed processes are electron and/or proton bombardment, X-ray and extreme ultraviolet (XEUV) heating, or Alfvén wave dissipation (for discussion see e.g. Metcalf et al., 1990). Many continuum enhancements detected during flares show good temporal and spatial correlation with hard X-ray (HXR) footpoint emission (see e.g., Neidig et al., 1993; Fletcher et al., 2007; Martínez Oliveros et al., 2012; Xu et al., 2012; Milligan et al., 2014; Kleint et al., 2016; Kuhar et al., 2016). This suggests that the accelerated electrons that generate HXR emission and deposit their energy in the flare footpoints are also responsible for the continuum emission. However, this mechanism is probably not sufficient to explain the observed emission at 1.56 μm (Xu et al., 2006), which is considered to form at the opacity minimum below $\tau_{500} = 1$ in an undisturbed atmosphere (τ_{500} is the optical depth at 500 nm). The required energy of accelerated particles that reach and affect such deep layers is typically higher than the energy determined from their HXR emission (e.g., Fletcher et al., 2011). Additionally, non-LTE radiative transfer computations incorporated in flare modelling also show that the photosphere and the chromosphere can be radiatively coupled via photospheric heating by H^- absorption of the hydrogen Balmer continuum, which originates in the chromosphere. This back-warming then can lead to increased photospheric H^- radiation (e.g., Machado et al., 1989).

Dedicated modelling of solar flare radiation is required to disentangle the various mechanisms affecting continuum emission. Mauas et al. (1990) combined non-LTE modelling and observations of several photospheric and chromospheric lines together with the visible-light continuum and constructed a semi-empirical model of a solar flare atmosphere. The formation of UV, visible, and IR continua due to electron beam heating has been modelled to various degrees of agreement with observations for example by Ding et al. (1999), Ding et al. (2003), Cheng et al. (2010), and Simões et al. (2017).

Studies of the continuum during solar flares also need dedicated observations and data analyses. Continuum enhancements in the ultraviolet (UV) range have been reported from space-borne observations. Heinzel et al. (2014), R. Joshi et al. (2021a), and Kleint et al. (2016) identified NUV wavelength ranges observed by IRIS where continuum flare emission could be identified. These authors attributed the observed enhancements to hydrogen Balmer recombination. Similarly, Dominique et al. (2018) adopted the same assumption and analysed continuum UV flare emission detected by the PROBA-2 mission. Continuum emission and its enhancement in the optical range during strong and even weak solar flares has also been detected in filtergrams and spectral data, see for example Jess et al. (2008), Kerr et al. (2014), Potts et al. (2010), and Yurchyshyn et al. (2017). Furthermore, Heinzel et al. (2017) interpreted the off-limb flare emission in HMI/SDO pseudocontinuum as being dominated by the hydrogen Paschen recombination. Jurčák et al. (2018a) derived optical continuum enhancement from SOT/Hinode spectropolarimetric observations during a solar flare and proposed that it was caused by chromospheric emission.

In this work we present the initial analysis from a unique dataset obtained during a coordinated campaign between GREGOR telescope (campaign supported by SOLARNET), IRIS and Hinode (HOP 422) and instruments located at Ondřejov Observatory. For the first time, IRIS and GREGOR co-observed the preflare, impulsive and gradual phase of a solar flare. The current analysis is inspired by previous studies focused on UV and optical flare continuum enhancements. Our data are unique in UV wavelength coverage and temporal resolution that is provided by the full read-out of IRIS NUV high-resolution spectra with time resolution of 3 s. Sub-arcsecond co-spatial observations in several optical wavelengths obtained with the High-resolution Fast Imager (HiFI+) at GREGOR telescope complement the dataset.

In Sect. A.2 we describe the investigated data, and present multi-wavelength lightcurves of the flaring atmosphere in Sect. A.3. The flare continuum enhancements in optical and UV are defined in Sect. A.4. In Sect. A.5 we determine the lower limit on temperature in the flaring chromosphere above the edge of a pore by assuming that the continuum enhancement is mainly due to hydrogen recombination. Finally, the results are discussed and summarised in Sect. A.6 and A.7.

A.2 Data

A.2.1 The 2022 May 4 flare

On 2022 May 4, a confined M5.7-class flare occurred in a bipolar active region (AR) NOAA 13004 (Hale classification β/β), starting at about 08:45 UT (Fig. A.1a). This AR was quite active, producing four other C-class flares before the M-class one, including a C1.4 starting at 07:14 UT and C3.5 at 08:08 UT.

The M-class flare was well-observed using multiple ground-based and space-borne instruments (Fig. A.1). The ground-based instruments focused on the visible and

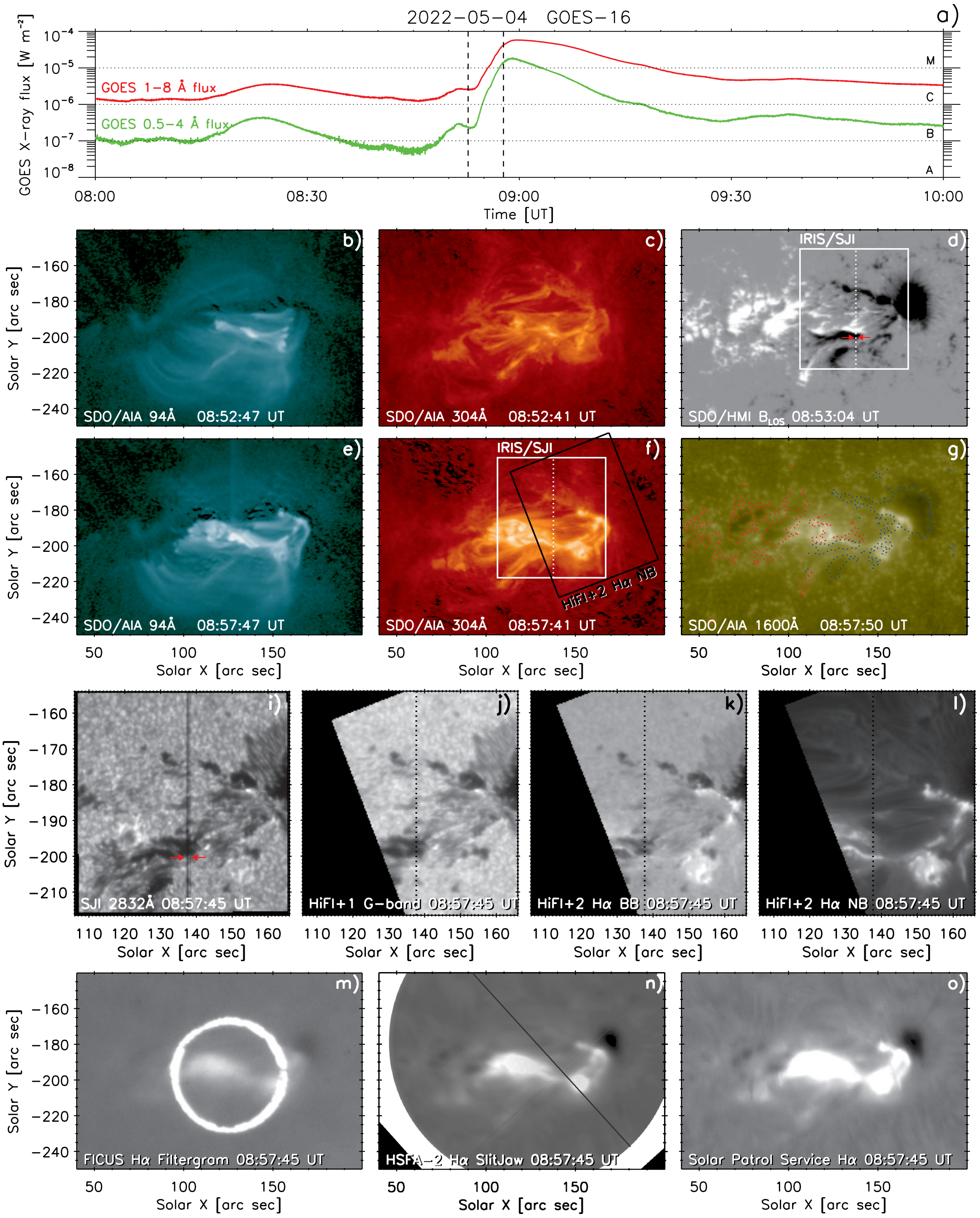

Figure A.1 Overview of the 2022 May 4 M5.7–class flare as observed by multiple instruments. Panel a) shows the GOES X-ray lightcurve of the flare. Panels b)–g) show the context SDO/AIA and SDO/HMI observations at 08:52:45 and 08:57:45 UT, denoted by vertical lines in panel a). Panel g) includes the contours of the positive/negative (red/blue) polarities from panel d). The FOVs of HiFI+2 and IRIS/SJI instruments are indicated in panel f) (only IRIS/SJI FOV in panel d), and the corresponding observations are shown in panels i)–l) with the location of the IRIS slit indicated and the HiFI+ images resampled to IRIS resolution and FOV. The red arrows in panels d) and i) point at the location of the studied pixel No. 53. Ondřejov ground-based observations from the spectrographs FICUS and HSFA-2, and the SPS are shown in panels m)–o), respectively. The black line in panel n) indicates the HSFA-2 slit position. Animations of the AIA, IRIS, and GREGOR imagers (panels e)– l)) are available **online**.

infrared portion of the spectrum, and included the GREGOR solar telescope (W. Schmidt et al., 2012) located in Tenerife (Spain), as well as the spectrographs HSFA-2 (Zapiór et al., 2022), FICUS (Kotrč et al., 2016), and the Solar Patrol Service located at the Astronomical Institute of the Czech Academy of Sciences (Ondřejov, Czech Republic). The space-borne instruments included the Atmospheric Imaging Assembly (AIA; Lemen et al., 2012) and Helioseismic and Magnetic Imager (HMI; Scherrer et al., 2012), on board the Solar Dynamics Observatory (SDO; Pesnell et al., 2012), as well as the Interface Region Imaging Spectrograph (IRIS; De Pontieu et al., 2014). Additionally, GOES-16 satellite and Konus spectrometer (Aptekar et al., 1995) on board the Wind spacecraft (Harten et al., 1995) provided X-ray context information.

A.2.2 Context observations from SDO/AIA

AIA observes the Sun in 10 EUV and UV filters, spanning a large range of temperatures of the transition region, corona, and flares (O'Dwyer et al., 2010; Lemen et al., 2012; Del Zanna, 2013). We investigated the EUV (UV) data with full cadence of 12 s (24 s) during the interval 07:00–11:00 UT, covering the entire flare as well as few additional hours for context. The AIA data have a pixel scale of $0.6''\text{pixel}^{-1}$ and spatial resolution of $1.5''\text{pixel}^{-1}$ (Lemen et al., 2012). The data were calibrated to level 1.5 using the `aia_prep` routine in the IDL SolarSoft System (SSWIDL; Freeland et al., 1998). The stray light was deconvolved using the routine of Poduval et al. (2013) and the data were corrected for differential rotation of the Sun.

To study the flare evolution, we used the 94 Å passband, which under flare conditions is dominated by the emission of Fe XVIII because the hotter 131 Å passband (dominated by Fe XXI) is at times saturated. The 94 Å indicates that the flare is a confined flare (denominated Type I by T. Li et al., 2019; Duan et al., 2022). The flare emission consists of multiple hot flare loops (Fig. A.1b and A.1e). The system of hot flare loops grows in size during the period of about 08:47–09:10 UT. A peak of the X-ray flare as measured by GOES is reached at 08:58 UT (Fig. A.1a).

The corresponding ribbons are captured by the 304 Å and 1600 Å passbands of AIA (Fig. A.1c, A.1f, and A.1g). These passbands are dominated by transition-region emission of He II at 303.8 Å, and C IV 1550 Å doublet with many other chromospheric lines producing flare signal in the 1600 Å passband, as well as about 20% contribution of photospheric continua (Simões et al., 2019). The 1700 Å passband is dominated by a multitude of chromospheric lines, with some contributions of He II (see Fig. 6 of Simões et al., 2019). Finally, the 94 Å channel of AIA, which we use to identify the flare loops (Fig. A.1b and A.1e), is dominated by the Fe XVIII (O'Dwyer et al., 2010). As there are several systems of hot flaring loops, the structure of the ribbons is quite complex with some small-scale substructure.

Since AIA is a full-disc instrument with good pointing, we used it to determine the absolute solar coordinates of the datasets using the following procedure. First, the 171 Å channel of AIA is taken as reference, and other AIA passbands are aligned to it. This corrects for minor spatial shifts in passbands such as 304 Å. The 1600 Å and 1700 Å passbands, which dominantly show the solar photosphere and not transition region or corona, are aligned to 304 Å using the location of flare ribbons. IRIS/SJI data (see Sect. A.2.3) are aligned to AIA 1600 Å using the location of photospheric features such as pores and sunspots. Similarly, the Hα data from Ondřejov observatory (Sect. A.2.6) are also aligned to 304 Å and 1600 Å data, using the locations of ribbons, sunspots, and pores. In this manner, a co-aligned set of data from multiple instruments is obtained, with uncertainties below $0.6''$.

A.2.3 IRIS observations

On 2022 May 4, IRIS observed in sit-and-stare mode between 07:30 and 13:00 UT as part of the Hinode Operation Plan (HOP) 422 (OBSID ref. 3884855852). During the whole period of observations 5984 exposures were taken, with an approximate cadence of 3 s. In order to achieve a good temporal resolution we had to sacrifice spatial resolution in all datasets (×2 binning), and spectral resolution. IRIS provided high-resolution spectra in the NUV channel (×2 binning) and low-resolution spectra in the far-ultraviolet (FUV) channel (×8 binning) for all exposures. In this work we did not analyse the FUV spectra due to the low resolution and to the abundance of lines that hindered the study of the continuum.

The IRIS NUV channel spans from 2783.63 to 2835.11 Å, and it includes Mg II lines, their far wings, and the continuum at the longer wavelengths end of the spectral window. In full read-out the spectra contain 1012 wavelength points with an spectral sampling of 0.051 Å. The spatial coverage of the slit corresponds to the Y-size of slit-jaw images (SJI) ($62''$, 203 pixels) and gives a spatial sampling of around $0.3''\mathrm{pixel}^{-1}$. SJI are only available in the 2832 Å channel, with a field-of-view of $60'' \times 62''$and a pixel scale of $0.3''$. An example is presented in Fig. A.1i.

We converted the signal given in data number (DN) units to absolute energetic units ($\mathrm{erg\,s^{-1}\,cm^{-2}\,sr^{-1}\,Å^{-1}}$) in all NUV spectra using the IRIS radiometric calibration (see Appendix A.9).

An animation of the SJI 2832 Å frames (available **online**) shows a rather complex evolution and motion of pores and small sunspots while the bigger, leading sunspot kept a relatively stable position at the western edge of the SJI field of view (FOV). The ribbons started to be visible at 08:54 UT for few minutes and were located above sunspots umbrae and penumbrae.

The transmission function of the 2832 Å filter peaks in the longer-wavelength end of the NUV spectral range and covers mainly the far wings of Mg II lines where continuum dominates. However, many other weak lines, as well as the Mg II k line, can contribute significantly to the total signal in the SJI 2832 Å passband during flares (Kleint et al., 2017). Therefore, we considered the flare ribbons observed in this passband as regions in which continuum emission might be dominant but not the only contributor.

A.2.4 GREGOR observations

GREGOR observed the flaring region from 08:45 to 09:16 UT. The GREGOR Infrared Spectrograph (GRIS; Collados et al., 2012) started scanning the AR at 08:45 UT, but from 08:50 to 08:52 UT we re-adjusted the FOV and changed the observing mode. This was a period of a mediocre seeing (Fried parameter r_0 = 5–10 cm) but thanks to the GREGOR adaptive optics system (Berkefeld et al., 2012) the pointing was stable and the image quality acceptable. Both spectra and images of the flare were acquired.

The spectra were retrieved with a slit in sit-and-stare mode with GRIS set to the 1.08 μm wavelength band, which includes photospheric and chromospheric lines. Since GRIS slit was not co-spatial with IRIS slit at any point, GRIS spectral observations were not analysed here and were left for future work.

Images of the flare were recorded by the improved High-resolution Fast Imager (HiFI+; Denker et al., 2023) that is composed by three sets of two synchronised cameras. HiFI+1 contains two sCMOS cameras with a FOV of $70.7'' \times 59.6''$ and a pixel scale of $0.028''\mathrm{pixel}^{-1}$, plus interference filters with wavelength bands at G-band 4307 Å and blue continuum 4506 Å and passbands of 11 Å. HiFI+2 has two Imager M-lite 2M CMOS cameras with a FOV of $76.5'' \times 60.5''$ and a pixel scale of $0.050''\mathrm{pixel}^{-1}$, plus a broadband interference filter and narrowband Lyot filter with wavelength bands at

Hα 6563 Å and passbands of 7.5 and 0.6 Å respectively. HiFI+3 has two Imager M-lite 2M CMOS cameras with a FOV of $48.2'' \times 30.8''$ and $76.5'' \times 60.5''$ and pixel scales of $0.025''$pixel^{-1} and $0.050''$pixel^{-1} respectively, plus interference filters with wavelength bands at Ca II H 3968 Å and TiO molecular band 7058 Å and passbands of 9 and 11 Å, respectively. Examples of the HiFI+ observations in G-band, and Hα broad- and narrowbands are shown in Fig. A.1j, A.1k, and A.1l.

The CMOS and sCMOS cameras allow for a fast image acquisition rate: HiFI+1 recorded at 49 Hz, and HiFI+2 and HiFI+3 at 100 Hz. The exposure times were constant for HiFI+1 (G-band: 2 ms; blue continuum: 1 ms) and HiFI+3 (TiO: 0.5 ms). In order to avoid saturation, the exposure times were reduced from 9 ms to 7 ms at 08:56 UT for HiFI+2 (broad- and narrowband) and from 8 ms to 6 ms at 08:52 UT for HiFI+3 (Ca II H). Even though each of the HiFI+ cameras sets is controlled by a different computer temporally synchronised with a time server, we found a temporal delay of ~ 6.5 s in HiFI+3 images respect to HiFI+1 and HiFI+2. The analysis was done correcting for this delay.

The image were calibrated using the `sTools` image processing pipeline (Kuckein et al., 2017)[1] for the full extent of the HiFI+ acquisition rate capabilities, that is, no frame selection was done.

In order to carry out a co-spatial analysis of GREGOR and IRIS observations, HiFI+ images were aligned to the IRIS SJI frame closest in time using routines in the SSWIDL. First, HiFI+ images were smoothed with a Gaussian filter to mimic IRIS spatial resolution. Preliminary linear transformation parameters (P_0, Q_0; rotation, scale, and shift per coordinate) were retrieved by `caltrans.pro`, which used as an input reference points created with `setpts.pro`. Following, we masked the pixels with high signal caused by the flare (bright pixels), and the pixels where the slit was located in IRIS SJI. A final alignment was done by the SSW routine `auto_align_images.pro` in two runs. The initial run imported P_0, Q_0 and calculated the P_1, Q_1 that produced the minimum cross correlation between IRIS and HiFI+ images using the faster *Amoeba* minimization algorithm. The second run corrected HiFI+ images for warping, and employed the more robust Powell minimization algorithm (Press et al., 1992). In this way we obtained the aligned HiFI+ images together with the P_f, Q_f (final) transformation parameters.

Each HiFI+ image was aligned independently, except for the entirely chromospheric HiFI+2 narrowband images. These were transformed and rescaled to IRIS FOV by `poly_2d.pro`, which applied the P_f, Q_f parameters obtained from the synchronous HiFI+2 broadband images. As seen in Fig. A.1, HiFI+ images do not completely overlap IRIS SJI, however IRIS slit is completely covered by all the HiFI+ imagers, except for HiFI+3 (Ca II H).

A.2.5 SDO/HMI observations

The SDO/HMI synoptic observations were used to estimate the excess in the optical continuum, therefore we required a dataset that allowed to study the intensity in the continuum. The standard product capturing the intensity of the pseudo-continuum around the Fe I 6173 Å line is the I_c product available via JSOC[2] with a cadence of 45 s. This product results from the reconstruction of the spectral line from a non-trivial sequence of line scans in various light-polarisation states, and it is known not to represent the true continuum signal very well in solar flares (Švanda et al., 2018).

To overcome this issue, we used level 1 data, the filtergrams, which are available upon request from JSOC. HMI scans the iron line at six nominal positions. The filtergrams

---

[1] `gitlab.aip.de/cdenker/stools`

[2] `http://jsoc.stanford.edu`

were aligned to IRIS/SJI using the `reproject_to` routine from the SunPy Project (The SunPy Community et al., 2020). In the following we focused only to the outer positions, that is, those representing −172 mÅ and +172 mÅ shifts from the nominal spectral-line position. A continuum enhancement should be registered at all scan positions, therefore utilising the measurements far in the spectral-line wings allows us to separate the continuum enhancement from a possible brightening in the spectral line. Unfortunately, these filtergrams are not recorded simultaneously, their time stamps differ due to the sequence scan performed by HMI. To have pseudo-continuous series, we interpolated both filtergram series to a uniform series with a cadence of 30 s. Then, we averaged the blue-most and the red-most filtergrams to represent the evolution of the continuum.

A.2.6 Hα and spectral observations from Ondřejov

The flare was also observed by ground-based instruments located at the Ondřejov observatory. These include an Hα telescope and two spectrographs that operate in the visible and infra-red portions of the solar spectrum. These instruments supported the coordinated campaign of GREGOR and the HOP 422 by observing the same target regions.

The Solar Patrol Service (SPS) observes the Sun in the photospheric continuum and Hα line filters, both in two modes: full-disc and detail of a selected active region. On 2022 May 04, SPS observed the AR with an Hα filter using a 210mm f/16.3 achromatic refractor producing images with $0.44''$ plate scale and 1 s temporal cadence. As the observations are not in a final configuration and not yet flare-optimized, the flare ribbons in Hα SPS image can get saturated (see Fig. A.1o).

The Horizontal-Sonnen-Forschungs-Anlage-2 (HSFA-2, horizontal device for solar research) is a high-dispersion spectrograph. It simultaneously observes 5 spectral regions in high spectral resolution along with slit-jaw Hα images of the target region. The last upgrade was done in 2020. In the current setup it observes a FOV with a radius of $\sim 280''$. An example of a slit-jaw image taken during the campaign is shown in Fig. A.1n. The gray line indicates the slit position. More details about the spectrograph can be found in Zapiór et al. (2022) and Kotrč (2009).

The Flare Intensity Continuum Ultrawide Spectrograph (FICUS) is a new low-dispersion spectrograph based on a setup described by Kotrč et al. (2016). The instrument is now relocated to its own dedicated coelostat. The FICUS instrument provides spectra in the 3500-9300 Å wavelength range and Hα images of a selected region with a time resolution on a (sub)second timescale and a plate scale of about $0.5''$. The FICUS design employs an image selector and several circular diaphragms of varying aperture to select the observed area. An example of a context Hα image from FICUS is shown in Fig. A.1m. There, the area observed by the spectrograph is delimited by the bright white circular rim of the diaphragm, denoting the selected $61''$ aperture diameter.

The coalignment of the three Hα observations from Ondřejov was done manually, first the SPS with AIA 1600 Å and then FICUS and HSFA-2 with respect to SPS.

SPS data were of maximum importance during the GREGOR campaign, where observers benefited from the real-time SPS Hα full-disc and detail observations to choose an interesting target for GREGOR. Due to the not-yet optimized configuration of SPS, its data were not used for further analysis. Spectral data from HSFA-2 were not analysed in this work either, since the HSFA-2 slit did not cross the flare region captured by the IRIS slit. Preliminary analyses of FICUS spectra did not show any continuum flare enhancement probably due to the small portion of the flare area within FICUS FOV.

A.2.7 X-ray observations

During the impulsive phase the flare emission in the X-ray domain was only observed by GOES-16 satellite and Konus-Wind instrument. The Wind spacecraft orbits in interplanetary space (L1 Lagrange point), which provides a stable background for Konus omnidirectional observations. Konus detected hard X-ray emission in the 19 - 80 keV energy range (G1 channel) during the so-called waiting mode. Therefore, the data are available as a count rate lightcurve in the wide energy channel G1 with an accumulation time of 2.944 s (Lysenko et al., 2022).

A.3 Multi-wavelength evolution of a flare kernel

Our aim is to study the flare continuum enhancement by exploiting the high temporal cadence of HiFI+ and IRIS datasets and full read-out of the NUV spectra provided by IRIS. IRIS slit was positioned above the polarity inversion line of the AR and it crossed quiet-Sun regions, pores, and penumbral filaments. Gentle brightenings in the shape of flare ribbons were visible between 08:54 and 09:01 UT. The brightest parts of the flare ribbons were located out of the IRIS slit position (see Fig. A.1i). Nonetheless, there was a faint flare emission crossing the slit at around 08:57:30 UT. This emission occurred on the border of a pore, and it was located in the pixel No. 53 (counting from the bottom) along the slit. The position of pixel No. 53 is marked with red arrows in Fig. A.1i. We investigated the multi-wavelength temporal evolutions of this pixel in order to extract the flare continuum emission.

A.3.1 IRIS NUV bands

The maximum flare continuum enhancement on IRIS slit was reached at 08:57:45 UT. The corresponding spectra along IRIS slit are plotted in Fig. A.2. We can see spatially narrow enhanced emission at the position Y = 53 in the whole spectral window. This enhancement is manifested by a strong emission in Mg II h, k, and triplet lines as well as a gentle increase of the continuous emission in the whole spectral range. Moreover, brightenings are also present in many other narrow lines. Pixel No. 53 is located at the edge of a dark structure that corresponds to a pore of a size of $\sim 3.3''$that spans from pixels No. 55 to 65.

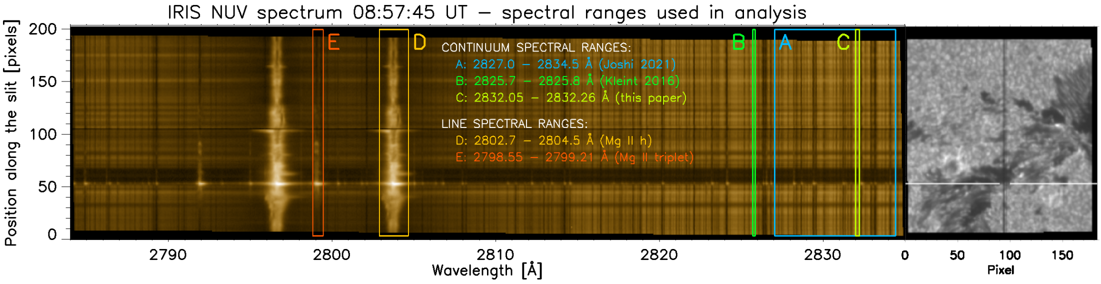

Figure A.2 IRIS NUV spectrum recorded at the time of maximum continuum emission (08:57:45 UT) along the full IRIS slit with color boxes marking the spectral ranges (A, B, C, D and E) used for the lightcurves plots and for the continuum analysis. On the right, a synchronous IRIS SJI snapshot with a horizontal white line marking the height of pixel No. 53. Animations of IRIS data are publicly available here.

The location of pixel No. 53 at the edge of the pore introduces complications in studying the long-term evolution of the flare continuum. This is because the IRIS pointing wobbles by about $0.6''$ in the Solar Y direction during the HOP 422 (see Appendix A.8.1). Fortunately, the flare occurred in one of the troughs of the wobble, when the pointing changes very slowly between about 08:40–09:00 UT (Fig. A.9). In the following, we restrict our analysis of IRIS flare spectra to this time interval.

For a detailed analysis of the temporal evolution of the flare emission within the NUV spectral window we delimited spectral bands A, B, C, D and E, inside which the emission was determined by averaging the intensity within the band. The positions of these bands in the spectra are presented in Fig. A.2. Bands A, B and C are meant to represent continuum emission, and bands D and E - line-dominated emission. Band A was defined by R. Joshi et al. (2021a) and covers the NUV spectrum between 2827.0 and 2834.5 Å, far from the Mg II lines. This band contains many other narrow lines, which exhibited enhanced emission in the flare kernel. Band B is much more narrow (2825.7 – 2825.8 Å) and was defined by Heinzel et al. (2014). It is located in a spectral region where no absorption lines are present. Finally, we defined band C spanning the range 2832.05 – 2832.26 Å. This band does not contain any spectral line and is located far away from Mg II lines, where the contribution from their far wings is negligible. Prominent Mg II lines can exhibit strong and wide wings during solar flares (see e.g., W. Liu et al., 2015), therefore a large spectral distance from them is needed. In addition, we defined band D (2802.7 – 2804.5 Å) and band E (2798.55 – 2799.21 Å) that represent the emission in the Mg II h line, and in the Mg II triplet, respectively.

In Fig. A.3 we present a photometric cut for pixel No. 53, where we plot the spectrum before, during and after the maximum intensity enhancement. We marked the spectral bands defined above with vertical color boxes. We clearly see that the spectrum intensity at the flare maximum is significantly enhanced in the whole spectral range with respect to the pre- and post- flare emission. The maximum flare emission is ~ 2.4 times stronger than preflare intensity and ~ 1.2 times stronger than after the maximum. To get a better understanding of the here-defined band C, we zoomed in the spectra from Fig. A.3. Figure A.4 shows that band C is not influenced by the far wings of Mg II lines nor other weaker lines. Therefore, any enhancement observed would be due to an enhancement of the continuum.

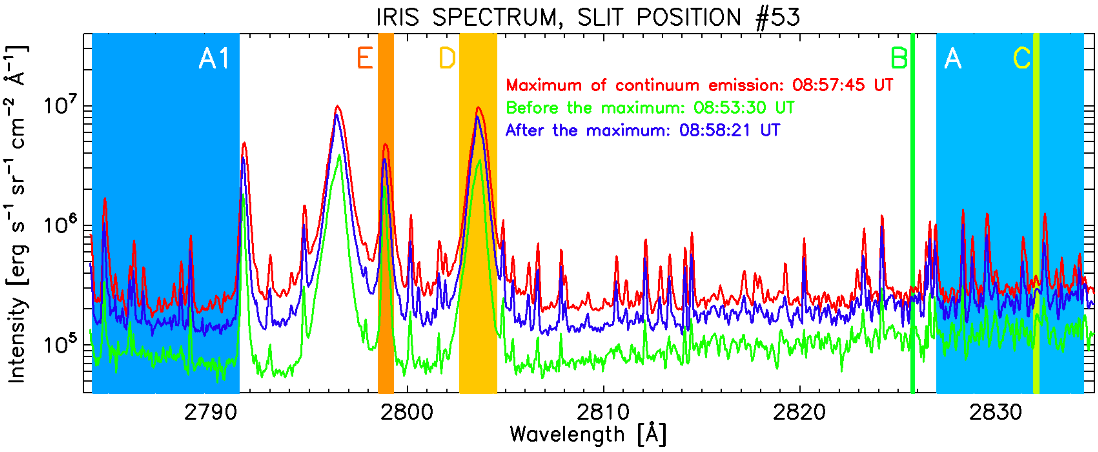

Figure A.3 IRIS NUV spectral profiles obtained at the position of the flare kernel (pixel No. 53 along the IRIS slit). The three curves represent the spectrum at the time of maximum enhancement of the continuum emission at 08:57:45 UT (red curve), and at times before and after the maximum (green and blue curves respectively). With different colors (see description in Fig. A.2) we also marked the spectral ranges A - E. We also marked the A1 range used in R. Joshi et al. (2021a) but excluded from our analysis (see the text for details).

It is worth to mention that in R. Joshi et al. (2021a) the authors did not investigate the flare continuum defining only band A, but also another spectral band, A1, covering 2784.0 – 2791.5 Å on the short-wavelength side from Mg II lines. This A1 band is marked as a blue box in Fig. A.3, where it is clear that it contains many weak lines. The enhancements of these lines in band A1 are visible as small brightenings in pixel No. 53 in Fig. A.2. Consequently, we decided not to use this spectral range for the continuum enhancement analysis.

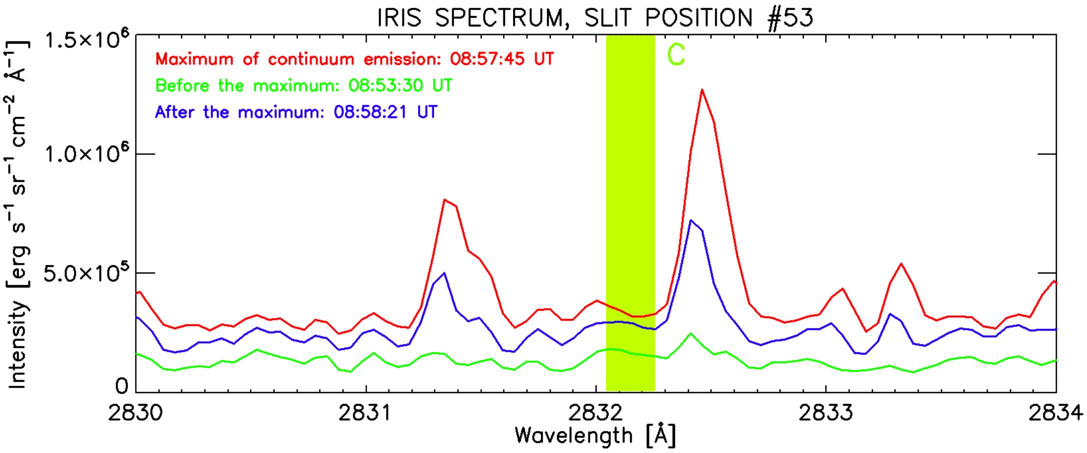

Figure A.4 Zoom of Fig. A.3 to show the spectral range used in this paper for the continuum enhancement analysis, IRIS band C (green box).

A.3.2 Lightcurves

We limited the lightcurves to the period between 08:52 and 09:00 UT. These times include the preflare, the impulsive phase and part of the gradual phase. Figure A.5 summarises the multi-wavelength temporal evolution of the flare kernel located at pixel No. 53 of IRIS slit.

Despite the lack of spatial information in flare hard X-ray sources, we were able to identify the flare impulsive phase using spatially integrated X-ray emission. Konus count rate in the 19 - 80 keV energy range corresponds to energies generally produced by non-thermal electrons accelerated during the flare. In addition, the time derivative of soft X-ray emission detected by GOES was used as a proxy for the presence of non-thermal particles assuming the Neupert effect (Neupert, 1968). The time variations of these lightcurves, shown in Fig. A.5a, agree reasonably well and suggest that the impulsive phase and the related hard X-ray emission started at ∼ 08:56 UT with two short spikes of several-second duration. Those were followed by a third, last hard X-ray pulse starting ∼ 08:56:54 UT.

AIA flare emissions in pixels co-spatial to pixel No. 53 of IRIS slit are depicted in Fig. A.5b. All AIA passbands (1700, 1600 and 304) show a gradual increase of the intensity with a first peak of emission at around 08:55 UT, followed by a second, more intense peak at around 08:57:20 UT. The coarse temporal cadence of AIA datasets does not allow for a precise determination of the flare maximum enhancements, but they provide context.

Regarding IRIS NUV emission, Fig. A.5 contains the flare evolution in all the defined bands A – E. Continuum-dominated bands (Fig. A.5c) display a sudden increase of the emission at ∼ 08:57 UT. All curves exhibit a first peak at 08:57:20 UT and a second, stronger peak at 08:57:45 UT. The whole increase of the emission was observed during 1:20 min, starting from 08:57 UT.

It is worth noticing that bands B and C show similar temporal evolution while curve A differs from them both. We interpret this situation in the context of the definition of the spectral bands. Band B and the here-defined band C contain only continuum

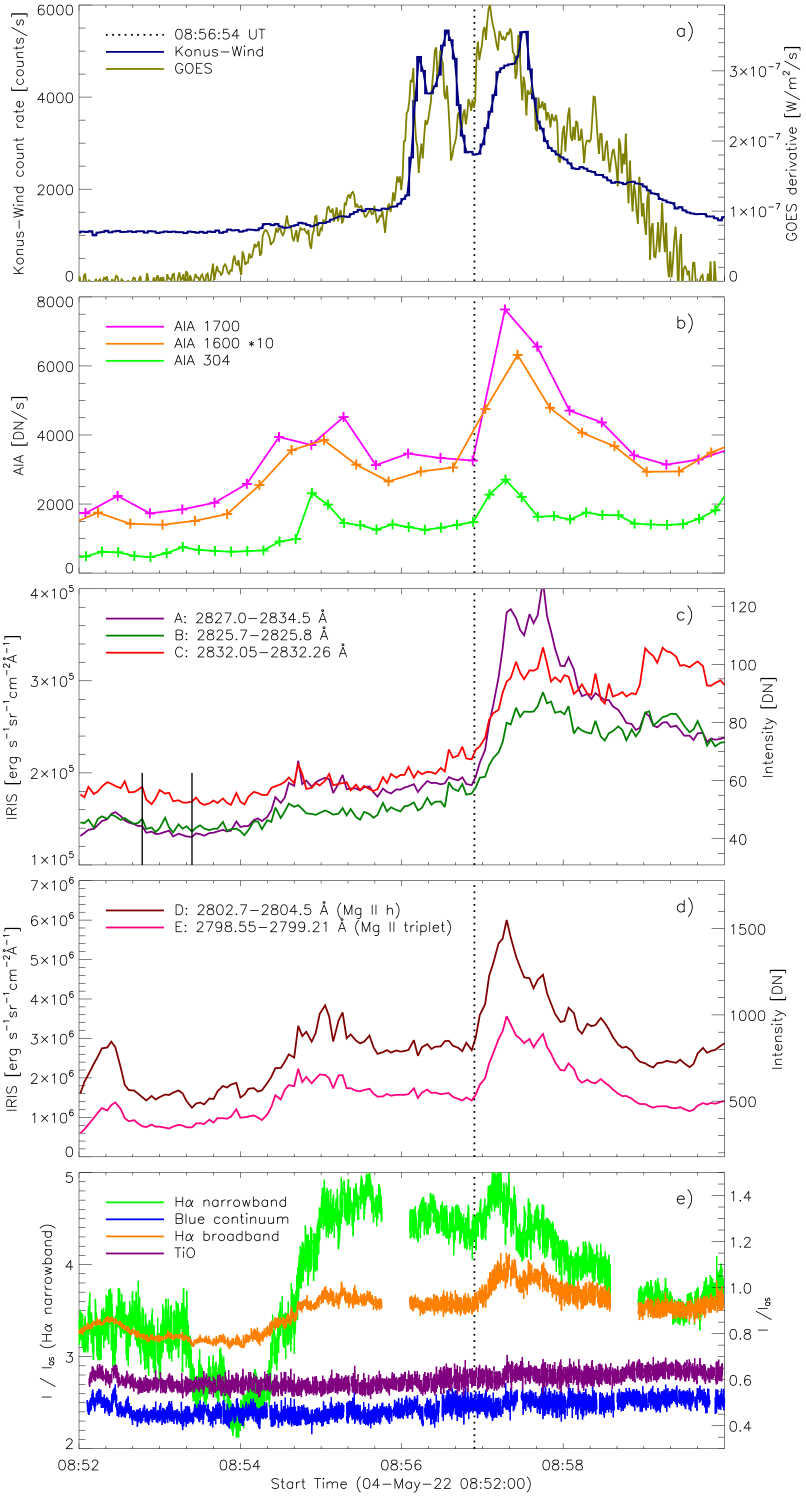

Figure A.5 Lightcurves in several wavelength bands corresponding to spatially integrated emission (panel a) and pixels co-spatial with the pixel No. 53 along the IRIS slit (panels b - e). a) Konus count rate in the G1 channel and GOES time derivative, b) emission in several SDO/AIA filters with the 1600 Å filter data scaled by 10 for plotting purposes, c - d) calibrated intensity averaged in the IRIS spectral bands A, B, C (panel c; continuum emission), D and E (panel d; line emission), e) emission relative to the quiet-Sun values in several GREGOR HiFI+ filters. The preflare time interval for evaluating the IRIS C band preflare emission is delimited by two solid vertical lines in panel c). The vertical dotted line indicates the start of the last HXR pulse.

emission, without spectral lines. On the contrary, band A contains also many narrow spectral lines (see Fig. A.2), that went into emission during the flare brightening in pixel No. 53. It is difficult to extract pure continuum emission from such a wide spectral band. Line emission may have different temporal evolution than continuum emission due to the different mechanisms responsible for their formation and their different formation heights. Bands B and C display an offset that is approximately constant during the whole analysed time and it is caused by the different wavelength distance from the Mg II lines.

In Fig. A.5d we plot the temporal evolution of Mg II line-dominated emission in bands D and E. These curves are very similar to each other. They show the first enhancement at around 08:55 UT that is co-temporal to the first enhancement observed in AIA lightcurves. Bands D and E also show one main maximum at 08:57:15 UT. Unlike the continuum emission, which is formed lower in the solar atmosphere, the Mg II line emission comes mainly from the chromosphere located higher and in a non-LTE regime.

It is interesting to note that, within the analysed period, there is a second intensity peak around 08:59 UT that is only present in the continuum emission (Fig. A.5c). This secondary maximum occurs at a time when the IRIS pointing started to change due to the wobble in the Y-axis direction (Appendix A.8.1). This means that the secondary maximum could contain contributions from different, brighter photospheric areas as a result of the change in pointing, plus contributions from the intrinsic evolution of the pore. Therefore, the secondary maximum does not necessarily reflect the evolution of the flaring continuum itself.

Lightcurves of optical emissions as detected by several GREGOR/HiFI+ filters corresponding to the IRIS pixel No. 53 are shown in Fig. A.5e. Both Hα filters show an evolution similar to those in the IRIS bands D and E (line emission), namely after $\sim$ 08:54 UT. On the other hand, the lightcurves of the continuum filters display intensity enhancements at $\sim$ 08:57:20 UT that are co-temporal to bad seeing conditions. That is, the intensity from the dark pore was contaminated by the nearby brighter granulation. All GREGOR/HiFI+ lightcurves in Fig. A.5e were scaled by time-dependent quiet-Sun values (from a quiet-Sun region in the HiFI+ cameras FOV). The gap in the Hα data at $\sim 08:56$ UT is due to an exposure time change.

Overall, the third hard X-ray pulse ($\sim$ 08:56:54 UT) is co-temporal to IRIS continuum and line bands and to Hα broad- and narrowband brightenings. Moreover, brightenings are also prominent in AIA 304, 1600, and 1700 Å lightcurves. Because these AIA passbands correspond to emission from transition region, chromosphere, and photosphere, we conclude that the co-temporal increase of emission in the position of IRIS pixel No. 53 with the HXR pulse was related to the heating of the solar atmosphere at that position by non-thermal electrons.

A.4 Continua enhancements

A.4.1 Near UV continuum in IRIS

We extracted the continuum enhancement due to the flare heating by subtracting the preflare emission to the flare emission in the here-defined band C between 08:56:54-08:58:50 UT. The preflare emission was calculated by averaging the intensity in a time interval indicated in Fig. A.5c. We note that X-ray and UV emissions at that time interval are also below flare values, as seen in Fig. A.5a and A.5b. Yet the preflare time interval precedes the start of the flare as seen in the GOES X-ray emission derivative by $\sim$ 1 min only. The IRIS band C preflare value is $(1.730 \pm 0.061) \times 10^5$ erg s^{-1} cm^{-2} sr^{-1} Å^{-1}, determined as the mean and standard deviation of the intensities during the preflare time interval. The standard deviation is further used as an estimate of the uncertainty of IRIS continuum intensities.

A.4.2 Optical continuum

The observations from GREGOR/HiFI+ and SDO/HMI were used to estimate the limit on the enhancement in the optical continuum. Both instruments recorded the intensity in arbitrary units. In order to comply with the theoretical model for the continuum, we needed to convert those values to physical units using a simplified procedure, similar to that described by Kleint et al. (2016) for HMI. They first determined the disc-centre intensity in the instrumental units. In order to do so, they used a small box around the disc centre from the same filtergrams as they used for the construction of the continuum lightcurve. Then they compared this value to the atlas (Neckel, 1994) value of the continuum near the Fe I 6173 Å line. The corresponding atlas value was 0.315×10^7 erg s^{-1} cm^{-2} sr^{-1} Å^{-1}. Assuming the linearity of the CCD chip, the ratio of the two numbers allowed them to convert HMI measurements to the physical units using this simplistic approach.

First, we analysed the possible continuum enhancement in the broad-band GREGOR/HiFI+ channels. We used only the channels of the blue continuum and TiO. We avoided the use of the G-band broad-band filter because this spectral region is filled with spectral lines and, moreover, there is a risk of cross-talk with the magnetic field. On the other hand, the lines in the TiO band appear only in sunspot umbrae because TiO molecules dissociate at $T > 4000$ K in atmospheres of the Sun and cool stars (Berdyugina et al., 2003; Bidaran et al., 2016). Otherwise, the intensity observed in the TiO band corresponds to the continuum intensity. Since pixel No. 53 is located at the edge of a pore where the probability of $T < 4000$ K is low, we expect that the observed TiO-band intensity is dominated by continuum and not by molecular lines. The procedure of converting the instrumental units to absolute units was somewhat complicated as compared to that described by Kleint et al. (2016) by the fact that the reference disc centre lied out of the field-of-view of the HiFI+ observations and hence the one-to-one conversion could not be done directly.

In order to overcome this shortcoming, we first estimated the limb darkening factor at the position of the IRIS slit. For the quiet-Sun reference we chose pixels No. 170–200 on the position of the IRIS slit and computed the median value for the blue continuum and TiO HiFI+ channels. At this position, the corresponding heliocentric distance equals to $\mu = 0.97$. Following the approximate formulae given by Cox (2000), we determined the limb-darkening factors of 0.984 for the blue continuum and 0.993 for TiO. By dividing the quiet-Sun reference on the slit by these factors, we obtained the expected value of the disc-centre intensity in the instrumental units.

The disc-centre intensity in the absolute units was obtained by integrating the atlas spectrum (Neckel, 1994) with the known filter transmission profiles (see Fig. 9 and Table 1 of Denker et al., 2023). The resulting values were 0.417×10^7 erg s^{-1} cm^{-2} sr^{-1} Å^{-1} for the blue continuum and 0.242×10^7 erg s^{-1} cm^{-2} sr^{-1} Å^{-1} for TiO. The one-to-one comparison of the filter-integrated atlas spectrum in the absolute units with the estimate of the disc-centre intensity in the instrumental units obtained in the previous step led to the multiplicative conversion factors. These factors were then used to convert the intensity in the broad-band filters at the position of the interesting pixel No. 53 of IRIS slit into absolute units.

In this way, we obtained the time series of the intensity in pixel No. 53 in the HiFI+ broad-band channels. The time cadence of the HiFI+ imaging system is very short (in the order of ms), so in order to minimise the effect of the atmospheric seeing, we averaged consecutive frames from each burst of 500 images stored within one file by

HiFI+. We averaged the 500 consecutive frames for TiO. The camera with the blue continuum filter took twice the time to record a burst, therefore we divided each burst in half and averaged the corresponding consecutive 250 frames. The final averaged frames have a larger temporal cadence of about 5 s. We note that the blue continuum and TiO lightcurves in Fig. A.5e look flatter than in Fig. A.6 due to the scaling and axis ranges.

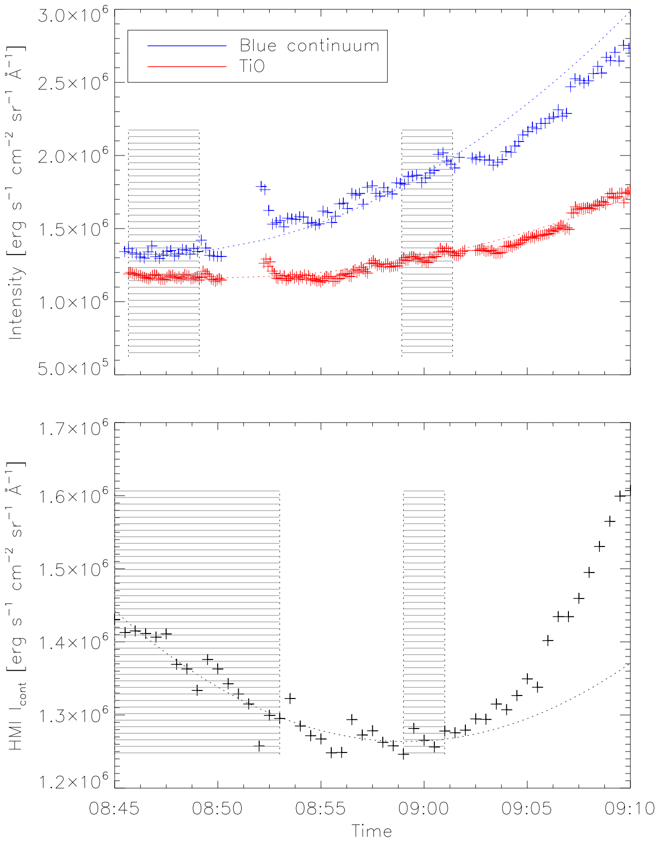

Figure A.6 Evolution of the signal in GREGOR/HiFI+ filters (upper panel; blue line indicates the blue continuum at 450.6 nm, and red the TiO band) and the far wings of the Fe I 6173 Å line from SDO/HMI (lower panel). The crosses indicate the measured signal in a pixel co-spatial with the pixel No. 53 on the IRIS slit, the dotted line indicates the fitted background, which represents the smooth evolution in the quieter period. The dashed regions indicate the time ranges used for the fitting of the smooth background.

As evident from the lightcurve of the GREGOR/HiFI+ measurements at position equivalent to pixel No. 53 on IRIS slit (see Fig. A.6 upper panel), there is no obvious continuum enhancement detected at the time of the flare except for an apparent brief enhancement after a short break in observations (~ 08:52 UT), which was caused by bad seeing. The flare kernel is also not detectable in running difference of GREGOR/HiFI+ observations. Therefore, the enhancement, if any, has to be lower than the fluctuations of non-flare origin, such as seeing fluctuations. Hence, only an upper limit on the possible continuum excess may be determined.

The upper limit on the excess was then determined as a root-mean-squared value of the deviations of the signal from the parabolic fit in the period around the flare. The background fit was obtained specifically excluding the span of the flare impulsive phase (see the dashed regions in Fig. A.6). In the physical units, those upper limits were 61 000 erg s^{-1} cm^{-2} sr^{-1} Å^{-1} for blue continuum and 27 000 erg s^{-1} cm^{-2} sr^{-1} Å^{-1} for

TiO.

For the HMI far-wing filtergrams, we followed the recipe by Kleint et al. (2016). The value of 45 600 DN/s determined for the small box around the disc centre was compared to the expected atlas value of 0.315×10^7 $\mathrm{erg\,s^{-1}\,cm^{-2}\,sr^{-1}\,Å^{-1}}$ and the ratio of the two served as a conversion factor from HMI instrumental values to absolute units. Once again, similarly to the procedure performed for the GREGOR observations described above, we fitted a smooth background curve to the time series following exactly the same reasoning, and computed the signal variations with respect to this smooth background change. In the corresponding lightcurve, no obvious enhancement at the time of the flare onset is visible. Hence (again, similarly to the case of GREGOR data) we estimated only the upper limit by calculating the root-mean-squared values of the smooth-background residuals. The obtained value was about 270 DN/s, which corresponded to 19 000 $\mathrm{erg\,s^{-1}\,cm^{-2}\,sr^{-1}\,Å^{-1}}$ assuming the conversion described above.

A.5 Estimation of temperature in the flaring chromosphere

A.5.1 Method

Building on the method employed by Heinzel et al. (2017), the temperature at the layer where the continuum enhancement is formed can be estimated. We assumed that any excess of the continuum emission is due to increased optically thin emission, I_ν, from hydrogen recombination processes occurring in a heated layer of thickness D

$$I_\nu = n_\mathrm{e}^2 D \sum_i F_i(\nu, T)\,, \tag{A.1}$$

where

$$F_i(\nu, T) \sim g_\mathrm{bf}(i,\nu) B_\nu(T) T^{-3/2} e^{h\nu_i/kT} (1 - e^{-h\nu/kT})/(i\nu)^3\,. \tag{A.2}$$

There, n_e is electron density and the subscript i (i = 2,3,4,5) denotes different hydrogen recombination continua - Balmer, Paschen, Brackett, and Pfund with corresponding wavelengths at continuum heads of λ_2 = 3646 Å, λ_3 = 8204 Å, λ_4 = 14584 Å, λ_5 = 22790 Å, respectively. The Gaunt factor $g_\mathrm{bf}(i,\nu) \approx 1$. The term $n_\mathrm{e}^2 F_i(\nu, T)$ is the recombination emissivity (see e.g., Heinzel et al., 2017) and $n_\mathrm{e}^2 D$ is emission measure (see e.g., Dominique et al., 2018).

This method requires two different wavelengths in the optical (Opt) and in the UV range. The bound-free emission at those wavelengths is:

$$\begin{aligned} I_\mathrm{UV} &= n_\mathrm{e}^2 D \sum_{i=2}^{5} F_i(\nu_\mathrm{UV}, T)\,, \\ I_\mathrm{Opt} &= n_\mathrm{e}^2 D \sum_{i=3}^{5} F_i(\nu_\mathrm{Opt}, T)\,. \end{aligned} \tag{A.3}$$

Assuming that all recombination continua are formed within the same layer, the ratio of their intensities is then only a function of temperature

$$I_\mathrm{Opt}/I_\mathrm{UV} = f(T)\,. \tag{A.4}$$

We point out that although the ratio is dimensionless, its numerical values depend whether I_ν or I_λ is used. Here, we use I_λ as all observed intensities were calibrated per wavelength. Additionally, we note that Kerr et al. (2014) use similar ratio method for their optically thick black-body model of flare white-light emission. Likewise, our approach follows similar steps as their other method to constrain temperature of a chromospheric slab under optically thin assumption.

This approach is straightforward to apply for off-limb flares, for example those in Heinzel et al. (2017), where D is the line of sight geometrical thickness of a flare loop. For such cases, it is reasonable to assume optically thin emission. The stratification of electron density and temperature along an off-limb flare loop then results in continuum intensity stratification with height.

In our case, that is for a flare on the disc, the observed intensity is given by the integral of the emissivity contributions along the flare loop. Therefore, the excess of intensity, ΔI_ν, with respect to a preflare state is

$$\Delta I_\nu \approx \int n_{\mathrm{e}}^2(z) \sum_i F_i(\nu, T(z)) e^{-\tau(z)} \mathrm{d}z \approx D \left\langle n_{\mathrm{e}}^2 \right\rangle \left\langle \sum_i F_i(\nu, T) \right\rangle \tag{A.5}$$

assuming still that the flare intensity enhancement is optically thin and that the photospheric layers, where the optically thick part of the continuum emission is formed, are not affected by the flare process. Therefore, the contribution of the undisturbed photosphere can be subtracted. This approach agrees with Potts et al. (2010) who show that optical continuum emission detected in X-class flare ribbons observed on the solar disc is of small optical depth.

Furthermore, assuming that the flare intensity enhancement comes predominantly from similar layers for both chosen wavelengths, the mean value $\langle n_{\mathrm{e}}^2 \rangle$ cancels out and the enhancement intensity ratio depends on the temperature similarly as in the Eq. (A.4)

$$\Delta I_{\mathrm{Opt}} / \Delta I_{\mathrm{UV}} = f\left(\langle T \rangle\right) , \tag{A.6}$$

where $\langle T \rangle$ is the mean temperature of the layers where the continuum enhancement originates.

Following the conclusions of Heinzel et al. (2017), here we neglect contributions from the hydrogen free-free emission and Thompson scattering. Details of the method and testing its validity are beyond the scope of this work and they are subjects of a follow-up paper (Kašparová et al., in prep.).

A.5.2 Determination of $\langle T \rangle$

This rather simple method permits an estimation of the $\langle T \rangle$ by solving Eq. (A.6) for the measured enhancements ratios. The temperature dependence of the theoretical enhancement ratios at typical flare chromospheric values is shown in Fig. A.7. In evaluating function f, Eq. (A.6), we accounted for relevant hydrogen recombination continua as in Eq. (A.3). We calculated the ratio between optical (HMI and TiO) and NUV (IRIS band C) enhancements, as seen in Fig. A.8b. For this calculation we used the enhancement of the IRIS band C above the preflare level, and the determined upper limits of enhancement for HMI and TiO, estimated in Sect. A.4.1 and Sect. A.4.2 respectively, and summarised in Fig. A.8a.

The resulting time evolution of $\langle T \rangle$ obtained from two enhancement ratios, that are $\Delta I_{\mathrm{HMI}} / \Delta I_{\mathrm{IRIS}}$ and $\Delta I_{\mathrm{TiO}} / \Delta I_{\mathrm{IRIS}}$, is plotted in Fig. A.8c. The time interval is constrained to the period of the first intensity increase in IRIS band C. The shaded region indicates the spread of $\langle T \rangle$ values taking into account the standard deviation of the intensities in band C during the preflare interval, see Sect. A.4.1. We note that since we use upper limits of HMI and TiO enhancements, we determine lower limits of the mean temperature $\langle T \rangle$. The real optical continuum enhancements could be lower, therefore leading to smaller ratios and thus to higher temperatures, according to the theoretical behaviour of $f(T)$ for HMI and TiO wavelengths in Fig. A.7. Also, we

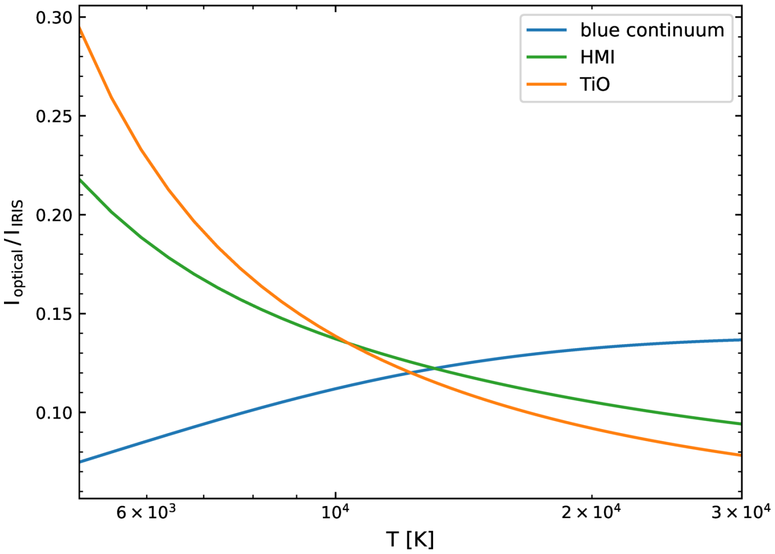

Figure A.7 Theoretical ratios, $f(T)$, for three wavelengths at the optical range, i.e., λ_{blue}, λ_{HMI}, and λ_{TiO}.

point out that the time resolution of the temperature lightcurve is dictated by the time resolution of IRIS spectral data.

The HiFI+ blue filter data and the corresponding $\Delta I_{\mathrm{blue}}/\Delta I_{\mathrm{IRIS}}$ ratio were not used for the determination of $\langle T \rangle$ because the limit of enhancements in GREGOR blue filter (Sect. A.4.2) leads to ratios higher than the theoretical ratios (the blue curve in Fig. A.7 is lower than ~ 0.14, and its behaviour does not change for higher temperatures). Similarly, as for the limits of HMI and TiO enhancements, the real enhancement in the blue filter could be lower but not zero. Our approach to determine the temperature of the layers where the flare continuum emission originates is valid only for non-zero optical enhancements. If we assume that the detected enhancement in IRIS NUV continuum is due to the bound-free contribution, there must be a corresponding contribution in the optical continuum. Yet, it could be below detection limits of the data we have at our disposal.

Additionally, the mean electron density, $\langle n_{\mathrm{e}} \rangle$, could be determined from the observed enhancement at IRIS band C and the modelled enhancement evaluated for the obtained $\langle T \rangle$, see Eq. (A.3). That is, $\langle n_{\mathrm{e}} \rangle = (\Delta I_{\mathrm{IRIS}}/I_{\mathrm{IRIS}}/D)^{1/2}$. The thickness of the layer where the continuum enhancements are formed, D, was obtained from Heinzel et al. (2017, Figs. 1, 2, Sect. 4.1). In that work, the optical continuum enhancements in the analysed off-limb flares extend over ~ 500 km above the limb as seen in HMI data. Adopting the results presented above, $\langle n_{\mathrm{e}} \rangle \sim 1 \times 10^{13}$ cm^{-3} was obtained.

A.6 Discussion

Based on Heinzel et al. (2014), the observed NUV flare continuum emission is produced by bound-free transitions, which implies that there is optical continuum enhancement as well. Due to the limitations to detect the continuum by HMI and to the seeing-induced intensity fluctuations at GREGOR, the flare kernel was not unambiguously detected in the optical broad-band observations. However, the construction of the lightcurves at the location corresponding to pixel No. 53 on IRIS slit allowed us to estimate an upper limit on the brightness changes caused by the flare. These upper limits contributed to constrain the temperature of the heated atmosphere.

We determined a lower limit on the mean temperature and its time evolution in the

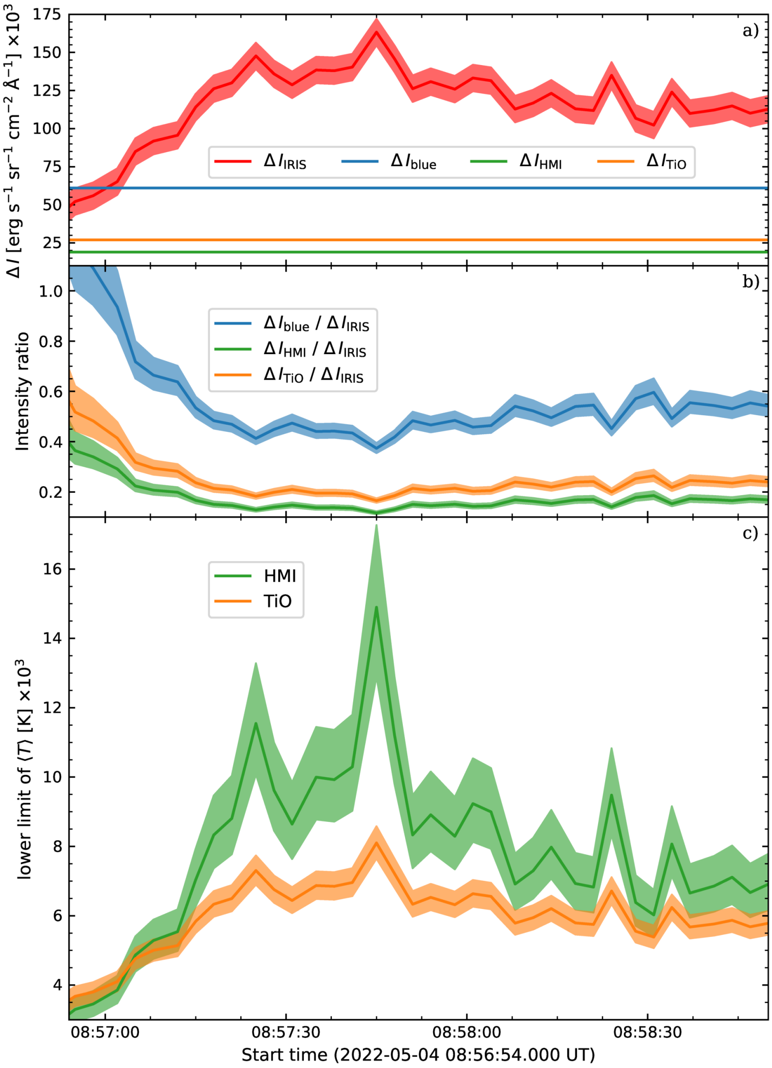

Figure A.8 Time evolution of a) the determined intensity enhancement at λ_{IRIS} and the upper limits at λ_{blue}, λ_{HMI}, and λ_{TiO}; b) the measured ratios for the three different wavelengths at the optical range, i.e. λ_{blue}, λ_{HMI}, and λ_{TiO}; c) the lower limit on the mean temperature as determined from $\Delta I_{\mathrm{TiO}}/\Delta I_{\mathrm{IRIS}}$ and $\Delta I_{\mathrm{HMI}}/\Delta I_{\mathrm{IRIS}}$.

layer where the optically-thin flare continuum enhancement is formed without assuming any value for the so-called emission measure, $n_{\mathrm{e}}^2 D$, in contrast with previous similar works, see for example Heinzel et al. (2017), Kerr et al. (2014), and Dominique et al. (2018). The determined lower limits of the temperature vary in the $\sim (3-15)\times 10^3$ K range which is similar to temperatures obtained in radiation-hydrodynamical simulations of beam heating of initial VAL C-like atmosphere (Heinzel et al., 2017; Kašparová et al., 2019; Carlsson et al., 2023) and to values determined by Kerr et al. (2014) in their optically-thin scenario.

Additionally, we obtained the mean electron density of the emitting chromospheric layer, $\langle n_{\mathrm{e}}\rangle \sim 1\times 10^{13}$ cm^{-3}, which is similar to the modelled values in Heinzel et al. (2017) and those discussed in Kerr et al. (2014) and Dominique et al. (2018) and lies within transition region densities determined from IRIS FUV line ratios (Polito et al., 2016a; R. Joshi et al., 2021b) or obtained in numerical models (Kerr et al., 2019).

The time evolution of the lower limit of the temperature shows rapid variations on a timescale of several seconds (see Fig. A.8), reflecting the IRIS temporal resolution of ~ 3 s. Individual peaks last less than ~ 10 s, with a single-point maximum, meaning that they are likely strongly undersampled, and possibly have even shorter duration. We note that similar fast changes in the intensity of different flaring lines have been observed before (see e.g., Jeffrey et al., 2018; Lörinčík et al., 2022a; Lörinčík et al., 2022b). The exact nature of these variations is beyond the scope of our present paper; nevertheless, there are several conceivable mechanisms, including intermittent particle acceleration (as suggested by both the GOES derivative and multi-peak Konus-Wind HXR lightcurve) and turbulence (Jeffrey et al., 2018), which itself can be related to particle acceleration (Bian et al., 2014). Finally, we note that microwave emission in the 5-15 GHz range shows similar time evolution to the HXR lightcurve (Smirnova et al., 2023). This suggests that both types of emission were produced by the same population of non-thermal elections.

Using the values of $\langle T \rangle$, $\langle n_\mathrm{e} \rangle$, and the limb darkening factor for near-Hα continuum, we estimated the expected relative continuum enhancement for FICUS. Since 15% of the observed area was covered by the Hα solar flare (based on Fig. A.1m), the relative continuum enhancement was below 1%. Such enhancement is smaller than the FICUS data uncertainties for this particular flare and confirms the lack of enhancement detection in FICUS near-Hα continuum.

A.7 Summary

We present the first results of the first successful joint GREGOR and IRIS observing campaign of solar flares. The campaign was supported by ground-based instruments located at the Astronomical Institute in Ondřejov. On 2022 May 4, we observed a confined M5.7 solar flare, with one flare ribbon crossing the slit of the IRIS spectrograph. We investigated the temporal evolution of spectral (IRIS NUV) and imaging (GREGOR HiFI+) data in a rather faint flare kernel at the edge of a pore. These data were complemented by space-based observations from AIA, HMI, GOES-16, and Konus.

We focused on the observations of the NUV and optical flare continuum obtained with unprecedented temporal resolution by IRIS and HiFI+, respectively. The NUV spectra recorded at full read-out mode allowed us to examine continuum enhancements at wavelengths further away from the strong Mg II lines than in previous studies. We found that the NUV continuum emission showed rapid temporal variations. On the other hand, due to limitations of the HMI instrument and seeing conditions at GREGOR, the HiFI+ and HMI datasets allowed us to estimate only an upper limit of the flare continuum enhancement in the optical range. The spatially-integrated HXR lightcurves supported our interpretation of flare related continuum emission.

The combination of the optical and NUV continuum analyses led to a lower limit on the temperature of $\sim (3-15)\times 10^3$ K and a mean electron density of $\sim 1\times 10^{13}$ cm^{-3} in the flaring chromospheric layers. This study demonstrates the rich diagnostic potential that multi-instrument and multi-wavelength flare campaigns have. Our findings support previous indications that continuum enhancement is also present in confined flares and in flaring areas of weak emission, and that the associated temperature varies on very short timescales.

A.8 Appendix

A.8.1 IRIS pointing wobble during the 2022 May 4 flare

The IRIS lightcurve analysis presented in Sect. A.4.1 is complicated by the changes in the IRIS pointing. During the HOP 422 (OBS 3884855852: Medium sit-and-stare), lasting from 7:30 to about 13:00 UT on 2022 May 4, IRIS tracked the AR 13004. This

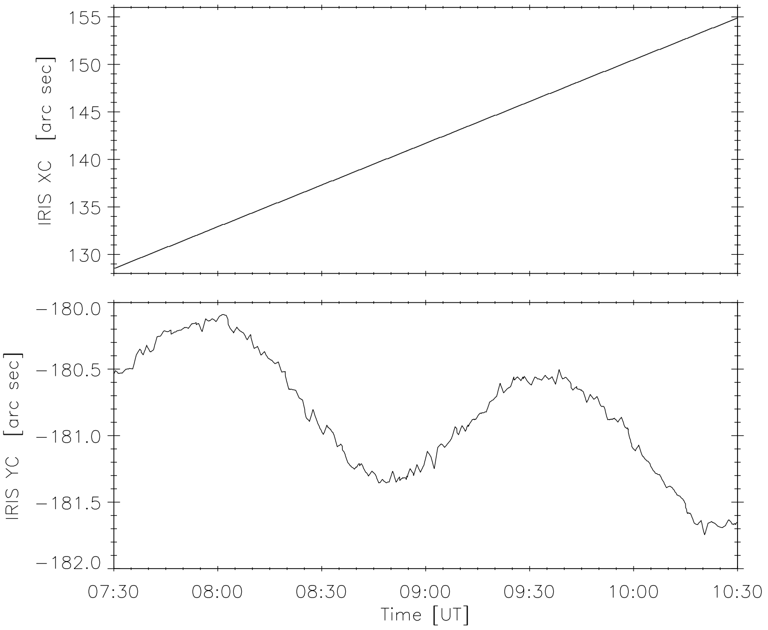

Figure A.9 IRIS pointing during the HOP 422 on 2022 May 4, showing the evolution of the pointing in terms of the center of the SJI field of view [XC, YC].

tracking is clearly identifiable as a continuous increase of the IRIS XC, the Solar X coordinate of the SJI field of view (top panel of Fig. A.9). Except for minute residuals, this tracking is easily rectified with the correction of the solar differential rotation.

However, the pointing in Y was not stable, as indicated by the IRIS YC coordinate. Here, IRIS showed an orbital wobble with an amplitude of about 0.6 $''$; that is, about 2 pixels (in the spatially binned SJI images). The wobble, as indicated by the bottom panel of Fig. A.9, is primarily sinusoidal, but with a secular component. This secular component is reduced, but not removed, by the correction for differential rotation. The wobble is not affected by this procedure.

We note that the orbital wobble occurs due to thermal bending of the mounting of the IRIS guide telescope (see Sect. 4.5 of De Pontieu et al., 2014) and is in phase with the IRIS orientation with respect to the illuminated side of the Earth. The orbital wobble is normally corrected using orbital wobble tables[3] to less than about 0.3 $''$(De Pontieu et al., 2014). Why the wobble is larger in the present observation is not known to us.

A.9 Testing the absolute calibration of the IRIS NUV spectra

To verify the IRIS calibration procedure and to check if it gives reasonable results we compared the Mg II quiet-Sun line profiles observed with IRIS slit with the previous calibrated observations obtained with RASOLBA experiment (Staath et al., 1995). For this purpose, we chose a pixel (pixel No. 190 along IRIS slit) as distant as possible from the observed AR, and generated a reference QS spectrum. The results of comparing our calibrated QS spectrum with RASOLBA calibration are presented in Fig. A.10. The good agreement between both spectra confirms the correctness of our radiometric calibration. Some differences in the signal, in particular in the line wings, could be caused by heterogeneity of the photospheric brightness.

---

[3] `https://iris.lmsal.com/itn51/iris_timeline.html`

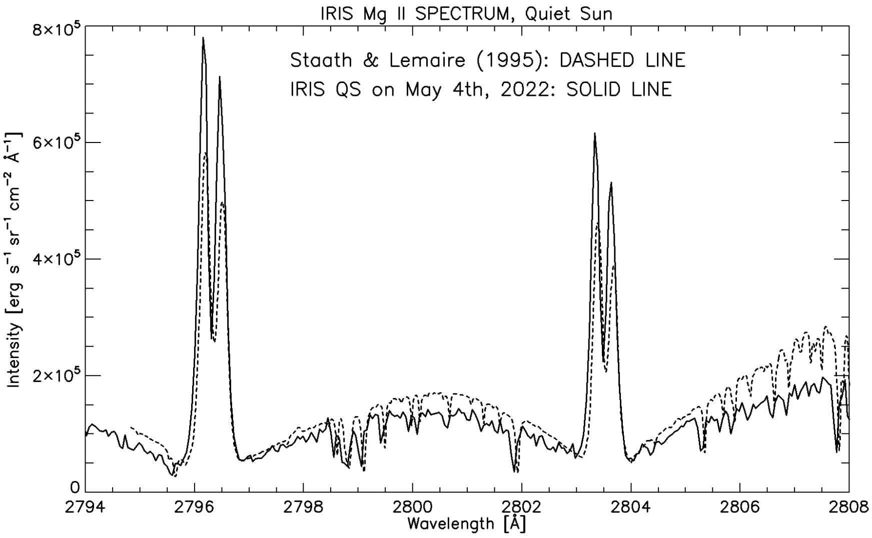

Figure A.10 Comparison of our calibrated mean quiet-Sun disc spectrum obtained on 2022 May 4, with RASOLBA calibrated spectrum.

Acknowledgements:

J. D. and J. K. acknowledge the Czech National Science Foundation, Grant No. GACR 22-07155S, as well as institutional support RWO:67985815 from the Czech Academy of Sciences. A.B. also acknowledges the support within the "Excellence Initiative-Research University" for years 2020-2026 at University of Wrocław, project no. BPIDUB.4610.96.2021.KG. and BPIDUB.4610.15.2021.KP.B. We thank Alexandra Lysenko for providing us with Konus-Wind data, http://www.ioffe.ru/LEA/kwsun/. This research data leading to the results obtained has been supported by SOLARNET project that has received funding from the European Union's Horizon 2020 research and innovation programme under grant agreement No. 824135. The 1.5-meter GREGOR solar telescope was built by a German consortium under the leadership of the Institute for Solar Physics (KIS) in Freiburg with the Leibniz Institute for Astrophysics Potsdam, the Institute for Astrophysics Göttingen, and the Max Planck Institute for Solar System Research in Göttingen as partners, and with contributions by the Instituto de Astrofísica de Canarias and the Astronomical Institute of the Academy of Sciences of the Czech Republic. IRIS is a NASA small explorer mission developed and operated by LMSAL with mission operations executed at NASA Ames Research Center and major contributions to downlink communications funded by ESA and the Norwegian Space Centre.

Bibliography

ALLRED, J. C.; HAWLEY, S. L.; ABBETT, W. P.; CARLSSON, M., 2005. Radiative Hydrodynamic Models of the Optical and Ultraviolet Emission from Solar Flares. *ApJ*. Vol. 630, no. 1, pp. 573–586. Available from DOI: `10.1086/431751`.

ANDRETTA, V. et al., 2021.
The first coronal mass ejection observed in both visible-light and UV H I Ly-α channels of the Metis coronagraph on board Solar Orbiter. *A&A*. Vol. 656, p. L14. Available from DOI: `10.1051/0004-6361/202142407`.

ANTONUCCI, E. et al., 2020.
Metis: the Solar Orbiter visible light and ultraviolet coronal imager. *A&A*. Vol. 642, A10. Available from DOI: `10.1051/0004-6361/201935338`.

ANZER, U.; HEINZEL, P., 2005. On the Nature of Dark Extreme Ultraviolet Structures Seen by SOHO/EIT and TRACE. *ApJ*. Vol. 622, no. 1, pp. 714–721. Available from DOI: `10.1086/427817`.

APTEKAR, R. L.; FREDERIKS, D. D.; GOLENETSKII, S. V.; ILYNSKII, V. N.; MAZETS, E. P.; PANOV, V. N.; SOKOLOVA, Z. J.; TEREKHOV, M. M.; SHESHIN, L. O.; CLINE, T. L.; STILWELL, D. E., 1995.
Konus-W Gamma-Ray Burst Experiment for the GGS Wind Spacecraft. *Space Sci. Rev.* Vol. 71, no. 1-4, pp. 265–272. Available from DOI: `10.1007/BF00751332`.

BALTHASAR, H., 2018.
The Problem of the Height Dependence of Magnetic Fields in Sunspots. *Sol. Phys.* Vol. 293, no. 8, p. 120. Available from DOI: `10.1007/s11207-018-1338-x`.

BECK, J. G.; CHAPMAN, G. A., 1993.
A Study of the Contrast of Sunspots from Photometric Images. *Sol. Phys.* Vol. 146, no. 1, pp. 49–60. Available from DOI: `10.1007/BF00662169`.

BECKERS, J. M.; SCHRÖTER, E. H., 1969. The Intensity, Velocity and Magnetic Structure of a Sunspot Region. IV: Properties of a Unipolar Sunspot. *Sol. Phys.* Vol. 10, no. 2, pp. 384–403. Available from DOI: `10.1007/BF00145526`.

BELLO GONZÁLEZ, N.; JURČÁK, J.; SCHLICHENMAIER, R.; REZAEI, R., 2019.
New Insights on Penumbra Magneto-Convection.
In: BELLUZZI, L.; CASINI, R.; ROMOLI, M.; TRUJILLO BUENO, J. (eds.). *Solar Polariation Workshop 8*. Vol. 526, p. 261. Astronomical Society of the Pacific Conference Series.

BELLO GONZÁLEZ, N.; KNEER, F.; SCHLICHENMAIER, R., 2012. Shear and vortex motions in a forming sunspot. Twist relaxation in magnetic flux ropes. *A&A*. Vol. 538, A62. Available from DOI: `10.1051/0004-6361/201118005`.

BELLO GONZÁLEZ, N.; OKUNEV, O.; KNEER, F., 2008. Small-scale magnetic field dynamics on the Sun at high spatial and temporal resolution. *A&A*. Vol. 490, pp. L23–L26. Available from DOI: `10.1051/0004-6361:200810464`.

BELLO GONZÁLEZ, N.; YELLES CHAOUCHE, L.; OKUNEV, O.; KNEER, F., 2009. Dynamics of small-scale magnetic fields on the Sun: observations and numerical simulations. *A&A*. Vol. 494, no. 3, pp. 1091–1106. Available from DOI: `10.1051/0004-6361:200810448`.

Bellot Rubio, L. R.; Tritschler, A.; Martínez Pillet, V., 2008. Spectropolarimetry of a Decaying Sunspot Penumbra. *ApJ*. Vol. 676, no. 1, pp. 698–703. Available from DOI: `10.1086/527366`.

Bendlin, C.; Volkmer, R.; Kneer, F., 1992. A new instrument for high resolution, two-dimensional solar spectroscopy. *A&A*. Vol. 257, pp. 817–823.

Benko, M.; González Manrique, S. J.; Balthasar, H.; Gömöry, P.; Kuckein, C.; Jurčák, J., 2018. Properties of the inner penumbral boundary and temporal evolution of a decaying sunspot. *A&A*. Vol. 620, A191. Available from DOI: `10.1051/0004-6361/201834296`.

Berdyugina, S. V.; Solanki, S. K.; Frutiger, C., 2003. The molecular Zeeman effect and diagnostics of solar and stellar magnetic fields. II. Synthetic Stokes profiles in the Zeeman regime. *A&A*. Vol. 412, pp. 513–527. Available from DOI: `10.1051/0004-6361:20031473`.

Berger, T. E.; Berdyugina, S. V., 2003. The Observation of Sunspot Light-Bridge Structure and Dynamics. *ApJ*. Vol. 589, no. 2, pp. L117–L121. Available from DOI: `10.1086/376494`.

Berkefeld, T.; Schmidt, D.; Soltau, D.; von der Lühe, O.; Heidecke, F., 2012. The GREGOR adaptive optics system. *Astronomische Nachrichten*. Vol. 333, p. 863. Available from DOI: `10.1002/asna.201211739`.

Bharti, L.; Joshi, C.; Jaaffrey, S. N. A., 2007. Observations of Dark Lanes in Umbral Fine Structure from the Hinode Solar Optical Telescope: Evidence for Magnetoconvection. *ApJ*. Vol. 669, no. 1, pp. L57–L60. Available from DOI: `10.1086/523352`.

Bian, N. H.; Emslie, A. G.; Stackhouse, D. J.; Kontar, E. P., 2014. The Formation of Kappa-distribution Accelerated Electron Populations in Solar Flares. *ApJ*. Vol. 796, no. 2, p. 142. Available from DOI: `10.1088/0004-637X/796/2/142`.

Bidaran, B.; Mirtorabi, M. T.; Azizi, F., 2016. A new titanium oxide index in the visual band. *MNRAS*. Vol. 457, no. 2, pp. 2043–2047. Available from DOI: `10.1093/mnras/stw051`.

Borrero, J. M.; Bellot Rubio, L. R.; Müller, D. A. N., 2007. Flux Tubes as the Origin of Net Circular Polarization in Sunspot Penumbrae. *ApJ*. Vol. 666, no. 2, pp. L133–L136. Available from DOI: `10.1086/521923`.

Borrero, J. M.; Ichimoto, K., 2011a. Magnetic Structure of Sunspots. *Living Reviews in Solar Physics*. Vol. 8, no. 1, p. 4. Available from DOI: `10.12942/lrsp-2011-4`.

Borrero, J. M.; Lites, B. W.; Lagg, A.; Rezaei, R.; Rempel, M., 2014. Comparison of inversion codes for polarized line formation in MHD simulations. I. Milne-Eddington codes. *A&A*. Vol. 572, A54. Available from DOI: `10.1051/0004-6361/201424584`.

Borrero, J. M.; Lites, B. W.; Solanki, S. K., 2008. Evidence of magnetic field wrapping around penumbral filaments. *A&A*. Vol. 481, no. 1, pp. L13–L16. Available from DOI: `10.1051/0004-6361:20079002`.

Borrero, J. M.; Tomczyk, S.; Kubo, M.; Socas-Navarro, H.; Schou, J.; Couvidat, S.; Bogart, R., 2011b. VFISV: Very Fast Inversion of the Stokes Vector for the Helioseismic and Magnetic Imager. *Sol. Phys.* Vol. 273, no. 1, pp. 267–293. Available from DOI: `10.1007/s11207-010-9515-6`.

BOURDIN, Ph. -A., 2017. Plasma Beta Stratification in the Solar Atmosphere: A Possible Explanation for the Penumbra Formation. *ApJ*. Vol. 850, no. 2, p. L29. Available from DOI: `10.3847/2041-8213/aa9988`.

BRAY, R. J.; LOUGHHEAD, R. E., 1964. *Sunspots*.

CABRERA SOLANA, D.; BELLOT RUBIO, L. R.; DEL TORO INIESTA, J. C., 2005. Sensitivity of spectral lines to temperature, velocity, and magnetic field. *A&A*. Vol. 439, no. 2, pp. 687–699. Available from DOI: `10.1051/0004-6361:20052720`.

CAMPOS ROZO, J. I.; VARGAS DOMÍNGUEZ, S.; UTZ, D.; VERONIG, A. M.; HANSLMEIER, A., 2023. Exploring magnetic field properties at the boundary of solar pores: A comparative study based on SDO-HMI observations. *A&A*. Vol. 674, A91. Available from DOI: `10.1051/0004-6361/202346389`.

CARLSSON, M.; FLETCHER, L.; ALLRED, J.; HEINZEL, P.; KAŠPAROVÁ, J.; KOWALSKI, A.; MATHIOUDAKIS, M.; REID, A.; SIMÕES, P. J. A., 2023. The F-CHROMA grid of 1D RADYN flare models. *A&A*. Vol. 673, A150. Available from DOI: `10.1051/0004-6361/202346087`.

CARRASCO, V. M. S.; GARCÍA-ROMERO, J. M.; VAQUERO, J. M.; RODRÍGUEZ, P. G.; FOUKAL, P.; GALLEGO, M. C.; LEFÈVRE, L., 2018. The Umbra-Penumbra Area Ratio of Sunspots During the Maunder Minimum. *ApJ*. Vol. 865, no. 2, p. 88. Available from DOI: `10.3847/1538-4357/aad9f6`.

CASTELLANOS DURÁN, J. S.; LAGG, A.; SOLANKI, S. K., 2021. How rare are counter Evershed flows? *A&A*. Vol. 651, p. L1. Available from DOI: `10.1051/0004-6361/202141159`.

CENTENO, R.; BLANCO RODRÍGUEZ, J.; DEL TORO INIESTA, J. C.; SOLANKI, S. K.; BARTHOL, P.; GANDORFER, A.; GIZON, L.; HIRZBERGER, J.; RIETHMÜLLER, T. L.; VAN NOORT, M.; OROZCO SUÁREZ, D.; BERKEFELD, T.; SCHMIDT, W.; MARTÍNEZ PILLET, V.; KNÖLKER, M., 2017. A Tale of Two Emergences: Sunrise II Observations of Emergence Sites in a Solar Active Region. *ApJS*. Vol. 229, no. 1, p. 3. Available from DOI: `10.3847/1538-4365/229/1/3`.

CENTENO, R.; LITES, B. W.; DE WIJN, A. G.; ELMORE, D., 2009. Hinode's SP and G-band Co-Alignment. In: LITES, B. W.; CHEUNG, M.; MAGARA, T.; MARISKA, J.; REEVES, K. (eds.). *The Second Hinode Science Meeting: Beyond Discovery-Toward Understanding*. Vol. 415, p. 323. Astronomical Society of the Pacific Conference Series. Available from DOI: `10.48550/arXiv.0902.0027`.

CENTENO, R.; SCHOU, J.; HAYASHI, K.; NORTON, A. A.; HOEKSEMA, J. T.; LIU, Y.; LEKA, K. D.; BARNES, G., 2014. The Helioseismic and Magnetic Imager (HMI) Vector Magnetic Field Pipeline: Optimization of the Spectral Line Inversion Code. *Sol. Phys.* Vol. 289, no. 9, pp. 3531–3547. Available from DOI: `10.1007/s11207-014-0497-7`.

CHANDRASEKHAR, S., 1961. *Hydrodynamic and hydromagnetic stability*.

CHAPMAN, G. A.; DOBIAS, J. J.; PREMINGER, D. G.; WALTON, S. R., 2003. On the decay rate of sunspots. *Geophys. Res. Lett.* Vol. 30, no. 4, p. 1178. Available from DOI: `10.1029/2002GL016225`.

CHARBONNEAU, P., 2005. Dynamo Models of the Solar Cycle. *Living Reviews in Solar Physics*. Vol. 2, no. 1, p. 2. Available from DOI: `10.12942/lrsp-2005-2`.

Chen, F.; Rempel, M.; Fan, Y., 2017.
Emergence of Magnetic Flux Generated in a Solar Convective Dynamo. I. The Formation of Sunspots and Active Regions, and The Origin of Their Asymmetries. *ApJ.* Vol. 846, no. 2, p. 149. Available from doi: `10.3847/1538-4357/aa85a0`.

Cheng, J. X.; Ding, M. D.; Carlsson, M., 2010. Radiative Hydrodynamic Simulation of the Continuum Emission in Solar White-Light Flares. *ApJ.* Vol. 711, no. 1, pp. 185–191. Available from doi: `10.1088/0004-637X/711/1/185`.

Chitre, S. M., 1963. The structure of sunspots. *MNRAS.* Vol. 126, p. 431. Available from doi: `10.1093/mnras/126.5.431`.

Cho, I. -H.; Cho, K. -S.; Bong, S. -C.; Lim, E. -K.; Kim, R. -S.; Choi, S.; Kim, Y. -H.; Yurchyshyn, V., 2015.
Statistical Comparison Between Pores and Sunspots by Using SDO/HMI. *ApJ.* Vol. 811, no. 1, p. 49. Available from doi: `10.1088/0004-637X/811/1/49`.

Chupp, E. L.; Forrest, D. J.; Higbie, P. R.; Suri, A. N.; Tsai, C.; Dunphy, P. P., 1973. Solar Gamma Ray Lines observed during the Solar Activity of August 2 to August 11, 1972. *Nature.* Vol. 241, no. 5388, pp. 333–335. Available from doi: `10.1038/241333a0`.

Collados, M.; Lagg, A.; Díaz Garcí A, J. J.; Hernández Suárez, E.; López López, R.; Páez Mañá, E.; Solanki, S. K., 2007. Tenerife Infrared Polarimeter II. In: Heinzel, P.; Dorotovič, I.; Rutten, R. J. (eds.). *The Physics of Chromospheric Plasmas.* Vol. 368, p. 611. Astronomical Society of the Pacific Conference Series.

Collados, M.; López, R.; Páez, E.; Hernández, E.; Reyes, M.; Calcines, A.; Ballesteros, E.; Díaz, J. J.; Denker, C.; Lagg, A.; Schlichenmaier, R.; Schmidt, W.; Solanki, S. K.; Strassmeier, K. G.; von der Lühe, O.; Volkmer, R., 2012. GRIS: The GREGOR Infrared Spectrograph. *Astronomische Nachrichten.* Vol. 333, p. 872. Available from doi: `10.1002/asna.201211738`.

Community Spectropolarimetric Analysis Center (CSAC), 2006a. *Hinode-SpectroPolarimeter (SP) Level 1 (calibrated) full Stokes data.* UCAR/NCAR - HAO/Community Spectropolarimetric Analysis Center. Available from doi: `10.5065/D6T151QF`.

Community Spectropolarimetric Analysis Center (CSAC), 2006b. *Hinode-SpectroPolarimeter (SP) Level 2 (vector magnetic field) spectral line inversions.* UCAR/NCAR - HAO/Community Spectropolarimetric Analysis Center. Available from doi: `10.5065/D6JH3J8D`.

Couvidat, S.; Schou, J.; Hoeksema, J. T.; Bogart, R. S.; Bush, R. I.; Duvall, T. L.; Liu, Y.; Norton, A. A.; Scherrer, P. H., 2016.
Observables Processing for the Helioseismic and Magnetic Imager Instrument on the Solar Dynamics Observatory. *Sol. Phys.* Vol. 291, no. 7, pp. 1887–1938. Available from doi: `10.1007/s11207-016-0957-3`.

Cox, A. N., 2000. *Allen's astrophysical quantities.* Springer.

Criscuoli, S.; Norton, A. A.; Whitney, T., 2017. Photometric Properties of Network and Faculae Derived from HMI Data Compensated for Scattered Light. *ApJ.* Vol. 847, no. 2, p. 93. Available from doi: `10.3847/1538-4357/aa8ad7`.

Culhane, J. L.; Harra, L. K.; James, A. M.; Al-Janabi, K.; Bradley, L. J.; Chaudry, R. A.; Rees, K.; Tandy, J. A.; Thomas, P.; Whillock, M. C. R.; Winter, B.; Doschek, G. A.; Korendyke, C. M.; Brown, C. M.; Myers, S.; Mariska, J.; Seely, J.; Lang, J.; Kent, B. J.; Shaughnessy, B. M.; Young, P. R.; Simnett, G. M.; Castelli, C. M.; Mahmoud, S.; Mapson-Menard, H.; Probyn, B. J.; Thomas, R. J.; Davila, J.; Dere, K.; Windt, D.; Shea, J.; Hagood, R.; Moye, R.; Hara, H.; Watanabe, T.; Matsuzaki, K.; Kosugi, T.; Hansteen, V.; Wikstol, Ø., 2007. The EUV Imaging Spectrometer for Hinode. *Sol. Phys.* Vol. 243, no. 1, pp. 19–61. Available from DOI: `10.1007/s01007-007-0293-1`.

De Pontieu, B. et al., 2014. The Interface Region Imaging Spectrograph (IRIS). *Sol. Phys.* Vol. 289, no. 7, pp. 2733–2779. Available from DOI: `10.1007/s11207-014-0485-y`.

del Toro Iniesta, J. C., 2007. *Introduction to Spectropolarimetry.*

Del Zanna, G., 2013. The multi-thermal emission in solar active regions. *A&A.* Vol. 558, A73. Available from DOI: `10.1051/0004-6361/201321653`.

Deng, N.; Choudhary, D. P.; Tritschler, A.; Denker, C.; Liu, C.; Wang, H., 2007. Flow Field Evolution of a Decaying Sunspot. *ApJ.* Vol. 671, no. 1, pp. 1013–1021. Available from DOI: `10.1086/523102`.

Deng, N.; Liu, C.; Yang, G.; Wang, H.; Denker, C., 2005. Rapid Penumbral Decay Associated with an X2.3 Flare in NOAA Active Region 9026. *ApJ.* Vol. 623, no. 2, pp. 1195–1201. Available from DOI: `10.1086/428821`.

Denker, C.; Verma, M.; Wiśniewska, A.; Kamlah, R.; Kontogiannis, I.; Dineva, E.; Rendtel, J.; Bauer, S. M.; Dionies, M.; Önel, H.; Woche, M.; Kuckein, C.; Seelemann, T.; Pal, P. S., 2023. Improved High-resolution Fast Imager. *Journal of Astronomical Telescopes, Instruments, and Systems.* Vol. 9, p. 015001. Available from DOI: `10.1117/1.JATIS.9.1.015001`.

Ding, M. D.; Fang, C.; Yun, H. S., 1999. Heating in the Lower Atmosphere and the Continuum Emission of Solar White-Light Flares. *ApJ.* Vol. 512, no. 1, pp. 454–457. Available from DOI: `10.1086/306776`.

Ding, M. D.; Liu, Y.; Yeh, C. -T.; Li, J. P., 2003. Interpretation of the infrared continuum in a solar white-light flare. *A&A.* Vol. 403, pp. 1151–1156. Available from DOI: `10.1051/0004-6361:20030428`.

Dominguez-Tagle, C.; Collados, M.; Lopez, R.; Cedillo, J. J. Vaz; Esteves, M. A.; Grassin, O.; Vega, N.; Mato, A.; Quintero, J.; Rodriguez, H.; Regalado, S.; Gonzalez, F., 2022. First Light of the Integral Field Unit of GRIS on the GREGOR Solar Telescope. *Journal of Astronomical Instrumentation.* Vol. 11, no. 3, p. 2250014. Available from DOI: `10.1142/S2251171722500143`.

Dominique, M.; Zhukov, A. N.; Heinzel, P.; Dammasch, I. E.; Wauters, L.; Dolla, L.; Shestov, S.; Kretzschmar, M.; Machol, J.; Lapenta, G.; Schmutz, W., 2018. First Detection of Solar Flare Emission in Mid-ultraviolet Balmer Continuum. *ApJ.* Vol. 867, no. 2, p. L24. Available from DOI: `10.3847/2041-8213/aaeace`.

Duan, X.; Li, T.; Jing, Q., 2022. Dynamic Property and Magnetic Nonpotentiality of Two Types of Confined Solar Flares. *ApJ.* Vol. 933, no. 2, p. 191. Available from DOI: `10.3847/1538-4357/ac75c1`.

Evershed, J., 1909. Radial movement in sun-spots. *MNRAS*. Vol. 69, p. 454. Available from doi: `10.1093/mnras/69.5.454`.

Falco, M.; Puglisi, G.; Guglielmino, S. L.; Romano, P.; Ermolli, I.; Zuccarello, F., 2017. Comparison of different populations of granular features in the solar photosphere. *A&A*. Vol. 605, A87. Available from doi: `10.1051/0004-6361/201629881`.

Felipe, T.; Collados, M.; Khomenko, E.; Kuckein, C.; Asensio Ramos, A.; Balthasar, H.; Berkefeld, T.; Denker, C.; Feller, A.; Franz, M.; Hofmann, A.; Joshi, J.; Kiess, C.; Lagg, A.; Nicklas, H.; Orozco Suárez, D.; Pastor Yabar, A.; Rezaei, R.; Schlichenmaier, R.; Schmidt, D.; Schmidt, W.; Sigwarth, M.; Sobotka, M.; Solanki, S. K.; Soltau, D.; Staude, J.; Strassmeier, K. G.; Volkmer, R.; von der Lühe, O.; Waldmann, T., 2016. Three-dimensional structure of a sunspot light bridge. *A&A*. Vol. 596, A59. Available from doi: `10.1051/0004-6361/201629586`.

Fletcher, L.; Dennis, B. R.; Hudson, H. S.; Krucker, S.; Phillips, K.; Veronig, A.; Battaglia, M.; Bone, L.; Caspi, A.; Chen, Q.; Gallagher, P.; Grigis, P. T.; Ji, H.; Liu, W.; Milligan, R. O.; Temmer, M., 2011. An Observational Overview of Solar Flares. *Space Sci. Rev.* Vol. 159, no. 1-4, pp. 19–106. Available from doi: `10.1007/s11214-010-9701-8`.

Fletcher, L.; Hannah, I. G.; Hudson, H. S.; Metcalf, T. R., 2007. A TRACE White Light and RHESSI Hard X-Ray Study of Flare Energetics. *ApJ*. Vol. 656, no. 2, pp. 1187–1196. Available from doi: `10.1086/510446`.

Freeland, S. L.; Handy, B. N., 1998. Data Analysis with the SolarSoft System. *Sol. Phys.* Vol. 182, pp. 497–500. Available from doi: `10.1023/A:1005038224881`.

Garcia de La Rosa, J. I., 1987. Umbral Dots - a Case of Penetrative Convection Between Sunspot Fragments. *Sol. Phys.* Vol. 112, no. 1, pp. 49–58. Available from doi: `10.1007/BF00148486`.

García-Rivas, M.; Jurčák, J.; Bello González, N., 2021. Magnetic properties on the boundary of an evolving pore. *A&A*. Vol. 649, A129. Available from doi: `10.1051/0004-6361/202039661`.

García-Rivas, M.; Jurčák, J.; Bello González, N., 2024a. Magnetic properties of the umbral boundary during sunspot decay. Comparative study of multiple datasets. *A&A*. Available from doi: `10.1051/0004-6361/202348068`.

García-Rivas, M.; Jurčák, J.; Bello González, N.; Borrero, J. M.; Schlichenmaier, R.; Lindner, P., 2024b. Onset of penumbra formation. *A&A*. Vol. 686, A112. Available from doi: `10.1051/0004-6361/202348764`.

García-Rivas, M.; Kašparová, J.; Berlicki, A.; Švanda, M.; Dudík, J.; Čtvrtečka, D.; Zapiór, M.; Liu, W.; Sobotka, M.; Pavelková'; Motorina, G. G., 2024c. Flare heating of the chromosphere: Observations of flare continuum from GREGOR and IRIS. *A&A*.

Giordano, S.; Berrilli, F.; Del Moro, D.; Penza, V., 2008. The photospheric structure of a solar pore with light bridge. *A&A*. Vol. 489, no. 2, pp. 747–754. Available from doi: `10.1051/0004-6361:20077928`.

Golub, L.; DeLuca, E.; Austin, G.; Bookbinder, J.; Caldwell, D.; Cheimets, P.; Cirtain, J.; Cosmo, M.; Reid, P.; Sette, A.; Weber, M.; Sakao, T.; Kano, R.; Shibasaki, K.; Hara, H.; Tsuneta, S.; Kumagai, K.; Tamura, T.; Shimojo, M.; McCracken, J.; Carpenter, J.; Haight, H.; Siler, R.; Wright, E.; Tucker, J.; Rutledge, H.; Barbera, M.; Peres, G.; Varisco, S., 2007. The X-Ray Telescope (XRT) for the Hinode Mission. *Sol. Phys.* Vol. 243, no. 1, pp. 63–86. Available from DOI: `10.1007/s11207-007-0182-1`.

Gough, D. O.; Tayler, R. J., 1966. The influence of a magnetic field on Schwarzschild's criterion for convective instability in an ideally conducting fluid. *MNRAS*. Vol. 133, p. 85. Available from DOI: `10.1093/mnras/133.1.85`.

Graham, D. R.; Fletcher, L.; Labrosse, N., 2015. Determining energy balance in the flaring chromosphere from oxygen V line ratios. *A&A*. Vol. 584, A6. Available from DOI: `10.1051/0004-6361/201425348`.

Grossmann-Doerth, U.; Schmidt, W., 1981. The brightness distribution in sunspot penumbrae. *A&A*. Vol. 95, no. 2, pp. 366–372.

Grossmann-Doerth, U.; Schmidt, W.; Schroeter, E. H., 1986. Size and temperature of umbral dots. *A&A*. Vol. 156, p. 347.

Hale, G. E., 1908. On the Probable Existence of a Magnetic Field in Sun-Spots. *ApJ*. Vol. 28, p. 315. Available from DOI: `10.1086/141602`.

Harten, R.; Clark, K., 1995. The Design Features of the GGS Wind and Polar Spacecraft. *Space Sci. Rev.* Vol. 71, no. 1-4, pp. 23–40. Available from DOI: `10.1007/BF00751324`.

Harvey, K.; Harvey, J., 1973. Observations of Moving Magnetic Features near Sunspots. *Sol. Phys.* Vol. 28, no. 1, pp. 61–71. Available from DOI: `10.1007/BF00152912`.

Hathaway, D. H.; Choudhary, D. P., 2008. Sunspot Group Decay. *Sol. Phys.* Vol. 250, no. 2, pp. 269–278. Available from DOI: `10.1007/s11207-008-9226-4`.

Heinzel, P.; Kleint, L., 2014. Hydrogen Balmer Continuum in Solar Flares Detected by the Interface Region Imaging Spectrograph (IRIS). *ApJ*. Vol. 794, no. 2, p. L23. Available from DOI: `10.1088/2041-8205/794/2/L23`.

Heinzel, P.; Kleint, L.; Kašparová, J.; Krucker, S., 2017. On the Nature of Off-limb Flare Continuum Sources Detected by SDO/HMI. *ApJ*. Vol. 847, no. 1, p. 48. Available from DOI: `10.3847/1538-4357/aa86ef`.

Hidalgo, S. L.; Muñoz-Tuñón, C.; Castro-Almazán, J. A.; Varela, A. M., 2021. Canarian Observatories Meteorology; Comparison of OT and ORM using Regional Climate Reanalysis. *PASP*. Vol. 133, no. 1028, p. 105002. Available from DOI: `10.1088/1538-3873/ac2a6c`.

Hirzberger, J., 2003. Imaging spectroscopy of solar pores. *A&A*. Vol. 405, pp. 331–340. Available from DOI: `10.1051/0004-6361:20030595`.

Hirzberger, J.; Bonet, J. A.; Sobotka, M.; Vázquez, M.; Hanslmeier, A., 2002. Fine structure and dynamics in a light bridge inside a solar pore. *A&A*. Vol. 383, pp. 275–282. Available from DOI: `10.1051/0004-6361:20011685`.

Hoeksema, J. T.; Liu, Y.; Hayashi, K.; Sun, X.; Schou, J.; Couvidat, S.; Norton, A. A.; Bobra, M.; Centeno, R.; Leka, K. D.; Barnes, G.; Turmon, M., 2014. The Helioseismic and Magnetic Imager (HMI) Vector Magnetic Field Pipeline: Overview and Performance. *Sol. Phys.* Vol. 289, no. 9, pp. 3483–3530. Available from DOI: `10.1007/s11207-014-0516-8`.

Hurlburt, N. E.; Rucklidge, A. M., 2000. Development of structure in pores and sunspots: flows around axisymmetric magnetic flux tubes. *MNRAS*. Vol. 314, pp. 793–806. Available from doi: `10.1046/j.1365-8711.2000.03407.x`.

Ichimoto, K.; Lites, B. W.; Elmore, D.; Suematsu, Y.; Tsuneta, S.; Katsukawa, Y.; Shimizu, T.; Shine, R.; Tarbell, T.; Title, A.; Kiyohara, J.; Shinoda, K.; Card, G.; Lecinski, A.; Streander, K.; Nakagiri, M.; Miyashita, M.; Noguchi, M.; Hoffmann, C.; Cruz, T., 2008. Polarization Calibration of the Solar Optical Telescope onboard Hinode. *Sol. Phys.* Vol. 249, no. 2, pp. 233–261. Available from doi: `10.1007/s11207-008-9169-9`.

Ichimoto, K.; Shine, R. A.; Lites, B.; Kubo, M.; Shimizu, T.; Suematsu, Y.; Tsuneta, S.; Katsukawa, Y.; Tarbell, T. D.; Title, A. M.; Nagata, S.; Yokoyama, T.; Shimojo, M., 2007. Fine-Scale Structures of the Evershed Effect Observed by the Solar Optical Telescope aboard Hinode. *PASJ*. Vol. 59, S593. Available from doi: `10.1093/pasj/59.sp3.S593`.

Iglesias, F. A.; Feller, A., 2019. Instrumentation for solar spectropolarimetry: state of the art and prospects. *Optical Engineering*. Vol. 58, p. 082417. Available from doi: `10.1117/1.OE.58.8.082417`.

Jahn, K.; Schmidt, H. U., 1994. Thick penumbra in a magnetostatic sunspot model. *A&A*. Vol. 290, pp. 295–317. Available from eprint: `astro-ph/9410011`.

Jeffrey, N. L. S.; Fletcher, L.; Labrosse, N.; Simões, P. J. A., 2018. The development of lower-atmosphere turbulence early in a solar flare. *Science Advances*. Vol. 4, no. 12, p. 2794. Available from doi: `10.1126/sciadv.aav2794`.

Jess, D. B.; Mathioudakis, M.; Crockett, P. J.; Keenan, F. P., 2008. Do All Flares Have White-Light Emission? *ApJ*. Vol. 688, no. 2, p. L119. Available from doi: `10.1086/595588`.

Joshi, J.; Lagg, A.; Hirzberger, J.; Solanki, S. K.; Tiwari, S. K., 2017. Vertical magnetic field gradient in the photospheric layers of sunspots. *A&A*. Vol. 599, A35. Available from doi: `10.1051/0004-6361/201527060`.

Joshi, R.; Schmieder, B.; Heinzel, P.; Tomin, J.; Chandra, R.; Vilmer, N., 2021a. Balmer continuum enhancement detected in a mini flare observed with IRIS. *A&A*. Vol. 654, A31. Available from doi: `10.1051/0004-6361/202141172`.

Joshi, R.; Schmieder, B.; Tei, A.; Aulanier, G.; Lörinčík, J.; Chandra, R.; Heinzel, P., 2021b. Multi-thermal atmosphere of a mini-solar flare during magnetic reconnection observed with IRIS. *A&A*. Vol. 645, A80. Available from doi: `10.1051/0004-6361/202039229`.

Jurčák, J., 2011. Azimuthal variations of magnetic field strength and inclination on penumbral boundaries. *A&A*. Vol. 531, A118. Available from doi: `10.1051/0004-6361/201015959`.

Jurčák, J.; Bello González, N.; Schlichenmaier, R.; Rezaei, R., 2014a. Evolution of magnetic field inclination in a forming penumbra. *PASJ*. Vol. 66, S3. Available from doi: `10.1093/pasj/psu080`.

Jurčák, J.; Bello González, N.; Schlichenmaier, R.; Rezaei, R., 2015. A distinct magnetic property of the inner penumbral boundary. Formation of a stable umbra-penumbra boundary in a sunspot. *A&A*. Vol. 580, p. L1. Available from doi: `10.1051/0004-6361/201425501`.

Jurčák, J.; Bello González, N.; Schlichenmaier, R.; Rezaei, R., 2017a. A distinct magnetic property of the inner penumbral boundary. II. Formation of a penumbra at the expense of a pore. *A&A*. Vol. 597, A60. Available from DOI: `10.1051/0004-6361/201628547`.

Jurčák, J.; Bellot Rubio, L. R.; Sobotka, M., 2014b. Orphan penumbrae: Submerging horizontal fields. *A&A*. Vol. 564, A91. Available from DOI: `10.1051/0004-6361/201322340`.

Jurčák, J.; Kašparová, J.; Švanda, M.; Kleint, L., 2018a. Heating of the solar photosphere during a white-light flare. *A&A*. Vol. 620, A183. Available from DOI: `10.1051/0004-6361/201833946`.

Jurčák, J.; Lemmerer, B.; van Noort, M., 2017b. Granular cells in the presence of magnetic field. In: Vargas Domínguez, S.; Kosovichev, A. G.; Antolin, P.; Harra, L. (eds.). *Fine Structure and Dynamics of the Solar Atmosphere*. Vol. 327, pp. 34–39. Available from DOI: `10.1017/S1743921317000126`.

Jurčák, J.; Martínez Pillet, V.; Sobotka, M., 2006. The magnetic canopy above light bridges. *A&A*. Vol. 453, no. 3, pp. 1079–1088. Available from DOI: `10.1051/0004-6361:20054471`.

Jurčák, J.; Rezaei, R.; González, N. Bello; Schlichenmaier, R.; Vomlel, J., 2018b. The magnetic nature of umbra-penumbra boundary in sunspots. *A&A*. Vol. 611, p. L4. Available from DOI: `10.1051/0004-6361/201732528`.

Jurčák, J.; Schmassmann, M.; Rempel, M.; Bello González, N.; Schlichenmaier, R., 2020. A distinct magnetic property of the inner penumbral boundary. III. Analysis of simulated sunspots. *A&A*. Vol. 638, A28. Available from DOI: `10.1051/0004-6361/202037852`.

Kano, R.; Sakao, T.; Hara, H.; Tsuneta, S.; Matsuzaki, K.; Kumagai, K.; Shimojo, M.; Minesugi, K.; Shibasaki, K.; DeLuca, E. E.; Golub, L.; Bookbinder, J.; Caldwell, D.; Cheimets, P.; Cirtain, J.; Dennis, E.; Kent, T.; Weber, M., 2008. The Hinode X-Ray Telescope (XRT): Camera Design, Performance and Operations. *Sol. Phys.* Vol. 249, no. 2, pp. 263–279. Available from DOI: `10.1007/s11207-007-9058-7`.

Kašparová, J.; Carlsson, M.; Heinzel, P.; Varady, M., 2019. Modelling of Flare Processes: A Comparison of the Two RHD Codes FLARIX and RADYN. In: Werner, K.; Stehle, C.; Rauch, T.; Lanz, T. (eds.). *Radiative Signatures from the Cosmos*. Vol. 519, p. 141. Astronomical Society of the Pacific Conference Series.

Kašparová, J.; Čtvrtečka, D.; Heinzel, P.; Mravcová, L., in prep. On the Nature of Off-limb Flare Continuum Sources Detected by SDO/HMI.

Katsukawa, Y.; Berger, T. E.; Ichimoto, K.; Lites, B. W.; Nagata, S.; Shimizu, T.; Shine, R. A.; Suematsu, Y.; Tarbell, T. D.; Title, A. M.; Tsuneta, S., 2007. Small-Scale Jetlike Features in Penumbral Chromospheres. *Science*. Vol. 318, no. 5856, p. 1594. Available from DOI: `10.1126/science.1146046`.

Keller, C. U.; von der Luehe, O., 1992. Solar speckle polarimetry. *A&A*. Vol. 261, no. 1, pp. 321–328.

Keppens, R.; Martinez Pillet, V., 1996. The magnetic structure of pores and sunspots derived from Advanced Stokes Polarimeter data. *A&A*. Vol. 316, pp. 229–242.

Kerr, G. S.; Carlsson, M.; Allred, J. C.; Young, P. R.; Daw, A. N., 2019. SI IV Resonance Line Emission during Solar Flares: Non-LTE, Nonequilibrium, Radiation Transfer Simulations. *ApJ*. Vol. 871, no. 1, p. 23. Available from doi: `10.3847/1538-4357/aaf46e`.

Kerr, G. S.; Fletcher, L., 2014. Physical Properties of White-light Sources in the 2011 February 15 Solar Flare. *ApJ*. Vol. 783, no. 2, p. 98. Available from doi: `10.1088/0004-637X/783/2/98`.

Kleint, L.; Heinzel, P.; Judge, P.; Krucker, S., 2016. Continuum Enhancements in the Ultraviolet, the Visible and the Infrared during the X1 Flare on 2014 March 29. *ApJ*. Vol. 816, no. 2, p. 88. Available from doi: `10.3847/0004-637X/816/2/88`.

Kleint, L.; Heinzel, P.; Krucker, S., 2017. On the Origin of the Flare Emission in IRIS' SJI 2832 Filter:Balmer Continuum or Spectral Lines? *ApJ*. Vol. 837, no. 2, p. 160. Available from doi: `10.3847/1538-4357/aa62fe`.

Kleint, L.; Sainz Dalda, A., 2013. Unusual Filaments inside the Umbra. *ApJ*. Vol. 770, no. 1, p. 74. Available from doi: `10.1088/0004-637X/770/1/74`.

Kopp, G.; Rabin, D., 1992. A Relation Between Magnetic Field Strength and Temperature in Sunspots. *Sol. Phys.* Vol. 141, no. 2, pp. 253–265. Available from doi: `10.1007/BF00155178`.

Kosugi, T.; Matsuzaki, K.; Sakao, T.; Shimizu, T.; Sone, Y.; Tachikawa, S.; Hashimoto, T.; Minesugi, K.; Ohnishi, A.; Yamada, T.; Tsuneta, S.; Hara, H.; Ichimoto, K.; Suematsu, Y.; Shimojo, M.; Watanabe, T.; Shimada, S.; Davis, J. M.; Hill, L. D.; Owens, J. K.; Title, A. M.; Culhane, J. L.; Harra, L. K.; Doschek, G. A.; Golub, L., 2007. The Hinode (Solar-B) Mission: An Overview. *Sol. Phys.* Vol. 243, no. 1, pp. 3–17. Available from doi: `10.1007/s11207-007-9014-6`.

Kotrč, P., 2009. The Modernized Horizontal Spectrograph at the Ondřejov Observatory. *Central European Astrophysical Bulletin*. Vol. 33, pp. 327–336.

Kotrč, P.; Procházka, O.; Heinzel, P., 2016. New Observations of Balmer Continuum Flux in Solar Flares. Instrument Description and First Results. *Sol. Phys.* Vol. 291, no. 3, pp. 779–789. Available from doi: `10.1007/s11207-016-0860-y`.

Kretzschmar, M., 2011. The Sun as a star: observations of white-light flares. *A&A*. Vol. 530, A84. Available from doi: `10.1051/0004-6361/201015930`.

Kuckein, C.; Denker, C.; Verma, M.; Balthasar, H.; González Manrique, S. J.; Louis, R. E.; Diercke, A., 2017. sTools - a data reduction pipeline for the GREGOR Fabry-Pérot Interferometer and the High-resolution Fast Imager at the GREGOR solar telescope. In: Vargas Domínguez, S.; Kosovichev, A. G.; Antolin, P.; Harra, L. (eds.). *Fine Structure and Dynamics of the Solar Atmosphere*. Vol. 327, pp. 20–24. Available from doi: `10.1017/S1743921317000114`.

Kuckein, C.; Martínez Pillet, V.; Centeno, R., 2012. An active region filament studied simultaneously in the chromosphere and photosphere. I. Magnetic structure. *A&A*. Vol. 539, A131. Available from doi: `10.1051/0004-6361/201117675`.

Kuhar, M.; Krucker, S.; Martínez Oliveros, J. C.; Battaglia, M.; Kleint, L.; Casadei, D.; Hudson, H. S., 2016. Correlation of Hard X-Ray and White Light Emission in Solar Flares. *ApJ*. Vol. 816, no. 1, p. 6. Available from doi: `10.3847/0004-637X/816/1/6`.

Lagg, A.; Solanki, S. K.; van Noort, M.; Danilovic, S., 2014. Vigorous convection in a sunspot granular light bridge. *A&A*. Vol. 568, A60. Available from doi: `10.1051/0004-6361/201424071`.

Landi Degl'Innocenti, E.; Landi Degl'Innocenti, M., 1985. On the solution of the radiative transfer equations for polarized radiation. *Sol. Phys.* Vol. 97, pp. 239–250. Available from doi: `10.1007/BF00165988`.

Landi Degl'Innocenti, E.; Landolfi, M., 2004. *Polarization in Spectral Lines*. Vol. 307. Available from doi: `10.1007/978-1-4020-2415-3`.

Ledoux, P., 1947. Stellar Models with Convection and with Discontinuity of the Mean Molecular Weight. *ApJ*. Vol. 105, p. 305. Available from doi: `10.1086/144905`.

Leenaarts, J.; Carlsson, M.; Hansteen, V.; Rutten, R. J., 2007. Non-equilibrium hydrogen ionization in 2D simulations of the solar atmosphere. *A&A*. Vol. 473, no. 2, pp. 625–632. Available from doi: `10.1051/0004-6361:20078161`.

Leka, K. D., 1997. The Vector Magnetic Fields and Thermodynamics of Sunspot Light Bridges: The Case for Field-free Disruptions in Sunspots. *ApJ*. Vol. 484, no. 2, pp. 900–919. Available from doi: `10.1086/304363`.

Leka, K. D.; Barnes, G.; Crouch, A., 2009a. An Automated Ambiguity-Resolution Code for Hinode/SP Vector Magnetic Field Data. In: Lites, B.; Cheung, M.; Magara, T.; Mariska, J.; Reeves, K. (eds.). *The Second Hinode Science Meeting: Beyond Discovery-Toward Understanding*. Vol. 415, p. 365. Astronomical Society of the Pacific Conference Series.

Leka, K. D.; Barnes, G.; Crouch, A. D.; Metcalf, T. R.; Gary, G. A.; Jing, J.; Liu, Y., 2009b. Resolving the 180° Ambiguity in Solar Vector Magnetic Field Data: Evaluating the Effects of Noise, Spatial Resolution, and Method Assumptions. *Sol. Phys.* Vol. 260, no. 1, pp. 83–108. Available from doi: `10.1007/s11207-009-9440-8`.

Leka, K. D.; Skumanich, A., 1998. The Evolution of Pores and the Development of Penumbrae. *ApJ*. Vol. 507, no. 1, pp. 454–469. Available from doi: `10.1086/306297`.

Lemen, J. R.; Title, A. M.; Akin, D. J.; Boerner, P. F.; Chou, C.; Drake, J. F.; Duncan, D. W.; Edwards, C. G.; Friedlaender, F. M.; Heyman, G. F.; Hurlburt, N. E.; Katz, N. L.; Kushner, G. D.; Levay, M.; Lindgren, R. W.; Mathur, D. P.; McFeaters, E. L.; Mitchell, S.; Rehse, R. A.; Schrijver, C. J.; Springer, L. A.; Stern, R. A.; Tarbell, T. D.; Wuelser, J. P.; Wolfson, C. J.; Yanari, C.; Bookbinder, J. A.; Cheimets, P. N.; Caldwell, D.; Deluca, E. E.; Gates, R.; Golub, L.; Park, S.; Podgorski, W. A.; Bush, R. I.; Scherrer, P. H.; Gummin, M. A.; Smith, P.; Auker, G.; Jerram, P.; Pool, P.; Soufli, R.; Windt, D. L.; Beardsley, S.; Clapp, M.; Lang, J.; Waltham, N., 2012. The Atmospheric Imaging Assembly (AIA) on the Solar Dynamics Observatory (SDO). *Sol. Phys.* Vol. 275, no. 1-2, pp. 17–40. Available from doi: `10.1007/s11207-011-9776-8`.

Li, Q.; Yan, X.; Wang, J.; Kong, D.; Xue, Z; Yang, L.; Cao, W., 2018. The Formation of a Sunspot Penumbra Sector in Active Region NOAA 12574. *ApJ.* Vol. 857, no. 1, p. 21. Available from DOI: `10.3847/1538-4357/aab6b0`.

Li, Q.; Yan, X.; Wang, J.; Kong, D.; Xue, Z.; Yang, L., 2019. The Formation and Decay of Sunspot Penumbrae in Active Region NOAA 12673. *ApJ.* Vol. 886, no. 2, p. 149. Available from DOI: `10.3847/1538-4357/ab4f84`.

Li, Q.; Zhang, L.; Yan, X.; Norton, A. A.; Wang, J.; Yang, L.; Xue, Z.; Kong, D., 2022. Dependence of the Continuum Intensities on the Magnetic Fields at Different Evolution Phases of Sunspots. *ApJ.* Vol. 936, no. 1, p. 37. Available from DOI: `10.3847/1538-4357/ac83b3`.

Li, Q.; Zhang, L.; Yan, X.; Wang, J.; Kong, D.; Yang, L.; Xue, Z., 2021. The Decay of α-configuration Sunspots. *ApJ.* Vol. 913, no. 2, p. 147. Available from DOI: `10.3847/1538-4357/abfa1b`.

Li, T.; Liu, L.; Hou, Y.; Zhang, J., 2019. Two Types of Confined Solar Flares. *ApJ.* Vol. 881, no. 2, p. 151. Available from DOI: `10.3847/1538-4357/ab3121`.

Lim, E. K.; Yurchyshyn, V.; Goode, P.; Cho, K.-S., 2013. Observation of a Non-radial Penumbra in a Flux Emerging Region under Chromospheric Canopy Fields. *ApJ.* Vol. 769, p. L18. Available from DOI: `10.1088/2041-8205/769/1/L18`.

Lindner, P.; Kuckein, C.; González Manrique, S. J.; Bello González, N.; Kleint, L.; Berkefeld, T., 2023. The role of the chromospheric magnetic canopy in the formation of a sunspot penumbra. *A&A.* Vol. 673, A64. Available from DOI: `10.1051/0004-6361/202245702`.

Lindner, P.; Schlichenmaier, R.; Bello González, N., 2020. Characterization of the umbra-penumbra boundary by the vertical component of the magnetic field. Analysis of ground-based data from the GREGOR Infrared Spectrograph. *A&A.* Vol. 638, A25. Available from DOI: `10.1051/0004-6361/202037716`.

Lites, B. W.; Akin, D. L.; Card, G.; Cruz, T.; Duncan, D. W.; Edwards, C. G.; Elmore, D. F.; Hoffmann, C.; Katsukawa, Y.; Katz, N.; Kubo, M.; Ichimoto, K.; Shimizu, T.; Shine, R. A.; Streander, K. V.; Suematsu, A.; Tarbell, T. D.; Title, A. M.; Tsuneta, S., 2013a. The Hinode Spectro-Polarimeter. *Sol. Phys.* Vol. 283, no. 2, pp. 579–599. Available from DOI: `10.1007/s11207-012-0206-3`.

Lites, B. W.; Bida, T. A.; Johannesson, A.; Scharmer, G. B., 1991. High-Resolution Spectra of Solar Magnetic Features. II. Magnetic Fields of Umbral Brightenings. *ApJ.* Vol. 373, p. 683. Available from DOI: `10.1086/170089`.

Lites, B. W.; Casini, R.; Garcia, J.; Socas-Navarro, H., 2007. A suite of community tools for spectro-polarimetric analysis . *Mem. Soc. Astron. Italiana.* Vol. 78, p. 148.

Lites, B. W.; Elmore, D. F.; Seagraves, P.; Skumanich, A. P., 1993. Stokes Profile Analysis and Vector Magnetic Fields. VI. Fine Scale Structure of a Sunspot. *ApJ.* Vol. 418, p. 928. Available from DOI: `10.1086/173450`.

Lites, B. W.; Ichimoto, K., 2013b. The SP_PREP Data Preparation Package for the Hinode Spectro-Polarimeter. *Sol. Phys.* Vol. 283, no. 2, pp. 601–629. Available from DOI: `10.1007/s11207-012-0205-4`.

Lites, B. W.; Low, B. C.; Martinez Pillet, V.; Seagraves, P.; Skumanich, A.; Frank, Z. A.; Shine, R. A.; Tsuneta, S., 1995. The Possible Ascent of a Closed Magnetic System through the Photosphere. *ApJ.* Vol. 446, p. 877. Available from DOI: `10.1086/175845`.

Litvinenko, Y. E.; Wheatland, M. S., 2015. Modeling Sunspot and Starspot Decay by Turbulent Erosion. *ApJ.* Vol. 800, no. 2, p. 130. Available from DOI: `10.1088/0004-637X/800/2/130`.

Liu, W.; Heinzel, P.; Kleint, L.; Kašparová, J., 2015. Mg II Lines Observed During the X-class Flare on 29 March 2014 by the Interface Region Imaging Spectrograph. *Sol. Phys.* Vol. 290, no. 12, pp. 3525–3543. Available from DOI: `10.1007/s11207-015-0814-9`.

Liu, Y.; Baldner, C.; Bogart, R. S.; Bush, R.; Couvidat, S.; Duvall, T. L.; Hoeksema, J. T.; Norton, A. A.; Scherrer, P. H.; Schou, J., 2016. On HMI's Mod-L Sequence: Test and Evaluation. In: *AAS/Solar Physics Division Abstracts #47.* Vol. 47, p. 8.10. AAS/Solar Physics Division Meeting.

Löfdahl, M. G., 2002. Multi-frame blind deconvolution with linear equality constraints. In: Bones, Philip J.; Fiddy, Michael A.; Millane, Rick P. (eds.). *Image Reconstruction from Incomplete Data.* Vol. 4792, pp. 146–155. Society of Photo-Optical Instrumentation Engineers (SPIE) Conference Series. Available from DOI: `10.1117/12.451791`.

Löhner-Böttcher, J.; Schlichenmaier, R., 2013. Correlations between sunspots and their moat flows. *A&A.* Vol. 551, A105. Available from DOI: `10.1051/0004-6361/201220543`.

Löptien, B.; Lagg, A.; van Noort, M.; Solanki, S. K., 2018. Measuring the Wilson depression of sunspots using the divergence-free condition of the magnetic field vector. *A&A.* Vol. 619, A42. Available from DOI: `10.1051/0004-6361/201833571`.

Löptien, B.; Lagg, A.; van Noort, M.; Solanki, S. K., 2020. No universal connection between the vertical magnetic field and the umbra-penumbra boundary in sunspots. *A&A.* Vol. 639, A106. Available from DOI: `10.1051/0004-6361/202037974`.

Lörinčík, J.; Dudík, J.; Polito, V., 2022a. Blueshifted Si IV 1402.77 Å Line Profiles in a Moving Flare Kernel Observed by IRIS. *The Astrophysical Journal.* Vol. 934, no. 1, p. 80. Available from DOI: `10.3847/1538-4357/ac78e2`.

Lörinčík, J.; Polito, V.; De Pontieu, B.; Yu, S.; Freij, N., 2022b. Rapid variations of Si IV spectra in a flare observed by interface region imaging spectrograph at a sub-second cadence. *Frontiers in Astronomy and Space Sciences.* Vol. 9, p. 334. Available from DOI: `10.3389/fspas.2022.1040945`.

Loughhead, R. E.; Bray, R. J., 1961. Phenomena Accompanying the Birth of Sunspot Pores. *Australian Journal of Physics.* Vol. 14, p. 347. Available from DOI: `10.1071/PH610347`.

Louis, R. E.; Beck, C.; Choudhary, D. P., 2020. The Formation of an Atypical Sunspot Light Bridge as a Result of Large-scale Flux Emergence. *ApJ.* Vol. 905, no. 2, p. 153. Available from DOI: `10.3847/1538-4357/abc618`.

Louis, R. E.; Beck, C.; Mathew, S. K.; Venkatakrishnan, P., 2014. Anomalous flows in a sunspot penumbra. *A&A*. Vol. 570, A92. Available from DOI: 10.1051/0004-6361/201424112.

Lysenko, A. L.; Ulanov, M. V.; Kuznetsov, A. A.; Fleishman, G. D.; Frederiks, D. D.; Kashapova, L. K.; Sokolova, Z. Ya.; Svinkin, D. S.; Tsvetkova, A. E., 2022. KW-Sun: The Konus-Wind Solar Flare Database in Hard X-Ray and Soft Gamma-Ray Ranges. *ApJS*. Vol. 262, no. 1, p. 32. Available from DOI: 10.3847/1538-4365/ac8b87.

Machado, M. E.; Emslie, A. G.; Avrett, E. H., 1989. Radiative Backwarming in White-Light Flares. *Sol. Phys.* Vol. 124, no. 2, pp. 303–317. Available from DOI: 10.1007/BF00156272.

MacTaggart, D.; Guglielmino, S. L.; Zuccarello, F., 2016. The Pre-penumbral Magnetic Canopy in the Solar Atmosphere. *ApJ*. Vol. 831, p. L4. Available from DOI: 10.3847/2041-8205/831/1/L4.

Magara, T., 2010. A Magnetohydrodynamic Model Focused on the Configuration of Magnetic Field Responsible for a Solar Penumbral Microjet. *ApJ*. Vol. 715, no. 1, pp. L40–L43. Available from DOI: 10.1088/2041-8205/715/1/L40.

Martínez Oliveros, J. C.; Hudson, H. S.; Hurford, G. J.; Krucker, S.; Lin, R. P.; Lindsey, C.; Couvidat, S.; Schou, J.; Thompson, W. T., 2012. The Height of a White-light Flare and Its Hard X-Ray Sources. *ApJ*. Vol. 753, no. 2, p. L26. Available from DOI: 10.1088/2041-8205/753/2/L26.

Martinez Pillet, V.; Moreno-Insertis, F.; Vazquez, M., 1993. The distribution of sunspot decay rates. *A&A*. Vol. 274, pp. 521–533.

Martínez Pillet, V., 2002. Decay of sunspots. *Astronomische Nachrichten*. Vol. 323, pp. 342–348. Available from DOI: 10.1002/1521-3994(200208)323:3/4\textless{}342::AID-ASNA342\textgreater{}3.0.CO;2-5.

Mathew, S. K.; Martínez Pillet, V.; Solanki, S. K.; Krivova, N. A., 2007. Properties of sunspots in cycle 23. I. Dependence of brightness on sunspot size and cycle phase. *A&A*. Vol. 465, no. 1, pp. 291–304. Available from DOI: 10.1051/0004-6361:20066356.

Mathew, S. K.; Solanki, S. K.; Lagg, A.; Collados, M.; Borrero, J. M.; Berdyugina, S., 2004. Thermal-magnetic relation in a sunspot and a map of its Wilson depression. *A&A*. Vol. 422, pp. 693–701. Available from DOI: 10.1051/0004-6361:20040136.

Mauas, P. J. D.; Machado, M. E.; Avrett, E. H., 1990. The White-Light Flare of 1982 June 15: Models. *ApJ*. Vol. 360, p. 715. Available from DOI: 10.1086/169157.

McIntosh, P. S., 1981. The birth and evolution of sunspots - Observations. In: Cram, L. E.; Thomas, J. H. (eds.). *The Physics of Sunspots*, pp. 7–54.

Metcalf, T. R., 1994. Resolving the 180-degree ambiguity in vector magnetic field measurements: The ‘minimum’ energy solution. *Sol. Phys.* Vol. 155, no. 2, pp. 235–242. Available from DOI: 10.1007/BF00680593.

Metcalf, T. R.; Canfield, R. C.; Saba, J. L. R., 1990. Flare Heating and Ionization of the Low Solar Chromosphere. II. Observations of Five Solar Flares. *ApJ*. Vol. 365, p. 391. Available from DOI: 10.1086/169494.

Meyer, F.; Schmidt, H. U.; Weiss, N. O.; Wilson, P. R., 1974. The growth and decay of sunspots. *MNRAS*. Vol. 169, pp. 35–57. Available from DOI: 10.1093/mnras/169.1.35.

MILLIGAN, R. O.; KERR, G. S.; DENNIS, B. R.; HUDSON, H. S.; FLETCHER, L.; ALLRED, J. C.; CHAMBERLIN, P. C.; IRELAND, J.; MATHIOUDAKIS, M.; KEENAN, F. P., 2014. The Radiated Energy Budget of Chromospheric Plasma in a Major Solar Flare Deduced from Multi-wavelength Observations. *ApJ*. Vol. 793, no. 2, p. 70. Available from DOI: `10.1088/0004-637X/793/2/70`.

MULLAN, D. J.; MACDONALD, J., 2019. The Umbral-penumbral Boundary in Sunspots in the Context of Magnetoconvection. *ApJ*. Vol. 873, no. 2, p. L10. Available from DOI: `10.3847/2041-8213/ab0a0f`.

MULLER, R., 1973. Étude morphologique et cinématique des structures fines d'une tache solaire. *Sol. Phys.* Vol. 29, no. 1, pp. 55–73. Available from DOI: `10.1007/BF00153440`.

MÜLLER, D.; ST. CYR, O. C.; ZOUGANELIS, I.; GILBERT, H. R.; MARSDEN, R.; NIEVES-CHINCHILLA, T.; ANTONUCCI, E.; AUCHÈRE, F.; BERGHMANS, D.; HORBURY, T. S.; HOWARD, R. A.; KRUCKER, S.; MAKSIMOVIC, M.; OWEN, C. J.; ROCHUS, P.; RODRIGUEZ-PACHECO, J.; ROMOLI, M.; SOLANKI, S. K.; BRUNO, R.; CARLSSON, M.; FLUDRA, A.; HARRA, L.; HASSLER, D. M.; LIVI, S.; LOUARN, P.; PETER, H.; SCHÜHLE, U.; TERIACA, L.; DEL TORO INIESTA, J. C.; WIMMER-SCHWEINGRUBER, R. F.; MARSCH, E.; VELLI, M.; DE GROOF, A.; WALSH, A.; WILLIAMS, D., 2020. The Solar Orbiter mission. Science overview. *A&A*. Vol. 642, A1. Available from DOI: `10.1051/0004-6361/202038467`.

MURABITO, M.; ROMANO, P.; GUGLIELMINO, S. L.; ZUCCARELLO, F.; SOLANKI, S. K., 2016. Formation of the Penumbra and Start of the Evershed Flow. *ApJ*. Vol. 825, p. 75. Available from DOI: `10.3847/0004-637X/825/1/75`.

MURAKÖZY, J., 2020. Study of the Decay Rates of the Umbral Area of Sunspot Groups Using a High-resolution Database. *ApJ*. Vol. 892, no. 2, p. 107. Available from DOI: `10.3847/1538-4357/ab7898`.

NECKEL, H., 1994. Solar Absolute Reference Spectrum. In: PAP, J. M.; FROHLICH, C.; HUDSON, H. S.; SOLANKI, S. K. (eds.). *Invited Papers from IAU Colloquium 143: The Sun as a Variable Star: Solar and Stellar Irradiance Variations*, p. 37.

NEIDIG, D. F.; KANE, S. R., 1993. Energetics and Timing of the Hard and Soft X-Ray Emissions in White-Light Flares. *Sol. Phys.* Vol. 143, no. 1, pp. 201–204. Available from DOI: `10.1007/BF00619106`.

NEUPERT, W. M., 1968. Comparison of Solar X-Ray Line Emission with Microwave Emission during Flares. *ApJ*. Vol. 153, p. L59. Available from DOI: `10.1086/180220`.

O'DWYER, B.; DEL ZANNA, G.; MASON, H. E.; WEBER, M. A.; TRIPATHI, D., 2010. SDO/AIA response to coronal hole, quiet Sun, active region, and flare plasma. *A&A*. Vol. 521, A21. Available from DOI: `10.1051/0004-6361/201014872`.

ORTIZ, A.; BELLOT RUBIO, L. R.; ROUPPE VAN DER VOORT, L., 2010. Downflows in Sunspot Umbral Dots. *ApJ*. Vol. 713, no. 2, pp. 1282–1291. Available from DOI: `10.1088/0004-637X/713/2/1282`.

PANJA, M.; CAMERON, R. H.; SOLANKI, S. K., 2021. Sunspot Simulations: Penumbra Formation and the Fluting Instability. *ApJ*. Vol. 907, no. 2, p. 102. Available from DOI: `10.3847/1538-4357/abccbf`.

PESNELL, W. D.; THOMPSON, B. J.; CHAMBERLIN, P. C., 2012. The Solar Dynamics Observatory (SDO). *Sol. Phys.* Vol. 275, no. 1-2, pp. 3–15. Available from DOI: `10.1007/s11207-011-9841-3`.

PETROVAY, K.; MARTÍNEZ PILLET, V.; VAN DRIEL-GESZTELYI, L., 1999. Making sense of sunspot decay - II. Deviations from the Mean Law and Plage Effects. *Sol. Phys.* Vol. 188, no. 2, pp. 315–330. Available from DOI: `10.1023/A:1005213212336`.

PETROVAY, K.; MORENO-INSERTIS, F., 1997a. Turbulent Erosion of Magnetic Flux Tubes. *ApJ.* Vol. 485, no. 1, pp. 398–408. Available from DOI: `10.1086/304404`.

PETROVAY, K.; VAN DRIEL-GESZTELYI, L., 1997b. Making Sense of Sunspot Decay. I. Parabolic Decay Law and Gnevyshev-Waldmeier Relation. *Sol. Phys.* Vol. 176, no. 2, pp. 249–266. Available from DOI: `10.1023/A:1004988123265`.

PETTAUER, T.; BRANDT, P. N., 1997. On Novel Methods to Determine Areas of Sunspots from Photoheliograms. *Sol. Phys.* Vol. 175, no. 1, pp. 197–203. Available from DOI: `10.1023/A:1004903201224`.

PODUVAL, B.; DEFOREST, C. E.; SCHMELZ, J. T.; PATHAK, S., 2013. Point-spread Functions for the Extreme-ultraviolet Channels of SDO/AIA Telescopes. *ApJ.* Vol. 765, no. 2, p. 144. Available from DOI: `10.1088/0004-637X/765/2/144`.

POLITO, V.; DEL ZANNA, G.; DUDÍK, J.; MASON, H. E.; GIUNTA, A.; REEVES, K. K., 2016a. Density diagnostics derived from the O iv and S iv intercombination lines observed by IRIS. *A&A.* Vol. 594, A64. Available from DOI: `10.1051/0004-6361/201628965`.

POLITO, V.; REEP, J. W.; REEVES, K. K.; SIMÕES, P. J. A.; DUDÍK, J.; DEL ZANNA, G.; MASON, H. E.; GOLUB, L., 2016b. Simultaneous IRIS and Hinode/EIS Observations and Modelling of the 2014 October 27 X2.0 Class Flare. *ApJ.* Vol. 816, no. 2, p. 89. Available from DOI: `10.3847/0004-637X/816/2/89`.

POTTS, H.; HUDSON, H.; FLETCHER, L.; DIVER, D., 2010. The Optical Depth of White-light Flare Continuum. *ApJ.* Vol. 722, no. 2, pp. 1514–1521. Available from DOI: `10.1088/0004-637X/722/2/1514`.

PRESS, W. H.; TEUKOLSKY, S. A.; VETTERLING, W. T.; FLANNERY, B. P., 1992. *Numerical recipes in FORTRAN. The art of scientific computing; Cambridge: University Press.* Numerical recipes in FORTRAN. The art of scientific computing; Cambridge: University Press. Cambridge: University Press.

PUSCHMANN, K. G.; KNEER, F.; SEELEMANN, T.; WITTMANN, A. D., 2006a. The new Göttingen Fabry-Pérot spectrometer for two-dimensional observations of the Sun. *A&A.* Vol. 451, pp. 1151–1158. Available from DOI: `10.1051/0004-6361:20054487`.

PUSCHMANN, K. G.; SAILER, M., 2006b. Speckle reconstruction of photometric data observed with adaptive optics. *A&A.* Vol. 454, no. 3, pp. 1011–1019. Available from DOI: `10.1051/0004-6361:20053918`.

RACHKOVSKY, D. N., 1962. Magnetic rotation effects in spectral lines. *Izvestiya Ordena Trudovogo Krasnogo Znameni Krymskoj Astrofizicheskoj Observatorii.* Vol. 28, pp. 259–270.

REMPEL, M., 2011. Penumbral Fine Structure and Driving Mechanisms of Large-scale Flows in Simulated Sunspots. *ApJ.* Vol. 729, no. 1, p. 5. Available from DOI: `10.1088/0004-637X/729/1/5`.

REMPEL, M., 2012. Numerical Sunspot Models: Robustness of Photospheric Velocity and Magnetic Field Structure. *ApJ.* Vol. 750, p. 62. Available from DOI: `10.1088/0004-637X/750/1/62`.

Rempel, M., 2015. Numerical Simulations of Sunspot Decay: On the Penumbra-Evershed Flow-Moat Flow Connection. *ApJ*. Vol. 814, no. 2, p. 125. Available from doi: `10.1088/0004-637X/814/2/125`.

Rempel, M.; Schüssler, M.; Cameron, R. H.; Knölker, M., 2009. Penumbral Structure and Outflows in Simulated Sunspots. *Science*. Vol. 325, no. 5937, p. 171. Available from doi: `10.1126/science.1173798`.

Rezaei, R.; Bello González, N.; Schlichenmaier, R., 2012. The formation of sunspot penumbra. Magnetic field properties. *A&A*. Vol. 537, A19. Available from doi: `10.1051/0004-6361/201117485`.

Riethmüller, T. L.; Solanki, S. K.; van Noort, M.; Tiwari, S. K., 2013. Vertical flows and mass flux balance of sunspot umbral dots. *A&A*. Vol. 554, A53. Available from doi: `10.1051/0004-6361/201321075`.

Riethmüller, T. L.; Solanki, S. K.; Zakharov, V.; Gandorfer, A., 2008. Brightness, distribution, and evolution of sunspot umbral dots. *A&A*. Vol. 492, no. 1, pp. 233–243. Available from doi: `10.1051/0004-6361:200810701`.

Rimmele, T., 2008. On the Relation between Umbral Dots, Dark-cored Filaments, and Light Bridges. *ApJ*. Vol. 672, no. 1, pp. 684–695. Available from doi: `10.1086/523702`.

Romano, P.; Frasca, D.; Guglielmino, S. L.; Ermolli, I.; Tritschler, A.; Reardon, K. P.; Zuccarello, F., 2013. Velocity and Magnetic Field Distribution in a Forming Penumbra. *ApJ*. Vol. 771, p. L3. Available from doi: `10.1088/2041-8205/771/1/L3`.

Romano, P.; Guglielmino, S. L.; Cristaldi, A.; Ermolli, I.; Falco, M.; Zuccarello, F., 2014. Evolution of the Magnetic Field Inclination in a Forming Penumbra. *ApJ*. Vol. 784, p. 10. Available from doi: `10.1088/0004-637X/784/1/10`.

Romano, P.; Murabito, M.; Guglielmino, S. L.; Zuccarello, F.; Falco, M., 2020. Restoring Process of Sunspot Penumbra. *ApJ*. Vol. 899, no. 2, p. 129. Available from doi: `10.3847/1538-4357/aba18b`.

Roudier, Th.; Bonet, J. A.; Sobotka, M., 2002. Properties of horizontal flows inside and outside a solar pore. *A&A*. Vol. 395, pp. 249–255. Available from doi: `10.1051/0004-6361:20021259`.

Rucklidge, A. M.; Schmidt, H. U.; Weiss, N. O., 1995. The abrupt development of penumbrae in sunspots. *MNRAS*. Vol. 273, no. 2, pp. 491–498. Available from doi: `10.1093/mnras/273.2.491`.

Ruiz Cobo, B.; del Toro Iniesta, J. C., 1992. Inversion of Stokes Profiles. *ApJ*. Vol. 398, p. 375. Available from doi: `10.1086/171862`.

Sainz Dalda, A., 2017. A Statistical Comparison between Photospheric Vector Magnetograms Obtained by SDO/HMI and Hinode/SP. *ApJ*. Vol. 851, no. 2, p. 111. Available from doi: `10.3847/1538-4357/aa97e3`.

Scharmer, G. B.; Gudiksen, B. V.; Kiselman, D.; Löfdahl, M. G.; Rouppe van der Voort, L. H. M., 2002. Dark cores in sunspot penumbral filaments. *Nature*. Vol. 420, no. 6912, pp. 151–153. Available from doi: `10.1038/nature01173`.

Scharmer, G. B.; Henriques, V. M. J.; Kiselman, D.; de la Cruz Rodríguez, J., 2011. Detection of Convective Downflows in a Sunspot Penumbra. *Science*. Vol. 333, no. 6040, p. 316. Available from doi: `10.1126/science.1206429`.

Scherrer, P. H.; Schou, J.; Bush, R. I.; Kosovichev, A. G.; Bogart, R. S.; Hoeksema, J. T.; Liu, Y.; Duvall, T. L.; Zhao, J.; Title, A. M.; Schrijver, C. J.; Tarbell, T. D.; Tomczyk, S., 2012. The Helioseismic and Magnetic Imager (HMI) Investigation for the Solar Dynamics Observatory (SDO). *Sol. Phys.* Vol. 275, no. 1-2, pp. 207–227. Available from DOI: `10.1007/s11207-011-9834-2`.

Schlichenmaier, R., 2009. Sunspots: From Small-Scale Inhomogeneities Towards a Global Theory. *Space Sci. Rev.* Vol. 144, no. 1-4, pp. 213–228. Available from DOI: `10.1007/s11214-008-9465-6`.

Schlichenmaier, R.; Bello González, N.; Rezaei, R., 2011. The formation of a penumbra as observed with the German VTT and SoHO/MDI. In: Prasad Choudhary, D.; Strassmeier, K. G. (eds.). *Physics of Sun and Star Spots*. Vol. 273, pp. 134–140. IAU Symposium. Available from DOI: `10.1017/S1743921311015134`.

Schlichenmaier, R.; Bello González, N.; Rezaei, R.; Waldmann, T. A., 2010a. The role of emerging bipoles in the formation of a sunspot penumbra. *Astronomische Nachrichten*. Vol. 331, p. 563. Available from DOI: `10.1002/asna.201011372`.

Schlichenmaier, R.; Rezaei, R.; Bello González, N., 2012. On the Formation of Penumbrae as Observed with the German VTT SOHO/MDI, and SDO/HMI. In: Bellot Rubio, L.; Reale, F.; Carlsson, M. (eds.). *4th Hinode Science Meeting: Unsolved Problems and Recent Insights*. Vol. 455, p. 61. Astronomical Society of the Pacific Conference Series. Available from arXiv: `1102.0965 [astro-ph.SR]`.

Schlichenmaier, R.; Rezaei, R.; Bello González, N.; Waldmann, T. A., 2010b. The formation of a sunspot penumbra. *A&A*. Vol. 512, p. L1. Available from DOI: `10.1051/0004-6361/201014112`.

Schmassmann, M.; Rempel, M.; Bello González, N.; Schlichenmaier, R.; Jurčák, J., 2021. Characterization of magneto-convection in sunspots. The Gough-Tayler stability criterion in MURaM sunspot simulations. *A&A*. Vol. 656, A92. Available from DOI: `10.1051/0004-6361/202141607`.

Schmassmann, M.; Schlichenmaier, R.; Bello González, N., 2018. Magnetic properties of a long-lived sunspot. Vertical magnetic field at the umbral boundary. *A&A*. Vol. 620, A104. Available from DOI: `10.1051/0004-6361/201833441`.

Schmidt, H. U., 1968. Magnetohydrodynamics of an Active Region. In: Kiepenheuer, Karl Otto (ed.). *Structure and Development of Solar Active Regions*. Vol. 35, p. 95.

Schmidt, W.; Grossmann-Doerth, U.; Schroeter, E. H., 1988. The solar granulation in the vicinity of sunspots. *A&A*. Vol. 197, no. 1-2, pp. 306–310.

Schmidt, W.; von der Lühe, O.; Volkmer, R.; Denker, C.; Solanki, S. K.; Balthasar, H.; Bello Gonzalez, N.; Berkefeld, Th.; Collados, M.; Fischer, A.; Halbgewachs, C.; Heidecke, F.; Hofmann, A.; Kneer, F.; Lagg, A.; Nicklas, H.; Popow, E.; Puschmann, K. G.; Schmidt, D.; Sigwarth, M.; Sobotka, M.; Soltau, D.; Staude, J.; Strassmeier, K. G.; Waldmann, T. A., 2012. The 1.5 meter solar telescope GREGOR. *Astronomische Nachrichten*. Vol. 333, no. 9, p. 796. Available from DOI: `10.1002/asna.201211725`.

Schou, J.; Scherrer, P. H.; Bush, R. I.; Wachter, R.; Couvidat, S.; Rabello-Soares, M. C.; Bogart, R. S.; Hoeksema, J. T.; Liu, Y.; Duvall, T. L.; Akin, D. J.; Allard, B. A.; Miles, J. W.; Rairden, R.; Shine, R. A.; Tarbell, T. D.; Title, A. M.; Wolfson, C. J.; Elmore, D. F.; Norton, A. A.; Tomczyk, S., 2012. Design and Ground Calibration of the Helioseismic and Magnetic Imager (HMI) Instrument on the Solar Dynamics Observatory (SDO). *Sol. Phys.* Vol. 275, no. 1-2, pp. 229–259. Available from DOI: `10.1007/s11207-011-9842-2`.

Schroeter, E. H.; Soltau, D.; Wiehr, E., 1985. The German solar telescopes at the observatorio del Teide. *Vistas in Astronomy.* Vol. 28, no. 2, pp. 519–527. Available from DOI: `10.1016/0083-6656(85)90073-X`.

Schüssler, M.; Vögler, A., 2006. Magnetoconvection in a Sunspot Umbra. *ApJ.* Vol. 641, no. 1, pp. L73–L76. Available from DOI: `10.1086/503772`.

Schwarzschild, K., 1906. On the equilibrium of the Sun's atmosphere. *Nachrichten von der Königlichen Gesellschaft der Wissenschaften zu Göttingen. Math.-phys. Klasse.* Vol. 195, pp. 41–53.

Sheeley N. R., Jr., 1972. Observations of the Horizontal Velocity Field Surrounding Sunspots. *Sol. Phys.* Vol. 25, no. 1, pp. 98–103. Available from DOI: `10.1007/BF00155747`.

Shimizu, T.; Ichimoto, K.; Suematsu, Y., 2012. Precursor of Sunspot Penumbral Formation Discovered with Hinode Solar Optical Telescope Observations. *ApJ.* Vol. 747, p. L18. Available from DOI: `10.1088/2041-8205/747/2/L18`.

Shine, R. A.; Title, A. M.; Tarbell, T. D.; Smith, K.; Frank, Z. A.; Scharmer, Goran, 1994. High-Resolution Observations of the Evershed Effect in Sunspots. *ApJ.* Vol. 430, p. 413. Available from DOI: `10.1086/174416`.

Simões, P. J. A.; Kerr, G. S.; Fletcher, L.; Hudson, H. S.; Giménez de Castro, C. G.; Penn, M., 2017. Formation of the thermal infrared continuum in solar flares. *A&A.* Vol. 605, A125. Available from DOI: `10.1051/0004-6361/201730856`.

Simões, P. J. A.; Reid, H. A. S.; Milligan, R. O.; Fletcher, L., 2019. The Spectral Content of SDO/AIA 1600 and 1700 Å Filters from Flare and Plage Observations. *ApJ.* Vol. 870, no. 2, p. 114. Available from DOI: `10.3847/1538-4357/aaf28d`.

Simon, G. W.; Weiss, N. O., 1970. On the Magnetic Field in Pores. *Sol. Phys.* Vol. 13, no. 1, pp. 85–103. Available from DOI: `10.1007/BF00963944`.

Siu-Tapia, A. L.; Lagg, A.; Solanki, S. K.; van Noort, M.; Jurčák, J., 2017. Normal and counter Evershed flows in the photospheric penumbra of a sunspot. SPINOR 2D inversions of Hinode-SOT/SP observations. *A&A.* Vol. 607, A36. Available from DOI: `10.1051/0004-6361/201730647`.

Siu-Tapia, A. L.; Rempel, M.; Lagg, A.; Solanki, S. K., 2018. Evershed and Counter-Evershed Flows in Sunspot MHD Simulations. *ApJ.* Vol. 852, no. 2, p. 66. Available from DOI: `10.3847/1538-4357/aaa007`.

Smirnova, V. V.; Tsap, Yu. T.; Ryzhov, V. S.; Motorina, G. G.; Morgachev, A. S.; Bárta, M., 2023. The Flare Emission of the May 4, 2022 Event and Its Millimeter Component. *Geomagnetism and Aeronomy.* Vol. 63, no. 5, pp. 527–535. Available from DOI: `10.1134/S0016793223600558`.

Sobotka, M.; Bonet, J. A.; Vazquez, M., 1993. A High-Resolution Study of Inhomogeneities in Sunspot Umbrae. *ApJ*. Vol. 415, p. 832. Available from doi: `10.1086/173205`.

Sobotka, M.; Bonet, J. A.; Vazquez, M., 1994. A High-Resolution Study of the Structure of Sunspot Light Bridges and Abnormal Granulation. *ApJ*. Vol. 426, p. 404. Available from doi: `10.1086/174076`.

Sobotka, M.; Bonet, J. A.; Vazquez, M.; Hanslmeier, A., 1995. On the Dynamics of Bright Features in Sunspot Umbrae. *ApJ*. Vol. 447, p. L133. Available from doi: `10.1086/309569`.

Sobotka, M.; Brandt, P. N.; Simon, G. W., 1997. Fine structure in sunspots. I. Sizes and lifetimes of umbral dots. *A&A*. Vol. 328, pp. 682–688.

Sobotka, M.; Brandt, P. N.; Simon, G. W., 1999a. Fine structure in sunspots. III. Penumbral grains. *A&A*. Vol. 348, pp. 621–626.

Sobotka, M.; Jurčák, J., 2009a. Evolution of Physical Characteristics of Umbral Dots and Penumbral Grains. *ApJ*. Vol. 694, no. 2, pp. 1080–1084. Available from doi: `10.1088/0004-637X/694/2/1080`.

Sobotka, M.; Jurčák, J.; Castellanos Durán, J. S.; García-Rivas, M., 2024. The relation between magnetic field inclination and the apparent motion of penumbral grains. *A&A*. Vol. 682, A65. Available from doi: `10.1051/0004-6361/202347979`.

Sobotka, M.; Puschmann, K. G., 2009b. Morphology and evolution of umbral dots and their substructures. *A&A*. Vol. 504, no. 2, pp. 575–581. Available from doi: `10.1051/0004-6361/200912365`.

Sobotka, M.; Vázquez, M.; Bonet, J. A.; Hanslmeier, A.; Hirzberger, J., 1999b. Temporal Evolution of Fine Structures in and around Solar Pores. *ApJ*. Vol. 511, no. 1, pp. 436–450. Available from doi: `10.1086/306671`.

Solanki, S. K., 2003. Sunspots: An overview. *A&A Rev.* Vol. 11, no. 2-3, pp. 153–286. Available from doi: `10.1007/s00159-003-0018-4`.

Solanki, S. K.; Montavon, C. A. P., 1993. Uncombed fields as the source of the broad-band circular polarization of sunspots. *A&A*. Vol. 275, pp. 283–292.

Staath, E.; Lemaire, P., 1995. High resolution profiles of the MG II H and MG II K lines. *A&A*. Vol. 295, pp. 517–528.

Stenflo, J., 1994. *Solar Magnetic Fields: Polarized Radiation Diagnostics*. Vol. 189. Available from doi: `10.1007/978-94-015-8246-9`.

Strecker, H.; Bello González, N., 2022. Evolution of the flow field in decaying active regions. II. Converging flows at the periphery of naked spots. *A&A*. Vol. 664, A195. Available from doi: `10.1051/0004-6361/202142564`.

Strecker, H.; Schmidt, W.; Schlichenmaier, R.; Rempel, M., 2021. On the (in)stability of sunspots. *A&A*. Vol. 649, A123. Available from doi: `10.1051/0004-6361/202040199`.

Suetterlin, P., 1998. Properties of solar pores. *A&A*. Vol. 333, pp. 305–312.

ŠVANDA, M.; JURČÁK, J.; KAŠPAROVÁ, J.; KLEINT, L., 2018. Understanding the HMI Pseudocontinuum in White-light Solar Flares. *ApJ.* Vol. 860, no. 2, p. 144. Available from DOI: `10.3847/1538-4357/aac3e4`.

ŠVANDA, M.; SOBOTKA, M.; MRAVCOVÁ, L.; VÝBOŠŤOKOVÁ, T., 2021. Evolution and motions of magnetic fragments during the active region formation and decay: A statistical study. *A&A.* Vol. 647, A146. Available from DOI: `10.1051/0004-6361/202040127`.

THE SUNPY COMMUNITY; BARNES, W. T.; BOBRA, M G.; CHRISTE, S. D.; FREIJ, N.; HAYES, L. A.; IRELAND, Jack; MUMFORD, Stuart; PEREZ-SUAREZ, David; RYAN, Daniel F.; SHIH, Albert Y.; CHANDA, Prateek; GLOGOWSKI, Kolja; HEWETT, Russell; HUGHITT, V. Keith; HILL, Andrew; HIWARE, Kaustubh; INGLIS, Andrew; KIRK, Michael S. F.; KONGE, Sudarshan; MASON, James Paul; MALONEY, Shane Anthony; MURRAY, Sophie A.; PANDA, Asish; PARK, Jongyeob; PEREIRA, Tiago M. D.; REARDON, Kevin; SAVAGE, Sabrina; SIPŐCZ, Brigitta M.; STANSBY, David; JAIN, Yash; TAYLOR, Garrison; YADAV, Tannmay; RAJUL; DANG, Trung Kien, 2020. The SunPy Project: Open Source Development and Status of the Version 1.0 Core Package. *The Astrophysical Journal.* Vol. 890, pp. 68–. Available from DOI: `10.3847/1538-4357/ab4f7a`.

THOMAS, J. H.; WEISS, N. O., 2004. Fine Structure in Sunspots. *ARA&A.* Vol. 42, no. 1, pp. 517–548. Available from DOI: `10.1146/annurev.astro.42.010803.115226`.

TIWARI, S. K; VAN NOORT, M.; LAGG, A.; SOLANKI, S. K., 2013. Structure of sunspot penumbral filaments: a remarkable uniformity of properties. *A&A.* Vol. 557, A25. Available from DOI: `10.1051/0004-6361/201321391`.

TRUJILLO BUENO, J., 2006. A Gentle Introduction to the Physics of Spectral Line Polarization. In: *Solar Physics and Solar Eclipses (SPSE 2006)*, pp. 77–92.

TSUNETA, S.; ICHIMOTO, K.; KATSUKAWA, Y.; NAGATA, S.; OTSUBO, M.; SHIMIZU, T.; SUEMATSU, Y.; NAKAGIRI, M.; NOGUCHI, M.; TARBELL, T.; TITLE, A.; SHINE, R.; ROSENBERG, W.; HOFFMANN, C.; JURCEVICH, B.; KUSHNER, G.; LEVAY, M.; LITES, B. W.; ELMORE, D.; MATSUSHITA, T.; KAWAGUCHI, N.; SAITO, H.; MIKAMI, I.; HILL, L. D.; OWENS, J. K., 2008. The Solar Optical Telescope for the Hinode Mission: An Overview. *Sol. Phys.* Vol. 249, no. 2, pp. 167–196. Available from DOI: `10.1007/s11207-008-9174-z`.

UNNO, W., 1956. Line Formation of a Normal Zeeman Triplet. *PASJ.* Vol. 8, p. 108.

VALIO, A.; SPAGIARI, E.; MARENGONI, M.; SELHORST, C. L., 2020. Correlations of Sunspot Physical Characteristics during Solar Cycle 23. *Sol. Phys.* Vol. 295, no. 9, p. 120. Available from DOI: `10.1007/s11207-020-01691-3`.

VAN DER LUEHE, O.; SOLTAU, D.; BERKEFELD, T.; SCHELENZ, T., 2003. KAOS: Adaptive optics system for the Vacuum Tower Telescope at Teide Observatory. In: KEIL, Stephen L.; AVAKYAN, Sergey V. (eds.). *Innovative Telescopes and Instrumentation for Solar Astrophysics.* Vol. 4853, pp. 187–193. Society of Photo-Optical Instrumentation Engineers (SPIE) Conference Series. Available from DOI: `10.1117/12.498659`.

Varela, A. M.; Muñz-Tuñón, C.; de Gurtubai, A.; Saviron, C., 2002.
Site-testing results at the Teide Observatory.
In: Vernin, Jean; Benkhaldoun, Zouhair; Muñoz-Tuñón, Casiana (eds.).
Astronomical Site Evaluation in the Visible and Radio Range. Vol. 266, p. 454.
Astronomical Society of the Pacific Conference Series.

Vargas Domínguez, S.; de Vicente, A.; Bonet, J. A.; Martínez Pillet, V., 2010. Characterization of horizontal flows around solar pores from high-resolution time series of images. *A&A*. Vol. 516, A91.
Available from doi: `10.1051/0004-6361/200913264`.

Verma, M.; Denker, C., 2014. Horizontal flow fields observed in Hinode G-band images. IV. Statistical properties of the dynamical environment around pores. *A&A*. Vol. 563, A112. Available from doi: `10.1051/0004-6361/201322476`.

Verma, M.; Denker, C.; Balthasar, H.; Kuckein, C.; González Manrique, S. J.; Sobotka, M.; Bello González, N.; Hoch, S.; Diercke, A.; Kummerow, P.; Berkefeld, T.; Collados, M.; Feller, A.; Hofmann, A.; Kneer, F.; Lagg, A.; Löhner-Böttcher, J.; Nicklas, H.; Pastor Yabar, A.; Schlichenmaier, R.; Schmidt, D.; Schmidt, W.; Schubert, M.; Sigwarth, M.; Solanki, S. K.; Soltau, D.; Staude, J.; Strassmeier, K. G.; Volkmer, R.; von der Lühe, O.; Waldmann, T., 2016. Horizontal flow fields in and around a small active region. The transition period between flux emergence and decay. *A&A*. Vol. 596, A3.
Available from doi: `10.1051/0004-6361/201628380`.

Verma, M.; Denker, C.; Balthasar, H.; Kuckein, C.; Rezaei, R.; Sobotka, M.; Deng, N.; Wang, H.; Tritschler, A.; Collados, M.; Diercke, A.; González Manrique, S. J., 2018.
High-resolution imaging and near-infrared spectroscopy of penumbral decay. *A&A*. Vol. 614, A2. Available from doi: `10.1051/0004-6361/201731801`.

Vigeesh, G.; Jackiewicz, J.; Steiner, O., 2017. Internal Gravity Waves in the Magnetized Solar Atmosphere. I. Magnetic Field Effects. *ApJ*.
Vol. 835, no. 2, p. 148. Available from doi: `10.3847/1538-4357/835/2/148`.

Wachter, R.; Schou, J.; Rabello-Soares, M. C.; Miles, J. W.; Duvall, T. L.; Bush, R. I., 2012. Image Quality of the Helioseismic and Magnetic Imager (HMI) Onboard the Solar Dynamics Observatory (SDO). *Sol. Phys.*
Vol. 275, no. 1-2, pp. 261–284. Available from doi: `10.1007/s11207-011-9709-6`.

Wang, H.; Liu, C.; Qiu, J.; Deng, N.; Goode, P. R.; Denker, C., 2004.
Rapid Penumbral Decay following Three X-Class Solar Flares. *ApJ*.
Vol. 601, no. 2, pp. L195–L198. Available from doi: `10.1086/382188`.

Wang, H.; Zirin, H., 1992. Flows around Sunspots and Pores. *Sol. Phys.*
Vol. 140, no. 1, pp. 41–54. Available from doi: `10.1007/BF00148428`.

Watanabe, H., 2014. Observations of umbral dots and their physical models. *PASJ*.
Vol. 66, S1. Available from doi: `10.1093/pasj/psu102`.

Watanabe, H.; Kitai, R.; Otsuji, K., 2014.
Formation and Decay of Rudimentary Penumbra around a Pore. *ApJ*.
Vol. 796, no. 2, p. 77. Available from doi: `10.1088/0004-637X/796/2/77`.

Wentzel, D. G., 1992. Structure of sunspot penumbrae - Fallen magnetic flux tubes. *ApJ*. Vol. 388, pp. 211–217. Available from doi: `10.1086/171145`.

Westendorp Plaza, C.; del Toro Iniesta, J. C.; Ruiz Cobo, B.; Martínez Pillet, V.; Lites, B. W.; Skumanich, A., 2001. Optical Tomography of a Sunspot. II. Vector Magnetic Field and Temperature Stratification. *ApJ.* Vol. 547, no. 2, pp. 1130–1147. Available from DOI: `10.1086/318376`.

Woods, T. N.; Eparvier, F. G.; Hock, R.; Jones, A. R.; Woodraska, D.; Judge, D.; Didkovsky, L.; Lean, J.; Mariska, J.; Warren, H.; McMullin, D.; Chamberlin, P.; Berthiaume, G.; Bailey, S.; Fuller-Rowell, T.; Sojka, J.; Tobiska, W. K.; Viereck, R., 2012. Extreme Ultraviolet Variability Experiment (EVE) on the Solar Dynamics Observatory (SDO): Overview of Science Objectives, Instrument Design, Data Products, and Model Developments. *Sol. Phys.* Vol. 275, no. 1-2, pp. 115–143. Available from DOI: `10.1007/s11207-009-9487-6`.

Xu, Y.; Cao, W.; Jing, J.; Wang, H., 2012. Characteristic Size of Flare Kernels in the Visible and Near-infrared Continua. *ApJ.* Vol. 750, no. 1, p. L7. Available from DOI: `10.1088/2041-8205/750/1/L7`.

Xu, Y.; Cao, W.; Liu, C.; Yang, G.; Jing, J.; Denker, C.; Emslie, A. G.; Wang, H., 2006. High-Resolution Observations of Multiwavelength Emissions during Two X-Class White-Light Flares. *ApJ.* Vol. 641, no. 2, pp. 1210–1216. Available from DOI: `10.1086/500632`.

Yadav, R.; Mathew, S. K., 2018. Physical Properties of Umbral Dots Observed in Sunspots: A Hinode Observation. *Sol. Phys.* Vol. 293, no. 4, p. 54. Available from DOI: `10.1007/s11207-018-1272-y`.

Young, P. R.; Doschek, G. A.; Warren, H. P.; Hara, H., 2013. Properties of a Solar Flare Kernel Observed by Hinode and SDO. *ApJ.* Vol. 766, no. 2, p. 127. Available from DOI: `10.1088/0004-637X/766/2/127`.

Yurchyshyn, V.; Kumar, P.; Abramenko, V.; Xu, Y.; Goode, P. R.; Cho, K. -S.; Lim, E. -K., 2017. High-resolution Observations of a White-light Flare with NST. *ApJ.* Vol. 838, no. 1, p. 32. Available from DOI: `10.3847/1538-4357/aa633f`.

Zapiór, M.; Heinzel, P.; Khomenko, E., 2022. Doppler-velocity Drifts Detected in a Solar Prominence. *ApJ.* Vol. 934, no. 1, p. 16. Available from DOI: `10.3847/1538-4357/ac778a`.

Zeeman, P., 1897a. VII. Doublets and triplets in the spectrum produced by external magnetic forces. *Phil. Mag.* Vol. 44, no. 266, pp. 55–60. Available from DOI: `10.1080/14786449708621028`.

Zeeman, P., 1897b. XXXII. On the influence of magnetism on the nature of the light emitted by a substance. *Phil. Mag.* Vol. 43, no. 262, pp. 226–239. Available from DOI: `10.1080/14786449708620985`.

Zeeman, P., 1897c. XXXIII. Doublets and triplets in the spectrum produced by external magnetic forces.—(II.) *Phil. Mag.* Vol. 44, no. 268, pp. 255–259. Available from DOI: `10.1080/14786449708621060`.

Zhang, Y.; Ichimoto, K., 2013. Properties of sunspot penumbral grains observed with Hinode. *A&A.* Vol. 560, A77. Available from DOI: `10.1051/0004-6361/201118119`.

Zuccarello, F.; Guglielmino, S. L.; Romano, P., 2014. Evolution and Dynamics of Orphan Penumbrae in the Solar Photosphere: Analysis from Multi-instrument Observations. *ApJ.* Vol. 787, p. 57. Available from DOI: `10.1088/0004-637X/787/1/57`.

Zwaan, C., 1985. The Emergence of Magnetic Flux. *Sol. Phys.* Vol. 100, p. 397. Available from DOI: `10.1007/BF00158438`.

Zwaan, C., 1987. Elements and patterns in the solar magnetic field. *ARA&A*. Vol. 25, pp. 83–111. Available from DOI: `10.1146/annurev.aa.25.090187.000503`.

List of Publications

1. V. Abbasvand, M. Sobotka, M. Švanda, P. Heinzel, **M. García-Rivas**, C. Denker, H. Balthasar, M. Verma, I. Kontogiannis, J. Koza, D. Korda, and C. Kuckein, 2020. Observational study of chromospheric heating by acoustic waves. *Astronomy & Astrophysics.* 642:A52. DOI: 10.1051/0004-6361/202038559
2. **M. García-Rivas**, J. Jurčák, and N. Bello González, 2024a. Magnetic properties of the umbral boundary during sunspot decay. A comparative study of multiple datasets. *Astronomy & Astrophysics.* In press. DOI:10.1051/0004-6361/202348068
3. **M. García-Rivas**, J. Jurčák, and N. Bello González, 2021. Magnetic properties on the boundary of an evolving pore. *Astronomy & Astrophysics.* 649:A129. DOI:10.1051/0004-6361/202039661
4. **M. García-Rivas**, J. Jurčák, and N. Bello González, 2019. Vertical magnetic field on the boundary of an evolving pore. *WDS'19 Proceedings of Contributed Papers — Physics*, pp. 131–137.
5. **M. García-Rivas**, J. Jurčák, N. Bello González, J.M. Borrero, R. Schlichenmaier, and P. Lindner, 2024b. Onset of penumbra formation. *Astronomy & Astrophysics.* 686:A112. DOI: 10.1051/0004-6361/202348764
6. **M. García-Rivas**, J. Kašparová, A. Berlicki, M. Švanda, J. Dudík, D. Čtvrtečka, M. Zapiór, W. Liu, M. Sobotka, M. Pavelková, and G. G. Motorina, 2024c. Flare heating of the chromosphere: Observations of flare continuum from GREGOR and IRIS. *Astronomy & Astrophysics.* (Submitted)
7. M. Sobotka, J. Jurčák, J.S. Castellanos Durán, and **M. García-Rivas**, 2024. The relation between magnetic field inclination and the apparent motion of penumbral grains. *Astronomy & Astrophysics.* 682:A65. DOI:10.1051/0004-6361/202347979

Conference contributions

Contributed talks:

- 21 - 24 September 2020. **Annual Meeting of the German Astronomical Society**. Virtual.
- 20 - 22 October 2020. **25th National Solar Physics Meeting**. SCO Hurbanovo. Virtual.
- 10 June 2022. **Student meeting**. General Assembly of the Czech Astronomical Society. Ostrava, Czech Republic.
- 19 - 23 September 2022. **Hinode-15 / IRIS-12**. Prague, Czech Republic.
- 8 -12 May 2023. **SOLARNET conference**. Potsdam, Czech Republic.

Posters:

- 30 June - 6 July 2019. **IAU Symposium 354**. Copiapó, Chile.
- 13 -15 July 2020. **XIV.0 Scientific SEA Meeting**, Spanish Astronomical Society. Virtual.
- 1 -4 March 2021. **II-50**. Indian Institute of Astrophysics. Virtual.
- 6 - 10 September 2021. **ESPM-16**. Virtual.
- 24 - 29 September 2023. **Hinode-16 / IRIS-13**. Niigata, Japan.